

**Novel Experiments for the Investigation of Non-Ideal Compressible Fluid Dynamics  
The ORCHID and First Results of Optical Measurements**

Head, A.J.

**DOI**

[10.4233/uuid:a3b03976-2df6-435c-b7df-1505718fcd3a](https://doi.org/10.4233/uuid:a3b03976-2df6-435c-b7df-1505718fcd3a)

**Publication date**

2021

**Document Version**

Final published version

**Citation (APA)**

Head, A. J. (2021). *Novel Experiments for the Investigation of Non-Ideal Compressible Fluid Dynamics: The ORCHID and First Results of Optical Measurements*. [Dissertation (TU Delft), Delft University of Technology]. <https://doi.org/10.4233/uuid:a3b03976-2df6-435c-b7df-1505718fcd3a>

**Important note**

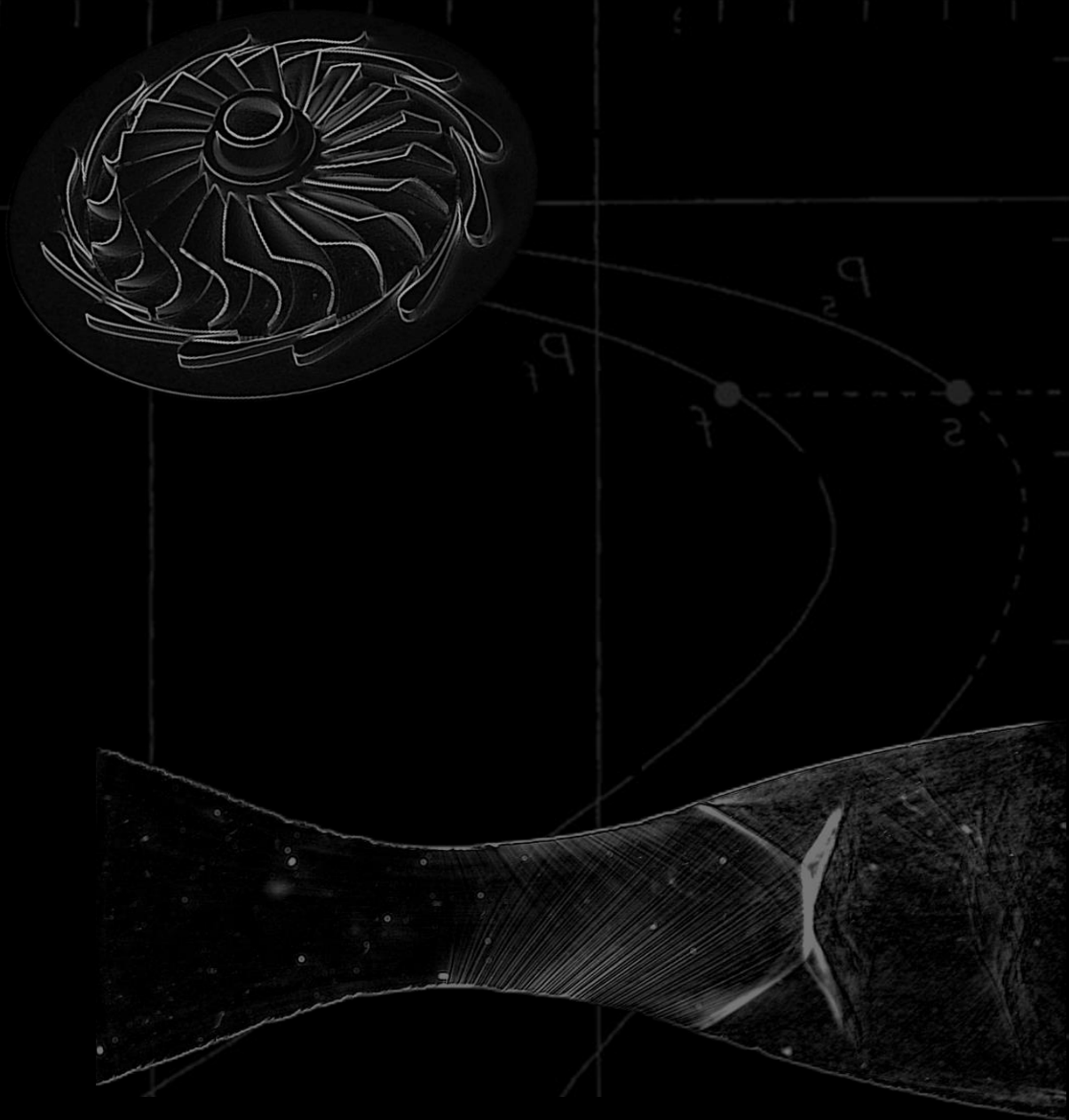
To cite this publication, please use the final published version (if applicable).  
Please check the document version above.

**Copyright**

Other than for strictly personal use, it is not permitted to download, forward or distribute the text or part of it, without the consent of the author(s) and/or copyright holder(s), unless the work is under an open content license such as Creative Commons.

**Takedown policy**

Please contact us and provide details if you believe this document breaches copyrights.  
We will remove access to the work immediately and investigate your claim.



# **Novel Experiments for the Investigation of Non-Ideal Compressible Fluid Dynamics: The ORCHID and First Results of Optical Measurements**

Adam Joseph Head





# **NOVEL EXPERIMENTS FOR THE INVESTIGATION OF NON-IDEAL COMPRESSIBLE FLUID DYNAMICS**

**THE ORCHID AND FIRST RESULTS OF OPTICAL  
MEASUREMENTS**

## **Proefschrift**

ter verkrijging van de graad van doctor  
aan de Technische Universiteit Delft,  
op gezag van de Rector Magnificus Prof.dr.ir. T.H.J.J. van der Hagen,  
voorzitter van het College voor Promoties,  
in het openbaar te verdedigen op  
woensdag 29 september 2021 om 10:00 uur

door

**Adam Joseph HEAD**

Bachelors of Engineering / Science  
University of Queensland, Australië  
geboren te Laura, Australië

Dit proefschrift is goedgekeurd door de

Promotor: Prof.dr.ir. P. Colonna

Copromotor: Dr. C.M. de Servi

Samenstelling promotiecommissie:

Rector Magnificus, voorzitter

Prof.dr.ir. P. Colonna, Technische Universiteit Delft, promotor

Dr. C.M. de Servi Technische Universiteit Delft, copromotor

*Onafhankelijke leden:*

Prof.dr.ir. W. de Jong Technische Universiteit Delft

Prof. R. Martinez-Botas Imperial College London, Verenigd Koninkrijk

Prof. Sotirios Karellas National Technical University of Athens, Griekenland

Dr. A. Spinelli Politecnico di Milano, Italië

Dr. M. White City University of London, Verenigd Koninkrijk

Prof. dr. ir. D. von Terzi Technische Universiteit Delft, reservelid



This research is supported by the Applied and Engineering Science Division (TTW) of the Dutch Research Council (NWO) and the Technology Program of the Ministry of Economic Affairs, the Netherlands, grant number 12811.

*Keywords:* Organic Rankine Cycle, transonic and supersonic flow, experiments, simulations, Verification, Validation and Uncertainty Quantification.

*Printed by:* Ridderprint B.V.; [www.ridderprint.nl](http://www.ridderprint.nl); [info@ridderprint.nl](mailto:info@ridderprint.nl)

*Front & Back:* M. Lammers.

Copyright © 2021 by A. J. Head<sup>1</sup>

ISBN Ebook 978-94-6366-442-4

ISBN Hardback 978-94-6366-450-9

An electronic version of this dissertation is available at

<http://repository.tudelft.nl/>.

---

<sup>1</sup> Author email: [adam.head@uqconnect.edu.au](mailto:adam.head@uqconnect.edu.au)

*To my loving parents Benjamin Joseph Head and Kathryn Fay Head. My wonderful  
brothers Luke and Joshua, and the love of my life Max Lammers.*

A. J. Head



# ABSTRACT

The vast number of pioneering theoretical developments in the area of non-classical gas dynamics together with the rising number of applications of organic Rankine cycle (ORC) technology have shaped a new branch of fluid mechanics called non-ideal compressible fluid dynamics (NICFD). This field of fluid mechanics is concerned with flows of dense vapors, whose properties do not comply with the ideal gas model. These types of flows occur in dense vapors, supercritical fluids and liquid-vapor mixtures.

NICFD is encountered in a variety of industrial processes, the most relevant in the power and propulsion sector, and is of interest for fundamental research. Chapter 2 documents an extensive literature review which covers the main developments in the numerical, theoretical and experimental areas. In particular, the review of current and past experiments was aimed at summarizing the lessons learned. Despite the relevance of NICFD applications, experimental information regarding this type of flows is scarce, due to the challenges inherent with the operating conditions of such experiments. The main objective of the research documented in this dissertation was to perform accurate measurements of NICFD flows which can then be used to assess the predictive capabilities of state-of-the-art numerical tools. To this end, the design and commissioning of suitable and fully instrumented facilities capable of generating NICFD flows in a multitude of steady, controlled conditions is necessary in order to provide high-quality and well characterised data. Arguably, state-of-the-art optical techniques are most suited for this goal, together with more conventional temperature, pressure and mass flow rate measurements.

Advanced laser diagnostic techniques such as particle image velocimetry (PIV) are possibly the measurement technique of choice when accurate measurements with a high spatial and temporal resolution are needed. However, the use of PIV or other optical techniques capable of providing local and instantaneous information within the flow is not documented. Therefore, a feasibility study was conducted by means of a simpler experiment: the planar PIV technique was applied to characterise the dense vapor of an organic fluid ( $D_4$ , a siloxane) stirred within a transparent container. Chapter 3 documents the successful results of this experiment. The optical properties of the dense vapor make PIV possible. Titanium dioxide ( $TiO_2$ ) seeding particles were used to track the low-speed motion of the fluid around a rotating disk. Vector fields of the natural convection flow and of the superposition of natural convection and rotating flow were acquired and studied as exemplary cases. The particles adequately trace the flow since the calculated Stokes number is  $6.5 \times 10^{-5}$ . The quality of the experimental data was assessed by means of particle seeding density and particle image Signal to Noise ratio (S/N). The results are deemed acceptable in view of envisaged high-speed flow experiments.

In order to obtain measurement data of high-speed vapor flows in the NICFD regime, new experimental facilities must be conceived, designed, realized and tested. Chapter 4 presents the organic Rankine cycle hybrid integrated device (ORCHID), which was de-

signed, built and commissioned at the Delft University of Technology. The facility can operate continuously and with a wide range of operating conditions. The maximum operating pressure and temperature are 25 bara and 350 °C. The facility has been designed to operate with siloxane MM as the working fluid, but it was numerically verified that it may also be operated with other working fluids such as MDM, MD<sub>2</sub>M, D<sub>4</sub>, D<sub>5</sub>, D<sub>6</sub>, pentane, cyclopentane, NOVEC649, PP2, PP80, PP90, and toluene. Two test sections allow to operate the ORCHID either as a supersonic/transonic vapor tunnel or as an ORC turbine test bed. Currently, a supersonic nozzle featuring a throat of 150 mm<sup>2</sup> with optical access allows to perform gas dynamic experiments for the validation of numerical simulation codes. A second test section, a test-bench for mini-ORC expanders, is being designed and will accommodate a fully instrumented 10 kW<sub>e</sub> machine, however machines of any configuration and with a rated power of up to approximately 80 kW<sub>e</sub> can be tested.

Chapter 5 documents the achievements reached during the commissioning of the ORCHID. The successful commissioning of the setup with MM as the working fluid is detailed and discussed based on the recordings of several test runs, including the start up and shut down of the facility. Data were acquired during the operation at steady state at the two main operating conditions typical of supersonic nozzle and ORC turbine tests. The operation of the facility is characterized with regards to the process stability, moreover process variables are assessed for their uncertainties. The correct operation of the nozzle test section was verified with a mass flow rate of fluid of  $\dot{m} = 1.15$  kg/s, and at a thermodynamic state at the nozzle inlet corresponding to  $T = 252$  °C and  $P = 18.36$  bara. The test section conditions typical of a turbine experiment were  $T = 275$  °C,  $P = 20.8$  bara, with a mass flow rate of  $\dot{m} = 0.17$  kg/s. All the relevant process variables of the test section are affected by a relative uncertainty that is lower than 0.6 %.

Chapter 6 reports the results of the first supersonic nozzle experiments. Schlieren images of the MM flow through the two-dimensional converging-diverging nozzle with the inlet in the NICFD regime were recorded, together with the static pressure profile along the nozzle. A series of schlieren photographs displaying Mach waves in the supersonic flow were obtained and are documented at two operating conditions, namely, for inlet conditions corresponding to a stagnation temperature and pressure of  $T_0 = 252$  °C and  $P_0 = 18.4$  bara, and to a back pressure of 2.1 bara. Furthermore, static pressure values were measured along the expansion path for operating conditions given by  $T_0 = 252$  °C and  $P_0 = 11.2$  bara at the nozzle inlet and by a back pressure of 1.2 bara. The two inlet conditions of the fluid correspond to a compressibility factor of  $Z_0 = 0.58$  and  $Z_0 = 0.79$ . These Mach number values together with the values of the static pressure along the top and the bottom profile of the nozzle were used for a first assessment of the capability of evaluating NICFD effects occurring in dense organic vapor flows by comparison with the results of CFD simulations. The outcome of this initial comparison was deemed satisfactory.

Chapter 7 introduces the first steps towards the validation of a CFD solver for non-ideal compressible flows. In particular, an industry-standard validation method was used together with synthetic experimental data (experimental data were not available yet) to illustrate, as an exercise, how the uncertainty of NICFD software can be quantified. The assessment is limited to determining how the uncertainties in model inputs, e.g., fluctuations in boundary conditions and thermodynamic property models influ-

ence the overall accuracy of NICFD simulations. The assessment of the uncertainty of the other sub-models is left for a successive phase of this research program. The validation exercise confirmed the applicability of the proposed method, but also pointed out that the adopted validation metrics should be complemented with additional statistical indicators. The error sources in the designed experiment are identified and all the uncertainties are adequately quantified.

The final chapter summarizes the answers to the research questions listed in the first chapter, above all that the ORCHID was successfully commissioned and can generate stable dense vapor flows of organic fluids for both fundamental gas dynamic experiments and ORC turbine testing. The first experiments demonstrate that it can be used to obtain accurate optical and non-optical measurements of supersonic nozzle flows for the validation of CFD codes, including flows in the NICFD regime. An overview of the next phases of the research program is also provided.





# SAMENVATTING

Het grote aantal baanbrekende theoretische ontwikkelingen op het gebied van niet klassieke gasdynamica hebben samen met het stijgende aantal toepassingen van *organic Rankine cycle* ORC-technologie een nieuwe tak van de vloeistofmechanica doen ontstaan, die *non-ideal compressible fluid dynamics* (NICFD) wordt genoemd. Dit gebied van de vloeistofmechanica houdt zich bezig met stromingen van dichte dampen, waarvan de eigenschappen niet voldoen aan het ideale gasmodel. Dit soort stromingen komen voor in dichte dampen, superkritische vloeistoffen en vloeistof-dampmengsels.

NICFD komt voor in een verscheidenheid van industriële processen, het meest relevant in de energie- en aandrijvingssector, en is van belang voor fundamenteel onderzoek. In hoofdstuk 2 wordt een uitgebreid literatuuroverzicht gegeven waarin de belangrijkste ontwikkelingen op numeriek, theoretisch en experimenteel gebied aan de orde komen. In het bijzonder was het overzicht van huidige en vroegere experimenten bedoeld om de geleerde lessen samen te vatten. Ondanks de relevantie van NICFD toepassingen is experimentele informatie betreffende dit type stromingen schaars, als gevolg van de uitdagingen die inherent zijn aan de werkingsomstandigheden van dergelijke experimenten. Het hoofddoel van het in dit proefschrift gedocumenteerde onderzoek was het uitvoeren van nauwkeurige metingen van NICFD-stromingen, die vervolgens kunnen worden gebruikt om de voorspellende capaciteiten van state-of-the-art numerieke hulpmiddelen te beoordelen. Daartoe moeten geschikte en volledig geïnstrumenteerde installaties worden ontworpen en in bedrijf gesteld, die in staat zijn NICFD-stromingen te genereren in een veelheid van stabiele, gecontroleerde omstandigheden, om hiermee gekarakteriseerde gegevens van hoge kwaliteit te kunnen leveren. Ongetwijfeld zijn de meest geavanceerde optische technieken hiervoor het meest geschikt, samen met meer conventionele temperatuur-, druk- en massastroommetingen.

Geavanceerde laserdiagnostische technieken zoals *particle image velocimetry* (PIV) zijn wellicht de juiste meettechniek indien nauwkeurige metingen met een hoge ruimtelijke en temporele resolutie nodig zijn. Het gebruik van PIV of andere optische technieken die plaatselijke en ogenblikkelijke informatie binnen de stroming kunnen verschaffen, is echter niet gedocumenteerd. Daarom werd een haalbaarheidsstudie uitgevoerd met behulp van een eenvoudiger experiment: de planaire PIV-techniek werd toegepast om de dichte damp te karakteriseren van een organische vloeistof ( $D_4$ , een siloxaan) die in een transparant vat werd geroerd. In hoofdstuk 3 worden de succesvolle resultaten van dit experiment beschreven. De optische eigenschappen van de dichte damp maken PIV mogelijk. (Zaai)Deeltjes van ( $TiO_2$ ) werden gebruikt om de lage snelheidsbeweging van de vloeistof rond een roterende schijf te volgen. Vectorvelden van de natuurlijke convectiestroom en van de superpositie van natuurlijke convectie en roterende stroming werden verzameld en bestudeerd als voorbeeldgevallen. De deeltjes traceren de stroming op adequate wijze aangezien het berekende Stokesgetal  $6.5 \times 10^{-5}$  bedraagt. De kwaliteit van de experimentele gegevens werd beoordeeld aan de hand van de dichtheid

van de zaaideeltjes en de signaal-ruisverhouding (S/N) van het deeltjesbeeld. De resultaten worden aanvaardbaar geacht met het oog op geplande experimenten met hoge snelheidsstromingen.

Om meetgegevens te verkrijgen van dampstromen met hoge snelheid in het NICFD-regime, moeten nieuwe experimentele faciliteiten worden bedacht, ontworpen, gerealiseerd en getest. In hoofdstuk 4 wordt de ORCHID (Organic Rankine Cycle Hybrid Integrated Device) gepresenteerd, die is ontworpen, gebouwd en in bedrijf gesteld aan de Technische Universiteit Delft. De installatie kan continu en met een breed scala van bedrijfsomstandigheden werken. De maximale bedrijfsdruk en -temperatuur zijn 25 bara en 350 °C. De installatie is ontworpen om te werken met siloxaan MM als werkvloeistof, maar er is numeriek geverifieerd dat deze ook kan werken met andere werkvloeistoffen, zoals MDM, MD<sub>2</sub>M, D<sub>4</sub>, D<sub>5</sub>, D<sub>6</sub>, pentane, cyclopentane, NOVEC649, PP2, PP80, PP90, and toluene. Twee testsecties maken het mogelijk de ORCHID te gebruiken als supersonische/transonische dampptunnel of als testbed voor ORC-turbines. Momenteel kunnen in een supersonisch Lavalstraalpijp met een keel van 150 mm<sup>2</sup> met optische toegang gasdynamische experimenten worden uitgevoerd voor de validatie van numerieke simulatiecodes. Een tweede testsectie, een testbank voor mini-ORC expanders, wordt momenteel ontworpen en zal plaats bieden aan een volledig geïstrumenteerde machine van 10 kW<sub>e</sub>, maar machines van elke configuratie en met een nominaal vermogen tot ongeveer 80 kW<sub>e</sub> kunnen worden getest.

In hoofdstuk 5 worden de resultaten van de inbedrijfstelling van de ORCHID gedocumenteerd. De succesvolle ingebruikname van de installatie met MM als werkvloeistof wordt gedetailleerd beschreven en besproken op basis van de registraties van verschillende testruns, inclusief het opstarten en afsluiten van de installatie. Er werden gegevens verzameld tijdens de werking in "steady state" bij de twee belangrijkste bedrijfsomstandigheden die typisch zijn voor supersonische straalpijp- en ORC-turbinetests. De werking van de installatie wordt gekarakteriseerd met betrekking tot de processtabiliteit, verder worden procesvariabelen beoordeeld op hun onzekerheden. De goede werking van het testgedeelte van de Lavalstraalpijp werd geverifieerd met een vloeistofmassastroom van 1.15 kg/s, en bij een thermodynamische toestand aan de straalpijpinlaat die overeenkomt met  $T = 252\text{ °C}$  en  $P = 18.36\text{ bara}$ . De voor een turbine-experiment typische omstandigheden in het testgedeelte waren  $T = 275\text{ °C}$ ,  $P = 20.8\text{ bara}$ , met een massastroom van 0.17 kg/s. Alle relevante procesvariabelen van het testgedeelte worden beïnvloed door een relatieve onzekerheid die kleiner is dan 0.6 %.

Hoofdstuk 6 rapporteert de resultaten van de eerste supersonische straalpijpxperimenten. Schlierenbeelden van de MM-stroming door de tweedimensionale convergerende-divergerende straalpijp met de inlaat in het NICFD-regime werden opgenomen, samen met het statische drukprofiel langs de straalpijp. Een reeks schlierenfoto's met Mach golven in de supersonische stroming waren opgenomen en zijn gedocumenteerd in twee werkingsomstandigheden, met name voor inlaatomstandigheden die overeenkomen met een stagnatietemperatuur en -druk van  $T_0 = 252\text{ °C}$  en  $P_0 = 18.4\text{ bara}$ , en met een tegendruk van 2.1 bara. Bovendien werden statische drukwaarden gemeten langs het expansiepad voor bedrijfsomstandigheden gegeven door  $T_0 = 252\text{ °C}$  en  $P_0 = 11.2\text{ bara}$  aan de nozzle-inlaat en door een tegendruk van 1.2 bara. De twee inlaatcondities van de vloeistof komen overeen met een samendrukbaarheidsfactor van  $Z_0 = 0.58$  en  $Z_0 = 0.79$ .

Deze Machgetalwaarden werden samen met de waarden van de statische druk langs het bovenste en onderste profiel van de Lavalstraalpijp gebruikt voor een eerste beoordeling van de mogelijkheid om NICFD-effecten te evalueren die zich voordoen in stromingen met dichte organische damp door vergelijking met de resultaten van CFD-simulaties. Het resultaat van deze eerste vergelijking werd bevredigend geacht.

In hoofdstuk 7 worden de eerste stappen naar de validatie van een CFD solver voor niet-ideale samendrukbare stromingen voorgesteld. In het bijzonder werd een industriestandaard validatiemethode gebruikt samen met synthetische experimentele gegevens (experimentele gegevens waren nog niet beschikbaar) om, bij wijze van oefening, te illustreren hoe de onzekerheid van NICFD software kan worden gekwantificeerd. De beoordeling is beperkt tot het bepalen hoe de onzekerheden in de modelinputs, bv. fluctuaties in randvoorwaarden en thermodynamische eigenschappenmodellen, de algemene nauwkeurigheid van NICFD-simulaties beïnvloeden. De beoordeling van de onzekerheid van de andere submodellen wordt overgelaten aan een volgende fase van dit onderzoeksprogramma. De validatie-opdracht bevestigde de toepasbaarheid van de voorgestelde methode, maar wees er ook op dat de aangenomen validatiemetriek moet worden aangevuld met aanvullende statistische indicatoren. De foutenbronnen in het ontworpen experiment zijn geïdentificeerd en alle onzekerheden zijn adequaat gekwantificeerd.

Het laatste hoofdstuk vat de antwoorden op de onderzoeksvragen van het eerste hoofdstuk samen, vooral dat de ORCHID met succes in gebruik is genomen en stabiele dichte dampstromen van organische vloeistoffen kan genereren voor zowel fundamentele gasdynamische experimenten als het testen van ORC-turbines. De eerste experimenten tonen aan dat de ORCHID-installatie kan worden gebruikt voor het verkrijgen van nauwkeurige optische en niet-optische metingen van supersonische straalpijpsromingen voor de validatie van CFD-codes, met inbegrip van stromingen in het NICFD-regime. Er wordt ook een overzicht gegeven van de volgende fasen van het onderzoeksprogramma.



# CONTENTS

<b>1</b>	<b>Introduction</b>	<b>1</b>
1.1	Background	1
1.2	Applications of NICFD	3
1.3	Motivation and Scope	7
1.4	Overview	9
<b>2</b>	<b>Non-ideal Compressible Fluid Dynamics with a Historical Perspective</b>	<b>11</b>
2.1	Pioneering Theoretical Developments	14
2.2	First Experiments	19
2.3	Extension of Theoretical, Experimental and Numerical Studies	25
2.4	Recent Progress	30
2.4.1	Shock Tube Experiments	30
2.4.2	Vapor Tunnels	32
2.4.3	Simulations and Applications	42
2.4.4	Consolidation of the Theory of Nonclassical Gasdynamics	47
2.5	Thermodynamic States of the Fluid in NICFD Expansions and Related $Z$ and $\Gamma$ Values	49
<b>3</b>	<b>Feasibility of PIV in Low Speed Organic Fluid Flows</b>	<b>51</b>
3.1	Introduction	51
3.2	Optical Properties and Particle Compatibility	52
3.3	The Non-Intrusive Vapor Analyser (NIVA)	53
3.4	Experimental Procedure	56
3.5	Exemplary Flow Fields	58
3.5.1	Rotating Disk	58
3.5.2	Natural Convection	59
3.5.3	Uncertainty Quantification	61
3.6	Conclusions and Outlook	61
<b>4</b>	<b>Preliminary Design of the ORCHID</b>	<b>63</b>
4.1	Introduction	64
4.2	ORC Vapor Tunnels	65
4.3	Research ORC Modules	66
4.4	The ORCHID Concept	67
4.5	Envisaged Test Section Experiments	68
4.5.1	Nozzle Test Section	68
4.5.2	Turbine Test Section	70
4.6	Fluid Candidates	71
4.7	Main Design Constraints	73

4.8	Design Procedure	73
4.8.1	Nozzle Test Section	74
4.8.2	Turbine Test Section	78
4.9	Results	79
4.9.1	Nozzle Test Section	79
4.9.2	Turbine Test Section	81
4.9.3	Design Specifications for the Balance of Plant	81
4.10	Conclusions	82
<b>5</b>	<b>Detailed Design and Commissioning of the ORCHID Balance of Plant</b>	<b>85</b>
5.1	Introduction	86
5.2	Design Requirements and Limitations	86
5.3	Balance of Plant Configuration	88
5.4	Main Equipment Characteristics	95
5.4.1	Working Fluid Feed Pump and Booster pump	95
5.4.2	Heat Transfer Equipment	99
5.5	Instrumentation, Data Acquisition & Control	107
5.5.1	Data Acquisition and Control System	107
5.5.2	Instrumentation	112
5.5.3	Control Strategy and Implementation	113
5.6	Commissioning	120
5.6.1	Validation of Operation	121
5.6.2	Results with Uncertainties	131
5.7	Conclusions and Outlook	136
<b>6</b>	<b>Design and Commissioning of the Nozzle Test Section</b>	<b>139</b>
6.1	Introduction	140
6.2	Specifications of the Commissioning Experiment	141
6.3	The Nozzle Test Section	144
6.3.1	Settling Chamber	144
6.3.2	Nozzle Housing	148
6.3.3	Receiver	149
6.4	Total and Static Pressure Measurements	152
6.5	Temperature Measurements	154
6.6	Schlieren Imaging	156
6.6.1	Refractive Index of Dense Siloxane Vapors and its Influence on Schlieren Flow Visualization	161
6.6.2	The Selected Layout of the Schlieren System	163
6.7	Experimental Procedure	166
6.7.1	Pressure Field Measurements	166
6.7.2	Flow Imaging for Mach Field Estimation	169
6.7.3	Estimation of the Local Mach Number	170
6.8	Operating Conditions of the Commissioning Experiments	173
6.8.1	Pressure Field: Process Run PR.027	174
6.8.2	Schlieren: Process Run PR.025	175
6.9	Results	175

6.9.1	Pressure Field, PR.027	175
6.9.2	Mach Field, PR.025	178
6.9.3	Simulations	183
6.9.4	Temperature and Pressure Measurement Uncertainties	187
6.9.5	Uncertainty of the Mach Number Estimations	189
6.9.6	Experimental Data with Uncertainty vs Simulations	195
6.10	Conclusions and Recommendations	197
<b>7</b>	<b>Towards the Validation of CFD Solvers for Non-ideal Compressible Flows</b>	<b>201</b>
7.1	Introduction	202
7.2	Validation of a CFD Code for NICFD Simulations	203
7.3	Envisaged Validation Experiments	204
7.4	Uncertainty Quantification (UQ) Framework	205
7.5	Model Uncertainties	207
7.6	Pseudo-Experimental Uncertainties	212
7.7	Results and Discussion	213
7.8	Conclusions	215
<b>8</b>	<b>Final Remarks and Outlook</b>	<b>219</b>
8.1	Closure	219
8.2	Future Work and Recommendations	223
<b>A</b>	<b>Settling Chamber</b>	<b>229</b>
<b>B</b>	<b>Nozzle Profiles and Meshes of the Flow Domains for CFD Simulations</b>	<b>231</b>
<b>C</b>	<b>Scanivalve Pressure Measurement System</b>	<b>235</b>
<b>D</b>	<b>Analysis of the Steadiness of the Experimental Runs</b>	<b>243</b>
	<b>Acknowledgements</b>	<b>275</b>
	<b>Curriculum Vitæ</b>	<b>279</b>





# 1

## INTRODUCTION

### 1.1. BACKGROUND

Aerodynamics is a major branch of fluid mechanics, and its theory is based on the assumption that the fluid, air, obeys the ideal gas law

$$Pv = RT. \quad (1.1)$$

Examples of flows of fluids whose properties can be modeled with the ideal gas law are numerous. Fluid flows exhibiting features different from those of typical aerodynamics are prominent, for example, when the gas undergoes ionization and dissociation, at very high temperature, in highly supersonic conditions [14]. Even if the properties of the gases can still be approximated using the perfect gas model, these flows are often termed *real gas* flows [14, 157]. However, also flows in which the fluid thermodynamic properties depart significantly from those provided by the perfect gas model are called real gas flows in the literature, causing some confusion, see e.g., Grossman [157].

The work documented in this dissertation is related to non-reacting compressible flows in which thermodynamic properties are related in a complex way. Examples of these flows include those characterized by low Mach numbers, and transonic or supersonic flows, provided that the thermodynamic properties of the fluid do not comply with the perfect gas model. For all simple compressible substances, in vapor or liquid states close to the critical point or in vapor states at temperatures and pressures near saturated conditions, thermodynamic properties are governed by complex relations, see Fig. 1.1. In addition, compressible flows entailing phase change also may require complex models for the estimation of fluid thermodynamic properties, thus they also belong to this category.

The branch of fluid mechanics that deals with this type of flows has been recently christened non-ideal compressible fluid dynamics (NICFD) [84, 162, 295]. NICFD flows are quantitatively and qualitatively different from ideal gas flows. Their scientific investigation is motivated by their multiple relevant engineering applications. Chapter 2

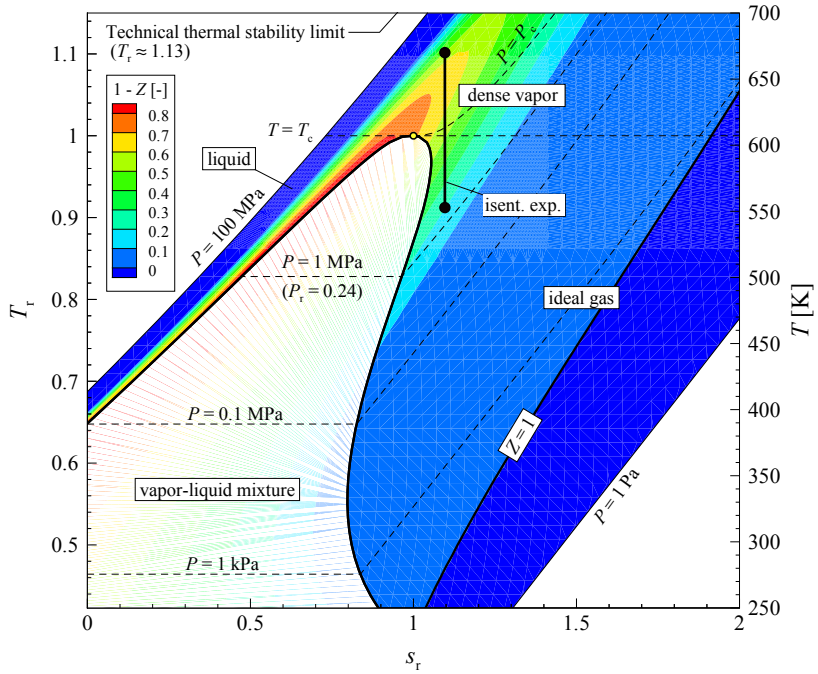


Figure 1.1:  $T - s$  state diagram for toluene. This chart shows the thermodynamic regions where the ideal gas law applies ( $Z - 1 \approx 0$ ) and where more complex property models must be employed to evaluate fluid thermodynamic properties, e.g., in proximity to the critical point. The representation of an exemplary isentropic expansion in the dense vapor region is also indicated. The diagram is obtained with FLUIDPROP (Model = REF-PROP). Taken from Reynolds & Colonna [321, p. 170].

provides an overview of the theory of NICFD flows, main terminology and definitions, together with a literature review covering these aspects, while in the following some application examples are illustrated to provide context and information about the relevance of this study, with its motivation and scope.

## 1.2. APPLICATIONS OF NICFD

NICFD flows occur in numerous industrial processes, in some special applications and are of interest for fundamental research. Fluid mechanics is a broad field with countless applications in every aspect of human activity. Aerodynamics and hydraulics are more commonly known and studied, still NICFD is relevant in many applications in industry. NICFD flows occur in processes employing steam at high pressure and temperature, and dense vapors of other inorganic and organic fluids. Many chemical processes, and power applications employ fluids made of organic molecules,<sup>1</sup> see, e.g., Figure 1.2, being expanded or compressed in states whereby the ideal gas law does not apply (Figure 1.1). Table 1.1 presents an overview of technologies in which knowledge of NICFD is relevant, subdivided into categories. It also provides few references to seminal scientific contributions in those technical fields.

Perhaps the most relevant industrial instances of NICFD flows occurs in the turbo-machinery equipment of both subcritical and supercritical Rankine power plants, either in the nozzle of the high-pressure stage of turbines or in the last stages, where condensation occurs, see Refs. [203, 296, 340] and Ref. [27, Ch. 2]. Thermal power plants where the turbine is steam-driven are the most common electricity generators in the world [67]. If an organic substance is the working fluid, the same Rankine cycle concept is used in small and medium power plants for the conversion of renewable energy sources such as geothermal reservoirs, solar radiation, biomass combustion, industrial waste heat recovery, urban solid waste and landfill gas combustion, thermal energy recovery from other prime movers (reciprocating engines, gas turbines, fuel cells, etc.) and ocean thermal gradients [83].

NICFD effects are of interest in the supersonic and transonic flow through an organic Rankine cycle (ORC) turbine nozzle [87], see the isentropic expansion in Fig. 1.1 or in the transonic flow occurring in the compressor [30, 234] of future supercritical CO<sub>2</sub> (sc-CO<sub>2</sub>) power plants [57, 291, 324]. These types of flows are also common in the compressors of CO<sub>2</sub> capture and sequestration plants [30], which are currently studied as one of the mitigation measures to climate change [20]. Incidentally, flows in power plant heat exchangers that work close to the critical point, e.g., the cooler of a sc-CO<sub>2</sub> power plant or the primary heater of a supercritical Rankine cycle system, are only very lightly compressible, but the fluid properties do not obey the ideal gas law, thus properties must be estimated with complex thermophysical models, and the resulting flows are quantitatively and qualitatively different from ideal gas and incompressible flows.

---

<sup>1</sup>To a first approximation, fluids made from chemical compounds that contain carbon and derivatives thereof resulting from a chemical reaction, are termed *organic*, as described in Natta & Farina [275]. Natta and Farina extend the definition of organic substances to other molecules, if they were to give rise to chains and rings of an 'organic' type. However, here the definition of organic is restricted to substances containing at least a carbon atom.

Table 1.1: Industrial processes involving NICFD flows with selected references.

Sector	Application	Fluid	References
Sub-/super-critical Rankine power systems	Thermal energy recovery from renewable energy sources and prime movers	Hydrocarbons, siloxanes, perfluorocarbons and ethanol	Colonna <i>et al.</i> [83]
	Steam and sc-CO <sub>2</sub> power plants	H <sub>2</sub> O and sc-CO <sub>2</sub>	Guo <i>et al.</i> [169], Ockendon [284], Pecnik <i>et al.</i> [291], Baltadjiev <i>et al.</i> [30], Lettieri <i>et al.</i> [234] & De Servi <i>et al.</i> [112]
Process Industry	Liquefaction natural gas (LNG) and Ethylene plants	Mixture of gases, e.g., hydrocarbons & refrigerants	Boncinelli <i>et al.</i> [48]
	Chemical and fuel transport	Methane & and natural gas	Bober & Chow [46], Leung & Epstein [235] & Thorley & Tiley [381]
	Valves	N <sub>2</sub>	Beune [40]
	Refrigeration and heat pump systems	R134a & R142b	Bassi <i>et al.</i> [33] & Bartosiewicz <i>et al.</i> [32]
Flight vehicles	Rockets (Turbopumps)	Cryogenic fuel (oxygen, hydrogen)	Masquelet [246]
Combustion	Fuel injection	Jet Fuel (JP-1)	Lettieri <i>et al.</i> [233], Rachedi <i>et al.</i> [308] & Rachedi <i>et al.</i> [309]

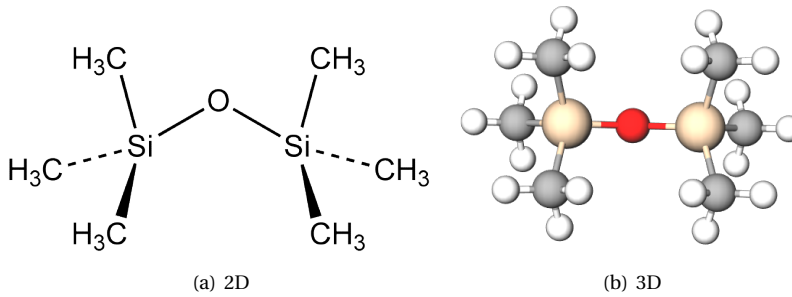


Figure 1.2: Stereo structural formula of hexamethyldisiloxane (MM).

Turbomachinery operating partly in the NICFD regime is also common in the oil and gas and in the process industry [48, 200, 287]. Liquefaction natural gas plants and ethylene synthesis [175] make use mainly of centrifugal cryogenic compressors which sometimes operate with a complex mixture of gases, e.g., hydrocarbons and refrigerants. Performance predictions and fluid dynamic designs are obtained with CFD simulation tools relying on thermodynamic properties calculated with a suitable equation of state. The accuracy of these predictions is highly dependent on the equation of state and its ability to provide gas or gas mixture thermodynamic properties. A poor evaluation of total pressure, temperature and density leads to an inaccurate prediction of the: 1. quantity of gas (mixture) delivered, 2. pressure rise produced, 3. head, 4. shaft power required, 5. efficiency, 6. surge point; and 7. choke point [11]. As an example, Pacheco *et al.* [287] presents the measurements and performance predictions of a LNG Propane Compressor. The work reports that the discrepancies between prediction and measurement of the performance of the 1<sup>st</sup> and 2<sup>nd</sup> stages of the centrifugal compressor are partly due to the inaccuracy of the employed fluid thermodynamic model.<sup>2</sup>

Chemical and fuel transport in the process industry also utilize a number of technologies requiring accurate NICFD flow simulations. In particular, technologies used in offshore production and transport of natural gas to consumption centers are often being improved or completely redesigned. Natural gas must be dehydrated when first extracted from reservoirs since it is often a two-phase mixture of water vapor, heavy hydrocarbons and various solids. One technology used to purify<sup>3</sup> natural gas is based on a device called *supersonic (swirling) separator* [181, 237, 273]. Its main components are: i) a de Laval nozzle, which is used to expand the mixture and which is affected by NICFD effects, ii) a swirling device, iii) a two-phase flow separator that separates the liquid from the gas, and, vi) a diffuser and directing vanes, which slows down the gas to recover part of the pressure. The supersonic separator is a compact device with no rotating parts. No fouling or deposition of solids and ice can occur due to the high gas speed (the dehy-

<sup>2</sup>The thermodynamic properties of a fluid are given by a thermodynamic model, which is comprised of a thermal/volumetric equation,  $P = P(v, t)$ , together with a caloric equation of state,  $c_p^0 = c_p^0(T)$  or alternatively, by a potential (or canonical) equation of state, like for example, an expression for the Helmholtz free energy in the form  $a = a(T, v)$  [321].

<sup>3</sup>The process of dehydration and separation of water vapor/heavy hydrocarbons and various solids.

dehydration efficiency increases with gas velocity) [200]. Since the gas flow mixture is compressible, shockwaves may occur and the prediction of their position is a key factor in determining the dehydration efficiency [53, 181]. Furthermore, design parameters for the separator, such as pressure loss ratio and flow rate, also influence the dehydration characteristics. Therefore, the code for flow simulations usually needed to design a device for the optimal dehydration of natural gas must be capable of correctly accounting for NICFD effects. Jassim & Muzychka [200] conducted a CFD study on the flow of natural gas through high-pressure supersonic nozzles. In the study they investigate the influence of the ideal gas assumption on the flow and on features such as shockwaves when simulating an expansion of methane and nitrogen. They conclude that shockwaves are predicted to occur upstream if the accurate modified Benedict-Webb-Rubin (MBWR) thermodynamic model is employed for the estimation of thermodynamic properties in the CFD simulations, if compared to simulations relying on the ideal gas model.

Flows of fluids in dense-vapor or two-phase conditions are relevant in throttling valves and ejectors of refrigeration and heat pump systems [32, 33]. In addition, matters of safety are imperative in the process industry and safety valves are usually sized with standardized methodologies. However, these methods are usually based on the ideal gas assumption, but at high pressures and low temperatures non-ideal effects cannot be ignored. Beune [40] evaluates the influence of complex thermodynamic models on the compressible gas dynamics occurring in safety valves. The discharge coefficient, i.e., the correction factor between the mass flow rate of an isentropic flow in a nozzle and the actual mass flow rate in a safety valve, is incorrectly predicted when compared to the *ideal*<sup>4</sup> valve sizing method.

Table 1.1 outlines that sub-components of rocket or aircraft engines also partly operate with NICFD flows. Advancements in manufacturing and material technologies have enabled combustors, e.g., those used in aircraft or space propulsion systems, to operate at conditions above the critical pressure and temperature of most fuels. In particular, the high-pressure combustion chamber of a liquid rocket engine operates above the critical pressure of most, if not all, liquid propellant combinations. For example, the operating pressures and temperatures of a typical hydrogen combustor are approx. 100 bar and 3600 K, respectively [246]. Turbopumps deliver liquid fuel, e.g., liquid hydrogen (LH2) ( $P_c = 13$  bar  $T_c = 33.2$  K), and oxygen LOx ( $P_c = 49.8$  bar  $T_c = 154.8$  K), into the main combustion chamber. These turbopumps are usually composed of radial pumps driven by axial turbines. These turbopumps operate at high speeds, high pressures, cryogenic temperatures, and steep temperature gradients. For example, supercritical hydrogen is injected in the combustion chamber inlet at conditions of around 100 bar, 106 K and 270 m/s, while oxygen is injected at 100 bar, 101 K and 11 m/s. As a result of the high pressures and cryogenic temperatures in the feeding system, the propellants are compressible and NICFD effects must be correctly accounted for. In the case of oxygen, the fluid is a compressible liquid when it is taken from the storage tanks through to the turbopump and then to the combustion chamber. In particular, oxygen behaves as a non-ideal vapor during the process of cryogenic injection into the high-pressure combustion chamber, e.g., when it undergoes phase transition from a compressed liquid to a supercritical vapor [246].

---

<sup>4</sup>Ideal refers to a critical nozzle flow model derived from the ideal gas theory, see Beune [40] for further details.

Similarly, the process of fuel injection in many current gas turbine combustors or high-pressure diesel engines [223] are notable examples of flows where fluid properties deviate significantly from those which can be described by an ideal gas law or by those of an incompressible liquid. It is common that during aircraft takeoff and landing, fuel is injected at supercritical conditions or near critical conditions into the gas turbine combustor, but also during climb and cruise [233, 308, 309].

Instances in which NICFD effects play an important role can be found not only in industrial processes and technologies, but also in research setups. Dense vapors made of heavy molecules can be used in supersonic wind tunnels instead of air to achieve higher Reynolds numbers, which can be varied almost independently from the Mach number [16]. In this wind tunnel, sulfur hexafluoride,  $\text{SF}_6$ , was used as working fluid. NICFD effects made it difficult to calculate the corrections necessary to obtain the shock locations and boundary layer properties in similar air flows.

### 1.3. MOTIVATION AND SCOPE

For centuries engineered systems underwent incremental improvements, usually as a result of the building and testing process. Modifications were made or a completely new design was adopted through the hard lessons learnt from previous iterations. This approach consumed resources such as time and money.

It was roughly around 1800 in England, during the industrial revolution, when the impact of modeling and simulation on engineering and design began to flourish. In the latter half of the 20th century, programmable digital computers reached a mature level of computational power, enabling the numerical solution of models based on partial differential equations. Today, simulations lead the design of engineered systems and terminology such as *virtual prototyping* or *virtual testing* is being used to describe the computer simulation of entire systems and their components [326]. As an example, even though the design of complex engineered systems such as gas turbine engines, commercial and military aircraft, and rocket engines continue to go through lengthy development programs — they do so with the support of simulation software. In particular, compressible fluid dynamics CFD codes are frequently used in the fluid dynamic design of process equipment, be it fluid machinery, heat exchangers, reactors and valves etc. This is due to the relatively high costs involved in building and maintaining experimental facilities. As a result, the importance of simulation tools has dramatically increased.

Software is now frequently used to assess the performance, reliability, robustness and safety of systems where little or no direct experimental data exist. However, the credibility of simulation tools, e.g., CFD or computational solid mechanics (CSM) software, must always be assessed with measurements in order to evaluate the accuracy of the results. This comparison is commonly referred to as the *validation step*. Wind tunnels and shock tubes were and still are commonly used in the field of fluid dynamics to acquire the detailed measurement data necessary for comparisons against predictions [280].

The field of NICFD is built upon sound theoretical and numerical foundations of which the seminal work is summarised in Chapter 2. However, despite the wealth of knowledge in these areas, dedicated facilities are scarce or are not flexible enough to accommodate all the operating conditions of interest. The technical challenges associated with the construction and operation of these new facilities are arguably higher in



comparison to traditional wind tunnels and shock tubes. The reasons being that most traditional facilities operate with air, nitrogen or other fluids at low temperatures and pressures.

New dedicated facilities for advancing the field of NICFD operate at higher temperatures and pressures, varying throughout the setup, with fluids which must be handled with care. This leads to strict operating procedures/checklists for start-up, nominal operation and shutdown. Additionally, maintenance procedures must be carried out on a frequent basis. Furthermore, trained personnel are mandatory in order to ensure a controlled and safe operation of the plant. These challenges have limited the successful construction and operation of these facilities and consequently, NICFD software codes still lack proper validation against measurement data.

The study of non-ideal phenomena occurring in components such as fluid machinery can help improve their design. One well known example is the Rankine cycle engine, in which compression shock waves often appear in the first turbine stages. The entropy loss associated with compression shock waves leads to a major reduction in the overall efficiency of the engine, see, e.g., Ref. [159].

The **main research question** of this dissertation is therefore

*How accurately can NICFD flows of dense organic vapors and supercritical fluids be simulated with current numerical tools?*

The term *accurately* implies a quantitative comparison between the prediction and what is measured. This can be achieved with an appropriate validation method and uncertainty quantification technique.

The aim of the present research is to provide accurate measurements of paradigmatic NICFD flows to allow the quantitative validation of state-of-the-art CFD tools. This can be done by designing specific experiments aimed at isolating some of the physical aspects affecting the flows in order to achieve higher accuracy and better understanding of the observed phenomena. The overall validation of the CFD code can be accomplished by assessing the various sub-models separately: thermodynamic and transport properties of the fluid, bulk flow and turbulence.

The research objectives and the main research question led to the following key research sub-questions:

1. *What are the key learnings from the previous studies involving NICFD theory, simulations and measurements, which can be useful for the design of the ORCHID and related experiments?*
2. *Which facility configuration and experiments should be designed to facilitate the means to obtain the experimental data needed for the validation of software?*
3. *What are the most feasible and accurate measurement techniques that could be used for studying these fluid flows?*
4. *Can all the main error sources in the designed experiment be identified and can the uncertainties be adequately quantified?*
5. *What validation method should be adopted to assess the accuracy of NICFD-capable CFD codes?*

The Non Intrusive Vapor Analyzer (NIVA) apparatus and the organic Rankine Cycle hybrid integrated device (ORCHID), together with the nozzle test section, were conceived, designed, engineered and commissioned in order to answer these research questions.

## 1.4. OVERVIEW

The aim of the research documented in this dissertation was to acquire measurement data in dense vapor flows and to make them available to the scientific community in order to assess the predictive features of computer codes capable of simulating NICFD flows. Chapter 2 presents a historical compendium regarding the development of NICFD over the past century.

In Chapter 3 particle image velocimetry (PIV) — a state-of-the-art laser diagnostic measurement technique — is used to investigate the flow field of a low speed organic flow. A feasibility study is conducted in a low speed vapor of  $D_4$  to assess the applicability of the PIV technique in these types of flows. Suggestions are made regarding improvements to the measurement chain and seeding procedure for use in higher speed organic flows.

Chapter 4 treats the preliminary design of the ORCHID; namely, a continuous steady state vapor tunnel with the capacity to generate supersonic flow conditions in several families of working fluids at numerous thermodynamic states. Chapter 5 reports the detailed design and commissioning of the ORCHID — characterizing the primary hardware and facility operation.

Chapter 6 presents the measurements characterising the flow features of high speed dense organic fluid vapor flow. In Chapter 7 a validation method is used to assess the

predictive capabilities of NICFD codes and is done so with a synthetic (numerically generated) experimental dataset.

# 2

## NON-IDEAL COMPRESSIBLE FLUID DYNAMICS WITH A HISTORICAL PERSPECTIVE

As it is often the case in the development of scientific knowledge, theory, experiments, and analytical and numerical work have been tightly intertwined since the very first scientists started their investigations on non-ideal compressible fluid dynamics (NICFD). The historical development of this branch of fluid mechanics was predominantly theoretical up until the late 20<sup>th</sup> century. Over the last 30 years it has been complemented with a vast body of mostly numerical work given the difficulty of realizing experiments, while now experimental efforts are gaining momentum.

Compressible fluid dynamics encompasses the study of flows in which the density of the fluid changes significantly. The assumption of three-dimensional compressible inviscid flow is often correct for many flow problems in aerodynamics, where the medium is a low-density fluid in the gaseous phase. Furthermore, in the absence of shock-waves and heat conduction, the flow is isentropic and homentropic. Therefore, the density variations of the bulk flow are of major importance in determining the main features of the flow [188]. The system of conservation equations applicable to such fluid flows is closed with the help of an equation of state for the fluid, which relates its thermodynamic properties, for example, pressure  $P$ , density  $\rho$  and temperature  $T$ . Additionally, information on the specific heat in the ideal gas state is needed. The ideal gas law, i.e.,  $P = \rho RT$  with the assumption of constant specific heat defines the simplest complete thermodynamic model for a fluid. This approximation is commonly adopted in several areas of study and engineering since it leads to convenient simplifications of gasdynamic relations without compromising accuracy.

In order to treat the influence of intermolecular forces, which are neglected in the ideal gas model, the concept of co-volume, that is a parameter related to the volume occupied by molecules, is said to have first been suggested by Clausius [382]. In 1862, Hirn

[184] is credited with first having written down a correction to the ideal gas law by introducing the co-volume in an equation of state. Sometimes, this thermodynamic model is also referred to as the Noble-Abel equation of state. Johannes Diderik van der Waals [393] was the first to propose a consistent thermodynamic model capable of describing the liquid, saturated and vapor phases by formulating an equation of state derived from the ideal gas equation of state, depending on the co-volume parameter and on a parameter describing attractive intermolecular forces. This cubic volumetric equation of state model is rather inaccurate, but it is theoretically sound, and a large multitude of current thermodynamic models for simple compressible substances is derived from it. The van der Waals equation

$$P = \frac{RT}{v - b} - \frac{a}{v^2},$$

where  $a$  is the molecular attraction parameter and  $b$  the co-volume parameter, predicts that close to vapor condensation and to the vapor-liquid critical point, vapor properties deviate significantly from what is predicted by the ideal gas model.

The characteristics of gaseous fluid flows whose volumetric and caloric behavior can be approximated with the ideal gas model are different from those for which the ideal gas assumption does not hold. These are called in the following *dense vapors*. The features of dense vapor flows are bound to be different because of the different way in which their thermodynamic properties vary. Thermodynamic non-ideality of the fluid introduces quantitative differences in gas dynamics. For example, the variation of the speed of

sound  $c \equiv \sqrt{\left(\frac{\partial P}{\partial \rho}\right)_s}$  with density over an isentropic compression or expansion, therefore the wave propagation speed within the fluid, is quantitatively rather different from that of the ideal gas, which depends only on temperature, that is  $c = \sqrt{\gamma RT}$ . Notwithstanding, the flow fields of dense gases or vapors in motion are qualitatively similar to those of fluids for which thermodynamic properties can be approximated with the perfect gas model. For example, in a supersonic expansion, compression waves (Prandtl–Meyer compression fans) coalesce to form shock waves if the flow is gradually turned through an angle of  $\delta$ . For this reason, both flows of ideal gases and of dense gases (non-ideal gases) that are qualitatively similar to those of ideal gases pertain to the realm of *classical gasdynamics*.

The volumetric non-ideality of a fluid may be quantified by the compressibility factor,  $Z \equiv Pv/RT$ , where  $v$  is the specific volume of the fluid.  $Z$  is therefore equal to one for a perfect gas. The volumetric non-ideality alone, however, cannot provide information regarding the propagation of small perturbations in the flow, i.e., about the isentropic variation of the speed of sound with density, which defines the gas dynamic behavior of fluid flows. Therefore,  $Z \neq 1$  is a necessary condition but not a sufficient one for fluids or vapors to exhibit non-ideal gas dynamic behavior. Classical gas dynamics therefore encompasses both ideal and non-ideal compressible flows of fluids that are thermodynamically ideal or non-ideal.

However, it has been theoretically demonstrated and shown in the following that, if a fluid molecule is sufficiently complex, compressible flows of such molecules can be gas-dynamically non-classical, if the molecules are in thermodynamic states in the vapor phase and close to the critical point and to saturation (therefore thermodynamically

non-ideal). In this case the large specific heat of the molecule determines a radically different isentropic variation of the speed of sound with density, namely the speed of sound increases over isentropic expansion to the point that waves coalesce into rarefaction shock waves. Conversely, compression fans in supersonic flows are possible if the molecularly complex fluid is in these non-ideal thermodynamic states.

*Non-ideal compressible fluid dynamics* (NICFD) therefore refers to compressible flows of fluids that are thermodynamically non-ideal and whose variation of the speed of sound with density over isentropic flows is opposite to that of ideal gases, for example the speed of sound increases over isentropic expansion. Among these, flows that are qualitatively similar to flows of ideal gases are classified as *non-ideal classical flows*. In this case, the speed of sound variation is not large enough to determine qualitative differences from ideal gas flows, but only quantitative. Those flows that are predicted to be qualitatively different from flows of ideal gases because the speed of sound variation is opposite and strong enough to determine such unconventional phenomena as rarefaction waves, are termed *non-classical flows*, and the resulting fluid dynamics *non-classical gas dynamics*.

Mathematicians pioneered the subject of non-classical gas dynamics throughout the course of the 20<sup>th</sup> century and their interest was merely theoretical. The mathematical treatment of non-classical gas dynamics came before the study of non-ideal compressible flows in classical gas dynamics. Then, owing to the rising number of applications of NICFD flows in the mid-20<sup>th</sup> and early 21<sup>st</sup> century, engineers became concerned with a better understanding of classical phenomena in NICFD. A particularly important aspect of compressible flows is shock-waves and both the classical and non-classical theory of these phenomena are extensively treated, also from a historical perspective in Kluwick [213, 214], while for a treatment of gas dynamics for arbitrary fluids, an excellent reference textbook is that of Thompson [375].

## 2.1. PIONEERING THEORETICAL DEVELOPMENTS

The history of non-classical gas dynamics starts with the study of shock waves around the nineteen hundreds and builds upon the work of Hugoniot [189, 190], Poisson [300], Rankine [311], Riemann [322], Stokes [370] and Rayleigh [313]. A rarefaction (expansion) shock wave is distinguished from a classical compression shock by featuring a negative pressure jump across it,<sup>1</sup> e.g.,  $[P] < 0$ . Among other theoretical aspects, Jouguet [207] derived an expression for the entropy change accross a small-amplitude shock wave in terms of the second derivative  $\left(\partial^2 P / \partial v^2\right)_s$ . The sign of the thermodynamic quantity  $\left(\partial^2 P / \partial v^2\right)_s$  determines, according to the second law of thermodynamics, the possibility of the existence of such a shock in a single-phase fluid. Since the adiabatic curve  $P(v)$  in the pressure-volume diagram, see Figure 2.1 (curve a), is concave up for all the most common substances — i.e.,  $\left(\partial^2 P / \partial v^2\right)_s$  is positive — Jouguet concluded that only compression shocks are possible over an expansion, and, conversely, rarefaction shocks are impossible because isentropes in the pressure-volume diagram are never concave down. Expansion shocks were formally dismissed by several other scientists around the same time, albeit only ideal gases were considered, on the basis that they violate the second law of thermodynamics, i.e., they feature a decrease in entropy through the shock wave, unlike compressive shock waves, which feature an entropy increase [204–206, 314, 415, 416].

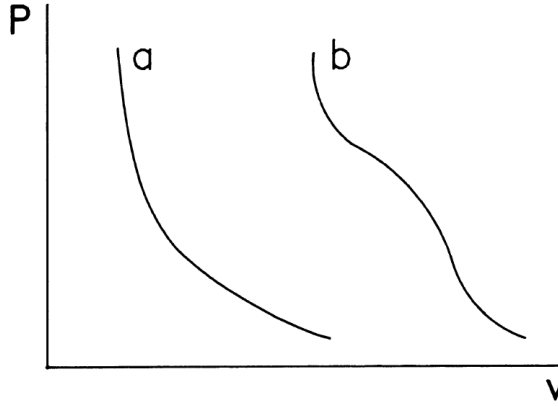


Figure 2.1:  $P$ - $v$  diagram: **Curve a:** Positive curvature of an ideal-gas isentrope, **Curve b:** Negative curvature required for a rarefaction shock. Taken from Kluwick [212, p. 156].

Duhem [124] was the first to state, focusing on weak shocks in arbitrary fluids, that shocks can be of compressive/expansive type if  $\left(\partial^2 P / \partial v^2\right)_s$  is greater or smaller than nil, see Figure 2.1 (curve b), without addressing the existence of fluids for which  $\left(\partial^2 P / \partial v^2\right)_s <$

<sup>1</sup>The convention about indicating a discontinuity in a quantity is to enclosed it in a square bracket, i.e., a jump in pressure is  $P_2 - P_1 = [P]$ .

0. The understanding of the formation of shocks in arbitrary fluids was further advanced by Becker [34]. He showed that compression/expansion waves steepen depending on the curvature of isentropes in the pressure-specific volume diagram. Additionally, he reported that the resulting shocks automatically satisfy the second law of thermodynamics, though, like Duhem, he did not address the existence of fluids for which rarefaction shocks are possible.

In 1942, using the van der Waals thermodynamic model for fluids, Nobel-laureate Hans Bethe developed a more complete shock-wave theory [38]. Apparently unaware of previous work, Bethe went several steps further than the conclusions of Duhem and Becker. He did so by searching for fluids whose thermodynamic properties are such that isentropes in the  $P, v$  thermodynamic plane are curved downward. Bethe therefore showed that rarefaction shocks can form in compressible flows of a polytropic van der Waals fluid provided that the ideal-gas isochoric heat capacity is sufficiently large, i.e.,  $c_v/R > 17.5$ . However, he eventually dismissed the fact that non-ideal vapors can feature a thermodynamic region of finite size, i.e., an ensemble of thermodynamic states, within which rarefaction shocks are admissible. He argued that such large values of the ideal gas isochoric heat capacity are “practically impossible” for any fluid vapor. He correctly identified the thermodynamic region in the vapor phase close to the critical point as that containing the states for which nonclassical gas dynamics might be possible, but erroneously concluded that, according to the van der Waals model,  $\left(\partial^2 P/\partial v^2\right)_s$  is always positive for all fluids.

Around the same period Zel’dovich, independently of Bethe’s work, argued that shock waves can indeed be either of a compressive or expansive type depending on the fluid and its thermodynamic state [414]. More specifically, he inferred that, with “the very rough assumptions of a constant specific heat  $c_v$  and low accuracy of the van der Waals equation”, a thermodynamic region where  $\left(\partial^2 P/\partial v^2\right)_s$  is negative in the vapor phase appears with  $c_v = 20 \text{ cal / mole} \cdot ^\circ\text{C}$ , that is for  $c_v/R \gtrsim 10$ . He also analyzed the entropy condition for shock-wave stability and theoretically predicted the existence of rarefaction shock waves.

Both Bethe and Zel’dovich realized that gas dynamics can be radically different in the case of flows of dense vapors of complex organic molecules, but it was Zel’dovich who was the first to theoretically show that non classical gas dynamic phenomena might occur for vapors of *actual* fluids.

Another notable theoretical effort was performed by Weyl, and it was summarized in a report in 1944. He developed and illustrated the fluid dynamics and thermodynamics of the shock phenomenon for an arbitrary fluid, thus the conditions for shock formation and the structure of the shock layer, with a predominantly mathematical approach. The same material was then published in a journal article [400], in which the author stated that the same theoretical development was treated in the antecedent report of Bethe [38], to which he had no access at that time because it was classified, being part of the American effort to develop the atomic bomb.

Even though it was shown with a strong theoretical basis that rarefaction shock waves (RSW’s) might occur in vapors of molecularly complex organic fluids, no experimental attempt to support these findings was performed at that time. It was, and still is, very



challenging to perform gas dynamic experiments with the fluid in thermodynamic states where RSW's are theoretically admissible since these states are very close to the thermal decomposition temperature of suitable organic fluids in contact with appropriate materials, like stainless steel, and thus at relatively high temperature.

In 1942 Landau introduced a non-dimensional parameter for the evaluation of the the curvature of isentropes in the  $P, v$  thermodynamic plane [225], namely

$$\frac{v^3}{c^2} \left( \frac{\partial^2 P}{\partial v^2} \right)_s, \quad (2.1)$$

in which  $s$  is the entropy,  $\rho$  is the density,  $P$  is the pressure,  $v = 1/\rho$  is the specific volume and  $c$  is the zero-frequency speed of sound, with  $c^2 = -v^2 (\partial P / \partial v)_s$ .

In 1958 Hayes [178, p. 426] assigned to this thermodynamic property, multiplied by  $1/2$ , the symbol  $\Gamma$  which is used to this day, resulting in the definition

$$\Gamma \equiv \frac{v^3}{2c^2} \left( \frac{\partial^2 P}{\partial v^2} \right)_s. \quad (2.2)$$

$\Gamma$  is a thermodynamic property and it indicates that the speed of sound, among other properties, can vary non-monotonically with the fluid velocity.

The theory of gas dynamics for arbitrary fluids was further developed by Landau & Lifshitz [226], who recognized that “the sign of the derivative  $\left( \frac{\partial^2 v}{\partial P^2} \right)_s$  is very important in gas dynamics”. However,  $\Gamma$  is assumed always positive in the treatment, but the authors mentioned in a footnote that Zel’dovich highlighted that it could be negative close to the vapor-liquid critical point, see Fig. 2.3(a).

For perfect gases  $\Gamma$  is constant and equal to  $(\gamma+1)/2$ , where  $\gamma$  is the specific heat ratio. Therefore,  $\Gamma$  exceeds unity and flows of perfect gases always exhibit so-called positive nonlinear behavior, that is, the convected speed of sound depends nonlinearly from the density disturbance caused by a wave and it increases over an isentropic compression and decreases over an isentropic expansion. As a consequence of this dependence of the speed of sound on density, in ideal gases, compressible shock waves are the only type admissible.

No major contributions followed in the sixties, and it was Philip Thompson who reported in a foundational 1971 article the results of his studies on the gasdynamics of fluids whose properties do not comply with the ideal gas assumption [374]. He started mainly from the work of Bethe, Zel’dovich, Weyl, Hayes, Landau and Lifshitz and organized the theory by naming  $\Gamma$  as the *fundamental derivative of gas dynamics*, and, based on it, he treated canonical topics, namely the flow through a transonic channel, the form of a Prandtl-Meyer wave, the adiabatic flow with friction, and nonlinear wave propagation (Figure 2.2), concluding that “for fluids with  $\Gamma < 0$ , the classical results of ordinary gasdynamics are inverted.” However, in this first article, he left open the question of the existence of fluids for which  $\Gamma$  is negative for some thermodynamic states. He also hinted at follow up studies, which would rule out that the interest in phenomena such as rarefaction shock waves is solely academic. Table 2.1 reports a summary of the possible

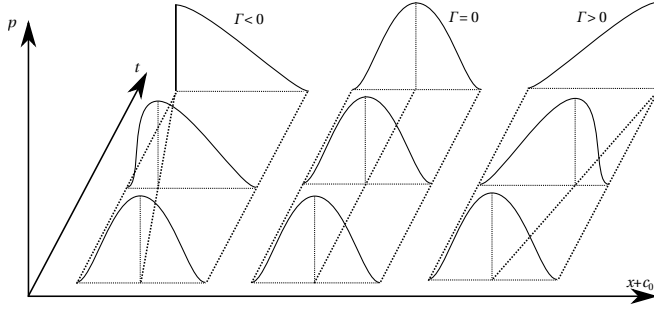


Figure 2.2: Time evolution of a sinusoidal pressure pulse in the  $(x)$  - time  $(t)$  diagram. Taken from Mathijssen [247, p. 14], who adapted it from the pioneering work of Thompson [374].

gas dynamic behavior of gaseous substances as it can be inferred from the treatment in Ref. [374] and from a similar table reported therein.

Table 2.1: Classification of gas dynamics regimes in gaseous (vapor phase) flows and their characteristics. Updated from Thompson [374, 375] and from Figure 1.1 in Ref. [247].

$\Gamma$	Possible phenomena	Classification	Speed of sound variation	Substance state
$\Gamma > 1$	Compression shocks, expansion fans	Classical Compressible Fluid Dynamics	$\left(\frac{\partial c}{\partial P}\right)_s > 0$	Perfect gas
$\Gamma = 1$	Flow with $c = \text{const.}^*$	Classical Non-ideal	$\left(\frac{\partial c}{\partial P}\right)_s = 0$	Gas made of molecules in states featuring $c = \text{const.}$
$0 < \Gamma < 1$	Compression shocks, Expansion fans	Compressible Fluid Dynamics	$\left(\frac{\partial c}{\partial P}\right)_s < 0$	Dense vapor
$\Gamma = 0$	Stationary acoustic wave <sup>*</sup>	Non-classical Non-ideal	$\left(\frac{\partial c}{\partial P}\right)_s < 0$	Dense vapor of sufficiently complex molecules
$\Gamma < 0$	Rarefaction shocks, Compression fans	Compressible Fluid Dynamics	$\left(\frac{\partial c}{\partial P}\right)_s < 0$	

\* Arguably, this type of flow is a limiting case and cannot occur in practice.

## THE FUNDAMENTAL DERIVATIVE OF GASDYNAMICS AND THE THEORY OF RAREFACTION SHOCK WAVES

Thompson and Lambrakis consequently explored the possibility of the existence of fluids for which “inverted” or *nonclassical* gas dynamics can occur and published their findings in Ref. [224], and more extensively in Ref. [379]. An investigation about the

existence of fluids with negative fundamental derivative was documented in Ref. [224], where a list of sixteen organic fluids, hydrocarbons and fluorocarbons, is reported together with the corresponding estimates of the minimum value of  $\Gamma$ . Recognizing that values of  $\Gamma$  calculated with the van der Waals model are too inaccurate and, in particular, too low, these estimates were obtained with more complex and accurate thermodynamic models available at that time, namely, the three-parameter virial equation of state, the Benedict-Webb-Rubin equation of state for light hydrocarbons, and the Martin-Hou equation of state. All of them are now known to inaccurately predict the curvature of isentropes in the  $P, \nu$  thermodynamic plane, and the authors realized the difficulty of correctly predicting the second derivative of a thermodynamic property by comparing results obtained for the same fluid and different thermodynamic models. In this publication it was stated for the first time that the region encompassing thermodynamic vapor states with negative fundamental derivative must be finite, small, and close to the vapor-liquid critical point and the vapor saturation line, see Figure 2.3(a). Ref. [379] reports an extensive theoretical study on the hypothesis that rarefaction waves may form in vapor flows of organic fluids formed by complex molecules. The study on the  $\Gamma$  property is extended by performing calculations with other simple equations of state, those of Redlich-Kwong and Clausius-Abbott, which leads to the conclusion that there must exist a region of negative  $\Gamma$  if “ $c_v/R$  is sufficiently large, i.e., for substances of sufficient molecular complexity”. In addition, the theory of the formation of negative shocks from plane waves in unsteady flow is presented, as well as the possibility of the formation of double-sonic shocks, that is, shocks for which the Mach numbers relative to the shock front are unity. The description of the method for the calculation of the pre- and post-shock states follows, and exemplary thermodynamic states upstream and downstream a rarefaction shock wave are reported for an idealized van der Waals fluid with constant specific heat, thus showing that the entropy jump across the shock wave is positive. Importantly, also the shock structure is treated, and a procedure to calculate the shock thickness is used to infer that the shock front of expansion waves should be thick.

In honour of the pioneering work conducted by Bethe, Zel'dovich and Thompson, substances for which non-classical gasdynamic phenomena are possible are named *Bethe-Zel'dovich-Thompson (BZT) fluids* following a proposal by Cramer in the early 1980s [101, 212, 214].

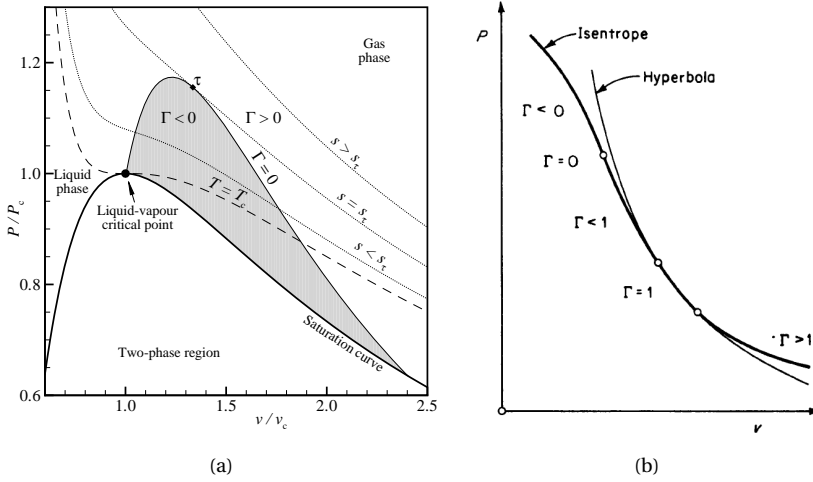


Figure 2.3: A pressure–specific volume thermodynamic diagram for a Bethe-Zel'dovich-Thompson (BZT) fluid. (a) Liquid–vapor saturation curve (–) and  $\Gamma < 0$  region (shaded region) for a BZT fluid in the volume–pressure plane computed with the van der Waals model under the assumption of a constant isochoric specific heat  $c_v$  and for  $c_v/R = 2000$ , with  $R$  gas constant. Selected isentropes (...) and the critical isotherm  $T = T_c$  (–) are also indicated. The isentrope  $s_\tau$  is tangent to the  $\Gamma = 0$  line in  $\tau$ . The isentropes are concave down in the  $\Gamma < 0$  shaded region, i.e., non-classical phenomena are admissible, e.g., RSWs. The isentropes are concave up everywhere else, i.e., classical phenomena such as compression shocks are the ones admissible. Taken from Guardone *et al.* [166]. (b) The sign of  $\Gamma$  gives the direction of the curvature of the isentrope in the  $P - v$  plane. Regions where  $\Gamma > 0$  correspond to an upward curvature and regions where  $\Gamma < 0$  correspond to a downward curvature.  $\Gamma = 0$  is also indicated. Taken from Thompson [375, p. 253].

## 2.2. FIRST EXPERIMENTS

Shock tubes and wind tunnels are the prominent type of experimental devices in use to study the fluid dynamics of compressible flows, and in particular the structure and propagation of shock waves. Shock tubes have been used since the beginning of the 20<sup>th</sup> century because their operating principle is rather simple [277]. Various types of supersonic and hypersonic wind tunnels were employed to simulate the flight conditions of aerospace systems in the laboratory [72], but they may also be used for other purposes. Wind tunnels are generally employed when long testing times and a steady and controllable fluid flow conditions are required. Until the mid-1960s these facilities were predominantly used to study compressible flow phenomena in air or steam.

A vast body of literature was dedicated to the documentation of experimental studies on homogeneous nucleation in compressible vapor flows; in particular, experiments were conducted in steam and ammonia vapor, see the work cited in Ref. [340]. This literature was of interest in various technical processes since condensation of supersaturated vapors influences the downstream flow field. For example, measurements are relevant for design improvements and operation of steam turbines. Phase change introduces large differences with flows of ideal gases, therefore high-speed condensing and vaporized flows are considered cases of NICFD flows.

## BLOW-DOWN TUNNELS AND SHOCK TUBES

To the author's knowledge, in the 60's Duff [123] was the first to conduct CO<sub>2</sub> expansion experiments using a de Laval nozzle setup at the Gas Turbine Laboratory of M. I. T. (see Fig. 2.4). The experiments were carried out over a range of steady flow conditions causing nucleation below the triple point. Testing times were of the order of 1 minute and the nozzle was fed by a bundle of nine 50 lb cylinders. The objective of the work was to better understand the condensation of various organic vapor flows in transonic and supersonic conditions in order to provide essential information for optimal turbine and power cycle design for space applications [183]. Interferometric density and static pressure measurements of non-condensing flows were used to verify the applicability of the 1D flow assumption, and the need to account for the departure from ideal gas behavior. Interferometer data provided a visual means of measuring the boundary layer thickness. These observations were estimated to be accurate within  $\pm 15\%$ . Furthermore, interferometric measurements of density variations in the core flow were recorded with an accuracy of 0.2 % [123, App. I. p. 3]. In particular, experimental results showed that values of density, pressure and total pressure predicted by relying on computations of fluid properties performed with the Plank equation of state [299] were sufficiently close to measured data, in the low temperature region of testing. The departure from the perfect gas thermodynamic behavior, as indicated by the compressibility factor, increased for states close to saturation, and values of  $Z$  for some of the measured states were as low as 0.9. For example, Tab. 14 in Ref. [123] reports the conditions at which the fluid condensed for each of the experimental tests. The first run, utilizing Nozzle I, expanded the fluid from a total pressure of 7.64 atm and total temperature of 227.2 K. In these conditions, the compressibility factor and fundamental derivative are  $Z = 0.9$  and  $\Gamma = 1.1$ , respectively (these values are calculated with state-of-the-art fluid libraries implementing reference equation of state models [93, 231]). In general, in the experiments of Duff the nozzle expansions occurred in the classical gas dynamics regime with the fluid molecules in a slightly non-ideal thermodynamic state ( $Z < 1$  and  $c_p \neq \text{const}$ ). These experimental studies treated only single and two-phase compressible expansions of dense organic fluid flows in the classical NICFD regime, and in the absence of discontinuities since the objective was to study homogeneous nucleation.

Until the mid-seventies, experimental work geared towards the study of non-ideal effects in flows of complex organic media, apart from those initial experiments of Duff, was still disproportionately little in comparison to the progress of analytical studies. In 1975, Thompson & Sullivan [380] authored a relevant theoretical contribution on the possibility of complete condensation due to compression shock waves in retrograde fluids.<sup>2</sup> Landau & Lifshitz [226] had suggested in 1959 that condensation shocks due to compression are impossible, only considering ordinary fluids like air, water or carbon dioxide, while Thompson disproved this assertion by extending the treatment to organic substances. This theoretical study was immediately followed by impressive experiments carried out by Thompson together with a group of scientists of the Max-Planck-Institut für Strömungsforschung, Göttingen [114, 115]. As a consequence of these studies, they

---

<sup>2</sup>A retrograde fluid features a positive slope of the saturation vapor curve in the temperature-entropy diagram. This is the case for organic fluids with a large heat capacity. Dense vapor flows of these substances can exhibit negative nonlinearity (which is an embedded region close to the thermodynamic critical point) [143, 377].

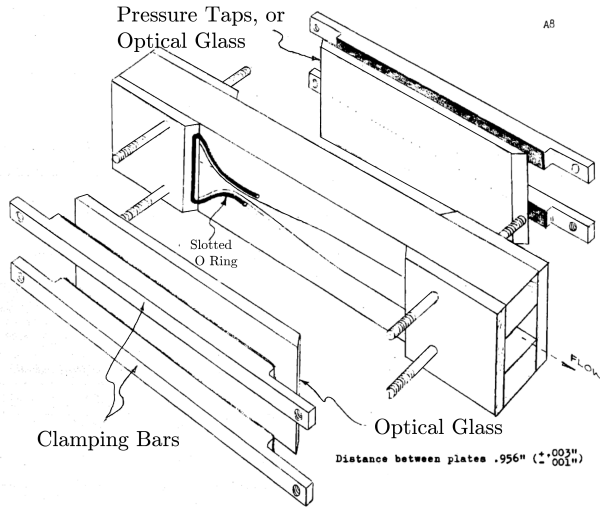


Figure 2.4: Assembly view and geometry of nozzle I. Taken from Duff [123, p. 72] and retouched by A. J. Head.

defined the term *liquefaction shock* in order to distinguish that newly discovered physical phenomenon from the well-known condensation of a vapor in an expanding flow, *the condensation shock*. Liquefaction shocks (partial and complete) were generated, measured and visualized, in a circular shock tube. Specifically, pressure, temperature, transmitted light intensity, index of refraction and shock velocity (determined from  $P(t)$  signals in two different locations) were measured at various states of the experiment. The working fluids were several retrograde fluorocarbons; namely,  $C_8F_{16}$  (PP3, CAS No. 335-27-3),  $C_{11}F_{20}$  (PP9, CAS No. 306-9-3). In addition, they also tested FC40, a substance whose chemical composition they did not know at that time, but its thermodynamic properties were reported by the manufacturer as similar to those of the other fluorocarbons. The chemical formula of FC40 is  $(C_7F_{16})_3N_2$ , CAS No. 51142-49-5. Following the suggestions of Thompson & Sullivan [380], the experiments were arranged to produce the liquefaction shock resulting from the reflection of a shock at the blind end of tube, where the observation section was placed, see Fig. 2.5. The experimental results were compared with the results of numerical simulations, whereby fluids thermodynamic properties were obtained with the BBR44 generalized equation of state improved by Yamada (a Benedict-Webb-Rubin functional form for the compressibility factor  $Z$  with 44 parameters) [410]. Given the inherent inaccuracy of generalized equations of state, these predictions were cross-checked in some cases using the virial-type equation of Hobbs [185]. For the complete liquefaction shock experiments the upstream state was a dry vapor and the different sets of initial conditions for the three fluids are reported in Tab. 4 of Ref. [114]. For example, an experimental run conducted with PP3, which was the most frequently adopted fluid during their campaigns, a set of initial state conditions are specified as  $T_0 = 130^\circ\text{C}$  and  $P_0 = 0.99$  bar. The corresponding  $Z$  and  $\Gamma$  values calculated with state-of-the-art thermodynamic models [93], are 0.95 and 0.96, respectively,

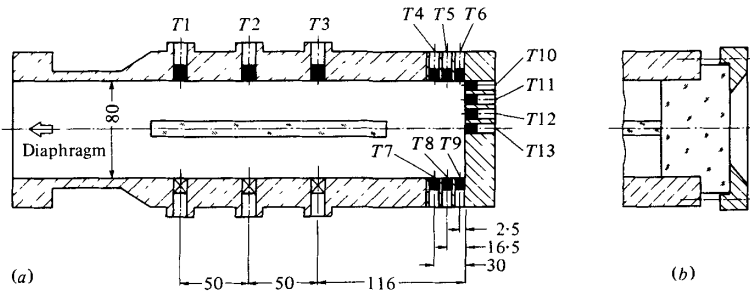


Figure 2.5: Sketch of the observation section of the shock tube used in the seventies to generate, measure and visualize liquefaction shock waves in retrograde fluids at the Max-Planck-Institut für Strömungsforschung, Göttingen. The designations T1 to T13 refer to the transducer locations. Dimensions in mm. Taken from Dettleff *et al.* [114].

thus a starting state for which classical NICFD flows are possible.

During the same period, other relevant experimental work on condensing compressible flows was carried out by the researchers from the Institut für Technische Thermodynamik und Kältetechnik der Universität Karlsruhe (TH), see Bier *et al.* [41]. They measured the annular flow of refrigerant R22 in an axially symmetric de Laval nozzle for Mach numbers up to 2.2, see Fig. 2.6. The experimental results were compared to one-dimensional simulations relying on thermodynamic property estimations obtained with the equation of state model of Rombusch [333], as well as to the results of an approximation procedure for the solution of the 1D isentropic nozzle flow problem, which could reproduce all measured values with deviations within a few percent. Image 2 in Ref. [41] displays numerous isentropic expansions. The stagnation conditions in the settling chamber of the nozzle featured pressures between 21 and 43 bar (thus always below the critical pressure value of 49.9 bar) and temperatures between 77.4 °C and 100 °C. In these thermodynamics states the  $Z$  and  $\Gamma$  values of the fluid range between 0.6 – 0.9 and 1 – 1.1, respectively.

In the second half of the eighties, the same group of researchers performed more experiments using both axially symmetric and planar de Laval nozzles [42–44]. The study was aimed at studying spontaneous condensation in stationary supersonic nozzle expansions of organic fluids, thus extending the investigation of Duff [123]. The fluids chosen for these experiments were carbon dioxide,  $\text{CO}_2$  / air mixtures, dichlorodifluoromethane ( $\text{CF}_2\text{Cl}_2$ , R12), and difluoromonochloromethane ( $\text{CHF}_2\text{Cl}$ , R22). Among the motivations for these studies, Bier *et al.* [43] mention that the process of homogeneous nucleation of supersaturated vapors in rapidly expanding flows is important for the design and operation of ORC turbines, in cases where the fluid is not retrograde. In Bier *et al.* [43] the measured pressure profiles are compared with reference profiles calculated for one-dimensional non-condensing isentropic flow. For the experiments with pure  $\text{CO}_2$ , the equation of state by Bender [36] was adopted for the computation of thermodynamic properties, and the predictions are extrapolated beyond the saturation line into the metastable supersaturated vapor state. The same equation of state was used in

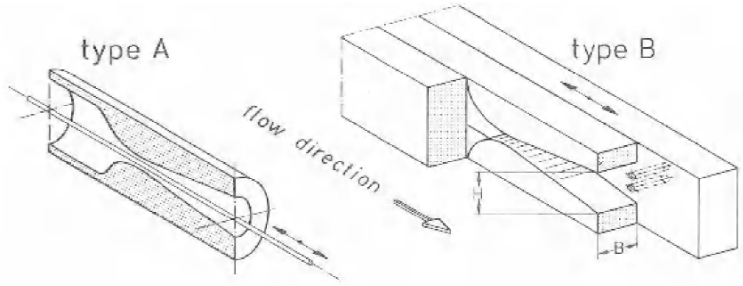


Figure 2.6: The two nozzle types (axisymmetric and planar) employed in the investigation of Bier *et al.* [43].

Ref. [42] and, where appropriate, the mixing and combination rules proposed by Sievers & Schulz [354] were employed. The research direction and experiments conceived by Duff and Bier *et al.* are of direct relevance to the work presented in this dissertation because the experimental apparatus at the core of the work documented here can perform similar experiments.

A first attempt to experimentally confirm the existence of rarefaction shock waves in dense organic vapor was performed by the group of Borisov at the Institute of Heat and Physics of Novosibirsk in the early 1980's [49, 218, 221]. A special shock tube (Fig. 2.7) was used to try to generate expansion shocks using refrigerant R13 (Freon-13,  $\text{CClF}_3$ ) as the working fluid. While a motivation for the choice of the working fluid was not provided by the authors, Borisov and Kutateladze stated that they were intrigued by the possible effects of the anomalies of thermodynamic variables near the critical point. The authors claimed that they observed and measured for the first time a rarefaction shock in a dense organic vapor flow, in conditions close to the critical point of the fluid. Their outstanding results were reported again few years later in the review article on nonclassical gas dynamics and rarefaction waves by Kutateladze *et al.* [222]. Incidentally, the celebrated scientist Yakov Borisovich Zel'dovich who first theorized the possibility that rarefaction shock wave existed, died in the same period in which the review article was published, on December 2, 1987 [253]. The findings of Borisov and his co-workers were challenged by numerous authors in the following years, namely by Cramer [100], Cramer & Sen [104], Ferguson *et al.* [143], Thompson [376] and more recently by Nannan *et al.* [269]. Nowadays it is believed that the observed wavefield is the result of condensation at subcritical thermodynamic conditions, as the molecule of R13 is not sufficiently complex for the curvature of vapor-phase isentropes in the  $P, v$  plane to be negative. However, the expansion and condensing shock wave documented by Kutateladze *et al.* [221] and Borisov *et al.* [49] could well be nonclassical according to the recent studies of Nannan *et al.* [270, 271].



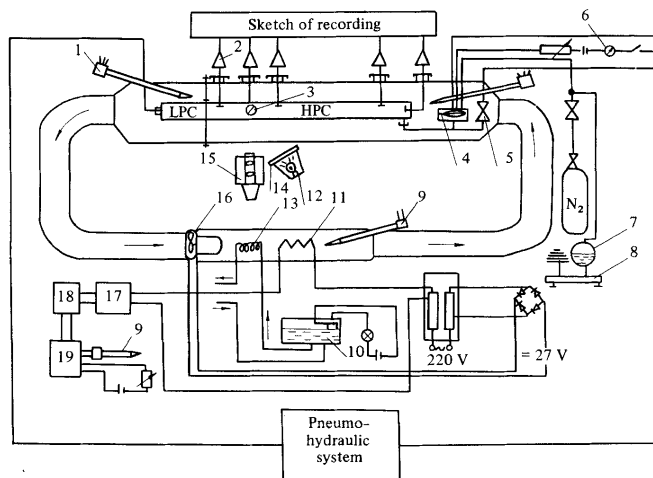


Figure 2.7: A schematic representation of the experimental arrangement used by Borisov, aimed at generating and measuring rarefaction shock waves in dense R13 vapor. Taken from Borisov *et al.* [49] and Kutateladze *et al.* [221].

### 2.3. EXTENSION OF THEORETICAL, EXPERIMENTAL AND NUMERICAL STUDIES

The use of numerical simulation to investigate NICFD flows started in the early eighties when computers became sufficiently powerful to run this type of relatively heavy calculations. Flatt [144, 145, 146] documented the modeling and simulation of the rupture of an off-shore gas pipeline in which high-pressure methane is flowing. The model could compute methane thermodynamic properties with both the ideal gas and a complex multiparameter equation of state. Several versions of the program (PIPE 1 & PIPE 2) implementing the method of characteristics (MoC) for the simulation of the unsteady compressible flow problem in a long tube were developed in order to predict the mass flow of methane escaping from the pipeline [146]. He then concluded that only the version (PIPE 2, see Refs. Flatt [144] and Flatt [145]) accounting for non-ideal effects would provide sufficiently accurate results for practical purposes. The choice of the thermodynamic model is documented in Ref. [144], in German.

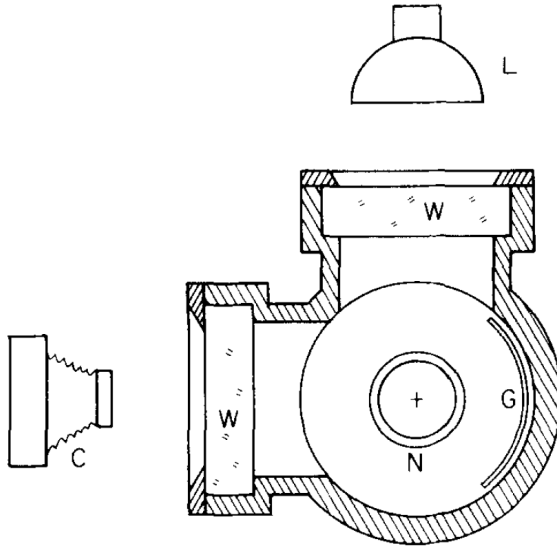


Figure 2.8: Experiments on non-classical flows with phase change. Arrangement for photography during measurements. View perpendicular to the axis of the shock tube: C = camera, L = light source, W = window, N = nozzle at the end of the shock tube, and G = curved sheet with grid lines. Taken from Ref. [378].

From the nineteen eighties to the early nineteen nineties, the group of Thompson at Rensselaer Polytechnic Institute focused investigations on the study of non-classical behaviour in two-phase flows. Thompson & Kim [378] used a shock-tube, see Fig. 2.8 for the experimental arrangement, to observe a single liquefaction shock wave split into a vapor-phase forerunner shock and a following condensation shock.<sup>3</sup> Reference [377]

<sup>3</sup>This phenomenon is formally known as shock splitting, and like rarefaction shocks, it follows the (inverted) rule that compression waves spread out in regions of negative nonlinearity [377].

provides a comprehensive investigation of shock waves and phase change in large-heat-capacity fluids, with stunning photographs of liquefaction shock fronts in perfluorocarbons FC-75 and PP3, see Fig. 2.9. The work is accompanied by a thorough theoretical treatment and calculations of the Rankine-Hugoniot jump conditions performed with a two-term virial equation, an extended virial equation, and the BWR 44 generalized equation of state, depending on the availability of data. Other calculations were performed with the self-consistent van der Waals model, but the authors correctly commented that the results must be considered “semi-quantitative”. The results of these studies were also treated more extensively in the two monographs Gulen *et al.* [167], Thompson [376].

During the same period, major advances in the theoretical treatment of non-ideal and non classical wave propagation in dense vapor flows were due to Cramer, Kluwick and their co-workers [100–106].

Cramer & Kluwick [103] studied the behaviour of one-dimensional small-amplitude waves propagating in a single phase fluid whose undisturbed state lies in the transition zone, i.e.,  $\Gamma(\rho, s) \equiv 0$ . This was done to further the understanding of how different parts of the waves could correspond to either positive ( $\Gamma > 0$ ) or negative ( $\Gamma < 0$ ) values of the fundamental derivative of gas dynamics. Cramer & Sen [104] extended the work of Cramer & Kluwick [103] by describing the shock formation process in inviscid *van der Waals vapors*. They explained that the shock formation process, for a dense vapor with sufficiently large specific heat, may differ significantly from that predicted by means of the perfect gas theory. The study shows these differences for both isolated pulses and periodic wave trains. The motivation for their work stems from the role wave steepening plays in the experimental determination of negative nonlinearity in various substances. The following year Cramer & Sen [105] presented exact closed-form solutions of the equations describing flows with finite-amplitude sonic shocks for the case of a van der Waals fluid having a constant specific heat. The authors provided exact closed-form solutions for both sonic and double-sonic shocks. This was a relevant contribution since previous authors had relied on graphical or approximate means for the computation of these types of shocks.

Cramer [100] used then the Martin-Hou equation to compute the fundamental derivative of gasdynamics for seven commercially available fluorocarbons in saturated vapor conditions. The author calculated values of  $\Gamma$  twice as low if compared to values reported in previous publications calculated with other thermodynamic models.<sup>4</sup> Cramer concluded that his contribution extended the list of fluids for which strong negative nonlinearity is predicted. In addition, he reasoned that the list of fluids is large enough to warrant designing experiments able to generate and detect non-classical gas dynamics phenomena, as well as justifying more numerical/experimental studies of the potential applications.

Cramer & Crickenberger [102] reported a detailed description of the dissipative structure of shock waves propagating in dense vapors of fluids having relatively large specific heats, and thus this work extended and verified the predictions of the Cramer-Kluwick weak-shock theory, see Refs. [103] and [105]. He presented new original simulations of the structure of finite-amplitude expansion shocks and provided examples of shock

<sup>4</sup>Nowadays it is well known that the model is quite inaccurate and in particular that the predicted values of  $\Gamma$  are excessively negative.

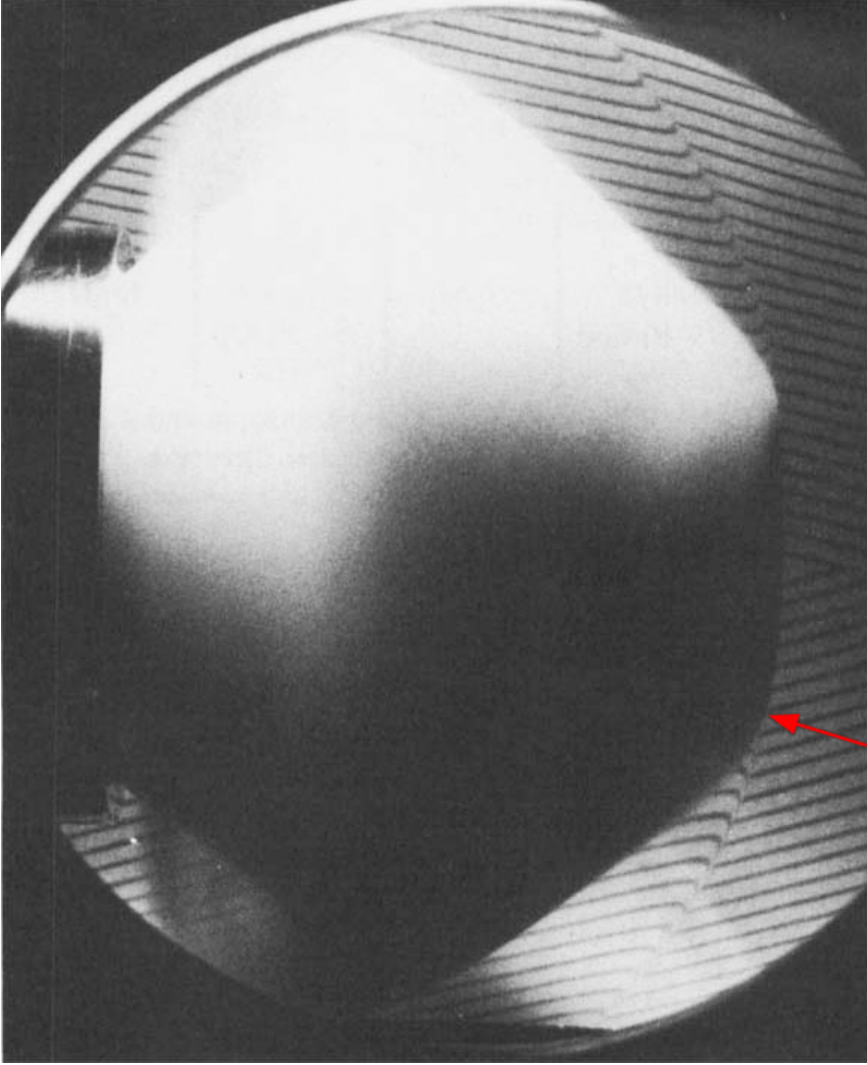


Figure 2.9: Emergence of the liquefaction shock from the open end of the shock-tube test section into the observation chamber. The flow direction is from left to right. A curved, vapor-phase forerunner shock and a condensation discontinuity have split off from the normal liquefaction shock at the triple point (indicated by the red arrow). Initial conditions  $P_0 = 0.726$  bar,  $T_0 = 100$  °C. Shock Mach number  $M_0 = 1.88$ . Taken from Ref. [377].

waves in which the thickness increases, rather than decreases, with strength. Furthermore, he identified a new gasdynamic phenomenon that he termed *impending shock splitting*. Cramer's aforementioned contributions are consolidated in a monograph [101] where he reviewed the gas dynamics of single-phase non-reacting fluids in the dense vapor regime.

In the nineties, simulation capabilities and theory on non-ideal vapor expansions in nozzles were extended with the work of several scientists [4, 71, 99, 346, 347, 350]. In particular, classical and non classical gas dynamic phenomena in steady two-dimensional transonic and supersonic flows of dense vapors were investigated.

Chandrasekar & Prasad [71] studied steady flows of a fluid whose fundamental derivative changes sign near the throat of a nozzle. More specifically, they examined the steady transonic flow of a non-ideal fluid through a nozzle and its local nonlinear stability to weak pulses. Cramer & Fry [99] modified the classical estimation technique for the critical Mach number to include effects commonly encountered in transonic flows of non-ideal gases. Schnerr & Molokov [346] studied the flows of dense vapors in both two-dimensional and axisymmetric nozzles. Specifically, the possibility of a sign change in the fundamental derivative during an isentropic expansion was considered. The influence on the nozzle geometry was studied in order to satisfy a shock-free acceleration to supersonic conditions.

Typical two-dimensional (2D) stationary nozzle flows were also studied numerically from a more applicative point of view, see, e.g., Drikakis & Tsangaris [120], Schnerr & Leidner [348, 350]. This body of work put into evidence the influence of the upstream stagnation conditions and of the exit pressure on the possible shock configurations. Notably, the first simulations of the classical two-dimensional flow of a dense vapor through a turbine cascade configuration is documented by Schnerr & Leidner [349]. Cramer and collaborators [264] numerically explored the possible beneficial effect of nonclassical gas dynamics through stationary turbine cascades, by first considering strongly simplified two-dimensional geometries, namely a flow of PP11 (C14F24) and FC-71 (C18F39N) around a compression corner and over a wedge. Moreover, the flow was assumed to be stationary and inviscid and entirely supersonic, thus the work complemented the transonic studies of Schnerr & Leidner [349]. The assumed free stream conditions for PP11 were  $T = 643.6$  K,  $P = 12.8$  atm and a Mach number of 1.5 for cases of a flow past a  $10^\circ$  compression corner and over a wedge with angle equal to  $15^\circ$ . The free stream conditions for FC-71 were  $T = 641$  K,  $P = 7.1$  atm and a Mach number of 1.6 for cases past a  $15^\circ$  and  $20^\circ$  wedge.

In the same years, analytical work, focusing on non-classical flow fields was further developed. Schnerr and co-workers studied transonic flows of BZT fluids and presented the exact solutions to the steady, two-dimensional transonic small disturbance equation in the physical and hodograph plane [347, 350]. In the mid-nineties, Aldo & Argrow [4] extended/developed the MoC for two-dimensional planar and axisymmetric flows of a van der Waals dense vapor and used it to design a minimum length nozzle, see, e.g. Fig. 2.21.

Towards the end of the nineties, new simulation capabilities were made possible by the increase in computational power, and the group of Argrow in Colorado developed CFD codes to study dense dry vapor tube flows [24, 54] and nonclassical flows for canon-

ical geometries [55].

Argrow and co-workers [24, 54] were the first to simulate nonclassical phenomena in typical shock-tube flows, which had been already studied analytically, see Ref. [104] and [255]. In particular, Argrow [24] provided a computational analysis of a transient, one-dimensional flow field of a single-phase dense vapor evolving in a shock tube. A time-accurate TVD predictor-corrector scheme based on the method of Davis [110], referred to as the TVD Mac-Cormack (TVDM) scheme by Causon [69], was applied for the solution of the one-dimensional Euler equations. Reflective boundary conditions were adopted and the van der Waals equation of state was chosen for the estimation of the fluid thermodynamic properties. Brown & Argrow [54] also described the computational analyses of single-phase dense vapor wave fields for transient two-dimensional shock tube flows with obstacles. The same predictor corrector TVD scheme was used for the simulations which showed compression and expansion shocks incident on wedges of varying angles as well as compression shocks evolving over circular arcs.

Brown & Argrow [55] extended this work by exploring transient and steady dense vapor flows for simple geometries by means of numerical simulations. In particular, a wider variety of nonclassical wave phenomena, such as disintegrating shocks, expansion shocks, and shockfan composite waves for wedges, ramps, circular arcs, and other geometries were considered. Two-dimensional wave fields were simulated for an inviscid van der Waals vapor, which was deemed representative of the flow of heavy fluorocarbons with high specific heat. Upstream thermodynamic conditions were selected so as to be close to the vapor-liquid critical point. They thus demonstrated significant differences in the predicted flow fields if compared to those that would take place if the perfect gas model were valid for those conditions.

Argrow, following the studies of Schnerr and Cramer on possible power applications involving BZT fluids, used two-dimensional simulations of turbine cascade to speculate on the possibility of expanding the fluids in a nozzle in nonclassical supersonic conditions in order to avoid the formation of compression shocks [56], something we now know is not feasible [165].

An interesting contribution to the experimental activity related to NICFD is due to Anders *et al.* [13], who modified a transonic wind tunnel, see Fig. 2.10, in order to operate it with the vapor of a fluid made of heavy molecules, namely sulfur hexafluoride ( $\text{SF}_6$ ). The main purpose in this case was to increase the Reynolds number range and not to study NICFD effects. This approach was deemed an alternative to the use of cryogenic wind tunnels, a standard choice for producing near-flight-level Reynolds numbers at transonic speeds. Cryogenic wind tunnels are affected by high operating costs and are complicated. Anders conducted static pressure measurements around a simple airfoil and found that the use of a heavier fluid may be a practical technique for increasing the test Reynolds number in existing transonic wind tunnels for flows not dominated by strong viscous effects, provided that the effects due to the non-ideality of the fluid are taken into account.

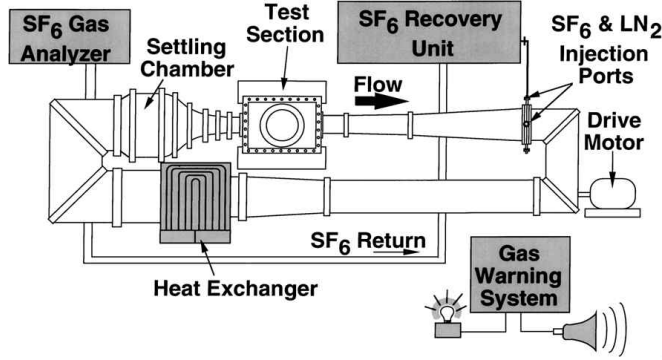


Figure 2.10: A schematic of 0.3 M transonic cryogenic tunnel with modifications for heavy-gas operation (shaded areas indicate heavy-gas components). Taken from Anders *et al.* [13].

## 2.4. RECENT PROGRESS

### 2.4.1. SHOCK TUBE EXPERIMENTS

At the brink of the 21<sup>st</sup> century, around the time of the death of Philip Andrew Thompson which happened on March 23<sup>rd</sup> 2001, the group of Argrow at the University of Colorado at Boulder started activities aimed at demonstrating experimentally the existence of rarefaction shock waves. Ferguson *et al.* [143] first developed a method, based on the use of the van der Waals state equation to compute the properties of perfluorotripropylamine (FC-70,  $C_{15}F_{33}N$ ), aimed at determining the experimental conditions to generate a single-phase rarefaction shock wave in the incident flow of a shock tube. The speed of the rarefaction shock wave would have been measured with a time-of-flight technique, thanks to high-frequency response pressure transducers placed at known distance along the pipe. As mentioned, they also challenged the results of the experimental study of Borisov *et al.* [49] by showing that the results are inconsistent with the thermodynamic requirements for non-classical behavior.

In support of the upcoming experimental work, shock tube flow simulations were performed and presented in Ref. [141]. A subsequent investigation dealt with the accuracy assessment regarding the use of various thermodynamic models for the computation of nonclassical gasdynamic phenomena, see Guardone *et al.* [164]. The analysis of the effects of a growing boundary layer on an incident rarefaction shock wave propagation, and the design and construction of a first-of-its-kind shock tube to generate single-phase rarefaction shock waves using PP10 ( $C_{13}F_{22}$ ) as a working fluid are reported in Refs. [140, 142]. Ferguson can be seen standing next to the facility in Fig. 2.11. Several trial experiments were carried out first in nitrogen, while the calculated initial operating conditions for PP10 in terms of temperature and pressure were 360 °C, and 15.5 bar, respectively [142]. Unfortunately, experiments with PP10 were unsuccessful since the working fluid underwent thermal decomposition, possibly also because the fluid was not properly deaerated and dehumidified. Oxygen and water are known catalysts for the thermal decomposition of organic substances at high temperature. The resulting for-



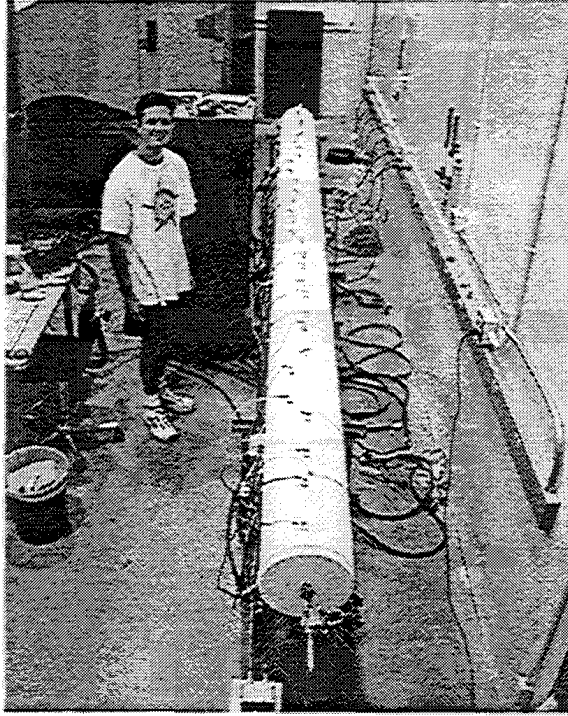


Figure 2.11: A photo of the apparatus from above with Ferguson standing on the side. Taken from Ferguson & Argrow [140].

mation of hydrofluoric acid irreparably damaged the equipment. In addition, the small pressure difference across the diaphragm was recognized as a major issue regarding the repeatability of the experiments. The facility was decommissioned shortly thereafter, and the research discontinued.

It was seven years after the experiments of Ferguson when, in 2008, the group of Colonna at the Delft University of Technology completed the construction of another facility called the Flexible Asymmetric Shock Tube (FAST), see Fig. 2.12. The design of this unconventional  $\approx 10$  m long shock tube [86, 412] greatly benefited from the lesson learned with the failed attempt of Argrow's group in Colorado. The working fluid selected for the experiments of the FAST was  $D_6$  (dodecamethylcyclohexasiloxane), given that it is nontoxic, highly thermally stable, and that its molecular complexity is large, and its flammability low. The measurement of expansion waves was also performed by means of dynamic pressure transducers along the charge tube. However, the challenges of operating the shock tube and its unique fast-opening valve at temperatures as high as  $\approx 350^\circ\text{C}$  were and remain extreme and only in 2015 Mathijssen *et al.* [248] published the description of the commissioning of the setup and some preliminary results, including the very first experiments with the fluid in the BZT region [247]. In 2013 the FAST had to be relocated to another building, and putting it back into operation required a long





Figure 2.12: A photograph of the FAST. Taken from Mathijssen *et al.* [248].

time, but activities regarding nonclassical gasdynamic experiments have been recently resumed.

#### 2.4.2. VAPOR TUNNELS

The Test Rig for Organic Vapors (TROVA), see Fig. 2.13, is a blow-down vapor tunnel whose construction was completed at the CREAlab of Politecnico di Milano in 2010 by the group of A. Guardone, with the aim of studying flows of dense organic vapors expanding from temperatures and pressures up to 400 °C and 50 bar [365, 366]. The blow-down solution was adopted to reduce the thermal energy input required to produce the needed mass flow for gas dynamic experiments in a de Laval nozzle. A power input of approximately 30 kW<sub>th</sub> is enough to slowly vaporize the fluid in a high-pressure vessel with a preparation time of a few hours. The short-duration experiment is then carried out by opening a controlled valve, which is arguably a limitation of this configuration [365], as the time for the measurements is limited to approximately 140 seconds [360]. The TROVA is equipped with instrumentation to record pressure and temperatures at relevant stations throughout the facility. Furthermore, the planar converging-diverging nozzle is equipped with fast-response pressure transducers mounted within a polished backplate, and optical access is provided on the other side. The schlieren technique has been used to obtain images of supersonic flows of dense organic vapors for the first time in 2015 [359]. In addition, the use of laser doppler velocimetry (LDV) is planned for the near future and initial results are documented in Ref. [149]. The first fluid selected for the experiments was MDM (octamethyltrisiloxane, C<sub>8</sub>H<sub>24</sub>O<sub>2</sub>Si<sub>3</sub>), therefore only expansions in the non-ideal compressible flow regime are possible, with inlet states in proximity of the critical point, at both subcritical and supercritical conditions, while nonclassical flow phenomena cannot be generated.

Spinelli *et al.* [359] and Cozzi *et al.* [97] report the first, albeit preliminary, designed experiments and associated results regarding supersonic expansions of MDM. A vapor expansion, in the close proximity of the liquid-vapor saturation curve, was generated at



Figure 2.13: The TROVA. The components which can be seen belong to the balance of plant (BoP), e.g., the high pressure vessel, the membrane pump and main valves. The test section (TS) is located in a dedicated room together with the measurement system. Photographed by Adam J. Head in the 4th International Seminar on ORC power Systems.

relatively low pressure and temperature of operation, e.g.,  $P_0 = 0.1$  bar and  $T_0 = 84$  °C.

A double-passage schlieren technique was used to visualize the flow field in throat and in the divergent section of the nozzle: a supersonic flow was attained within the divergent section of the nozzle, as demonstrated by the observation of an oblique shock wave at the throat section, where a 0.1 mm recessed step is located — machined to fix the throat position and to investigate complex flow structures. Initial experiments were hampered by the occurrence of condensation along the mirror side of the nozzle. Pressure measurements were also obtained along the axis of the nozzle and are compatible with the observed flow field. Subsequently, the refinement of the experimental work is documented in Ref. [364]: also in this case the total conditions in the settling chamber are subcritical and superheated. The total pressure was 3.15 bar and the total temperature 246 °C. In these conditions, the thermodynamic model of Ref. [90] predicts the compressibility factor and fundamental derivative to be  $Z = 0.884$  and  $\Gamma = 0.885$ , respectively. The nozzle used in this experiment was a planar converging-diverging (CD) nozzle with throat dimensions of  $h = 16.8$  mm and  $w = 18.7$  mm. The authors present time series data of the stagnation  $T$  and  $P$  conditions, and respectively the calculated  $Z(t)$  and  $\Gamma(t)$ , for an experimental duration of 33 seconds. Furthermore, the authors clearly identify a complex wave system originating from a recessed step.

Spinelli *et al.* [362, 363] reported several more experiments at different total conditions, but with the same experimental run times as in previous tests. The operating total pressures and temperatures were kept below  $P_0 = 5$  bar and  $T_0 = 250$  °C. Ref. [362] documents the results of experiments carried out with two different nozzle geometries, featuring exit Mach number of 1.5 and 2.0 (Nozzle M1.5 & Nozzle M2.0), respectively. A wide range of thermodynamic inlet conditions and diverse levels of non-ideality were investigated with tests lasting 195 seconds, thus approximately five times longer than previous

tests. The vapor was expanded from a moderate non-ideal state, indicated by a compressibility factor of approx. 0.80, to dilute gas conditions with  $Z \geq 0.97$  at the exit of the nozzle. The nozzle flow was characterized in terms of total pressure, total temperature, static pressure at discrete locations along the nozzle axis and with schlieren imaging. All these articles document, for the first time, satisfactory comparisons between experimental results and results of CFD simulations of NICFD flows obtained with the SU2 software suite. In particular, Ref. [362] presents detailed images, see Fig. 2.14, of a complex wave system that is clearly visible in the divergent, supersonic portion of the nozzle. In this contribution the authors also assess the effect of using different thermodynamic models on the prediction of the flow quantities.

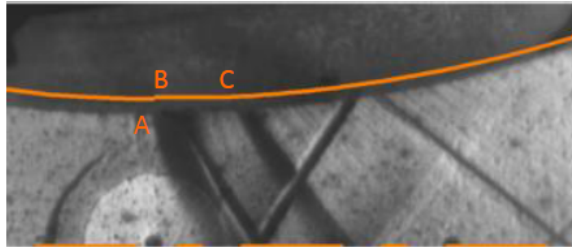


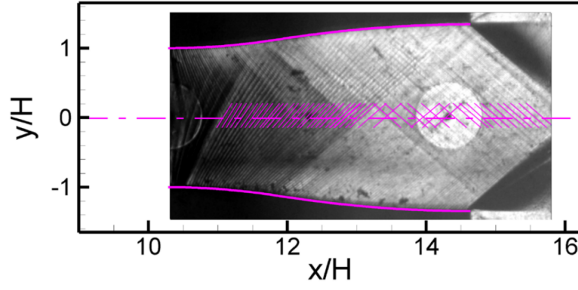
Figure 2.14: A schlieren image of the detailed flow field at time  $t = 0.0$  s showing the recessed step. The actual nozzle profile is superimposed to the gasket profile which is thermally dilated. The line segments A, B and C define the recessed step geometry. Adapted from Ref. [362].

The following experimental campaign, Refs. [360, 361] and [419], were dedicated to the measurement of flows in more strongly non-ideal conditions, and, analogously to the previous campaign, the predictive capabilities of SU2 were also tested [155]. Spinelli *et al.* [361] published flow data associated to the two nozzle designs mentioned previously (Nozzle M1.5 & Nozzle M2.0), and with various inlet conditions, e.g., with the highest reported pressure,  $P_o = 9$  bar, and the highest temperature,  $T_o = 270$  °C, resulting in a compressibility factor at the nozzle inlet as low as  $Z_o = 0.63$ . Their publication also includes a description of the flow structures similarly to what was already reported in detail in Ref. [364]. Furthermore, owing to the surface roughness of the nozzle profiles causing small density perturbations, Mach waves were observed in all documented tests, see Fig. 2.15(a). Post-processing of the images allowed to determine the local Mach number and the associated uncertainties, which was limited to the angular resolution. The scientists document also the evaluation of the expanded uncertainty of the Mach number estimates for several time instants. For example, towards the end of the Nozzle Test M1.5H ( $Z_{Tmid,2}$ ) the minimum Mach number uncertainty was  $\pm 0.011$  close to the throat and the maximum  $\pm 0.05$  at the nozzle exit, see supplementary material 1 [361]. Additionally, to complement the Mach number estimation, the pressure distribution along the axis of the nozzle is also quantified. The scientists conclude that the local pressure ratio  $P/P_o$  and Mach number  $M$  measurements feature a dependence on the inlet total state, a feature that is typical of NICFD flows, as opposed to flows of dilute gases. In other words, the quantities characterizing isentropic expansions of dense vapors are dependent on flow stagnation conditions and not only on the expander geometry, as it is the case for

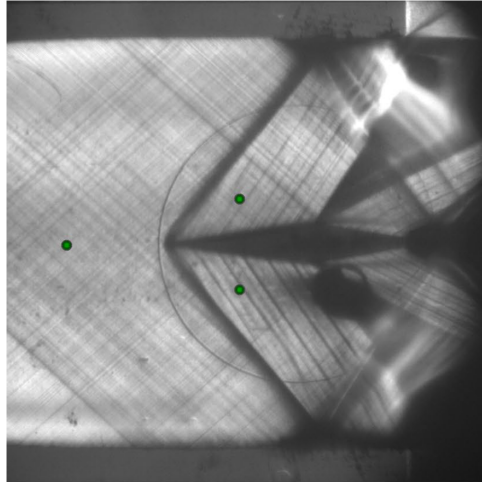
ideal gas flows.

Zocca *et al.* [419] designed and realized another type of experiment performed with the TROVA facility. A diamond-shaped airfoil with a flow turning angle of  $7.5^\circ$  at the leading edge was placed within a uniform supersonic stream (Mach number  $M = 1.5$ ) of siloxane MDM, see Fig. 2.15(b). Steady oblique shock waves were observed for the first time at varying stagnation conditions in the pre-shock state, for a set of flow deviation angles obtained by changing the attitude of the model with respect to the wind tunnel axis. The shock waves were characterised by independent measurements of pressure, temperature and Mach number. Results were in good agreement with the shock wave theory for two-dimensional steady flows in case the NICFD effects due to the dense vapor conditions are correctly taken into account.

Furthermore, Gallarini *et al.* [150] extended the diagnostics capabilities of the TROVA setup by applying the LDV technique to investigate a high speed dense vapor flow of MDM. Point-wise velocity data were acquired in a measurement volume positioned 15 mm downstream of the nozzle geometrical throat. The newly designed and commissioned seeding system was of a batch-charged type, which consisted of a tank pressurized with nitrogen and containing the MDM-seeding suspension. The chosen seeding powder was  $\text{TiO}_2$  & Aerosil 200. The measuring system was tested with temperature and pressure conditions in the plenum in the range  $P_0 = 1 - 2.2$  bar and  $T_0 = 225 - 250$  °C [149, p. 104]. Test results were not satisfactory as the velocity measurements did not match calculated values. This is most likely owed to the uneven particle distribution. Future work is planned and the devised particle spraying equipment is also suitable to provide the necessary seeding if the PIV technique will be used.



(a)



(b)

Figure 2.15: Detailed schlieren images from two different tests in a dense vapor expansion of MDM. **(a)** The Mach field with lines are identified via a line detection algorithm, implementing the Hough transform. Taken from [361]. **(b)** Diamond with angle of incidence  $\alpha = 0$  degrees placed at the exit of the nozzle. Taken from Ref. [419].

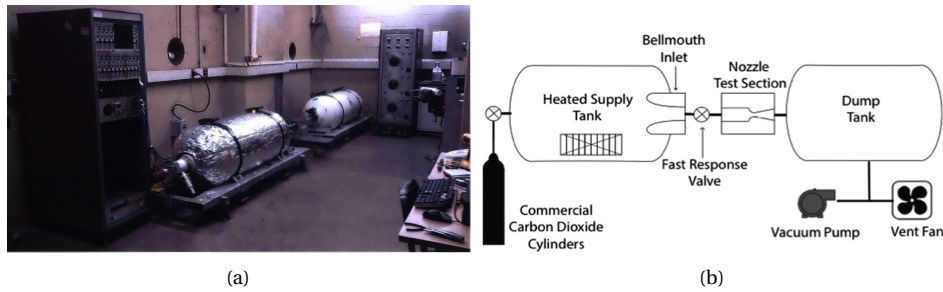


Figure 2.16: The CO<sub>2</sub> blow-down test rig of the gas turbine laboratory at MIT. **(a)** Realised test rig. Taken from Paxton [290, p. 62]. **(b)** Simplified process flow diagram (PFD). Taken from Lettieri *et al.* [234].

A laboratory scale experiment to study compressible flows of supercritical CO<sub>2</sub> in the vicinity of the critical point was designed, built and operated at the Gas Turbine Laboratory of M. I. T. between 2012 and 2016 under the guidance of Z. Spakovszky [290, 411], see Fig. 2.16(a). The research was motivated by the need of studying the peculiar flows occurring in compressors for carbon dioxide sequestration, where also condensation is possible and detrimental. The supercritical CO<sub>2</sub> flows were generated in a blowdown facility using a CD nozzle in an open-loop arrangement as shown schematically in Figure 2.16(b). As in the experiments of Duff [123], pressure readings were taken along the converging nozzle wall and were used to detect the onset of condensation. The speed of sound was also measured using a Helmholtz resonator [234, 290], however, while the device could measure the speed of sound in the static test section, measurements in transonic flow were not possible due to poor speaker performance and post processing issues. This difficulty then led to a solution whereby optical access to the nozzle was implemented in order to directly observe the onset of condensation. A shearing interferometer was used for measuring the static density of supercritical CO<sub>2</sub> during the experiments and an accuracy of at least 2 % was achieved [290, p. 32], allowing for the assessment of methods for the estimation of metastable states. The Wilson line for CO<sub>2</sub> was established for a range of conditions of interest for CO<sub>2</sub> compressors, providing insights into the behavior of CO<sub>2</sub> undergoing non-equilibrium condensation. This information is of paramount importance in the determination of the safe operational envelope for supercritical CO<sub>2</sub> compressors.

More recently, an ORC vapor tunnel for continuous operation, called the Closed Loop Organic Wind Tunnel (CLOWT), has been designed and built at the Muenster university of Applied Sciences in Germany, as described by Hasselmann *et al.* [176] and by Reinker *et al.* [317], see Fig. 2.17. The working fluid of the facility is Novec<sup>TM</sup> 649 and the maximum operating pressure and temperature is 0.5 MPa and 382 K, respectively. Its main objective is to study the flow of organic vapors expanding through linear turbine cascades, in order to develop loss correlations for the design and performance estimation of turboexpanders. This setup adopts the so-called gas cycle configuration [365]: the vapor exiting the test section enters a diffuser in order to recover part of its kinetic energy content, is then cooled, and its pressure finally restored to the test section inlet value by means of a high-temperature compressor, thus closing the cycle. The facility is con-

ceived to operate at sub-sonic and trans-sonic regimes, whereas higher Mach number operation is hindered by the compressor capabilities.

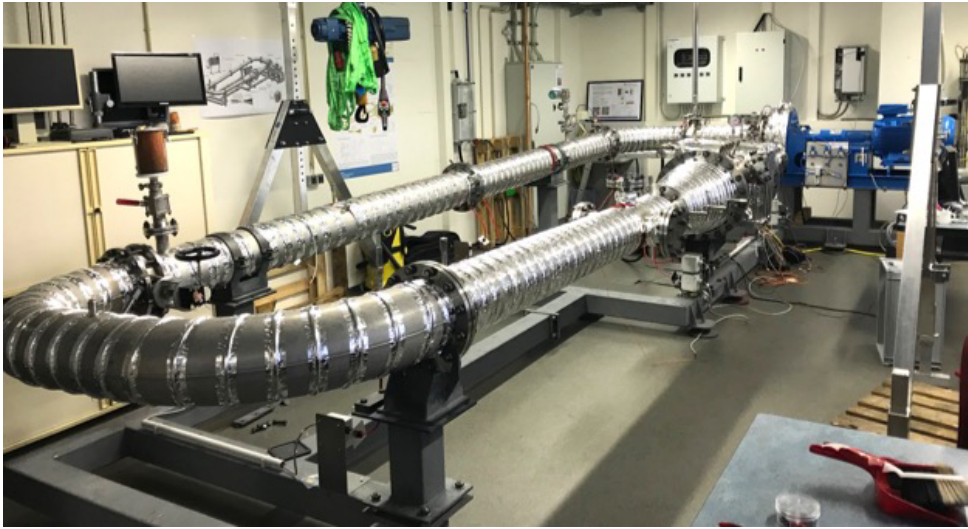
Reference [318] presents the detailed design aspects of the facility and outlines some notable features, e.g., the compressor shaft sealing, the wide angle diffuser, the chiller, the conical contraction and, in particular, the modular test section — see the basic test section shown in Fig. 2.17(b). This test section can implement a variety of configurations including: 1. turbomachinery components such as de Laval nozzles and turbine cascades, and 2. fans, blowers and compressors. Specifically, pressure distributions over airfoils/turbine blades in the transonic regime is of interest. In the de Laval nozzle, losses can be studied across the shock by quantifying the total pressure drop. The performance testing of small axial turbines and compressors are foreseen together with investigations into shaft sealings. The results of the commissioning are presented in Refs. [319, 320] where first measurements, leakage issues, thermal behaviour and compressor performance are discussed.

Also, very recently, White & Sayma [402] presented the preliminary design of a closed-loop supersonic test facility adopting the gas-cycle concept, which is being realized at the City University, London, see Fig. 2.18(a). The purpose of the facility is to provide experimental data-sets of flows in the same conditions of ORC turbines. A variety of testing sections are envisioned and include: a screw compressor, a de Laval nozzle, heat exchangers and a turbine. The selected working fluid is R1233zd and the facility is designed for testing conditions up to 20 bar and 125 °C, with a mass flow rate of 1 kg/s. The de Laval nozzle is designed with an exit Mach number of 2. Particle Image Velocimetry is the preferred measurement technique and the authors include considerations regarding a suitable seeding method including various possible particles and discussion about contamination issues.

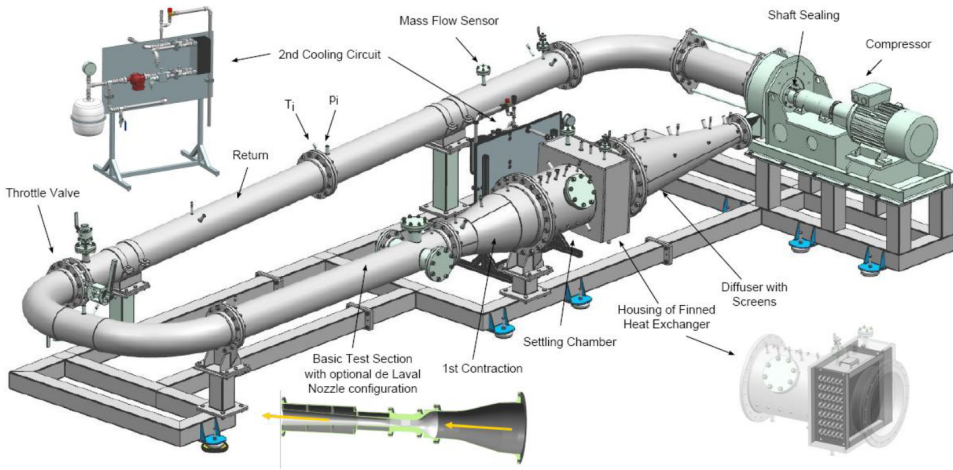
During the same period, a blow-down configuration was designed and commissioned, see Fig. 2.18(b), by the group of Ricardo F. Martinez-Botas at Imperial College London [331]. The purpose of the setup is also to facilitate the validation of CFD software for the simulation of highly non-ideal flows. The research interest is geared towards small-scale ORC turbines with a power range of 5 – 30 kW. Given that the flow non-ideality is usually confined to the first stage of the turbine, the testing section is modular and can implement different de Laval nozzle geometries. The selected working fluid is R1233zd(E) (trans-1-Chloro-3,3,3-trifluoropropene) and the facility is designed for nozzle stagnation testing conditions up to 20 bar and 138 °C, with a mass flow rate of 0.3 kg/s. The de Laval nozzle is designed for an exit Mach number of 2. The first experiments and comparisons made between 3D CFD and experiments for both nitrogen and R1233zd(E) are reported in Ref. [330].

The hybrid high-temperature ORC *vapor tunnel* and *expander test-bed* at the core of the work documented in this dissertation was commissioned at the Aerospace Propulsion and Power laboratory of the Delft University of Technology in a period between mid 2018 and early 2019. The ORCHID is conceived for both fundamental studies on NICFD flows and for testing of ORC components, initially high-speed mini ORC turbines and later heat exchangers. It features a *balance of plant* implementing a high-temperature regenerative organic Rankine cycle. Currently only the nozzle test section is installed, and it is foreseen that in the near future the design of the turbine test section will be





(a)



(b)

Figure 2.17: The Closed Loop Organic Vapor Wind Tunnel (CLOWT). **(a)** Picture of the realised test rig taken during the commissioning, from Ref. [319]. **(b)** An isometric view showing the primary hardware. Taken from Ref. [320].



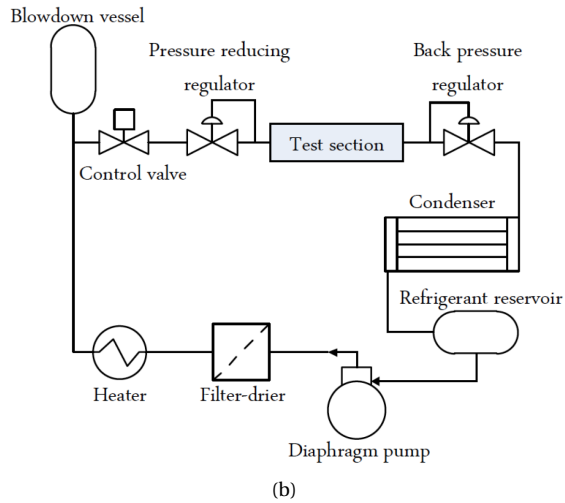
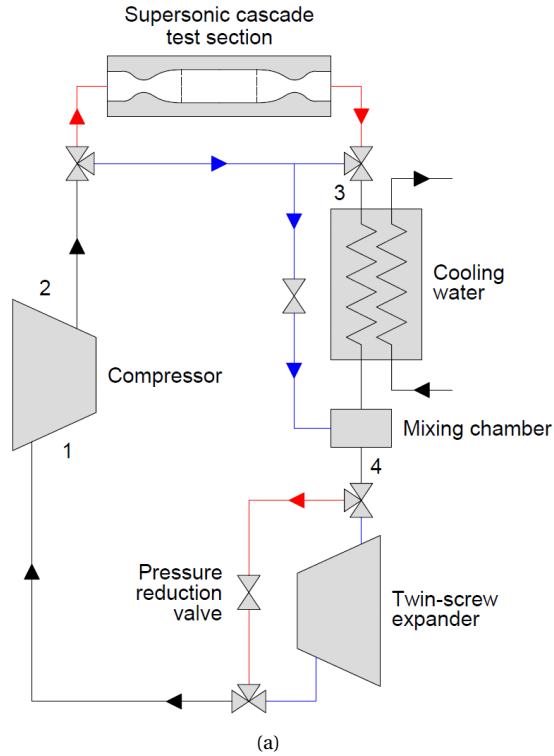


Figure 2.18: Preliminary design of gas-cycle and blow-down vapor tunnel concepts. **(a)** Schematic representation of the gas-cycle expander test facility of the City University of London. Blue: Expander test loop (loop 1); Red: Supersonic test section (loop 2). Taken from Ref. [402]. **(b)** Schematic representation of the blow-down facility of the Imperial University of London. Taken from Ref. [331].



Figure 2.19: The ORCHID located in the Aerospace Propulsion and Power laboratory of the Delft University of Technology. The surrounding structure is a ventilation cabinet containing the BoP and TS together with the measurement systems. Photographed by Henk-Jan Siemer.

realized and inserted into the setup. The ORCHID allows to attain a temperature and pressure of up to  $T$  of  $350\text{ }^{\circ}\text{C}$  and  $P$  of 25 bara at the inlet of the test sections. It has been designed taking into consideration the possibility of using many different working fluids and MM (hexamethyldisiloxane) has been selected for the first experimental campaigns. The fundamental studies on NICFD flows, similarly to other setups, rely on a two-dimensional converging-diverging nozzle, but in this case the optical access is on both sides. At the moment of this writing, only schlieren imaging and pressure measurements along the nozzle have been obtained. However, the preliminary design of a system for the injection of particles has already been accomplished, and measurements using particle image velocimetry (PIV) are planned. The ORCHID design, its commissioning, first measurements and their analysis are treated in Chapters 4, 5 and 6.

### 2.4.3. SIMULATIONS AND APPLICATIONS

Accurate numerical tools are required for the study of flows of vapors close to saturation conditions, or in the supercritical region, or in the two-phase regime. The development and implementation of spatial numerical schemes generalized for complex thermodynamic models enabled in recent times the improvement of numerous open-source and in-house software tools for the simulation of NICFD flows, e.g., OpenFOAM [397], zFlow [92], Finflow [187], Joe [292], and SU2 [132], each capable of different levels of fidelity.

OpenFOAM is a software framework for the modeling and numerical solution of problems in continuum mechanics, more prominently CFD [285]. Nabla Ltd. owned the software FOAM up until 2004 and at that time it was limited with respect to simulating compressible turbulent flows because its pressure-density / density-based solvers (*rhoSonicFoam* and *rhoSonicFoam*) were still in developmental phases, see the FOAM 2.3 release documentation.<sup>5</sup> To the knowledge of the author, NICFD simulations are not documented in the literature. As far as flows of fluids whose properties depart from ideal gas behavior are concerned, OpenFoam has been used, for example, in 2012 for the simulation supercritical fluid injection of propellants into modern combustion chambers by Jarczyk & Pfitzner [199], who implemented thermophysical fluid models to account for non-ideal gas effects and subsequently verified and validated the results against several test cases.

Appropriate types of spatial numerical schemes are needed for the simulation of non-ideal compressible flows [159]. These methods can be subdivided into central schemes, such as the Lax-Friedrich method and the Kurganov-Tadmor scheme [220], or ad hoc Riemann solvers such as the Godunov's and Roe's methods [236]. A rather complete overview of the numerical methods suitable for NICFD codes is treated in Refs. [159, 405]. The topic of adapting standard numerical techniques to be applicable to NICFD flows has been extensively reviewed by Rinaldi *et al.* [323].

In the early 2000's, aside from the developments in openFOAM, several researchers started to embed into their CFD codes complex fluid thermodynamic models or to link CFD solvers to external thermodynamic libraries with the aim of studying NICFD flows, both fundamental aspects and applications to turbomachinery, see, for example, Refs. [75, 76, 78, 80, 87, 91, 107, 160, 186]. Test cases have been often used for the verification of numerical schemes for the Euler equations [75], albeit no validation was possible given the lack of experimental information on NICFD flows. In 2004 Colonna & Rebay [91] integrated a NICFD-capable numerical discretization scheme with an external library of accurate thermodynamic models into a computer code named zFlow which was capable of accurately simulating inviscid dense gas flows with complex geometries. They successfully verified the correctness of the implementation of their numerical methods by comparing simulation results relying on a cubic equation of state for the fluid properties estimation with the experimental data of a well known ideal-gas test case, namely, the RAE2822 airfoil. In 2008 Colonna *et al.* [87] published the results of a study in which they used the same code to investigate non-ideal effects occurring in subcritical and supercritical organic Rankine cycle turbine nozzles. Also using zFlow, Harinck *et al.* [172] first investigated the effect of the complexity of the fluid molecule on the fluid dynamics

<sup>5</sup>In 2004 FOAM was released under a GPL and was renamed to OpenFOAM. OpenFOAM is currently distributed by OpenCFD Ltd.

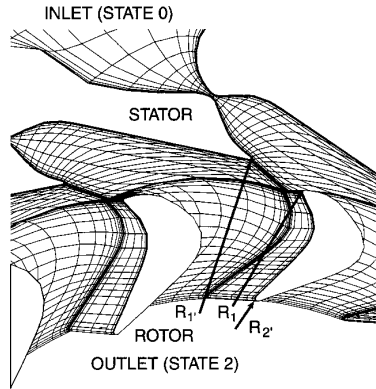


Figure 2.20: A radial turbine design is considered, shown by a coarse grid. Taken from Hoffren *et al.* [187].

of canonical expansions through nozzles and in two-dimensional turbine cascades. Not long afterwards, the researchers assessed the importance of the accuracy of thermodynamic models for turbomachinery applications [171].

In the first years of the 21<sup>st</sup> century, the fluid dynamic design of ORC turbines in which the nozzle was affected by NICFD effects was performed using quasi one-dimensional inviscid or two-dimensional (2D) viscous flow solvers coupled to thermodynamic models that at the time were the most accurate [48, 60, 187], see Fig. 2.20 for the typical meshing arrangement regarding a 2D radial turbine. However, in these early years, it was not yet possible to run a viscous 3D simulation of a complete stage of an ORC turbine.

Commercial software suites, e.g., Fluent in 2006 [21] and later CFX [22], did allow for the simulation of turbomachinery operating with NICFD effects, and companies started to utilize them in their design chains. These software offered and offer the possibility of calculating fluid thermodynamic properties with cubic equation of state models, or to link with external libraries providing even more complex and accurate models. In addition, they also implement look-up-table methods in order to speed up calculations.

The development of computer programs in academia was justified by the need of i) performing research also on specific computational methods, ii) collaborating with other academic groups without the problems inherent in the use of commercial licenses, and, iii) sharing best practices. In addition to these drivers, the framework of so-called *open source* communities like that of OpenFOAM and that of SU2, offered the advantage of a semi-professional quality control of the code, a larger collaborative community of developers, and, in case of SU2, a structured legal framework for the collaboration with commercial partners.

Starting from 2007, Cinnella documented the addition of new simulation capabilities to NICFD codes, mainly the coupling of fluid dynamic simulation and shape optimization methods, even if initially limited to highly idealized cases [74, 94]. More recently, the group reported on the results of more realistic simulations of supersonic ORC turbine cascades [283]. Furthermore, the group contributed to the development of knowledge on NICFD by quantifying the influence of uncertainties of the various computational

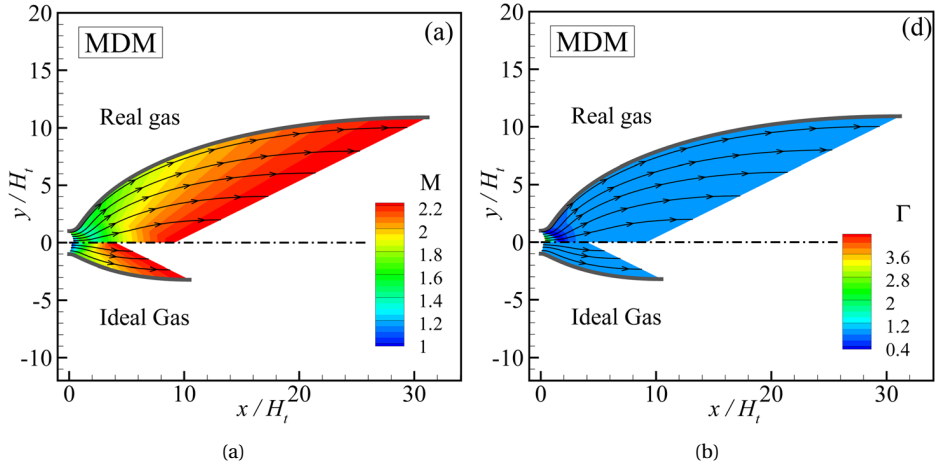


Figure 2.21: Comparison of a supersonic nozzle designed with the method of characteristics and by computing fluid properties with the ideal gas model (bottom half) and one designed with the same method but with properties estimated with the iPRSV EoS (top half). Stagnation conditions (the same):  $P_0 = 25$  bar,  $T_0 = 310.3^\circ\text{C}$  with an expansion ratio:  $\beta = 25$  and exit Mach number:  $M = 2.25$ . (a) Mach contours. (b)  $\Gamma$  contours. Note the region for which  $\Gamma < 1$  close to the nozzle throat if fluid properties are computed with a model capable of accounting for non-ideality. Taken from Guardone *et al.* [163].

sub-models [59, 77, 79, 133, 257].

A relevant example, aimed at clarifying to turbomachinery designers and practitioners the importance of using accurate thermodynamic models and in general of accounting for NICFD effects when dealing with turbine nozzles operating in the NICFD regime, was reported by Guardone *et al.* [163]. Figure 2.21 shows a comparison between two nozzles designed with the MoC and whose flow is impacted by NICFD effects. The nozzles are designed for the same set of conditions, but one is designed using the ideal gas model and the other using a thermodynamic model based on the improved Stryjek-Vera Peng-Robinson (iPRSV) cubic equation of state (EoS) [88, 368]. The nozzle designed by calculating the fluid properties with a model correctly accounting for non-ideal thermodynamic properties is much longer. If the ideal gas models were used in the generation of the nozzle shape, the nozzle would perform very poorly because of the formation of strong compression shocks.

In the last decade, the literature testifies a strong impulse towards the development of codes enabling the high-fidelity simulation and design of turbomachinery operating partially in the NICFD regime. These new computer codes are capable of steady and unsteady three-dimensional (3D) turbulent Reynolds-Averaged Navier-Stokes (RANS) simulations and are coupled with a variety of fluid thermodynamic models, even those based on highly accurate multi-parameter equations of state. These simulation capabilities were exploited for the development of blade shape optimization strategies, including, recently, computationally efficient procedures based on discrete adjoint methods.

Pecnik *et al.* [291] reported in 2012 on a three-dimensional CFD study of the impeller of a high-speed centrifugal compressor operating with  $\text{CO}_2$  in the thermodynamic

region slightly above the vapor-liquid critical point. Steady-state fluid dynamic simulations were performed with JOE, a fully implicit parallel Reynolds-averaged Navier-Stokes code based on a finite volume formulation computing the solution over a domain discretized with arbitrary polyhedral mesh elements. In order to validate the flow solver, the geometry corresponding to an impeller tested at the Sandia sc-CO<sub>2</sub> compression loop facility was selected and simulation results compared, for what was possible, with experimental information. Simulations showed that for some operating conditions, condensation over the tip of the impeller was possible. Rinaldi *et al.* [324] then extended the study and computed the performance map of that radial compressor. Numerical results were compared to experimental data over a range of mass flow rates and for three values of the impeller rotational speed.

After the seminal study of Colonna *et al.* [87], the topic of NICFD effects in ORC turbomachinery was further examined with numerical simulations by Wheeler & Ong [401], taking as an exemplary case a radial inflow turbine operating with refrigerant R245fa as the working fluid. Also in 2013, Harinck *et al.* [173] documented an investigation in which the geometry of a commercial high-temperature ORC radial-inflow turbine was optimized by means of numerical simulations and optimizations. The 3D viscous flow through the turbine passages was modeled under the steady-state assumption. The properties of the working fluid, toluene, were computed with the most accurate available model and a look-up table approach was employed for computational efficiency. The shape of the two-dimensional highly supersonic nozzle, a critical aspect for fluid dynamic efficiency, was optimized with a genetic algorithm method. The nozzle was manufactured, the new turbine tested experimentally, and the article put into evidence the achievement of a considerable efficiency improvement. The results demonstrated furthermore the importance of accurately estimating the thermodynamic properties of the fluid, by comparing with design simulations carried out a decade before with a less accurate thermodynamic model.

In 2016, Rinaldi *et al.* [325] published for the first time in the open literature about the possibility and advantages of simulating the flow of high-expansion ratio ORC turbines operating in the NICFD regime by also taking into account the inherently unsteady character of the fluid. The considered turbine was the same as that in Refs. Harinck *et al.* [173, 174].

In analogy with what is current practice with conventional turbomachinery, a clear goal of the scientific community became the development of automated procedures for the end-to-end fluid dynamic optimization of entire stages and machines. This task, in case part of the machine operated in the NICFD regime, is particularly demanding, also for the computational point of view. The possibility of using gradient-based optimization algorithms in order to cope with the computational load and large number of design variables was first documented by Pini *et al.* [298] in 2015.

Starting from 2013, several academic groups, namely the group of Colonna at Delft University of Technology, the group of Alonso at Stanford University, the group of Gauger at the Technical University of Kaiserslautern and the group of Guardone at Politecnico di Milano, teamed up in order to add NICFD and turbomachinery features to the SU2 open-source platform, which was initially developed at Stanford for design shape optimization in external flow problems using RANS simulations, mostly for aircraft design

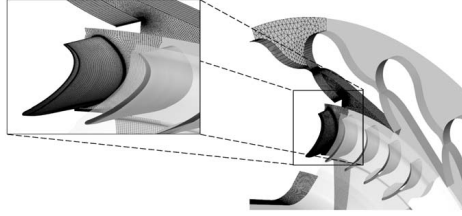


Figure 2.22: A radial ORC turbine. The three-dimensional geometric model with selected surface meshes of the stator, rotor and diffuser. Taken from Harinck *et al.* [173].

[132]. The unique feature of the code is that it was developed since the beginning with an adjoint solver. The first results of the extension of the method to the treatment of NICFD flows and its application to paradigmatic two-dimensional ORC stator blades was documented in 2017 in Ref. [390]. Note in passing that the acronym NICFD appeared for first time in the literature in Ref. [391] and in the 1<sup>st</sup> International Seminar on Non-Ideal Compressible Fluid Dynamics for Propulsion and Power [162].

The implementation and use of look-up table algorithm for the fast estimation of fluid thermodynamic properties based on unstructured discretization of the thermodynamic space of interest was presented by Rubino *et al.* [338] in 2018. The method relies on a trapezoidal-map searching algorithm and a piece-wise interpolation method based on the duality approach.

The adjoint based optimization method for turbomachinery was extended to the treatment of unsteady effects and the initial implementation and application to simple two-dimensional geometries was documented in 2018 in Ref. [337]. In order to tackle the issue of the computational time, a harmonic balance approach was devised and implemented into the SU2 code.

Re & Guardone [315] investigated the application of mesh adaptation techniques for flows in the NICFD regime. This paper describes the assessment of an adaptive Euler solver over 2D and 3D unstructured grids for moving body problems and is the first documentation of the application of unsteady mesh adaptation strategies to NICFD problems.

Gori *et al.* [155] very recently provided a preliminary accuracy assessment of simulations of NICFD flows. The assessment relies on a comparison between numerical predictions obtained with SU2, and pressure and Mach number measurements of compressible fluid flows in the non-ideal regime obtained with the TROVA facility. A non-intrusive polynomial chaos-based technique was used to forward propagate the physical uncertainties associated to the inlet conditions, temperature and pressure, through the numerical solver. The authors then compared the uncertainties attributed to the prediction and to those belonging to the experiment.

The most recent contribution related to the study of NICFD effects in turbomachinery is due to Romei *et al.* [334], who investigated some of the loss mechanisms that are peculiar of flows in which the non-ideality of fluid thermodynamic properties is relevant.



#### 2.4.4. CONSOLIDATION OF THE THEORY OF NONCLASSICAL GASDYNAMICS

A comprehensive review on the advancements in non-classical gas dynamics from a theoretical and experimental perspective, covering up until the turn of the millennium, is due to Kluwick [213]. Incidentally, Hans Albrecht Bethe died in 2005 at the age of ninety nine. Around the same time, in 2005, Colonna & Guardone [84], using the van der Waals model, theoretically investigated the role of attractive and repulsive intermolecular forces and the influence of molecular complexity on the non-ideal and nonclassical gas dynamic behavior of vapors near the liquid-vapor saturation curve.

This foundational study was followed in 2007 by a publication regarding the analysis of siloxanes, light silicon oils, as candidate Bethe-Zel'dovich-Thompson fluids [85]. A nonclassical rarefaction shock wave propagating in fluid D<sub>6</sub> is studied to demonstrate the possibility of using siloxane fluids in experiments aimed at experimentally verify the existence of nonclassical wavefields in the vapor phase. The sensitivity of the presented results to the considered thermodynamic model of the fluid is also briefly discussed.

This work together with those reported in following publications of the research work are linked to the experimental investigation on non-classical gas dynamics with the FAST setup mentioned in Sec. 2.4.1.

Zamfirescu *et al.* [413] investigated the conditions for admissibility of rarefaction shocks, the thermodynamic states for which it is theoretically possible to generate a rarefaction shock wave. This resulted in the definition of a new thermodynamic region — the rarefaction shocks region — which embeds the  $\Gamma < 0$  region. The influence of molecular complexity on the shape and size of the rarefaction shocks region is also illustrated by means of computations based on the van der Waals model; these results are confirmed by more accurate multi-parameter thermodynamic models applied to siloxane fluids that the group had developed in the mean time in collaboration with the National Institute of Standards and Technology [89, 90, 268, 272]. These same models were then used to compute the fundamental derivative of gas dynamics of molecularly complex siloxanes and compare the values with those obtained with other models [88] in an attempt to assess the accuracy of the predictions. They also concluded that the estimations for a fluid composed of complex molecules are less affected by the inaccuracy of  $C_v$ -information, if compared to  $\Gamma$  for simple molecules.

Again in preparation to experiments and in order to extend the theory of non-classical gas dynamics, Guardone *et al.* [166] studied the conditions needed to generate a rarefaction shock wave (RSW) with maximum intensity in terms of pressure jump, wave Mach number and shock strength. The upstream state of the RSW with maximum pressure drop is found to be located along the double-sonic locus formed by the thermodynamic states associated with an RSW having both pre- and post-shock sonic conditions.

In the same period Kluwick & Meyer [217] considered transonic high-Reynolds-number flows of BZT fluids through narrow channels where the classical boundary-layer approach fails locally in the presence of a weak stationary normal shock to predict the correct fluid dynamic behavior. The set-up described in this publication could be an alternative to shock tubes currently in use to try to experimentally prove the existence of rarefaction shocks.

In 2013, another theoretical discovery in the area of NICFD is due to the continuation of the collaboration between the researchers at TU Delft and Guardone of Politec-



nico di Milano: in the assumption of homogeneous liquid vapor mixture in thermodynamic equilibrium, any simple compressible substance is predicted to exhibit a thermodynamic region in which  $\Gamma$  is negative for values of temperature and pressure not too different from the critical values [269]. The investigation was extended and reported in Ref. [270], where the conditions for the admissibility of nonclassical gas dynamic phenomena involving phase change were discussed and a possible experiment aimed at their verification briefly outlined.

In addition, again in 2014 researchers at TU Delft and Guardone extended the investigation to the theoretical study of non classical gas dynamic for mixtures [161]. The thermodynamic properties of binary mixtures of organic fluids were computed with state-of-the-art models. Also for some mixtures, a finite thermodynamic region exists where the nonlinearity parameter  $\Gamma$  is negative and therefore non-classical gas dynamics phenomena are admissible. A non-monotone dependence of  $\Gamma$  on the mixture composition was observed in the case of binary mixtures of siloxane and perfluorocarbon fluids, with the minimum value of  $\Gamma$  in the mixture being always larger than that of its more complex component.

Guardone & Vimercati [165] then focused their work on the exact solutions to the equations for the supersonic flow of a mono-component dense vapor expanding from a reservoir into a stationary atmosphere through a conventional converging-diverging nozzle, starting from the quasi one-dimensional inviscid flow approximation.

In very recent years, the veteran among the scientists involved in the study of non-classical gasdynamics, Alfred Kluwick, published the results of his latest theoretical investigations. He first addressed, in a review paper, the theoretical framework of shock discontinuities by comparing the classical and nonclassical phenomenon [214]. In the mathematical treatment he shows how to select the physically realizable solutions, among all mathematically possible solutions of the Rankine–Hugoniot jump relations for classical and non-classical shocks, the so-called shock admissibility problem.

Then, also in 2018, together with the group of Guardone, he published the derivation of the steady self-similar solutions to the supersonic flow of Bethe–Zel’dovich–Thompson fluids past compressive and rarefactive ramps [389]. In particular, the authors studied the general properties of oblique waves in steady, inviscid, single-phase BZT vapor flows. The proposed theoretical framework can be conveniently applied to the study of shock reflections and shock interactions. The authors also pointed out that an important problem for further study is the stability of oblique waves in the ramp configuration, which is required for the experimental observation of these non-classical phenomena, and is the topic of another study of Kluwick & Cox [215]. Here the authors illustrate a complete picture of dense gas transonic flow past a configuration frequently used in wind tunnel experiments, which also represents a simple model of the entry region of a gas turbine designed to exploit possible advantages such as increased efficiency resulting from the use of gases with high molecular complexity. A more realistic model problem is treated in the following publication co-authored by Kluwick, Ref. [216], where Kluwick and Cox focus on the analysis of weak shock reflection in a transonic dense vapor flow in a channel. Results are presented in terms of similarity parameters associated with the fundamental derivative of gas dynamics, its derivative with respect to the density at constant entropy and the Mach number of the upstream flow. The problem of shock refraction properties

in dense vapor flows was also treated by Alferez & Touber [6] in a one-dimensional framework. This led to the identification of a new class of non-ideal-gas shock/perturbation interaction properties near the vapor–liquid critical point of molecularly complex fluids.

## 2.5. THERMODYNAMIC STATES OF THE FLUID IN NICFD EXPANSIONS AND RELATED $Z$ AND $\Gamma$ VALUES

The research topic at the basis of this dissertation is the experimental study of transonic and supersonic nozzle expansions affected by NICFD effects. For this reason, a simple overview of the thermodynamic states in which such expansions occur provides a general context in a simple form.

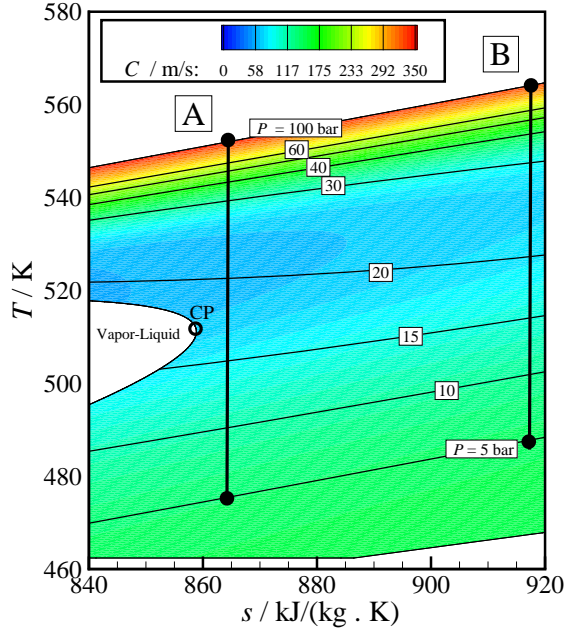
Figure 2.23 show  $Ts$  charts of an exemplary organic fluid limited to states in proximity of the vapor liquid critical point, where NICFD effects are stronger. All the points are calculated with a rather accurate multiparameter equation of state model for fluid MM [373], an exemplary organic substance of the siloxane class. The molecule is not complex enough for  $\Gamma$  to be lower than zero in the vapor phase, thus MM is not a BZT fluid and nonclassical phenomena are theoretically impossible.

Figure 2.23(a) shows the contours of pressure and of the speed of sound. Figure 2.23(b) indicate the contours of  $Z - 1$  and of the fundamental derivative  $\Gamma$ . Such information provides a graphical illustration of thermodynamic states affected by thermodynamic non-ideality, namely the departure of  $Z$  from unity, and, as a consequence, of the flow processes in which gas-dynamic non-ideality ( $\Gamma$ ) is present.

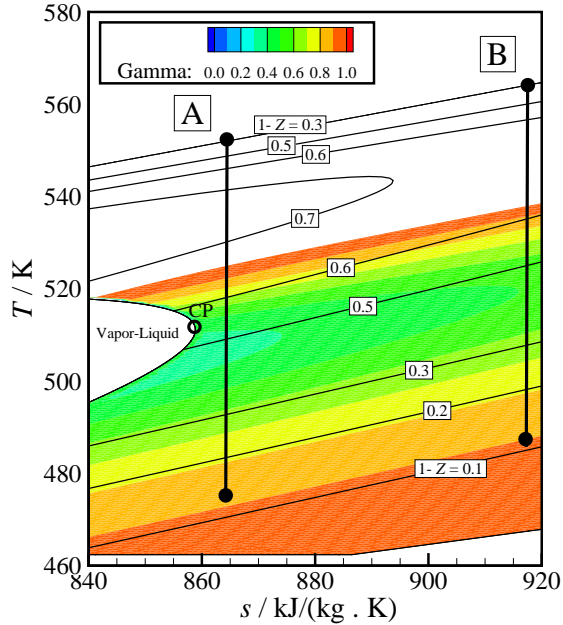
Two exemplary isentropic expansions, labelled A and B, are also indicated. In both cases the fluid expands from 100 bar to 5 bar and both the inlet and the outlet states are non-ideal thermodynamic states. In addition, both expansions involve thermodynamic states characterized by  $0 < \Gamma < 1$ , thus they are classical non-ideal processes, see Tab. 2.1.

As the fluid expands, the speed of sound  $c$  first decreases and then increases. Expansion A is subjected to stronger classical non-ideal behavior as it is closer to the vapor–liquid critical point, i.e., values of  $Z$  and  $\Gamma$  are lower, i.e.,  $1 - Z \rightarrow 1$  and  $\Gamma \rightarrow 0$ , and the variation of properties are larger.

As a final remark, it can arguably be stated that a consistent theoretical framework encompassing all the possible aspects of NICFD and the complex interplay between complex thermodynamics and classical and nonclassical gasdynamics is arguably still missing, and quite possibly one of the upcoming developments.



(a)



(b)

Figure 2.23: A  $T - s$  chart showing two isentropic expansions in the fluid MM. **(a)** Contours of the SOS and pressure. **(b)** Contours of the fundamental derivative,  $\Gamma$  and the complement of the compressibility factor,  $Z$  outlining the interplay between  $\Gamma$  and  $Z$ . Fluid properties are estimated with the in-house program FLUIDPROP [93] implementing the multiparameter equation of state model (Model = REFPROP) documented in Ref. [231].

# 3

## FEASIBILITY OF PIV IN LOW SPEED ORGANIC FLUID FLOWS

Contents from:

Head, A. J., Novara, M., Gallo, M., Schrijer, E., Colonna, P. (2019) Feasibility of Particle Image Velocimetry for Low-Speed Unconventional Vapor Flows. *Experimental Thermal and Fluid Science* 102:589-594

### ABSTRACT

This chapter assesses the feasibility of the planar PIV technique to study the characteristics of a siloxane vapor D<sub>4</sub>. Titanium dioxide (TiO<sub>2</sub>) seeding particles were used to track the motion around a rotating disk in a low speed flow. Vector fields of natural convection (NC) and a superposition of NC and rotating flow were selected as exemplary cases. The particles were capable of tracing the flow since the calculated Stokes number  $St$  is  $6.5 \times 10^{-5}$ . The quality of the experimental data is assessed by means of particle seeding density and particle image Signal to Noise ratio (S/N). The final results are deemed acceptable for an accurate assessment of the flow field. Rejected outliers are below 2.3% and the relative uncertainties corresponding to the average velocity fields are below 1 %.

### 3.1. INTRODUCTION

Organic compounds are used as working fluids in many power and refrigeration applications, such as ORC and supercritical carbon dioxide power systems, vapor compression cycle systems, and in other chemical, and transport processes. In many of these processes, flows occur in the NICFD regime at high relative pressure and temperature [172]. The fluid dynamic design of machinery operating in these conditions necessitates validated CFD codes. Validation can be performed only if accurate experimental information covering a representative range of conditions is available. Particle image

velocimetry PIV is arguably the experimental technique of choice for providing these data. Some initial attempts of using PIV in this type of flows are documented in [341], [149] and [385]. The investigation described here aims at addressing some of the issues related to utilizing PIV in high-temperature organic vapors moving at low speed. This work serves also as a precursor study before performing PIV in transonic and supersonic flows of organic fluids in a newly built experimental facility [179].

This chapter is structured as follows. Section 3.2 outlines the common issues arising when using the measurement technique such as, choice of particles, optical properties and the method to introduce the particles to the flow. Titanium dioxide (TiO<sub>2</sub>) seeding particles were used to track the motion around a rotating disk in a low speed flow. The apparatus designed and realized is described in Section 3.3. The experimental procedure is discussed in Sec. 3.4 and covers the adopted seeding methodology. Section 3.5 includes the results for several exemplary flow cases, namely, a flow field characterised by natural convection and another one generated by a rotating disk. Finally, the applicability of the technique to higher speed organic fluid flows is briefly assessed.

## 3.2. OPTICAL PROPERTIES AND PARTICLE COMPATIBILITY

PIV measurements require a transparent fluid, i.e., laser light absorption should be insignificant. In addition, ideally, the index of refraction should remain constant, such that aero-optical aberrations are minimal [135]. The refractive index  $n$  and the extinction coefficient  $k$  characterize how light propagates through a medium. With regards to members of the siloxane family, e.g., MM and D<sub>4</sub>, these parameters are not available for the vapor state because measurements of reflectance, transmittance or ellipsometric parameters are not documented. However, the refractive index can be estimated from measurements of the molar refractivity

$$A = \frac{4\pi}{3} N_A \alpha,$$

together with the Lorentz-Lorenz formula

$$\alpha = \frac{3}{4\pi N} \frac{n^2 - 1}{n^2 + 2},$$

and the molar volume

$$V_m = \frac{N_m}{N} = \frac{M}{\rho}.$$

This results in an explicit equation relating the refractive index to the density of the medium, namely

$$n = \sqrt{\frac{2A_s\rho + 1}{1 - A_s\rho}},$$

where  $N_A$  is Avogadro's number ( $6.02214076 \times 10^{23}$  1/mol),  $N$  is the number of molecules per unit volume, and

$$A_s = \frac{A}{M}$$

is the specific refractivity, with  $M$  being the molar mass, giving units  $\text{cm}^3\text{kg}^{-1}$ . If measurements of the molecular refractivity are unavailable then  $A$  may be estimated by the concept of *additivity of bond refractions* and by simplified methods given by Warrick [395]. The  $A$  for  $\text{D}_4$  is calculated as  $74.5 \text{ cm}^3\text{mol}^{-1}$  which results in a similar index of refraction value if compared to that of air at low density; namely,  $\approx 1$  and therefore no additional difficulties are expected with respect to PIV measurements. However, for high speed organic flows the density variations are larger and can change by two orders of magnitude over a short distance [179], imposing up to a 7 % variation in the refractive index over the expansion path, see Sec. 6.6 and 6.6.1 for the full theoretical treatment. In this case, the apparent shift (normal or lateral) or blurring (smearing) of the particle image could change substantially [127], and measures should be taken to ensure an appropriate depth of focus is selected. Absorption spectra have not been reported for organosilicon compounds in the vapor state and thus the extinction coefficient cannot be estimated. However, provided that the medium is sufficiently transparent for the particles to scatter enough light, then the particle image signal to noise (S/N) ratio, i.e., the ratio between the particle peak intensity and the image noise level, will be large enough to perform PIV measurements. If the medium is  $\text{D}_4$ , this condition is satisfied and results are discussed in Sec. 3.4 and 3.5.

Particles for PIV experiments should be preferably inexpensive, non-toxic, non-corrosive, non-abrasive, non-volatile, and chemically inert. Commonly used seeding materials for high temperature flows are dry metal oxide powders, e.g., Aluminum Dioxide  $\text{Al}_2\text{O}_3$  or Titanium Dioxide  $\text{TiO}_2$ , and Silica spheres  $\text{SiO}_2$ . However, dispersing the solid particles uniformly in a hot gas flow is challenging. Especially if the flow to be studied is formed by organic molecules, since it must not be contaminated by, e.g., water or air, as this would affect its thermal stability [62]. The introduction of solid particles by atomization of a suspension is the most viable possibility for the envisaged experiments [127].

### 3.3. THE NON-INTRUSIVE VAPOR ANALYSER (NIVA)

PIV experiments were performed in the NIVA: organic vapor is enclosed in a vessel with optical access, and a rotating disk provides fluid motion. Figure 3.1 shows the back-side view of the NIVA together with the control hardware. The setup characteristics and design specifications are listed in Tab. 3.1.

A stainless steel cube with two borosilicate (Borofloat 33) windows is positioned on top of a heating plate (max. power 2.2 kW). The set-point temperature is controlled by a relay and a thermocouple which is located inside the bottom flange. The temperature at the top flange can be monitored with an additional thermocouple and readout device. In order to limit thermal losses, the stainless steel cube's exterior was insulated with rock-wool. The interior of the cube is air-tightened by means of a metal lid and snap-clamp. The air can be removed from the cube through a ball-valve such that the organic vapor will not be contaminated. A sheet of Viton is used as a gasket, which, in addition, serves as insulator minimizing the thermal stresses of the windows. Since the operational temperature of the Siemens Sitran P200 pressure transmitter must not exceed  $145^\circ\text{C}$ , the sensor was mounted at the end of a pipe which protrudes from the lid. This allows for monitoring the pressure inside the cube. Furthermore a safety blow-off valve is installed to ensure that the maximum operating pressure cannot be exceeded. A 0-50 Hz (0 - 2800

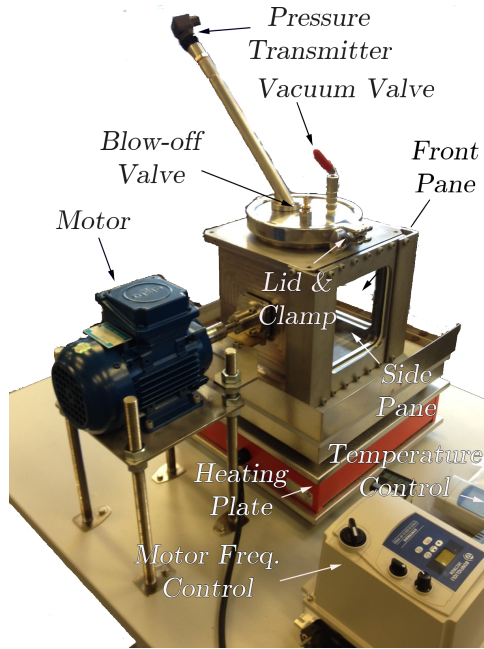


Figure 3.1: The NIVA apparatus.

RPM) frequency controller modulates a 0.18 kW electric motor, which connects to a 100 mm circular flat disk (located inside the cube and visible in the top-right of Fig. 3.2) via a flexible shaft coupling. The shaft is sealed with a Viton o-ring and is situated in a bearing holder. The inverter frequency and corresponding disk rotation was checked directly using an optical approach. A reference point was imaged at the edge of the rotating disk at several different time instances for a specific inverter control frequency, e.g., 10, 20 ... 50 Hz. Knowing the  $\Delta t$  between images, e.g.,  $1000 \mu s$ , with a fixed distance from the center of the disk, one could estimate the tangential velocity and rotational speed. The corresponding maximum tangential velocity at the edge of the disk is 15 m/s. The inside of the cube, together with the disk, was painted matt black in order to limit laser light reflections.

Figure 3.2 shows the layout of the PIV system. A high speed camera (Imager Pro 4M) with pixel size of  $11 \times 11 \mu m$  and a Nikkor lens is used to record the particle images. Illumination is provided by a Litron LDY300 (Nd:YLF) laser. Furthermore a LaVision high speed controller is used to synchronize the camera, laser and data acquisition PC. An exploded isometric view of the NIVA shows the location of the measurement plane, which is situated 10 mm from the surface parallel to the disk. This distance was chosen as a trade-off between laser light reflections and identifying phenomena induced by the disk, e.g., the closer the measurement plane the easier it was to capture the flow vortices but resulted in more background noise due to the surface of the rotating disk. The field of view (FOV) is  $0.12 m \times 0.12 m$  and is large enough to capture the flow rotating with

Table 3.1: Characteristics of the experiment.

NIVA Apparatus		
Design Pressure	$P_{\max, \text{abs}} / \text{bar}$	2
Design Temp	$T_{\max} / ^\circ\text{C}$	180
Motor	$\omega_{\max} / \text{RPM}$	2800
Disk Diameter	$D / \text{m}$	0.1
Inner Box Dimensions	$L \times H \times W / \text{m}^3$	$0.178 \times 0.178 \times 0.178$
Glass Dimensions	$L \times H \times W / \text{m}^3$	$0.15 \times 0.15 \times 0.015$
Wall thickness	$t / \text{m}$	0.01
Imaging and Illumination		
Magnification Factor	$M$	0.19
fstop	$f_{\#}$	4
Thickness of the light sheet	$t / \text{mm}$	1
Focal length of lens	$f / \text{mm}$	60
Particle image diameter	$d_{\text{r}} / \text{pixels}$	3
Depth of Focus	$\delta Z / \text{mm}$	1.6
Laser pulse separation	$\Delta t = 1 / f_{\text{acq}} / \text{sec}$	0.003

and around the disk. The cross-correlation analysis of the image-pairs was done with the LaVision Davis software version 8.3.0 and data post processing was conducted with MATLAB. Sequences of 1000 images were acquired, which, at the 300 Hz acquisition frequency in single frame mode, results in a total acquisition time of 3.3 seconds. The seeding material was  $\text{TiO}_2$ , with a primary crystal size of  $0.17 \mu\text{m}$  (CAS no. 13463-67-7) and effective bulk density of  $\rho = 10^3 \text{ kg/m}^3$  [310], since it is a typical choice for high temperature flows. A larger primary crystal size of  $0.30 \mu\text{m}$  was also used in the experiments but resulted in larger particle agglomeration and a less even seeding distribution. Table 3.1 further summarizes all the primary characteristics of the imaging and illumination system.

Experiments were conducted in siloxane  $\text{D}_4$  at an average temperature of  $160^\circ\text{C}$  and 0.283 bara. The amount of working fluid was determined based on the requirement that the temperature of the experiment cannot be larger than  $180^\circ\text{C}$ , which is constrained by the operation of pressure safety valve and pressure transmitter. Given that at ambient temperature the quantity of fluid in the vapor phase is negligible, the amount of liquid is determined by the smallest density achievable at that temperature. The fluid charge is therefore 20 ml. In order to determine if the particle velocity accurately represents the fluid velocity, a simplified situation of forced vortex flow is considered, whereby the particle dynamics is governed by simple rotational motion. It is reasonable to neglect the tangential and radial acceleration — similarly to what is typically done for many centrifugal filters — especially in cases where particles have reached the tangential fluid velocity, and the particles' radial velocity is comparatively small. Additionally, if it is assumed that the spherical particles move according to Stokes' law, then the centrifugal and Stokes' force can be equated, from which the particles' radial velocity becomes

$$u_{\text{pr}} = \frac{r\omega^2 d_p^2 \rho_p}{18\mu}.$$

This expression is valid for small particles with a Reynolds number



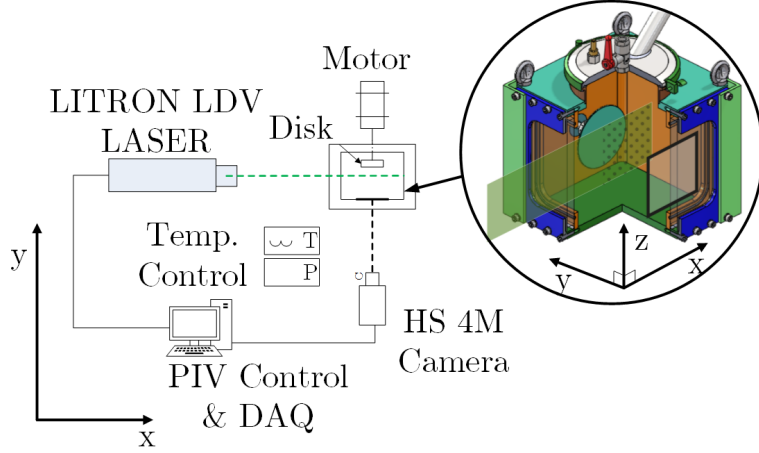


Figure 3.2: The layout of the system.

$$Re_p = \frac{\rho_f u_{pr} d_p}{\mu} < 1,$$

such that the flow around the particle is within the Stokes regime [127].  $\rho_p$  and  $d_p$  are the particle density and diameter, respectively. Thermophysical properties of  $D_4$  are calculated by means of a library [93] implementing a variety of models, e.g, the thermodynamic and transport property values are calculated by using the iPRSV equation of state [368] and Chung's model, respectively.  $\mu$  is the viscosity (equal to  $7.7 \times 10^{-5} \text{ kg.s}^{-1}.\text{m}^{-1}$  in the experimental conditions defined above), and  $r$  is the characteristic dimension of the disk. Considering the particles' radial velocity as defined above, then  $Re_p$  is lower than one, and together with the tangential velocity  $u_{tp} = r\omega$ , where  $\omega$  is the angular velocity, then

$$\frac{u_{rp}}{u_{tp}} = \frac{\omega d_p^2 \rho_p}{18\mu}$$

equals  $6.5 \times 10^{-5}$ . This is similar in form to Stokes' law, as reported by Lapple & Shepherd [228], but for simple rotational motion. Given that the tangential component dominates, it can be inferred that the chosen particles are suitable for accurately tracing the motion of the flow around the disk.

### 3.4. EXPERIMENTAL PROCEDURE

A 20 ml suspension of  $D_4$  and  $TiO_2$  particles was prepared at room temperature and subsequently poured over the bottom of the cubic vessel. Then the chamber was sealed by affixing the lid to the vessel and by tightening the quick-release-clamp. Air was extracted via the ball-valve, with a vacuum pump. The final vacuum pressure was 5 mbar and monitored for approx. 1 hr to ensure that the container was leak tight. The vessel was then insulated with rockwool, and then the thermal control was initiated. In the meantime, the actuator disk was set to rotate anticlockwise at 10 Hz (600 RPM) in order to

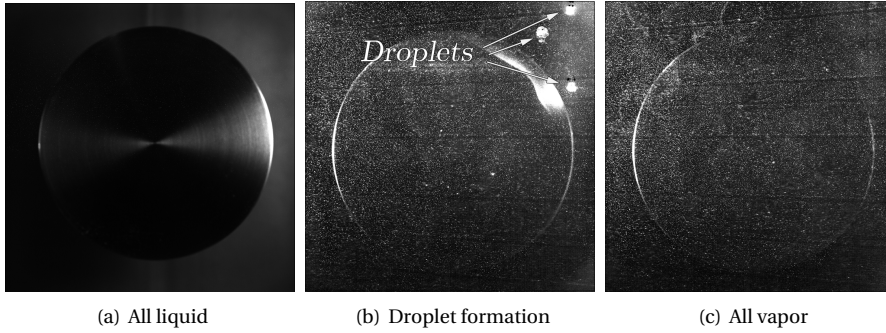


Figure 3.3: Evaporation process and seeding distribution. **(a)** A particle-liquid suspension resides on the bottom of the box. **(b)** Liquid not fully evaporated. A cloud of particles are circulating due to the motion of the disk. **(c)** Particles circulating in a vapor of  $D_4$ .

provide some forced convection inside the vessel during the phase transition. Without forced convection most of the particles tended to settle on the bottom of the container, thus their density in the vapor would be insufficient to perform PIV measurements.

The evaporation process can be seen in Fig. 3.3. During the heating, a turbulent convective circulation establishes, whereby the suspension moves upward due to the heating from the bottom, and then the vapor condenses due to the lower temperature of the upper surface of the box, and sizable droplets fall to the bottom. Once the fluid was completely vaporized, the required control speed of the disk was set, insulation removed and then images acquired.

The amount of particles required to provide sufficient seeding was chosen on the basis of the vector validation procedure together with observations of particle deposition inside the cube. In the initial stages of phase transition there were large agglomerates of particles at the bottom of the vessel, and the top was predominately occupied by vapor. Towards the end of the evaporation process an almost homogeneous particle distribution was attained. However, in a small layer right above the bottom, the particle density was notably lower as can be seen in Fig. 3.3(c). This might either be explained by an uneven illumination or an unfavorable temperature gradient between the bottom and the ceiling of the container, resulting in a higher out-of-plane particle motion. Despite the precautions taken with the insulation, thermal losses from the system resulted in a temperature at the bottom plate of  $180^\circ\text{C}$  and approx.  $140^\circ\text{C}$  at the ceiling.

An average particle peak intensity of 80 counts was measured, and this can be attributed to the low intensity of the laser. The corresponding average noise level was 25 counts. At the top right of the FOV, particles appear out-of-focus, see for example Fig. 3.3(b). These particles are illuminated by the light reflected by surfaces inside the vessel, thus they do not reside on the measurement plane. In any case, it appears that the design of the container is suitable for performing measurements with sufficient contrast.

No noticeable particle or laser light compatibility issues were observed, and the vapor turned out to be sufficiently transparent to conduct PIV. In summary, no beam dispersion due to the density of the media occurred, and the laser light propagated with

negligible absorption. In order to assess the quality of the measurements, an analysis of the instantaneous and average vector fields was conducted.

### 3.5. EXEMPLARY FLOW FIELDS

Several experimental runs, corresponding to disk rotations of 10 Hz (600 RPM), 20 Hz (1280 RPM), 30 Hz (1900 RPM) and 40 Hz (2500 RPM), were carried out. Two cases were considered for the present investigation. In the first set of experiments the rotational frequency of the disk was set to 40 Hz. In the second, the disk was kept still, and the motion of the fluid was due to natural convection alone.

The preprocessing method of Mendez *et al.* [254] was used to improve the image quality of the raw data before it was processed with a cross-correlation technique. This is accomplished by removing the background noise, i.e., unsteady and non-uniform reflections originating from the surface of the disk, which is correlated and well approximated by the first Proper Orthogonal Decomposition (POD) modes of the image sequence. Background noise was satisfactorily removed without an appreciable alteration of the particle image brightness.

During the processing stage, the multi-grid window deformation cross-correlation technique of Scarano & Riethmuller [345] was adopted for all datasets. A final window size of 24 x 24 pixels (Gaussian weighted) with 75 % overlap was selected, yielding a vector spatial resolution of 1.4 mm. The universal outlier detection approach of Westerweel & Scarano [398] was used to identify invalid vectors. Discarded vectors were replaced with a distance-weighted average of valid neighbor vectors.

#### 3.5.1. ROTATING DISK

Figure 3.4(a) shows the time-averaged vector field resulting from an anticlockwise disk rotation of 2500 RPM. The flow field is a non-linear superposition of an Ekman-type structure, originating from the constant forcing motion of the disk, and a Rayleigh-Bénard type flow. In order to assess the quality of the data, instantaneous flow fields were analysed at several instances. The average correlation peak ratio  $Q$  was 2.2, whereby  $Q = \frac{P1 - \min(P)}{P2 - \min(P)}$ , with  $P1$  and  $P2$  being the heights of the first and second highest correlation peaks, while  $\min(P)$  is the lowest value of the correlation plane. The image seeding density was 0.02 particles per pixel (ppp) and corresponds to approximately 12 particles in the final window size. The seeding concentration could be increased if a higher spatial resolution were of interest. The (normalized) cross-correlation coefficient is defined as follows [344, 404],

$$\phi_{fg}(m, n) = \frac{\sum_{i,j=1}^M f(i, j) \cdot g(i-m, j-n)}{\sqrt{\sum_{i,j=1}^M [f(i, j)]^2 \cdot \sum_{i,j=1}^M [g(i, j)]^2}}$$

where  $f$  and  $g$  denote the grey intensity distributions of the interrogation areas and  $M$  is the window size (in pixels). Cross-correlation values of 0.8 are observed, where values near one indicate that many particle images match up with their corresponding shifted partners. However, there were lower values in the FOV (approximately 0.5) which originate from the combined forcing motion of the disk together with the uneven thermal gradient, effectively promoting out-of plane particle movement. Furthermore, as

the rotation speed increases, the pumping force from the disk increases the loss of particle pairs.

The percentage of outlier vectors which were removed is 2.3 %. The flow conditions inside the cube made it difficult to obtain vector field images with a smaller number of outlier vectors. The other experimental runs which were made at different disk rotational speeds showed that the number of outliers decreased with decreasing disk speed. This can be explained by the fact that the pumping forces increases as the disk rotating speed augments thus promoting movement of the particles out of the measurement plane.

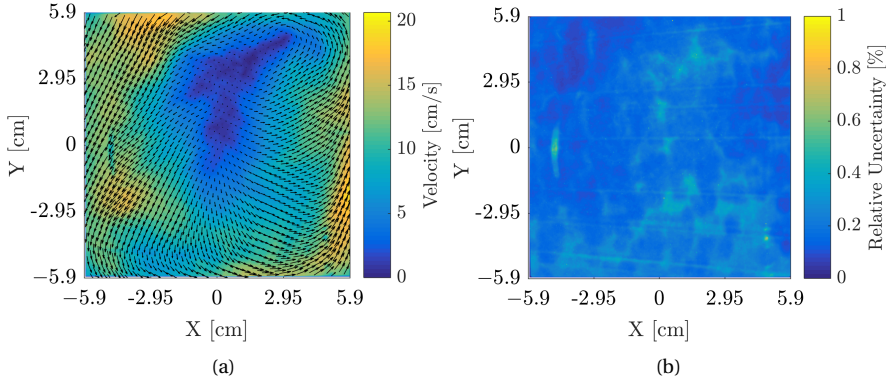


Figure 3.4: The disk is located in the center of the FOV and is rotating at 2500 RPM. The FOV is 12 cm · 12 cm. (a) Avg. vel. field. (b) Relative uncertainty.

### 3.5.2. NATURAL CONVECTION

Figure 3.5(a) shows the averaged vector field with the disk standing still. In this case, 1 image every 20 images was processed, resulting in an effective acquisition frequency of 15 Hz. The average  $Q$  of the instantaneous fields is 2.6, somewhat larger than in case of rotating disk. The cross-correlation coefficient reaches a value of 0.9, and is higher than what was estimated for the rotating disk case, because the particles maintained the in-plane motion due to the absence of the pumping effect. The image seeding density of the FOV is 0.025 ppp, giving an average of 13 particles per window. The seeding concentration is even more inhomogeneous (larger concentration at the top) compared to the rotating disk case, also because of the absence of forcing, thus particles were convected upwards. The number of outliers that were removed was 0.7 %. The NC, originating from the base of the cube, together with the thermal losses from the sides, which progressively increases towards the top (increase in metal surface area), promote an acceleration of the fluid towards the ceiling. When a colloidal suspension is subjected to a temperature gradient, the dispersed particles display a drift velocity toward the colder regions in addition to the Brownian motion.

The NIVA can be approximated by a case of horizontal convection heated from the bottom with a uniform temperature profile distribution, occurring within an enclosure. The relative importance between the effects of the buoyancy forces, and the effects of the viscosity forces and thermal conduction can be assessed with the Rayleigh number. For

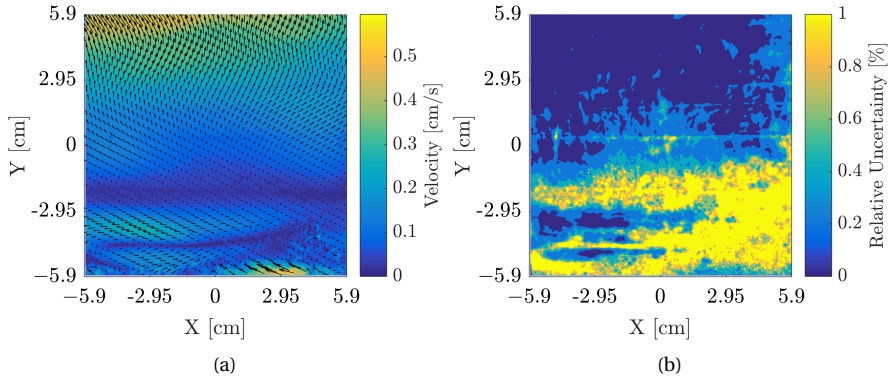


Figure 3.5: NC case. The FOV is 12 cm · 12 cm. **(a)** Avg. vel. field. **(b)** Relative uncertainty.

Rayleigh number values lower than a certain critical value, which is dependent on the geometry, the system is in steady state, e.g., no free convection. For values higher than that value, the system becomes unstable and natural convection movements take place. Under the assumption of infinite horizontal plates the critical value is 1708, above which natural convection initiates. However, for an enclosure heated from the bottom, where the aspect ratio between the L, W and H is 1, the critical Rayleigh number is not equal to 1708. Soong *et al.* [358] found that the presence of confining side walls results in a higher critical Rayleigh number, and Papanicolaou & Gopalakrishna [288] reported that for a discrete heat source with confining side walls, there is a range of critical Rayleigh numbers, depending on the length of the source and the height of the domain.

The Rayleigh number is defined as

$$Ra = \frac{g \cdot \beta}{\mu \cdot \alpha} \cdot \Delta T \cdot H^3$$

where  $g$  is the gravitational acceleration and  $\mu$  is the dynamic viscosity.  $\Delta T = T_s - T_\infty$  is temperature difference between the surfaces of the bottom and top plate. For an ideal gas with pressure held constant, the volumetric thermal expansivity (i.e. relative change in volume due to temperature change),  $\beta$  is the inverse of temperature. The properties of fluid are taken at an absolute pressure  $P$  of 0.283 bara and at an average temperature  $T$  inside the cube, e.g.,  $(T_s + T_\infty)/2$ . Therefore, for natural convection from a horizontal plate, given the experimental conditions above,  $\beta = 1/T = 0.00231$ . This assumption is validated by calculating the compressibility factor,

$$Z = \frac{P}{\rho \cdot R/M \cdot T},$$

for the conditions inside the cube, which results in approximately 0.98.  $R$  is the universal gas constant and  $M$  the molar mass.  $H$  is the thickness of the fluid layer – or characteristic length of the fluid domain. For a flat plate,  $H$  is the area (of the bottom side) of the plate divided by its perimeter  $H = \frac{w \cdot l}{2(w+l)} = 0.0445$ .  $\alpha$  is the thermal diffusivity and is defined as

$$\alpha = \frac{k}{\rho \cdot C_p}$$

and is equal to  $3.7 \times 10^{-6}$ , where  $k$  is the thermal conductivity,  $\rho$  is the local density and  $c_p$  is the specific heat at constant pressure. Therefore, the Rayleigh number is calculated as approx.  $3 \times 10^6$ . The calculated Rayleigh number indicates that it is much larger than the criterion for the onset of natural convection and falls within the range  $5 \times 10^4 < Ra_L < 7 \times 10^9$ , and thus there is thermally unstable turbulence [192, pg. 588].

### 3.5.3. UNCERTAINTY QUANTIFICATION

The correlation statistics approach of Wieneke [403] was used to calculate the absolute and relative uncertainty in the displacement vector from the average vector field. Figures 3.4(b) and 3.5(b) show the corresponding relative uncertainty maps. The RMS uncertainties for Rotating case are 0.7 Abs./px and 0.4 % relative, while for the NC case are 0.4 Abs./px and 1 % relative. The RMS absolute uncertainty is lower for the NC case due to the lower occurrence of out-of-plane particles movement. Since the particle displacement is lower and the absolute uncertainty of the particle displacement is similar for the two cases, the relative uncertainty is higher for the NC case. The relative uncertainty is higher in the layer at the bottom of the cube, also see Fig. 3.5(b), because of the lower particle concentration.

## 3.6. CONCLUSIONS AND OUTLOOK

The work documented here allows to draw the following conclusions regarding the use of PIV in low-speed organic vapor flows.

- The D<sub>4</sub> vapor is sufficiently transparent to conduct PIV.
- Evaporating the fluid together with TiO<sub>2</sub> seeding particles allows to obtain a proper tracer distribution: an external seeder is not needed.
- A seeding density of 0.02 to 0.03 ppp can be achieved with limited particle agglomeration and sufficient contrast ( $Q > 2.5$ ).
- Particles follow the flow with sufficient accuracy ( $St = 6.5 \times 10^{-5}$ ).
- The Rayleigh number is calculated as approx.  $3 \times 10^6$  which is larger than the criterion for the onset of natural convection.
- The relative uncertainty is lower than or equal to 1%.

It can be inferred that PIV is feasible in low speed flows of hot organic vapors. Further work will be devoted to devising a seeding strategy that allows to perform PIV in supersonic and transonic flows in the newly built ORCHID [179].

## ACKNOWLEDGEMENTS

The authors are grateful to H. Lakkad for his help with vector processing, to A. Sciacchitano for his guidance on UQ analysis, and to S. van Herk for the design and realization of the NIVA.



# 4

## PRELIMINARY DESIGN OF THE ORCHID

Contents from:

Head, A., De Servi, C., Casati, E., Pini, M., Colonna, P. Preliminary design of the ORCHID: A facility for studying non-ideal compressible fluid dynamics and testing ORC expanders. In: ASME Turbo Expo. GT2016-56103; 2016, p. 14.

### ABSTRACT

Organic Rankine Cycle (ORC) power systems are receiving increased recognition for the conversion of thermal energy when the source potential and/or its temperature are comparatively low. Mini-ORC units in the power output range of 3 – 50 kW<sub>e</sub> are actively studied for applications involving heat recovery from automotive engines and the exploitation of solar energy. Efficient expanders are the enabling components of such systems, and all the related developments are at the early research stage. Notably, no experimental gasdynamic data are available in the open literature concerning the fluids and flow conditions of interest for mini-ORC expanders. Therefore, all the performance estimation and the fluid dynamic design methodologies adopted in the field rely on non-validated tools. In order to bridge this gap, a new experimental facility capable of continuous operation has been designed and built at Delft University of Technology, the Netherlands. The Organic Rankine Cycle Hybrid Integrated Device (ORCHID) is a research facility resembling a state-of-the-art high-temperature ORC system. It is flexible enough to treat different working fluids and operating conditions with the added benefit of two interchangeable Test Sections (TS's). The first test section is a supersonic nozzle with optical access whose purpose is to perform gas dynamic experiments on dense organic flows in order to validate numerical codes. The second one is a test-bench for mini-ORC expanders of any configuration up to a power output of 80 kW<sub>e</sub>. This chapter



presents the preliminary design of the ORCHID, discussing how the required operational flexibility was attained. The envisaged experiments of the two TS's are also described.

## 4.1. INTRODUCTION

Decentralized systems constitute a promising alternative to improve the sustainability of energy conversion processes. Among the technologies considered for this new scenario, ORC power systems are a proven and cost-effective solution. Recently, systems with power output in the 3 – 50 kW<sub>e</sub> range are receiving more attention, due to their potential in applications such as heat recovery from heavy-duty automotive engines and exploitation of solar power [83, 307]. A challenge for the success of mini-ORC systems is the realization of efficient and reliable expanders for which, however, the available design tools are missing proper validation against experimental evidence [64, 243, 297, 356]. More so than with large machines, the design of small-scale expanders depends on correctly representing the fluid-dynamic losses encountered within the flow passages.

A major point of uncertainty in the design process is the reliability of the adopted (i) thermophysical models, (ii) turbulence models (in case of CFD simulations), and (iii) methods for performance estimation of expanders. The closure parameters of the turbulence models and the material-dependent ones associated with the EoS need to be calibrated against an experimental database [111, 133, 257, 268]. Similarly, the loss correlations used in the expander preliminary design phase are typically the result of extensive testing as is the case, e.g., of measurement campaigns on planar turbine cascades [96, 98, 117].

These kinds of data are unavailable for geometries and flows typically encountered in ORC expanders and, more in general, for those constituting the research subject of NICFD, such as transcritical expansions close to the critical point and compressible two-phase flows. New experimental campaigns are mandatory in order to bridge this gap. However, the existing wind-tunnel facilities cannot be easily refurbished to accommodate the operating conditions and fluids necessary for investigating the fundamentals of NICFD flows, and/or the performance of ORC expanders. Therefore construction of new dedicated facilities is of the greatest interest.

The focus of this chapter is on the design of one such setup, called the organic Rankine cycle hybrid integrated device (ORCHID), which at the time of this writing was under construction at Delft University of Technology. The ORCHID consists of a single Balance of Plant<sup>1</sup> (BoP) which realizes an ORC, as shown by the simplified process flow diagram of Fig. 4.1. Two different test sections are closely *integrated* into this BoP, and they can be alternatively fed and used, thus making the setup *hybrid*. The first one is a nozzle with optical access to perform fundamental experiments, whose research objectives are (i) to verify the NICFD theoretical fundamentals [161, 172, 375], and (ii) to validate the CFD flow solvers implementing the related thermodynamic models and turbulence models [89, 90, 257, 391]. The second is a test-bench for mini-ORC expanders of any configuration (i.e., turbines, scroll, screw, and piston) up to a power output of 80 kW<sub>e</sub>, whose aim is to provide data to validate or develop semi-empirical correlations for fluid-dynamic losses, to assess design methodologies, and to evaluate the accuracy of CFD

---

<sup>1</sup>The BoP consists of all infrastructural components of the setup with the exception of the two test sections.

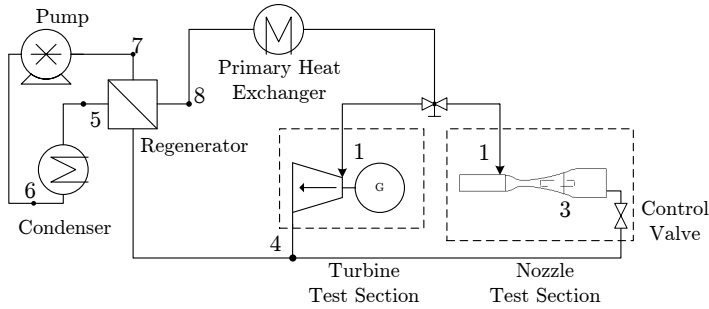


Figure 4.1: Simplified process flow diagram of the ORCHID.

tools [64, 87, 174, 243, 297, 356, 391].

The first expanders that are going to be tested will be turbines of different flow configurations with a rated power of 10 kW<sub>e</sub>, since the focus of ongoing research is on the development of mini-ORC systems for solar power conversion in commercial or residential buildings, and heat recovery on board long-haul trucks. Turbines are deemed more suited for the mentioned applications than volumetric expanders due to their envisaged higher reliability and efficiency [64]. For such a reason, this section of the test-rig is hereafter referred to as the turbine TS.

The ORCHID can be operated with a variety of working fluids. The maximum achievable working fluid temperature and pressure can be as high as 400 °C and 25 bar, respectively, allowing for the realization of a wide range of thermodynamic regimes of interest for NICFD studies and ORC applications: subcritical, supercritical, and two-phase liquid-vapor expansions can be investigated in both test sections [83, 307].

This chapter is structured as follows. Previous and current activities in the field of experimental NICFD are described in Sec. 4.2, while those related to ORC expanders testing in Sec. 4.3. How the ORCHID relates with these research efforts is detailed in Sec. 4.4, whereas the experiments planned for the novel facility are discussed in Sec. 4.5. The design methodologies devised for the ORCHID and its test sections in order to overcome the challenges posed by the desired operational flexibility are detailed in Secs. 4.6, 4.7, 4.8, and 4.9. The conclusions and an outlook for future work are presented in Sec. 4.10.

## 4.2. ORC VAPOR TUNNELS

Experimental setups such as shock-tubes and wind tunnels embraced a long tradition in aerodynamics research [31, 301, 302]. These facilities are typically classified by their geometrical configuration, flow speed, and WF, although air is the most commonly adopted. Given the growing interest in investigating NICFD flows, and in particular the expansion of ORC fluids vapors, several concepts for new dedicated test rigs have been presented in the literature.

These can be first classified according to their mode of operation as *intermittent*, or *continuous*. The fundamental choice of the setup configuration is the result of a complex trade-off analysis involving the envisaged experiments, the test section dimension, the thermal input/output required/discharged by the facility, and finally the needed equipment. Among the intermittent setups, shock-tubes have been used to perform NICFD experiments for decades, mainly in the attempt of proving the existence of so-called non-classical gasdynamic effects [142, 168, 248, 375]. For a more in-depth treatment of this topic the reader is referred to Ch. 2.

More recently, also ORC vapor tunnel concepts have been described. The TROVA setup, designed and built at the Politecnico di Milano University, aims at studying NICFD expanding flows of ORC vapors up to temperatures and pressures of 400 °C and 50 bar, and implements an intermittent blow-down configuration [365, 366].

The blow-down solution is adopted to reduce the thermal energy input required for the experiments. Notably, an input of approximately 30 kW<sub>th</sub> is enough to slowly vaporize the fluid in a high pressure vessel over few hours, and then feed the nozzle at a lower pressure. The drawback of this solution is that the duration of the experiments may only last a few minutes and the pressure ratio across the nozzle is not constant [365]. The experimental campaigns dealt with vapor expansion of siloxane MDM and MM close to the critical point [63, 359].

An ORC vapor tunnel of the continuous type is being designed and built in Germany, as discussed in Ref. [176]. Its main objective is to study the flow of ORC vapors through linear turbine cascades, in order to develop loss correlations for turboexpanders. This setup adopts the so-called gas cycle configuration [365]: the vapor exiting the test section enters a diffuser in order to recover part of its kinetic energy content, is then cooled, and its pressure finally restored to the TS inlet value through an high-temperature compressor, thus closing the cycle. The facility is conceived to operate at sub-sonic and trans-sonic regimes, whereas higher Mach number operation is hindered by the compressor capabilities.

### 4.3. RESEARCH ORC MODULES

In the ORC field, alongside to the vapor tunnels, there are also facilities dedicated to investigations both at system level – e.g., dealing with cycle configurations and control strategies – and at component level – e.g., aiming at the assessment of the performance of heat exchangers or expanders. Since expanders are arguably the most critical components, the objective of the majority of the research modules presented in the literature is the study of ORC expanders. A short selection of these systems is collected in Tab. 4.1, focusing on those tailored to turbine testing; the interested reader is referred to Refs. [307, 356] for an overview of ORC modules intended to test volumetric expanders. For each facility reported in Tab. 4.1, the following information is listed: the year in which the results were published; the considered turbine type (T-AX = axial, and T-RAD = radial inflow); the power capacity  $\dot{W}$ ; the temperature and pressure at the turbine inlet  $T_{in}$  and  $P_{in}$ ; the pressure ratio across the machine; and the speed of revolution  $\omega$ .

According to the authors' knowledge, few other high-temperature facilities are currently in the commissioning phase such as, e.g., those described in Refs. [219, 384].

Table 4.1: Review of research ORC modules.

Year	Exp. type	$\dot{W}$ / $\text{kW}_e$	$T_{\text{in}}$ / $^{\circ}\text{C}$	$P_{\text{in}}$ / bar	$\Delta p$ / –	$\omega$ / $\text{krPM}$	Ref.
1961	T-AX	2–10	150	n.a.	n.a.	18	Tabor & Bronicki [372]
1975	T-RAD	2	93	3.7	5.4.	52	Prigmore & Barber [306]
1980	T-AX	40	110	0.7	14	7	[65] and Angelino <i>et al.</i> [17]
1978	T-AX	50	216	11	150	7	Verneau [388]
1988	T-AX	25	400	42	n.a.	60	Jaffe [198]
2007	T-RAD	15	80	1.1	5	20	Inoue <i>et al.</i> [193]
2012	T-RAD	35	80	8	3	20	Kang [209]
2013	T-AX	4–7	52–66	7 - 9	2	3	Borsukiewicz-Gozdur [51] and Klonowicz <i>et al.</i> [211]

n.a. stands for not available

#### 4.4. THE ORCHID CONCEPT

As previously mentioned, the ORCHID is conceived for both fundamental studies on NICFD flows and for testing of ORC components, most notably expanders. It features a BoP implementing a high-temperature regenerative ORC system configuration, as this is deemed the best solution in relation to the research objectives outlined in Sec. 4.1.

With respect to existing ORC vapor tunnels (see Sec. 4.2), the configuration selected for the ORCHID allows to

- avoid limitations on the testing time: once the setup reaches steady operation continuous measurement campaigns are possible;
- avoid critical issues concerning the use and control of high-temperature control valves;
- reduce the complexity of interpretation of experimental data, since the boundary conditions given by the BoP are expected to be stable throughout the test; and,
- attain highly supersonic flow regimes. Notably, a design Mach number of the order of 2 is selected for the nozzle TS (see Sec. 4.8.1), since it is characteristic of flow conditions typically encountered in supersonic ORC turbines.

With respect to existing ORC research modules (see Sec. 4.3), the configuration selected for the ORCHID allows to:

- attain all the thermodynamic conditions of interest for present and currently envisaged mini ORC applications, i.e., up to  $T_{\text{max}} \approx 400^{\circ}\text{C}$  and  $P_{\text{max}} \approx 25$  bara, operating in the liquid-vapor two phase, sub-, and super-critical regimes;
- perform global measurements (e.g., expander efficiency) and, most notably, detailed investigations of the flow features within the machines. This could be achieved by adopting flow visualization techniques such as PIV. This makes the ORCHID the first facility conceived to deepen the study of ORC expanders by using advanced investigation techniques, presently adopted only in much more mature research fields such as, e.g., that of gas turbines [407]; and,

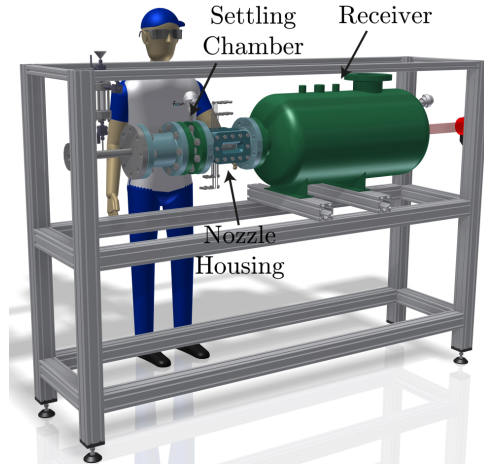


Figure 4.2: Conceptual view of the nozzle TS.

- reproduce the operating conditions of a real-world ORC system.

## 4.5. ENVISAGED TEST SECTION EXPERIMENTS

The nozzle TS is composed of three primary components: the settling chamber, the nozzle housing, and the receiver, see Fig. 4.2. The settling chamber contains flow straighteners and wire meshes in order to promote flow uniformity at the inlet of the nozzle. The nozzle housing guarantees a smooth transition between the circular section of the settling chamber and the rectangular one characterizing the measurement section, which consists of a de Laval nozzle. The receiver is a pressure vessel wherein the flow is slowed down by dissipating part of its kinetic energy.

The turbine TS will be constituted by an assembly incorporating all the mechanical components needed to test expanders and, in particular, turbines. The load absorbing equipment is comprised of a reversible generator/motor electric machine, and an electronic power modulation unit.

Both TS's are configured to accommodate conventional measurements – e.g., static pressure through wall-taps – and laser based diagnostics – e.g., velocity field through PIV – such that several types of experiments can be designed. All the test section's components are replaceable in order to perform experiments with different WFs and operating conditions. Irrespective of the experiment considered, the stagnation pressure and temperature are measured upstream and downstream of the TS, since these quantities are essential to control the ORCHID and also to interpret the other measured data.

### 4.5.1. NOZZLE TEST SECTION

The first envisaged experimental campaigns aim at investigating shock wave patterns in a NICFD flow by means of the schlieren and PIV techniques. The shock waves are generated by inserting models/obstacles of varying geometry – e.g., surface steps, and

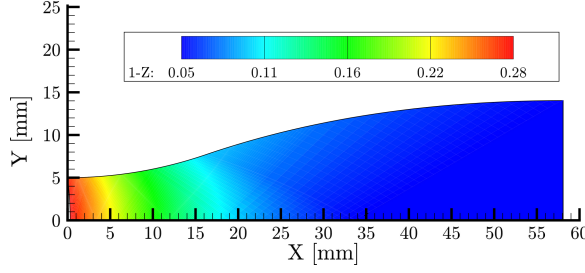


Figure 4.3: Upper part of the diverging portion of nozzle A as designed with the method of characteristics for the MM working fluid and with nominal total inlet conditions corresponding to  $T_0 = 252\text{ °C}$ ,  $P_0 = 18.4\text{ bar}$  and with a back pressure of  $2.1\text{ bar}$  ( $M_{\text{exit}} = 2.0$ ). The nozzle profile is created with a program implementing the method of characteristics, see Ref. [163], with the departure function,  $1 - Z$ , contours plotted using the same program. Fluid properties are estimated with an in-house program [93] implementing the multiparameter equation of state model documented in Ref. [231]. The conditions for which the nozzle was designed are summarized in Tab. 4.5. The nozzle throat is located at  $X = 0$ .

instrumented wedge or diamond shapes – within the diverging part of the measurement section [182]. This information on the flow field characteristics is complemented by pneumatic measurements of the static pressure field along the nozzle profile.

The non-ideality of the flow is commonly represented by the compressibility factor  $Z = p/(\rho RT)^{-1}$ , whose complement to unity, i.e.  $1 - Z$ , is shown in Fig. 4.3 for the expansion process of the first candidate WF siloxane MM. The figure displays the diverging portion of the measurement section,<sup>2</sup> designed according to the method described in Ref. [163] in order to achieve uniform outflow conditions with outlet Mach number  $M = 2$ . As expected, the non-ideal gas effects are more pronounced in the initial part of the expansion, while at the exit section a value of  $Z \approx 0.95$  is predicted, i.e., the fluid approaches the ideal gas behavior. However, even in these conditions, certain flow features – such as, notably, shock waves – cannot be accurately simulated with the ideal gas model, and result in being significantly affected by the adopted thermodynamic model.

As an example, Fig. 4.4 shows the relation between the shock wave angle  $\beta$  and the flow turning angle  $\theta$  – i.e., the wedge semi-aperture angle – for a wedge inserted in the nozzle flow at the nozzle exit section where  $M = 2$ .

This chart is obtained by solving the steady oblique shock wave problem for an arbitrary fluid flow [157], and unveils two important facts. Firstly, the  $\beta$  values predicted with the two thermodynamic models show increasingly large differences as  $\theta$  increases, until the detachment angle is reached. It is thus possible to appreciate the influence of the WF properties on the shock wave pattern established in the nozzle, even in conditions of comparatively low departure from ideality. Secondly, the predicted  $\beta$  values are clearly independent from the adopted EoS for  $\theta$  approaching zero, i.e., when slender conical models are used in place of a wedge. In this case Mach waves originate at the tip of the model and the following relation holds between the Mach number of the impinging flow  $M_1$  and  $\beta$  [157]:

<sup>2</sup>This is the first of two nozzle profiles used for the experiments of Ch. 5.

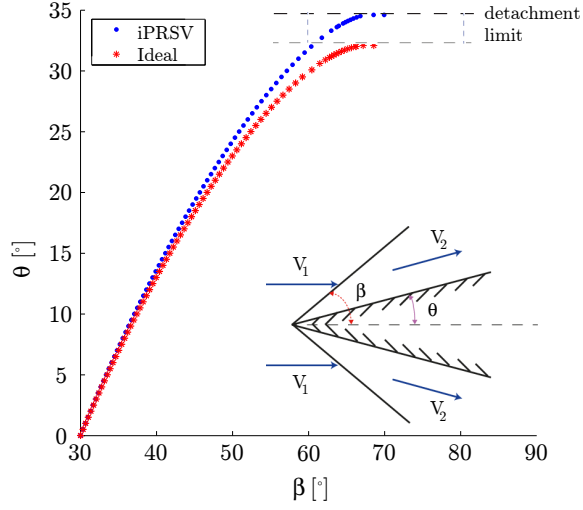


Figure 4.4:  $\theta - \beta - M$  diagram for the Siloxane MM nozzle shown in Fig. 4.3, considering the iPRSV and the ideal gas thermodynamic models, for a wedge positioned at the nozzle outlet where  $M_1 = 2$ ,  $\rho_1 = 5.12 \text{ kg/m}^3$ ,  $h_1 = 3.73 \times 10^5 \text{ J/kg}$ .

$$\lim_{\theta \rightarrow 0} M_1 = \frac{1}{\sin(\beta)}. \quad (4.1)$$

According to Eqn. 4.1, the experimental determination through schlieren imaging of the  $\beta$  angle generated by a slender pin makes it possible to directly estimate  $M_1$ , without resorting to any thermodynamic model [182]. This, in turn, allows for the determination of the local speed of sound  $c$  if the velocity  $v_1$  is also measured, e.g., through PIV, being  $c = v_1 M_1^{-1}$  by definition of  $M$ .

In summary, the first experimental campaign allows to visualize and characterize shock and Mach waves by means of different types of models positioned at varying stream-wise locations. The information collected both in the non-ideal and ideal gas region will then serve to assess the accuracy of the NICFD tools. With the same scope, further envisaged experiments will employ PIV to investigate the velocity fields and the boundary layer evolution along the nozzle, in order to characterize the turbulence properties of NICFD flows.

#### 4.5.2. TURBINE TEST SECTION

The experiments to be performed in the turbine TS aim at investigating the performance of mini-ORC expanders of any configuration (i.e., turbines, scroll, screw, and piston) up to a power output of  $80 \text{ kW}_e$ . Furthermore, all the measured quantities listed in the following can be estimated at both design and off-design operating conditions.

Firstly, the turbine TS allows to assess global quantities such as, most notably, the expander efficiency. Since the experimental determination of this fundamental quantity

is quite challenging, particularly for small-scale turbines, several concurrent estimation methods ought to be adopted [66, 219]. The simplest method of evaluation makes use of the pressure and temperature measurements at the inlet and outlet sections of the machine. The efficiency is assessed by estimating the enthalpy drop of the WF across the expander and the corresponding isentropic enthalpy difference. Furthermore, the use of a reversible generator/motor electric machine – e.g., instead of a brake – permits, in principle, to estimate losses such as those caused by friction in the bearings, seals, and over the rotating disks. This is an important feature since, as the turbine size is reduced, such penalties have a progressively large impact on the performance of the machine [117, 180, 388]. In addition, if the mentioned loss mechanisms can be accurately modeled, an alternative quantification of the efficiency is possible on the basis of the electrical power of the generator.

Secondly, the turbine TS is fully equipped to investigate the detailed flow features within the machine blade passages. The average – i.e., stationary – pressure field can be derived by measurements performed through wall-taps placed along the blade profiles of the stators and aerodynamic probes traversed downstream stationary and rotating blades [58]. However, as discussed also in Ref. [365], the use of aerodynamic probes cannot be easily applied in the NICFD field, due to the difficulty of performing a proper calibration. Also the occurrence of WF condensation in the pneumatic measurement lines is known to be a critical issue, which is counteracted in the ORCHID by a proper purging system employing compressed nitrogen. Finally, the possibility of using optical flow visualization techniques such as PIV – presently adopted only in much more mature research fields [407] – will be explored.

## 4.6. FLUID CANDIDATES

The ORCHID must be able to operate with a wide range of WFs of interest in ORC technology practice, and particularly with those that are promising for mini-ORC systems. A list of these compounds, see Refs. [83, 227], which are the candidates considered during the preliminary design of the setup, is reported in Tab. 4.2.



Table 4.2: Candidate fluids and associated data.

Name	CAS Nr.	$T_{CR}$ / °C	$P_{CR}$ / bar	$T_{boil}$ / °C	$T_{TD}$ / °C	Ref.
Siloxanes						
D <sub>4</sub>	556-67-2	313.3	13.3	175.3	350	Colonna <i>et al.</i> [90], and Invernizzi & Bonalumi [196]
D <sub>5</sub>	541-02-6	346.0	11.6	210.9	350	Colonna <i>et al.</i> [90], and Invernizzi & Bonalumi [196]
D <sub>6</sub>	540-97-6	372.6	9.61	245.0	380	-
MM	107-46-0	245.6	19.4	100.2	300	Preissinger & Bruggemann [305], and Weith <i>et al.</i> [396]
MDM	107-51-7	290.9	14.2	152.5	350	Colonna <i>et al.</i> [90], and Invernizzi & Bonalumi [196]
MD <sub>2</sub> M	141-62-8	326.2	12.3	194.4	350	Colonna <i>et al.</i> [90], and [196]
MD <sub>3</sub> M	141-63-9	355.2	9.4	229.9	350	-
MD <sub>4</sub> M	107-52-8	380.1	8.8	260.7	350	-
Hydrocarbons						
Toluene	108-88-3	318.6	41.3	110.6	400	Havens <i>et al.</i> [177], and Angelino <i>et al.</i> [19]
Pentane	109-66-0	196.5	33.7	36.1	270	Leslie <i>et al.</i> [232]
Cyclo- pentane	287-92-3	238.5	45.1	49.3	300	Ginosar <i>et al.</i> [153]
Organofluorines						
PP2	355-02-2	212.9	20.2	76.0	400	F2Chemicals [137]
PP80	354-97-2	233.97*	16.85*	103.2	400	van der Stelt & Colonna [369]
PP90	50285-18-2	256.85*	16*	125.1	400	van der Stelt & Colonna [369]
R245fa	460-73-1	154.0	36.5	15.1	260	Angelino & Invernizzi [18], and Zyhowski [420], and Dai <i>et al.</i> [109]

\* Estimated by thermodynamic predictive models.

These fluids belong to different classes, namely, hydrocarbons, organofluorines, and siloxanes. Table 4.2 shows, for each substance, the critical temperature and pressure  $T_{CR}$  and  $P_{CR}$ , the boiling temperature  $T_{boil}$ , and the estimated thermal stability limit  $T_{TD}$ , i.e., the temperature above which the fluid in contact with stainless steel undergoes fast thermal decomposition leading to irreversible degradation [289]. It is therefore important that, during operation, the WF is maintained at temperatures lower than  $T_{TD}$ .

## 4.7. MAIN DESIGN CONSTRAINTS

The limitation on the maximum temperature of the setup related to the thermal stability of the selected working fluid is not the only requirement to be taken into account in the design process. Several important constraints common to both the test sections have been identified, and these are listed in the following.

*Maximum thermal input.* After a detailed investigation about the available technical options, it has been decided to adopt an electric oil heater as the thermal power source of the test rig. An electric heater allows for an easy modulation of the thermal power, reducing the uncertainty affecting the thermal input value  $\dot{Q}_{in}$ , and consequently the measurements. Moreover, the use of a synthetic oil enables liquid-phase heat transfer at high temperatures, e.g., in excess of 300 °C, with pressure levels in the oil circuit close to atmospheric values. This implies lower operational risks and costs with respect to, for instance, steam boilers. The maximum power output for the electric heater is assumed in the thermodynamic analysis equal to 400 kW<sub>th</sub>. This value has been determined based on technical constraints on the existing power cabin of the lab, as well as by the need of limiting the investment and operating cost.

*Maximum cycle temperature.* The main thermodynamic implication deriving from the adoption of the intermediate oil loop is that the maximum cycle temperature is limited by the thermal stability temperature threshold of the Heat Transfer Fluid (HTF) and of the working fluid. In particular, for thermal oils commonly used in high-temperature industrial applications, e.g., Therminol VP1, such a limit is about 400 °C. However, the maximum cycle temperature is also constrained by the flammability characteristics of the working fluid, see Sec. 5.2 for more information, resulting in a lower achievable temperature. Therefore, assuming an approx. temperature difference of 25 °C at the hot end of the Primary Heat Exchanger, i.e., the evaporator (PHX, see Fig. 4.1), a limiting value of  $T_{max} = 320$  °C is estimated for all working fluids in the analysis.

*Maximum cycle pressure.* The maximum working fluid pressure in the system is set to 25 bara. This limit has been selected due to a preliminary investigation about the typical pressure rating of compact heat exchangers for high-temperature applications.

## 4.8. DESIGN PROCEDURE

In addition to the general requirements of the balance of plant, each TS features its own design specifications – e.g., in terms of condensing pressure or WF mass flow rate – because the nature of the envisaged experiments is so different. For this reason, during the preliminary design of the facility, the nozzle and the turbine TS's are initially considered independent from one another. In a second phase, the results of the thermodynamic analysis are compared in order to determine which working fluids are compatible with

the operation of both the test sections, and to define the design specifications for the main equipment.

#### 4.8.1. NOZZLE TEST SECTION

The procedure for the preliminary design of the nozzle test section involves four fundamental variables, namely:

- the pressure at the inlet of the nozzle  $P_1$  (nomenclature referring to Fig. 4.1);
- the temperature at the inlet of the nozzle  $T_1$ ;
- the pressure at the nozzle outlet  $P_3$ ; and,
- the area of the nozzle throat  $A_{th}$ , which is the minimum flow passage area where the flow attains sonic – or choking – conditions.

As anticipated, in order to perform the NICFD experiments of interest, it is necessary to achieve thermodynamic conditions at the inlet of the nozzle TS such that (i) the expanding fluid is in the so-called dense vapor regime (see Sec. 4.2), and (ii) a supersonic flow is established. To attain these conditions, the pressure  $P_1$  is to be as high as possible, as shown in Fig. 4.5(a): the thermodynamic state at the nozzle inlet has to be located at supercritical pressure levels or in the proximity of the critical point of the working fluid, so that the expansion process is influenced to a greater extent by NICFD effects. However, the higher  $P_1$ , the larger the circulating  $\dot{m}_{WF}$  required, due to the consequent increase of the fluid density in the nozzle throat, which largely prevails with respect to the simultaneous decrease of speed of sound, see Fig. 4.5(b) and 4.5(c). This trend of  $\dot{m}_{WF}$  versus  $P_1$  occurs independently of the considered WF; and of the chosen nozzle discharge pressure, provided that the throat remains choked. The speed of sound increases along the expansion process since all the substances listed in Tab. 4.2 exhibit values of the so-called fundamental derivative of gas dynamics lower than 1 (but positive) in the considered thermodynamic region [99, 374].

As  $\dot{m}_{WF}$  increases, the required  $\dot{Q}_{in}$  grows proportionally according to the relation

$$\dot{Q}_{in} = \dot{m}_{WF} (h_1 - h_8) \propto \dot{m}_{WF} h_1 = A_{TH} \rho_{TH} v_{TH} h_1 . \quad (4.2)$$

Thus, in order to limit  $\dot{Q}_{in}$ , the value of the nozzle inlet pressure has been restricted to a slightly supercritical value for all the candidate WFs, i.e.,  $P_1 = 1.1 P_{cr}$ .

Regarding the nozzle inlet temperature  $T_1$ , its value has to be such that it prevents condensation during the expansion in the nozzle, and therefore it depends on  $P_1$ .  $T_1$  is defined as

$$T_1 = T(P_1, 1.05 s^*), \quad (4.3)$$

where  $s^*$  is the maximum specific entropy of the saturated vapor in the pressure range involved in the nozzle expansion process ( $P_1 \rightarrow P_3$ ), and the multiplicative factor allows to maintain a certain safety margin with respect to the saturation curve. In case  $T_1$  is greater than the thermal stability limit of the considered fluid  $T_{TD}$  (see Tab. 4.2) or the maximum cycle temperature  $T_{max}$  (see Sec. 4.8), the value of  $P_1$  is lowered in order to match the more stringent temperature constraint, i.e.,

$$P_1 = P(\min(T_{TD}, T_{\max}), s^* + \Delta s), \text{ or} \quad (4.4a)$$

$$P_1 = P_{\text{sat}}(\min(T_{TD}, T_{\max}) - \Delta T_{\text{sh}}). \quad (4.4b)$$

Eq. 4.4b is used in case the cycle is subcritical, whereby a minimum degree of superheating is specified, namely 10 °C.

Considering the goals of the research program to which the realization of the OR-CHID belongs, it is deemed important that the value of the Mach number at the nozzle exit  $M_3$  is comparable to the typical values encountered in mini-ORC turbines, which are generally in the range of 1.8 – 2.2 [83]. Since the thermodynamic conditions at state 1 are already fixed, this requirement is fulfilled by varying  $P_3$ . In particular, a pressure of 2.1 bar in the nozzle receiver is adequate to establish the desired flow conditions for all the candidates WFs. Given the nominal pressure drop of the primary controlling valve placed downstream of the receiver (1 bar), and the estimated pressure losses in the regenerator (0.1 bar), it results that the condenser nominal operating point is at atmospheric pressure when the nozzle TS is in operation.

The throat area  $A_{\text{th}}$  does not affect the thermodynamic region in which the nozzle operates like the other design variables. Instead, it influences the circulating  $\dot{m}_{\text{WF}}$  and consequently the required  $\dot{Q}_{\text{in}}$ , according to Eq. 4.2. Concurrently, the value of  $A_{\text{th}}$  determines the size of the diverging part of the nozzle, being the thermodynamic conditions at the inlet and outlet of the TS fixed. Therefore,  $A_{\text{th}}$  has to be minimized, provided that the blockage effects caused by the insertion of models in the nozzle during the experiments remains negligible. To this end, the nozzle is first sized based on *a priori* criteria — such as the  $A_{\text{th}}/A_{\text{model}}$  ratio used in Ref. [365] and treated extensively in Refs. [111, 351] — and then checked using an open source CFD solver [391], which, in particular, has been employed to investigate the flow field in the nozzle when a model is placed inside its diverging part. Several simulations have been repeated with different types of models, changing their position along the nozzle, as well as adopting diverse WFs. Even though the obtained results are expected to be affected by fairly large uncertainties (see Sec. 4.1), the analysis has allowed to conclude that a rectangular throat with height 10 mm and width 20 mm is adequate for the purposes of the envisaged experiments. Therefore, a value of  $A_{\text{th}} = 200 \text{ mm}^2$  considered in the following design phases.

In addition to the design variables and requirements detailed above, a number of assumptions regarding the performance of the BoP components have to be considered in order to perform the thermodynamic analysis of the system. Such parameters, whose values follow the common practice for commercial ORC systems, are collected in Tab. 4.3, and include: the pressure drop  $\Delta P$  in the heat exchangers, the minimum temperature difference  $\Delta T_{\text{pinch}}$  in the regenerator, and the efficiencies of the components constituting the pump-group, i.e., the pump isentropic efficiency  $\eta_{\text{is,PUMP}}$ , the mechanical efficiency of its transmission system  $\eta_{\text{m,TRANSM}}$ , and the electrical efficiency of its drive motor  $\eta_{\text{e,EM}}$ .

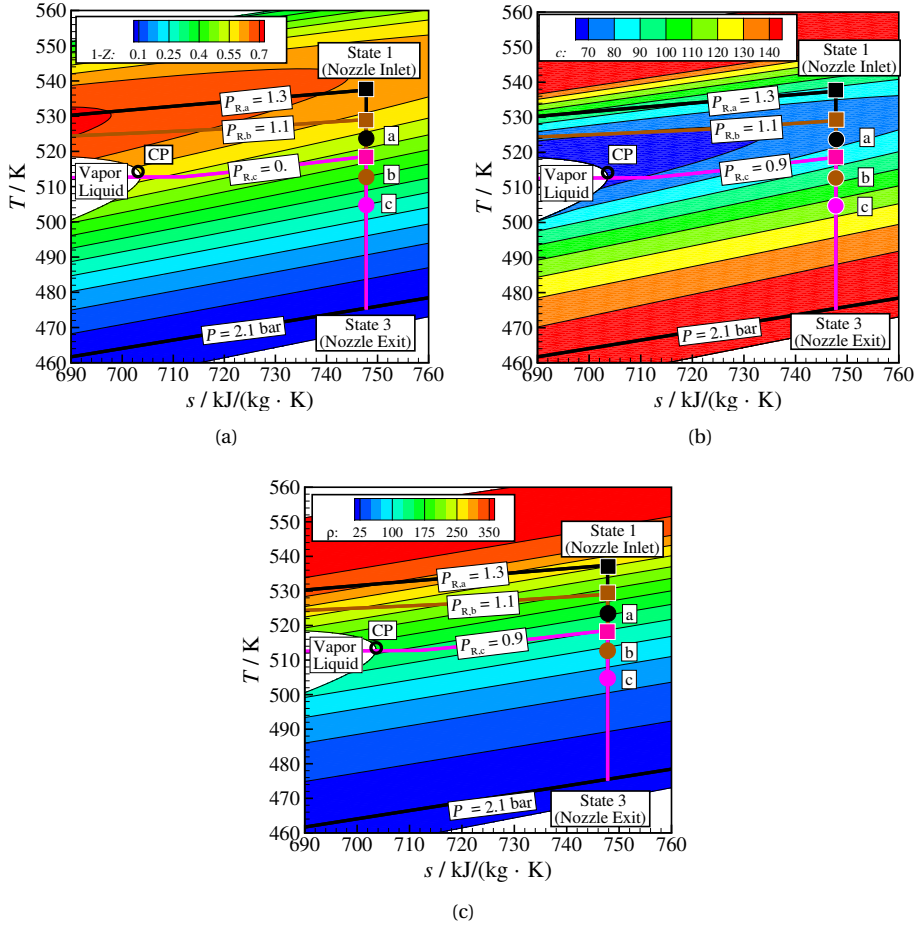


Figure 4.5:  $T - s$  Diagram of MM with contours of (a) the complement to unity of the compressibility factor ( $1 - Z$ ), i.e., the volumetric departure function, (b) speed of sound  $c$ , and (c) density  $\rho$ . The coloured circles along the expansion process highlight the thermodynamic state in the throat for three different values of the reduced pressure  $P_R$  at the nozzle inlet (see squares): 0.9 (see a), 1.1 (see b), and 1.3 (see c). The aim is to show the increase in  $\rho$  and the concurrent decrease in  $c$  in the nozzle critical section as the inlet pressure  $P_1$  is raised. Since the density effect is larger than the speed-of-sound effect,  $\dot{m}_{WF}$  increases with  $P_1$ .

Table 4.3: Design constraints and model assumptions for the thermodynamic analysis of the nozzle TS.

	Variable	Value
Thermal input (max), see Sec. 4.7	$\dot{Q}_{\text{in,max}} / \text{kW}_{\text{th}}$	400
WF temperature (max), see Sec. 4.7	$T_{\text{I,max}}$	$\min(320^\circ\text{C}, T_{\text{TD}})$
WF pressure (max), see Sec. 4.7	$P_{\text{I,max}} / \text{bar}$	25
Nozzle Mach number (out)	$M_{\text{min}}$	1.8
Condenser pressure	$P_6 / \text{bar}$	1.0
Throttling valve pressure drop	$\Delta P_{\text{TV}} / \text{bar}$	1.0
Nozzle discharge pressure	$P_3 / \text{bar}$	2.1
Minimum condenser temperature	$T_6 / ^\circ\text{C}$	50
Regenerator, $T$ diff. @ pinch point	$\Delta T_{\text{PREG}} / ^\circ\text{C}$	20
Heat exchangers $P$ losses	$\Delta P_{\text{HX}}$	$\max(1.0\% P_{\text{in}}, 0.1 \text{ bar})$
Pump efficiency	$\eta_{\text{is,PUMP}} / \%$	50
Mechanical transmission efficiency	$\eta_{\text{m,TRANSM}} / \%$	92
Electric machine efficiency	$\eta_{\text{e,EM}} / \%$	96

#### 4.8.2. TURBINE TEST SECTION

As anticipated, the purpose of this testing system is to experimentally investigate the performance of mini-ORC expanders. Moreover, the same test bench may be used to prove the potential of ORC technology in the small power range, since the setup resembles an ORC unit when the turbine TS is in operation. To pursue this second objective, the design methodology adopted for the turbine TS is based on a system-level optimization aimed at maximizing the thermal efficiency of the test rig, i.e.  $\eta_{th}$ . The manipulated variables are the temperature and pressure at the expander inlet, i.e.,  $T_1$  and  $P_1$ . The goals of the procedure are to identify (i) the working fluids enabling conversion efficiencies around 20% for an application of 10 kW<sub>e</sub> of gross power output, and (ii) the corresponding optimal cycle parameters in order to define the nominal operating conditions of the expander(s) to be tested.

The constraints of the problem are reported in Tab. 4.4 together with the modeling assumptions needed to perform the thermodynamic cycle calculations. The considered design space allows to investigate both subcritical and supercritical cycle arrangements. For supercritical cycle testing, a minimum degree of superheating of 10 °C is specified, while for the superheated cycle testing, a minimum value of  $T_1$  is estimated as a function of  $P_1$  by following the same approach adopted for the nozzle TS, see Sec. 4.8.1.

In accordance with the objective of maximizing the cycle efficiency, the condensing pressure  $P_6$  is lowered with respect to that chosen for the nozzle TS. A value of  $P_6$  equal to 0.3 bar is considered, provided that the corresponding  $T_6$  is higher than 50 °C, i.e., the minimum condensing temperature that can be guaranteed by the cooling system of the setup under all foreseen operating conditions. In other words, in the thermodynamic cycle calculations,  $P_6$  is set to the value of 0.3 bar or to the saturation pressure corresponding to the minimum condensing temperature, whichever value results larger (see Tab. 4.4).

Table 4.4: Design constraints and model assumptions for the thermodynamic analysis of the turbine TS.

	Variable	Value
WF temperature (max), see Sect 4.8	$T_{1,max}$	min(320 °C, $T_{TD}$ )
WF pressure (max), see Sect 4.8	$P_{1,max}$ / bar	25
Gross power output	$\dot{W}_{ORC}$	10 kW <sub>e</sub>
Condenser pressure (min)	$P_{6,min}$ / bar	0.3
Condenser temperature (min)	$T_{6,min}$ / °C	50
Regenerator $T$ diff. @ pinch point	$\Delta T_{PP,REG}$ / °C	10
Superheating (subcritical cycles)	$\Delta T_{sh}$ / °C	10
Heat exchangers pressure losses	$\Delta P_{HX}$	max(1.0 % $P_{in}$ , 0.1 bar)
Turbine efficiency	$\eta_{ts,TURB}$	70 %
Pump hydraulic efficiency	$\eta_{is,PUMP}$ / %	50
Mechanical transmission efficiency	$\eta_{m,TRANSM}$ / %	92
Electric machine efficiency	$\eta_{e,EM}$ / %	96

In order to model the expansion process in the turbine, a total-to-static efficiency  $\eta_{ts,TURB}$  of 70% is assumed. According to preliminary calculations related to machines of this type, such a performance seems to be within practical reach. Finally, as for the pump-electric motor assembly, the losses due to the mechanical transmission and to the efficiency of the electric generator are considered in the calculation of the turbo-

generator output through the value of  $\eta_{m,TRANS}$  and  $\eta_{e,EM}$ .

## 4.9. RESULTS

This section presents the results of the design procedure detailed in Sec. 4.8 for the candidate WFs listed in Sec. 4.6. As previously mentioned, the two TS's are first treated independently in Sec. 4.9.1 and Sec. 4.9.2, respectively. Finally, Sec. 4.9.3 describes how the ORCHID has been designed in order to properly combine the operating conditions required by the two test sections.

### 4.9.1. NOZZLE TEST SECTION

The results discussed in the following are obtained with an in-house code implementing the problem formulation presented in Sec. 4.8.1. The general trend, clearly depicted in Fig. 4.6(a), is that more complex WFs feature lower  $c_{th}$  values, which, in turn, tend to decrease the needed  $\dot{Q}_{in}$ , as already discussed in Sec. 4.8.1. Another important characteristic influencing the results is the shape of the liquid-vapor region in the temperature-entropy thermodynamic plane. WFs exhibiting a positive slope of the vapor saturation curve if plotted on the temperature-entropy diagram (the so-called retrograde shape) enable efficient cycle configurations employing internal regeneration: the thermal energy of the superheated vapor discharged by the turbine is recovered to preheat the WF entering the primary heat exchanger, thus decreasing the required  $\dot{Q}_{in}$ . The amount of regenerated thermal power tends to increase with the slope of the dew line, which is a function of several interrelated properties of the WF. To a first approximation, it is generally observed that the higher the molecular complexity of the substance the more retrograde the shape of the saturation curve is. The interested reader is referred to the work of Invernizzi [195] for a detailed description of these aspects.

Among the candidate fluids listed in Tab. 4.2 and included in the chart of Fig. 4.6, only those for which the needed  $\dot{Q}_{in}$  does not exceed the limit of 400 kW<sub>th</sub> have been considered. In particular, all the candidate siloxanes and perfluorocarbons meet this constraint, as shown in Fig. 4.6(a). The other criterion which determines the rejection of several other WFs is the limit on  $T_1$ , see Fig. 4.6(b). In particular, for some candidate fluids the pressure level at the nozzle inlet has to be reduced in order to match the thermal stability limit or the constraint on the maximum cycle temperature (see Eq. 4.4). As a consequence, the corresponding total reduced pressure reduces from 1.1 to values lower than 0.9, thus making these WFs less suited for the NICFD experiments of interest. This occurs for the following substances: D<sub>5</sub> ( $P_R = 0.58$ ), D<sub>6</sub> ( $P_R = 0.38$ ), MD<sub>2</sub>M ( $P_R = 0.79$ ), MD<sub>3</sub>M ( $P_R = 0.5$ ), MD<sub>4</sub>M ( $P_R = 0.32$ ). The fluid MM has been calculated with a reduced pressure of  $P_R = 0.96$  in order to allow for a realistic margin to the  $\dot{Q}_{in,limit}$ . It follows that the substances suitable for gas dynamic experiments in the nozzle TS are MM, MDM, D<sub>4</sub>, PP2, PP80 and PP90. The main results of the thermodynamic analysis are collected, for these WFs only, in Tab. 4.5, which reports the values of the input thermal power  $\dot{Q}_{in}$ , the thermal power exchanged in the regenerator  $\dot{Q}_{reg}$  and in the condenser  $\dot{Q}_{cond}$ , the pump electrical power  $\dot{W}_p$ , the temperature and pressure levels at the nozzle inlet  $T_1$  and  $P_1$ , the condensing temperature  $P_6$ , and the circulating mass flow rate  $\dot{m}_{WF}$ .



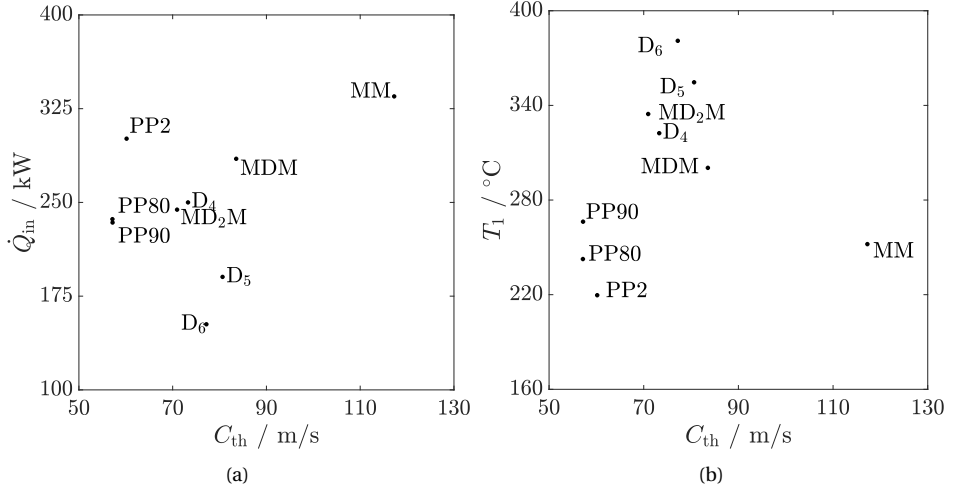


Figure 4.6: Results of the thermodynamic analysis for the experiments: **(a)** Required thermal input  $\dot{Q}_{in}$  against speed of sound in the nozzle throat  $c_{th}$  for a reduced pressure at the nozzle inlet of 1.1 (nb. fluid MM calculated with  $P_r$  of 0.96). **(b)** Maximum WF temperature  $T_1$  against sound speed in the nozzle throat  $c_{th}$ , for all the candidate WFs.

Table 4.5: Results of the thermodynamic analysis for the nozzle experiment: selected WFs.

	MM	PP2	PP90	D <sub>4</sub>	MDM	PP80
$\dot{Q}_{in} / \text{kW}_{th}$	354	302	235	260	291	238
$\dot{Q}_{reg} / \text{kW}_{th}$	327.5	254	254	267	284	250
$\dot{Q}_{cond} / \text{kW}_{th}$	361.5	309	240	265	298	243
$\dot{W}_p / \text{kW}_e$	7.5	8	6	6	7	6
$T_1 / ^\circ\text{C}$	252	219	264	320	299	241
$P_1 / \text{bar}$	18.4	22.7	17.6	14.7	15.6	18.5
$T_6 / ^\circ\text{C}$	100	75	124	176	153	100
$\dot{m}_{WF} / \text{kg} \cdot \text{s}^{-1}$	1.55	3	2.6	1.6	1.5	2.6

Table 4.6: Results of the thermodynamic analysis for the turbine experiment: selected WFs.

	MM	PP2	PP90	Toluene
$Q_{\text{in}} / \text{kW}_{\text{th}}$	48.9	44.9	55.1	47.7
$Q_{\text{reg}} / \text{kW}_{\text{th}}$	53.4	74.4	93.7	21.6
$Q_{\text{cond}} / \text{kW}_{\text{th}}$	38.5	34.4	44.8	36.9
$W_{\text{p}} / \text{kW}_{\text{e}}$	1.1	0.9	1.2	0.6
$T_1 / ^\circ \text{C}$	300	320	320	320
$P_1 / \text{bar}$	22.0	22.0	20.0	25.0
$P_6 / \text{bar}$	0.30	0.43	0.30	0.30
$T_6 / ^\circ \text{C}$	63	50	88	73
$m_{\text{WF}} / \text{kg/s}$	0.17	0.35	0.48	0.09
$\eta_{\text{th}}$	18.2	20.2	16.0	19.7

#### 4.9.2. TURBINE TEST SECTION

The same in-house code mentioned in the previous section is used to implement the problem formulation presented in Sec. 4.8.2. The analysis of the cycle calculation results shows that few candidate WFs allow to reach  $\eta_{\text{th}}$  values around 20%, which is the targeted system performance. These WFs are siloxane MM, perfluorocarbons PP2 and PP90, and toluene. Notably, a value of  $\eta_{\text{th}} \approx 20\%$  is rather ambitious for such a small experimental system, since these performance levels are nowadays achieved by state-of-the-art ORC turbogenerators in the power range of hundreds of  $\text{kW}_{\text{e}}$  [83].

#### 4.9.3. DESIGN SPECIFICATIONS FOR THE BALANCE OF PLANT

By comparing the results pertaining to the design of the nozzle and of the turbine TS's, collected respectively in Tab. 4.5 and 4.6, it can be seen that different candidate WFs are suitable for both experiments. However, it was decided to select one single fluid among all those considered in order to ease the design of the ORCHID and the selection of the BoP equipment. In a second stage, the obtained BoP design will be verified against the operating conditions required by all the other WFs collected in Tab. 4.5 and 4.6, in order to ensure the desired flexibility of operation of the setup. The selected design fluid is siloxane MM since:

- for the nozzle experiment it requires the largest thermal input among the WFs considered at this stage and, in this sense, dimensioning the BoP with MM as the WF can be considered as a conservative choice since it represents the most demanding design case;
- it is already successfully employed in commercial ORC power systems [83];
- there are data about its thermal stability characteristics, see [396], and rather accurate thermodynamic models have been developed to predict its properties [90]; and,
- it is bulk-produced for the cosmetic industry, and its cost is thus comparatively low.

Siloxane MM will also be the first WF to be tested in the ORCHID, and Fig. 4.7 shows thermodynamic cycles corresponding to the nominal operation of the two TS's. In the

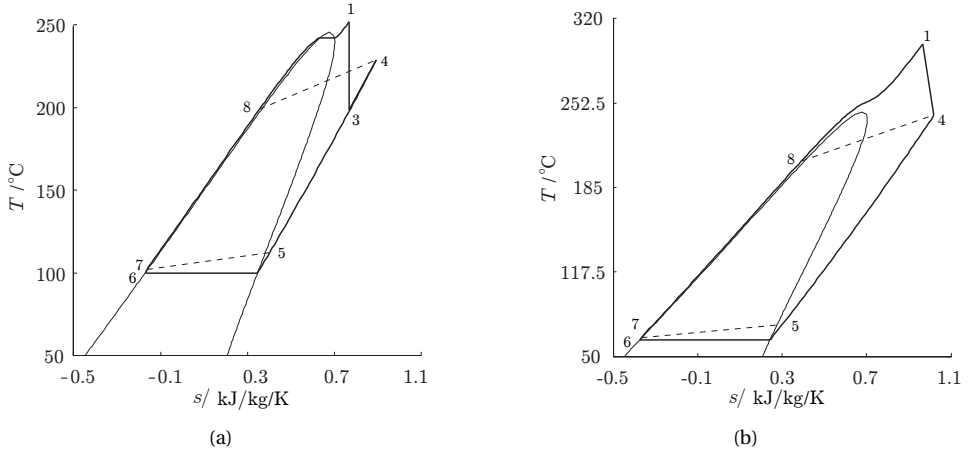


Figure 4.7:  $T - s$  diagram of the design fluid, i.e. siloxane MM, showing the ORCHID thermodynamic cycles during nominal operation of the two TS's. (a) Nozzle TS, (b) Turbine TS.

case of MM the reduced pressure  $P_r$  has been decreased from 1.1 to 0.96, see Fig. 4.7(a), in order to allow for a sufficient margin on the thermal input for the given constraints.

## 4.10. CONCLUSIONS

This chapter describes the preliminary design of a novel experimental facility, named ORCHID, being constructed at the Delft University of Technology at the time of this writing. The ORCHID aims at bridging some of the knowledge gap existing in the fields of NICFD and ORC expander design. In particular, the research objective is to provide suitable experimental data for the validation of CFD tools and design methods for mini-ORC systems. The proposed configuration of the setup features a single BoP for continuous operation of two experimental test sections: a converging-diverging nozzle for fundamental NICFD studies, and a turbine test bench for testing mini-ORC expanders of any configuration up to a power output of approximately 80 kW<sub>e</sub>. The main results of the analysis are as follows:

1. a single and integrated BoP for the operation of the two test sections is conceivable. This implies a number of design challenges, but offers economic advantages that are deemed preponderant with respect to the construction of two distinct facilities.
2. Regarding the nozzle TS, only few WFs among those listed in Tab. 4.2 are compatible with the desired experimental conditions and, in particular, with a supercritical reduced pressure at the inlet of the test sections ( $P_{1,R} = 1.1$ ). These are siloxanes D<sub>4</sub>, MDM, and MM; and perfluorocarbons PP2, PP80 and PP90. The corresponding results are listed in Tab. 4.5.
3. Considering the design constraints of the turbine TS (see Tab. 4.4), only a few WFs among those collected in Tab. 4.2 are compatible with a cycle thermal efficiency

of the order of 20 %. These are siloxane MM, perfluorocarbons PP2 and PP90, and toluene. The corresponding results are listed in Tab. 4.6.

4. Siloxane MM is chosen among the selected WFs as the *design fluid*, i.e., the WF on which the sizing of the BoP components is based. The data pertaining to the other working fluids are used to verify that the obtained BoP design still conforms to the requirements allowing to test all the WFs of interest.
5. In general, the nozzle experiments require a thermal input which is of one order of magnitude larger than what is required by the turbine experiments. Consequently, the circulating WF mass flow rate and the thermal load of all the heat exchangers are much larger in this case. On the contrary, the turbine experiments require more demanding heat exchanger performance in terms of maximum WF temperature and pressure.

## ACKNOWLEDGEMENTS

The research work was conducted in the framework of two research programs on mini-ORC systems funded by the Dutch Technology Foundation STW and the partners Dana-Spicer Corp. and Robert Bosch GmbH (grant numbers 12811 and 13385). The financial support is gratefully acknowledged. The authors would like also to express their gratitude to their colleague Sebastian Bahamonde for his contribution to the development of the models used herein for the thermodynamic calculations, and to Prof. Alberto Guardone for sharing the tools required to design the nozzle profiles. Additionally, our thanks go to Andrea Spinelli and Maximilian Hombsch for their helpful suggestions and feedback related to the design of the ORCHID. Finally, our thanks go to Steve van Herk for his help with the design of the nozzle test section.



# 5

## DETAILED DESIGN AND COMMISSIONING OF THE ORCHID BALANCE OF PLANT

Contents from:

Head, A., De Servi, C., Casati, E., Pini, M., Colonna, P. Commissioning of the ORCHID. Applied Thermal Engineering (TO BE SUBMITTED)

### ABSTRACT

The work described in this chapter is related to the detailed design, the commissioning stages, and the initial operation of a novel experimental setup implementing a recuperated organic Rankine cycle (ORC) capable of feeding dense vapor to both a supersonic nozzle test section and to a mini-turbine test section. The supersonic nozzle is aimed at fundamental gas dynamic investigations, while the high-speed ORC turbine test section will provide unique experimental data for turbomachinery research. The working fluid selected for the first experiments is siloxane MM but the setup is designed to operate with various working fluids. Design requirements are briefly illustrated together with the system configuration. Hardware such as the selected heat exchangers, pumps, electric heater, aircoolers, measurement & actuation instrumentation together with the control procedures are reported and features discussed in relation to the objectives of the experiments. The successful commissioning of the setup with MM as the working fluid is documented by detailing and discussing the recordings of several test runs, including the start up and shut down of the facility and the operation at steady state at the two main operating conditions typical of supersonic nozzle tests and ORC turbine tests. The operation of the facility is characterized with regards to the process stability, moreover process variables are assessed for their uncertainties. The correct operation of the

nozzle test section was verified with inlet conditions at  $T = 252\text{ }^{\circ}\text{C}$ ,  $P = 18.36\text{ bara}$  and  $\dot{m} = 1.25\text{ kg/s}$ , while that of the turbine test section was verified with inlet conditions at  $T = 275\text{ }^{\circ}\text{C}$ ,  $P = 20.8\text{ bara}$  and  $\dot{m} = 0.17\text{ kg/s}$ . All the relevant process variables of the test section are affected by a relative process uncertainty that is lower than 0.6 %.

## 5.1. INTRODUCTION

The literature reviewed in Ch. 2 regarding theoretical, numerical and experimental aspects of non ideal compressible fluid dynamics and one of the prominent technologies in which it plays a role, organic Rankine cycle power systems, puts into evidence the motivation that led to the design, construction and commissioning of the ORCHID. On the one hand, accurate measurements of supersonic flows of organic fluids expanding in the non ideal regime at high reduced temperature and pressure are scarce and are greatly needed to corroborate the rather extensive theory and to validate simulation codes. On the other hand, the development of guidelines for the design and performance evaluation of high-temperature and high-speed ORC turbines necessitates reliable experimental information. The reader is referred also to the introduction of Ch. 4 on the preliminary design of the ORCHID for further considerations regarding the motivation for its realization.

This chapter gives a detailed overview of the ORCHID design requirements (Sec. 5.2), balance of plant configuration (Sec. 5.3), technical characteristics of all major components (Sec. 5.4) and of measuring instruments and actuators forming the data acquisition and control system (Sec. 5.5). All this information is conducive to the detailed description of the commissioning experiments (Sec. 5.6), including the validation of operation (Sec. 5.6.1) and the results of the commissioning of the setup Sec. 5.6.2 entailing stable operation at two conditions representative of the operation of the two test sections, one related to supersonic nozzle experiments and one to turbine testing. Section 5.6.2 discusses the uncertainty of the main variables defining the operational conditions of the test sections, while concluding remarks and an outlook to future developments are treated in Sec. 5.7.

## 5.2. DESIGN REQUIREMENTS AND LIMITATIONS

As introduced in Ch. 4, the ORCHID must be able to operate with a wide range of working fluids of interest for use in novel ORC power and propulsion systems. Its design should lead to high thermodynamic cycle efficiency and stable working conditions over a broad operating envelope encompassing different types of flow and thermodynamic states at the inlet of the two test sections, both subcritical and supercritical. The facility must therefore feature a balance of plant<sup>1</sup> implementing a state of the art high-temperature ORC and, in addition, measures must be taken to guarantee a high degree of operating flexibility.

The maximum cycle temperature is constrained by the thermal stability limit of the working fluid, see Sec. 4.2, and of the heat transfer fluid of the electric heater adopted as the thermal source of the system. The maximum operating temperature of thermal oils

<sup>1</sup>The balance of plant consists of all infrastructural components of the setup with the exception of the two test sections.

commonly used in industrial applications is around 400 °C. *Therminol VP1*, an eutectic mixture of 73.5 % diphenyl oxide (CAS no. 101-84-8) and 26.5 % diphenyl (CAS no. 92-52-4) was chosen for the heating loop of the setup because of the proven thermal stability performance, even if its melting point (12 °C) is relatively high. The piping of the heating loop thus requires electrical resistance tracing to avoid operational problems during the winter.

Apart from the thermal stability of the working fluid and of the thermal oil, other constraints on the maximum cycle temperature is imposed by the European Directive 1999/92/EC, also known as ATEX 137 directive [136, 201],<sup>2</sup> which prescribes the requirements for workplaces in environments where an explosive atmosphere may occur. Given the flammability characteristics of siloxane MM, the compound chosen as the working fluid for the design of the ORCHID and the first test campaigns, and the maximum fluid temperature, the solution identified to comply with the ATEX 137 directive (Zone 2 with temperature class T2, see [201]) was the enclosure of the working fluid loop of the ORCHID within a cabinet. A dedicated ventilation system extracts a constant mass flow of 1000 m<sup>3</sup>/h of air while the system is in operation. The results of the safety analysis indicated that in this way any vapor leakage during normal operation cannot lead to an explosive mixture, and, if an explosive mixture occurs during abnormal operation, it persists only for a short time.

The other safety measure that must be complied with in order to satisfy the requirements of the ATEX 137 directive is that the maximum surface temperature of the equipment must be kept well below the auto-ignition point of the working fluid, which is 340 °C for MM [126, 151]. The maximum temperature of the working fluid must therefore be limited to 300 °C. According to the ATEX directives, the maximum temperature in the working fluid loop must be limited to 300 °C, which represents the upper limit of the temperature class T2 [201]. For the same reason, the maximum temperature of the heat transfer fluid must be controlled to the value of 320 °C. This value was calculated by taking into account the estimated temperature drop in the piping due to heat losses and the temperature difference between the oil and the working fluid in the primary heat exchanger.

These limitations as well the ATEX classification of the zones surrounding the setup may change if another working fluid is used in place of MM. A dedicated ATEX study is required if the new working fluid is a flammable compound.

In light of all these considerations, of the results of the preliminary design of the test-rig described in Sec. 4.7, and of budgetary constraints, the operational limits prescribed for the design of the ORCHID are those listed in Tab. 5.1. The maximum power output for the selected electric heater is 400 kW<sub>th</sub>, while the maximum working fluid pressure in the system is set to 25 bara. These values have been determined by the need of limiting the investment and operating costs of the ORCHID. The design pressure and temperature of the working fluid loop downstream of the test sections and up to the inlet of the feedpump was set to 5 bara and 150 °C by examining the envisaged operating conditions that are possible at the outlet of the test sections with the considered working fluids.

Consequently, the nominal volume flow rate of the main pump of the facility must be 136 l/min ( $2.26 \times 10^{-3}$  m<sup>3</sup>/s). Mass flow rate values close to the maximum capacity of

---

<sup>2</sup>Based on the Article 153 of the TFEU (ex-Article 137 of the EC Treaty).



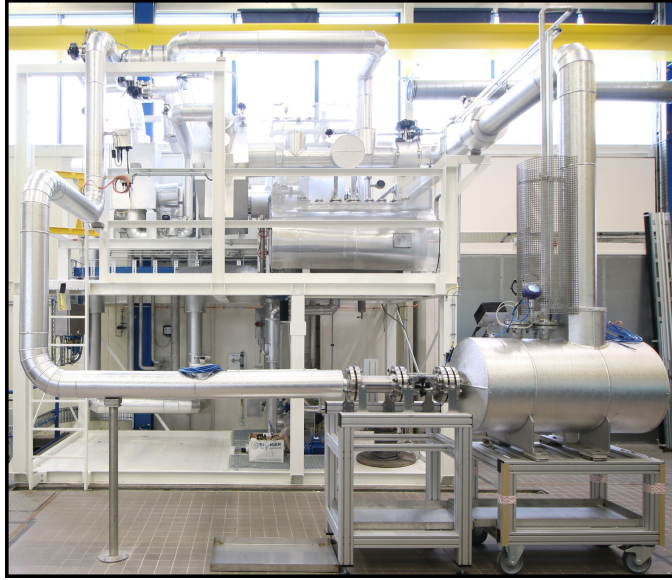


Figure 5.1: The working fluid loop of the ORCHID, before the installation of the ventilation cabinet.

the pump are required for the nozzle NICFD experiments, while the turbine test section will be operated with a working fluid volume flow rate in the range of 10 to 20 l/min ( $1.7 \times 10^{-4}$  to  $3.3 \times 10^{-4}$  m<sup>3</sup>/s).

Table 5.1: Main design specifications for the ORCHID balance of plant.

Working fluid loop	
Maximum temperature / °C	300
Maximum pressure / bara	25
Volume flow rate range / l/ min	10 – 140
Maximum condensing pressure / bara	5
Maximum temperature in the condenser / °C	90
Heating Loop	
Maximum temperature / °C	320
Maximum thermal power / kW	400

### 5.3. BALANCE OF PLANT CONFIGURATION

Figure 5.1 shows a photograph of the ORCHID before the realization of the ventilation enclosure. The configuration adopted for the balance of plant of the ORCHID can be inferred from the simplified Process and Instrumentation Diagram (P&ID) of the ORCHID shown in Fig. 5.2.

The process flow diagram of the facility comprises three fluid loops, i.e., the heating

loop, the working fluid loop which includes the nozzle test section, and the cooling loop. These are indicated in Fig. 5.2 by the colors red, orange and blue, respectively. In the coming years, the setup will be equipped with a second test section to perform experimental studies on mini-ORC turbines. The nozzle test section (dashed-dotted rectangle in Fig. 5.2), can be isolated from the working fluid loop by means of a bypass line and of two pneumatically actuated gate valves installed at the inlet and outlet of the test section. The area of Fig. 5.2 reporting the P&ID of the ORCHID is subdivided in quadrants identified by numbers and letters whose purpose is to facilitate the pinpointing of the components of the system, which are tagged according to the ANSI/ISA S5.1 standard, see Ref. [9]. Figure 5.4 displays a CAD isometric view of ORCHID listing all the main components by number. Each ORCHID component can therefore be singled out on the P&ID by means of a quadrant identifier, and on the CAD isometric view by means of an item number. For instance, the main pump corresponds to D2/item 2, because it is located in the D2 quadrant of Fig. 5.2 and is item 2 in Fig. 5.4.

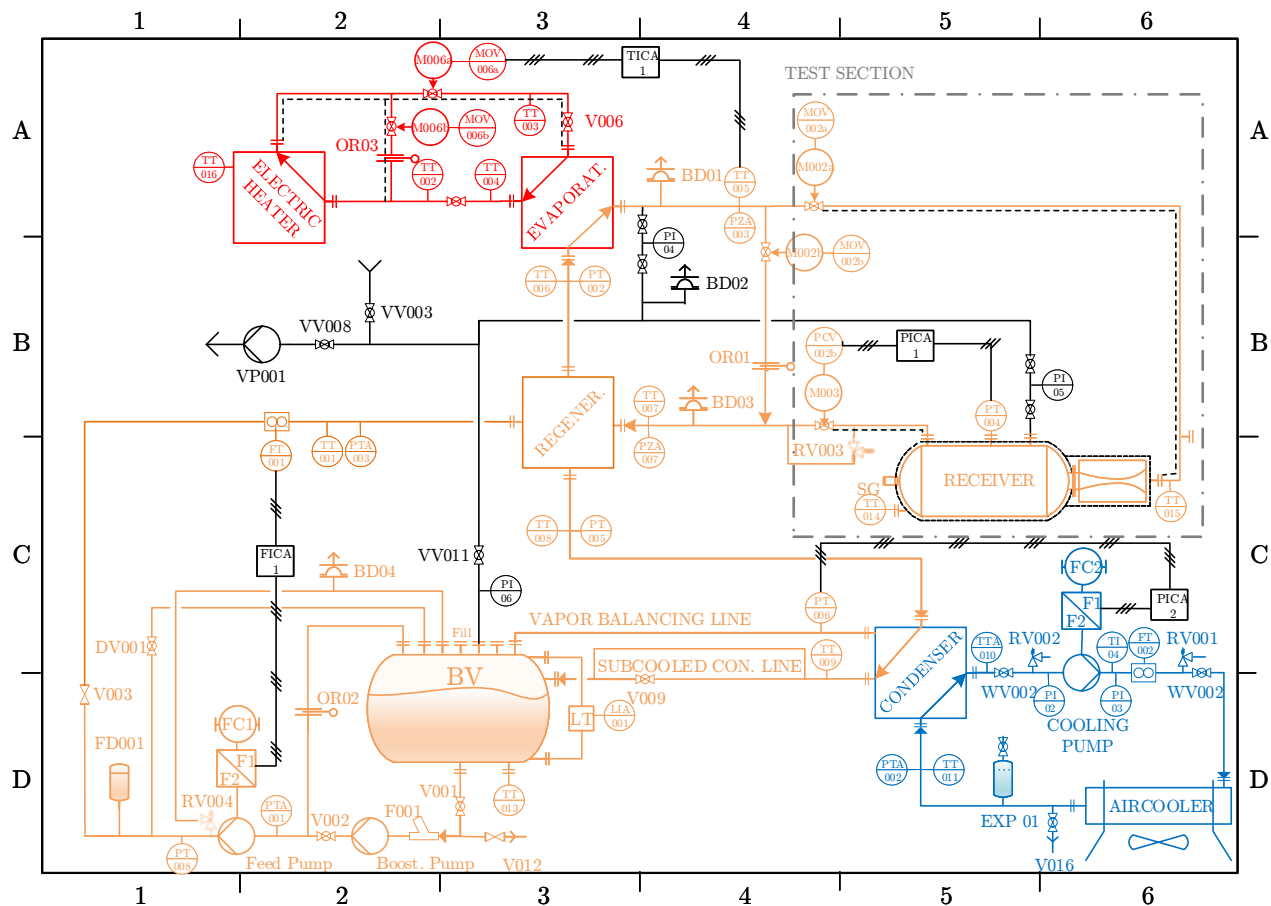


Figure 5.2: Piping and Instrumentation Diagram (P&ID) of the ORCHID. The nomenclature for the symbols is reported in Fig. 5.3.

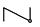



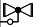

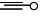
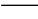
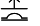


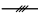
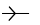



Devices and Actuators	Identification of ducts in relation to the operating medium
 Check Valve	 Working Fluid
 Ball Valve	 Heat Transfer Fluid
 Regulator	 Cooling Fluid
 Orifice Plate	 Vacuum
 Bursting Disk	 Tracing
 Relief Valve	 E-Wiring
 Plug	
 Flow Meter	
 Filter	
 Expansion Vessel	

Figure 5.3: Nomenclature for the symbols of the P&ID of Fig. 5.2.

The working fluid loop can be subdivided into a high-temperature section and low-temperature section. With reference to Fig. 5.2, the high-temperature section is the part of the setup between the booster pump (D2/item 3) and the orifice plate OR01 (B4) positioned on the bypass line or the test section nozzle receiver (C5). The low-temperature section includes the return line of the vapor which extends from the test sections' outlet ports and the orifice plate to the condenser (C5-D5/item 6) and the fluid buffer vessel (C2-C3/item 5). All the piping and components of the circuit, with a few exceptions, e.g., the pumps casing, are made of stainless steel.

The use of carbon steel would have lowered the cost of the facility but also significantly reduced the thermal stability temperature of the working fluid due to higher chemical reactivity of the metal surfaces of carbon steel if compared to that of stainless steel [196, Pg. 126]. A similar effect is exerted by the air that is normally diluted in liquid organic compounds: oxygen tends to promote a breakdown of the molecular bonds, see, e.g., Refs [62, 196, 305]. For this reason, incondensable gases are removed for the major part from the working fluid loop before start-up by means of a vacuum pump.

Both the high-temperature and the low-temperature sections of the working fluid loop are protected against overpressure by a dedicated bursting disk. Bursting disks were preferred to pressure-relief valves owing to the requirement that the working fluid loop must be leak-tight.

As far as the process is concerned, the fluid is first extracted from the buffer vessel by a booster pump, whose primary purpose is to increase the suction head upstream of the main pump (D1-2/item 2). The main pump, then, pressurizes the fluid through the high-temperature section of the circuit, where the working fluid is first preheated in the regenerator (B3/item 7) by recovering thermal energy from the superheated vapor

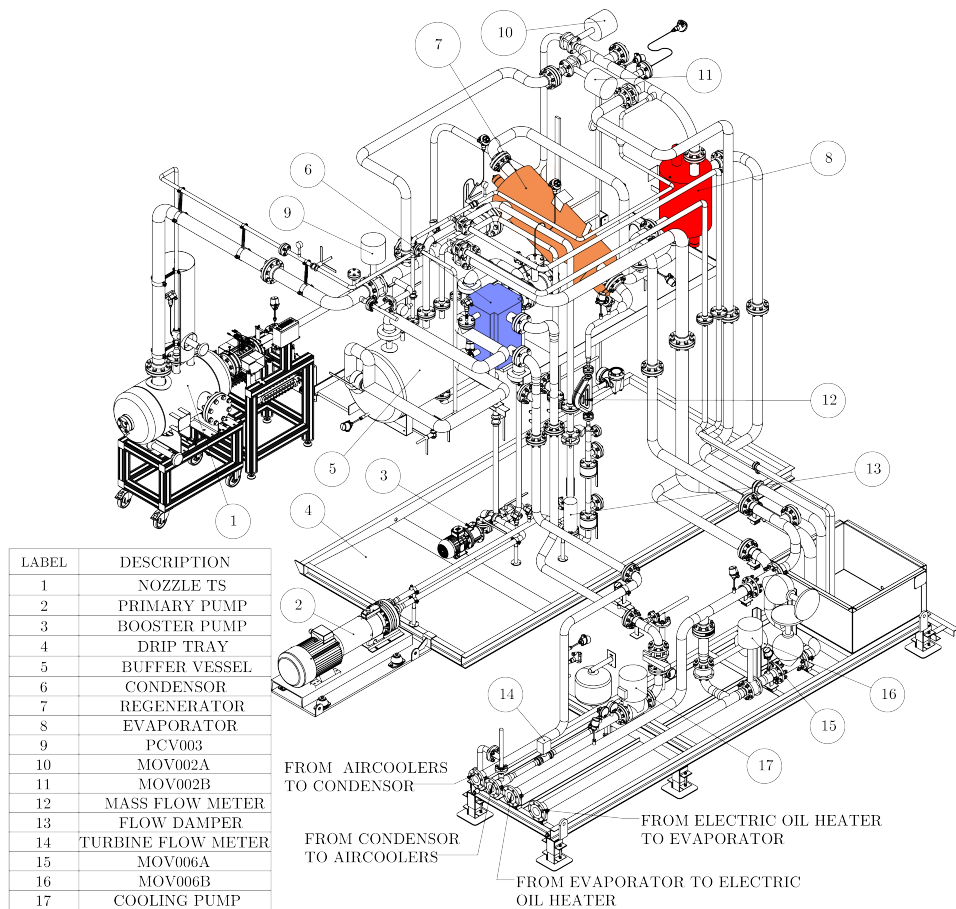


Figure 5.4: CAD isometric view of the ORCHID, highlighting all its main components.

flowing towards the condenser. The regenerator, also named recuperator, is a shell-and-plate heat exchanger, whose nominal thermal capacity is about  $317 \text{ kW}_{\text{th}}$ . The evaporator, which the liquid fluid enters after leaving the recuperator, is also a shell and plate heat exchanger. The working principle of this evaporator is analogous to that of a once-through boiler: the transition from liquid to vapor occurs along the pipes of the heat exchanger without a separation drum. The working fluid then leaves the evaporator as a superheated vapor or as a liquid-vapor mixture, depending on the thermal input and the fluid inlet temperature and mass flow rate. The maximum thermal capacity of the evaporator corresponds to the maximum thermal power that the heating loop can deliver considering the thermal losses in the electric heater and in the piping of the loop, namely  $372 \text{ kW}_{\text{th}}$ .

Downstream of the evaporator, the working fluid is directed towards the test sections or back to the condenser through the bypass line. The two pneumatically actuated gate valves used to isolate the nozzle test section are MOV002a (A4) and PCV003 (B4). The purpose of the MOV002b valve (B4) is, instead, to regulate the flow through the bypass line. The percentage flow characteristic of the three valves is the same, so as to rapidly divert the fluid from the test sections to the bypass line in the case of a failure in the test section or of a vapor leakage. The orifice OR01 of the bypass line has a conical bore of 16.5 mm diameter.

The function of the orifice is to allow for a progressive pressure build-up in the evaporator during the start-up of the setup as the vapor mass flow rate increases. Therefore, during the start-up phase the MOV002b bypass valve need not be regulated, but it can be kept fully open. Moreover, the pressure drop due to the orifice is designed to be similar to that of the nozzle test section at the operational conditions envisaged for the nozzle experiments. In this way, the pressure fluctuations in the working fluid loop are damped when the fluid is diverted from the bypass line to the test section and vice versa.

The thermodynamic cycle realized by the balance of plant of the ORCHID is closed by directing the fluid to a water-cooled condenser (D5/item 6): first, the superheated vapor or liquid/vapor flow passes through the regenerator, thus preheating the cold liquid on the cold side of the heat exchanger, and then it reaches the condenser, and becomes subcooled liquid at its outlet. The condenser is a two-pass plate heat exchanger designed for a maximum thermal duty of  $400 \text{ kW}_{\text{th}}$ . It features two outlet ports, see quadrant C4-D4 in Fig. 5.2. The first one is located on the top of the heat exchanger, at the beginning of the second pass, and it is connected to the so-called vapor-balancing line. The second port is, instead, located at the bottom of the heat exchanger, below the condensate level and it is connected to the line which directs the subcooled fluid to the buffer vessel. This condensate line features a siphon or *gooseneck*, which ensures a sufficient liquid level in the condenser and thus a proper subcooling of the condensate. The degree of subcooling can be manually regulated by means of the V009 valve (D3-D4), which allows a portion of the flow to bypass the gooseneck of the condensate line. The more the flow through the V009 valve is, the lower the liquid level in the condenser and thus the degree of subcooling of the condensate decreases. Conversely, the purpose of the vapor balancing line is to equalize the pressure in the second pass of the condenser and that in the buffer vessel, thereby maintaining the condensate in the buffer vessel in a subcooled liquid state. Without the vapor balancing line, the liquid in the vessel would be in

saturated conditions, at the saturation pressure corresponding to the temperature of the vapor above the liquid level in the vessel. In the case of a pressure mismatch between the condenser and the vessel, the pressure difference causes a vapor flow which tends to restore the hydrostatic equilibrium: the vapor reaching the vessel through the balancing line condenses and heats up the liquid. As a result, the vessel remains sub-cooled though the degree of sub-cooling decreases by about 5 °C.

The main equipment of the cooling loop consists of a centrifugal pump (D6/item 17), whose rotational speed is modulated through a variable-frequency drive to regulate the pressure in the condenser, and in an aircooler (D6) whereby the thermal energy released by the working fluid during condensation is discharged to the environment. Part of the cooling loop is located outdoors, therefore a mixture of water and ethylene glycol (CAS nr. 107-21-1) is used as coolant in order to prevent the freezing of the cooling fluid during winter.

The thermal source of the system is an electric heater in which a bank of resistors supplies energy to a *Therminol VP1* loop, which in turn heats up the working fluid in the evaporator. The volume flow rate of *Therminol VP1* has to be maintained during operation at the design value of 40 m<sup>3</sup>/h prescribed by the manufacturer, in order to ensure the proper cooling of the heating elements. The amount of oil delivered to the evaporator is modulated by two pneumatically driven linear percentage gate valves, namely MOV006a, MOV006b from *Schubert and Salzer* which allows to divert part of the oil flow rate to a line bypassing the evaporator (A2). The opening of the two valves is regulated and synchronized. In order to ease the flow regulation, an orifice is located on the bypass line so that its pressure drop matches the pressure drop across the evaporator. The adoption of a bypass line also enables a quick cut-off of the thermal power supply to the evaporator in the case of a failure of the working fluid loop.

Differently from the working fluid loop, the heating and cooling loops are protected against over-pressure by pressure relief valves. More in detail, the pressure relief valves of the cooling loop RV002 and RV003 (C5-C6) are located up and downstream the pump, and they are rated at 4 barg. The set pressure of the pressure relief valve of the heating loop is, instead, 9 barg. This valve is not reported in Fig. 5.2 since it is embedded in the electric heater skid whose P&ID is not shown for simplicity.

Finally, the facility is equipped with a vacuum system, indicated in black in Fig. 5.2, consisting in a vacuum pump connected through different access points to the working fluid loop. The vacuum system is used to remove the non-condensable gases before the working fluid is charged into the circuit and to verify the leak-tightness of the working fluid loop before start-up. The vacuum system can also be activated during operation to remove the non-condensable gases accumulating in the fluid vessel. The vacuum access points or vacuum ports are located in correspondence with the most bulky components, i.e., the heat exchangers, the buffer vessel and the test section. Each vacuum port features a pressure indicator and a manual ball valve. The vacuum ports connected to the high temperature section of the working fluid loop feature an additional ball valve upstream of the pressure indicator to isolate the indicator from the high temperature vapor during operation. The port associated with VV003 valve (B2) is connected to a nitrogen supply line, which is used for the working fluid loop blanketing after the system is shut down.

## 5.4. MAIN EQUIPMENT CHARACTERISTICS

Table 5.2 summarizes the characteristics and specifications of the primary components of the setup.

Table 5.2: Primary components of the ORCHID.

	Model	Main Specifications
(Volumetric) Primary Pump & variable speed drive (VSD)	<i>PromoTek Wanner Hydra Cell G35, G35XKCTHFEHH</i>	Motor: 400/690 V 50-60 Hz, 15 kW <sub>e</sub> 1050 RPM & max flow rate 136 l.m <sup>-1</sup> (8.2 m <sup>3</sup> /h) with a <i>Siemens SINAMICS G120</i> Controller ( <i>CU240B-2</i> )
Pulsation damper	<i>FlowGuard, FG-40-30-NBR</i>	Volume: 1 litre Bladder: Nitrile membranes
(Centrifugal) Booster Pump	<i>RTOS SDM 3x12</i>	Motor: 400 V 50 Hz, 1.5 kW <sub>e</sub> 2900 RPM & max flow rate of 167 l.m <sup>-1</sup> (10 m <sup>3</sup> /h)
(Centrifugal) Cooling Pump & VSD	<i>KOLMEKS, L-65B/2</i>	Motor: 400 V 50 Hz, 2.2 kW <sub>e</sub> 3000 RPM & max flow rate of 705 l.m <sup>-1</sup> (42.3 m <sup>3</sup> /h) with a NC406 Controller
Evaporator	<i>Alfa Laval, DuroShell</i>	372 kW <sub>th</sub>
Regenerator	<i>Alfa Laval, DuroShell</i>	316.7 kW <sub>th</sub>
Condenser	<i>Alfa Laval COMPABLOCK (Plate)</i>	377.5 kW <sub>th</sub>
Air coolers	<i>Alfa Laval, Alfablue, BDMSE803DD45, CR Feet ICM</i> Single fan row	415 kW <sub>th</sub>
Electric Heater	<i>HTT energy, WTE 10-10-400-2-B</i>	Nominal power, 400 kW <sub>e</sub>
Control Valves (Working fluid Loop)	<i>Schubert and Salzer, GS (Gate Series) pneumatically actuated gate valves</i>	Type: equal-percentage with Diaphragm Actuator 8021/24/26, Flow coefficient $K_V = 0.247$ & $\Delta P = 0.5$ bar
Control Valves (Heating Loop)	<i>Schubert and Salzer, GS (Gate Series) pneumatically actuated gate valves</i>	Type: linear with Diaphragm Actuator 8021/24/26, Flow coefficient $K_V = 4.383$ & $\Delta P = 0.5$ bar

### 5.4.1. WORKING FLUID FEED PUMP AND BOOSTER PUMP

The feed pump (D1/item 1) is a *Wanner Hydra-Cell G35* from *PromoTek*, see Fig. 5.5. It is a positive-displacement diaphragm-type pump, with a rated power of 15 kW<sub>e</sub> and it can operate with a volumetric flow rate between 10 to 136 l/min ( $1.6 \times 10^{-4}$  to  $2.2 \times 10^{-3}$  m<sup>3</sup>/s) by means of a frequency drive. At the maximum flow rate, the motor revolves at 1050 RPM, which corresponds to 54.4 Hz. The volumetric displacement is provided by five multiple rubber diaphragms, which are alternatively flexed by a prime mover to vary the volume of the pump chamber. The working principle is, thus, similar to that of a piston



pump. When the volume is increased, the pressure decreases and the fluid is drawn into the pump chamber. When the volume reduces, the pressure is increased and the fluid is forced out of the pump. The choice of this pump was driven by the following considerations.

- Positive displacement pumps feature higher operating flexibility than centrifugal pumps, both in terms of operational range and working fluids. This is a crucial characteristic for the application at hand, given the desired specifications in terms of multiple working fluids and thermodynamic conditions considered for the ORCHID. The required wide range of mass flow rates ( $0.1 - 3 \text{ kg/s}$ ) resulting from the different operating conditions of the nozzle and turbine test sections could be fulfilled by a centrifugal pump only if complemented by a recirculation line with a control valve.
- The flow rate of a volumetric pump does not vary or varies only marginally with the pump head. This characteristic, together with the simple configuration without recirculation line and control valve, implies that the mass flow rate of the working fluid loop is easy to set and to control. Stable and defined operating conditions are essential requirements for both the nozzle and the turbine experiments.
- Diaphragm pumps can process also low-viscosity liquids, as it is generally the case with working fluids of interest for ORC power systems. Differently from other volumetric pumps, like, e.g., gear pumps, no oil needs to be added to the working fluid to ensure a proper lubrication of the pump. The contamination of the working fluid with oil is detrimental, especially in high-temperature ORC power systems because the lubricant oil decomposes in the evaporator and causes fouling. Furthermore, the oil addition may increase the uncertainty associated with the experiments, since the fluid composition may vary over time as the oil may tend to accumulate in some components and the estimation of the working fluid properties, a mixture, are affected by larger uncertainty.
- the diaphragms provide a hermetic dynamic seal, thus preventing any contamination of the working fluid with the oil of the actuating mechanism.



Figure 5.5: The *Wanner Hydra-Cell G35* feed pump. Image courtesy of *PromoTec*.

There are several technical aspects associated with a diaphragm pump that need to be accounted for when designing the working fluid loop. The most relevant issues include flow pulsations, and the need for a considerably high net pressure suction head (NPSH), which is comparatively larger than that of a centrifugal pump. Since each of the five diaphragms alternatively draws in and pushes out the fluid from the pump chamber, the instantaneous flow rate cyclically varies. For the selected pump, the amplitude of the mass flow rate fluctuations is equal to 5 % of the average mass flow rate value. To reduce this effect, a pulsation damper (FD001, D1/item 13) was added to the circuit, downstream of the main pump. The selected bladder-type damper is manufactured by *Flowguard* (model *FG-40*), its capacity is 1 litre and it is designed to reduce the fluctuations to  $\pm 0.5$  % of the average mass flow rate.<sup>3</sup> Given the design specifications of the ORCHID operated with MM as working fluid, if the pump is at the maximum capacity, the flow rate varies at most between 135.3 and 137.7 l/min. The pulsation damper must be pre-charged with nitrogen at a pressure  $P_{N_2 \text{ charge}}$ , whose value depends on the predicted discharge pump pressure  $P_2$  and temperature  $T_2$  at design conditions according to

$$P_{N_2 \text{ charge}} = P_2 \left( \frac{T_{N_2 \text{ charge}} + 273.15}{T_2 + 273.15} \right),$$

where  $T_{N_2 \text{ charge}}$  is the nitrogen estimated temperature in Celsius. The nitrogen pressure of the pulsation damper for  $P_2 = 18.4$  bara and  $T_2 = 80$  °C and  $T_{N_2 \text{ charge}} = 20$  °C is therefore  $P_{N_2 \text{ charge}} = 15.3$  bara. The casing of the pulsation damper is in stainless-steel, while the bladder or membrane is made out of a Nitrile rubber (also known as Buna-N), the same material as that of the diaphragms of the main pump.

As far the risk of cavitation is concerned, the *required* NPSH is as high as 7.8 m<sub>H<sub>2</sub>O</sub>, considering the worst operating scenario and including a safety margin of 0.5 m<sub>H<sub>2</sub>O</sub>. The pump could be installed only 2 m below the fluid buffer vessel. The *available* NPSH can be increased by subcooling the working fluid in the condenser. However, to guarantee the required suction head at the inlet, it would have been necessary to cool down the condensate by as much as 40 °C below the saturation temperature. This would have led to an unacceptable increase of about 120 kW<sub>th</sub> of the thermal power needed for the envisaged operating conditions. A more efficient solution was then to adopt a booster pump and to mount it upstream of the feed pump and in series.

The selected booster pump (D2/Item 3) is a single stage magnetically driven centrifugal pump (*ROTOS SDM 3 x 12*) and is used to pressurize the fluid on the suction side of the feed pump. The *available* NPSH of the installation can therefore be estimated as

$$\text{NPSH}_A = H_A - H_{VP} - H_{Ac} \pm H_Z - H_F \quad (5.1)$$

where  $H_A$  is the absolute pressure on the free suction surface of the liquid in the buffer vessel (D2-3/item 5) expressed in m<sub>l<sub>c</sub></sub>,  $H_{VP}$  is the vapor pressure of the liquid at the pumping temperature expressed in m<sub>l<sub>c</sub></sub>,  $H_{Ac}$  is the head loss due to the acceleration of the fluid upstream of the pump under consideration,  $H_Z$  is the vertical distance between

<sup>3</sup>The theoretical amplitude of the flow fluctuations could be as low as 0.022 % of the average mass flow rate. The actual pulsation in the flow is, however, related to the installation and operating conditions and tends to be larger than the theoretical value.

the free suction surface of the liquid in the buffer vessel and the pump (2 m in this case), and  $H_F$  is the friction loss.  $H_F$  is assumed equal to  $0.2 m_{lc}$  in each of the suction lines of the pumps. The values of  $H_A$  and  $H_{VP}$ , instead, depend on the specific operating conditions. Finally, the acceleration head loss  $H_{Ac}$  is relevant only for the diaphragm pump as its operating principle is similar to that of reciprocating pumps.  $H_{Ac}$  is estimated equal to  $2.6 m_{lc}$ .<sup>4</sup> As the the differential head provided by the booster pump is approximately 16 m, the *available* NPSH of the diaphragm pump is substantially larger than the required 7.8 m. This may not be the case for the booster pump, whose *required* NPSH is  $1.5 m_{lc}$ . The most critical condition occurs at the start-up of the working fluid loop: the pressure above the liquid level in the buffer vessel equals the vapor pressure of the working fluid, thus  $H_A - H_{VP}$  is equal to zero. Equation 5.1, then, reduces to  $H_Z - H_F$ , which gives  $1.8 m_{lc}$  as *available* NPSH for the booster pump. The difference with respect to the *required* NPSH is thus rather limited and equal to  $0.3 m_{lc}$ . However, the possibility of limited cavitation occurs for a short time at start-up. As the setup warms up, the pressure in the buffer vessel rises and the working fluid can be effectively subcooled in the condenser, thus increasing the *available* NPSH. As an example, at the design conditions, the pressure in the buffer vessel is 1 bara, while the liquid temperature is approximately 95 °C, i.e., 5 °C below the saturation temperature of the fluid. The corresponding MM vapor pressure is about 0.87 bara, resulting in a difference between  $H_A$  and  $H_{VP}$  of about  $1.9 m_{lc}$ . The total *available* NPSH for the booster pump, then, increases to  $3.7 m_{lc}$ . The safety margin with respect to the *required* NPSH is therefore more than 2 m.

As far as other limitations are concerned, the selected booster pump can handle liquid temperatures up to 200 °C. This is not the case for the feed pump, whose maximum operational temperature is limited to 120 °C. However, such a limiting temperature must be reduced further to comply with the ATEX requirements: the supplier of the diaphragm pump does not certify it as ATEX-compliant if the temperature of the oil exceeds 80 °C. To meet this limitation, there are two options: the temperature of the condensate must be always cooled below 80 °C or an air cooler must be added to the oil circuit of the feed pump to cool the oil. At present, the first solution is adopted, therefore the maximum pressure in the condenser is controlled to about 0.7 bara. However, the cooling capacity may not be sufficient during summer to keep the temperature in the condenser at 80 °C. However, to overcome such a limitation, the second option will soon be implemented. Moreover, both pumps are protected from debris by a Y-shaped filter (F001, D2), namely a KSB BOACHEM FSA DN40 PN10-40 with a 1 mm mesh.

Importantly, the rotational speed of the booster pump need not to be controlled. Although the actual flow rate of the booster pump varies based on the load of the main pump, the flow rate provided by the booster pump is larger than that of the feed pump in all operating conditions. The exceeding amount of fluid pumped by the booster pump is sent back to the buffer vessel by a bypass or return line with an orifice plate, (OR02, D1). In this way, the feed pump can be operated at a volumetric flow rate that is lower than the minimum required by the booster pump, i.e. 25 l/min.

---

<sup>4</sup>  $H_{Ac}$  is calculated as  $H_{Ac} = \frac{L_{sl} \cdot \nu \cdot \omega_p \cdot K_p}{1.5 \cdot g}$  and given a suction line length  $L_{sl}$  of 3 m, a fluid velocity  $\nu$  of 0.3 m/s, a pump speed  $\omega_p$  of 1050 RPM, a gravitational constant  $g$  of  $9.81 \text{ m/s}^2$  and a pump constant  $K_p$  of 0.04 results in  $H_{Ac} = 2.58 \text{ m}$ .

Also the feed pump requires the installation of a return line. Actually, two additional lines are installed downstream of this component. The first one incorporates a pressure relief valve (RV004, D1), to direct the flow back to the fluid tank in case there is a sudden blockage in the working fluid circuit, thus preventing overpressure. This is compulsory considering that the main pump is of the positive displacement type. The second line, instead, is used only when the circuit is empty and is charged with the fluid. The DV001 valve is open only during the fluid-charging operation to allow for the liquid to flood the pump flow passages before the pump is operated, as prescribed by the operational manual.

#### 5.4.2. HEAT TRANSFER EQUIPMENT

The three main heat exchangers of the ORCHID working fluid loop are the condenser, the regenerator, and the primary heat exchanger. The selection of this heat transfer equipment was performed based on the following requirements:

- compact footprint, given the space limitations for the installation in the lab;
- high mechanical reliability and resistance due to the cyclic nature of the ORCHID operation, with frequent daily start-up and shut-down per year;
- a leakage-proof design in the light of the potential hazards posed by a working fluid leakage during operation; and,
- ease of maintenance and of cleaning of the heat transfer surfaces, as fouling build-up may occur in the case of a thermal degradation of the working fluid. A slow, minimal, but continuous thermal decomposition process of the working fluid may occur even if the substance is maintained at a temperature below the threshold of its thermal stability limit with a sufficient safety margin. Thermal decomposition is a chemical reaction whose rate has an Arrhenius-like dependency on temperature. The thermal stability limit of a fluid, thus, represents the temperature below which thermal decomposition occurs at an acceptably slow rate. This also applies to the thermal oil of the heater, which, for this reason, also requires periodic replacement.

Other heat transfer equipment of the ORCHID are the aircoolers and the oil electrical heater.

#### PRIMARY HEAT EXCHANGER AND REGENERATOR

In the light of the requirements above, the heat exchanger topology deemed most suitable for the primary heat exchanger and the regenerator is therefore shell-and-plate. With respect to plate heat exchangers, which are widely used in power plants, chemical processes and many other industrial applications owing to their effectiveness and compactness, shell-and-plate heat exchangers feature a similar degree of compactness, but higher resistance to thermal fatigue [148], and lower cost if the high temperature and pressure of the application requires the adoption of a fully welded design. The units,

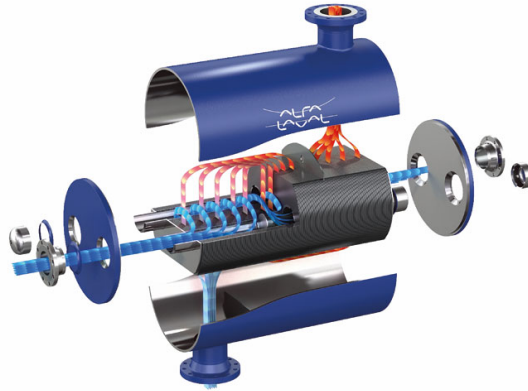


Figure 5.6: Exploded view of the *Alfa Laval DuroShell* shell-and-plate heat exchanger, the type selected for the primary heat exchanger and regenerator of the ORCHID, showing the cross-flow arrangement determined by the plates configuration. Image courtesy of *Alfa Laval*.

thus, cannot be opened for maintenance purposes, but they can be cleaned by chemicals, although this can lead to a subsequent contamination of the working fluid, therefore precautions must be taken to avoid it.

The shell and plate heat exchangers selected as primary heat exchanger and regenerator are manufactured by *Alfa Laval*. The commercial brand name adopted by *Alfa Laval* for their shell-and-plate units is *DuroShell*. An exploded view of this kind of heat exchanger is illustrated in Figure 5.6, where it is possible to recognize the cross-flow arrangement of the unit, as the direction of the two fluid streams is normal to each other. *Alfa Laval* claims that the *DuroShell* heat exchangers are different from other shell-and-plates heat exchangers on the market because of the proprietary geometrical pattern of the plates, dubbed *roller-coaster pattern*. This plate shape is deemed optimal regarding fluid distribution across the plate surface, reduction of thermal stresses, and the risk of fouling build-up [260]. The condenser and the air coolers are also from *Alfa Laval*.

The thermal data used to design the primary heat exchanger and the regenerator are summarized in Tab. 5.3 and 5.4, respectively. The verification that the heat exchangers can operate with the other working fluids has not been performed yet and is planned for the near future. The primary heat exchanger must be capable of evaporating and superheating the fluid but also of heating it to a supercritical state. The primary heater designed by *Alfa Laval*, see Tab. 5.5, features 120 plates in 316L stainless steel of 0.8 mm thickness. The thermal oil enters the plates from the shell, which is, instead, made of carbon steel. The overall net weight of the empty unit is 544 kg. The flow channels are equally distributed over three flow passages. As the total number of channels is equal to the plate number minus 1, each pass has 20 channels, except the first one on the hot side where there are 19 channels. The effective heat transfer area per plate is  $0.093 \text{ m}^2$ , which, if multiplied by 118, since first and last plate do not contribute to thermal energy transfer, gives a total heat transfer area for the primary heat exchanger of about  $11 \text{ m}^2$ . The plate pitch or channel height is constant along the entire heat exchanger and is equal

to 3.0 mm. Finally, the hot-side pressure drop estimated by the manufacturer is 22.8 kPa while that of the cold side is 3.3 kPa. The internal volume of the hot side is 40.2 dm<sup>3</sup>, while the cold side is 20.4 dm<sup>3</sup>. The external dimensions excluding flanges are 475 × 603 mm (D × L).

Table 5.3: Design specifications of the shell-and-plate primary heat exchanger.

		Hot Side (Therminol VP1, liquid)	Cold Side (MM, vapor)
Inlet Temperature	$T_{in} / ^\circ\text{C}$	288	192
Outlet Temperature	$T_{out} / ^\circ\text{C}$	274.9	242
Mass flow rate	$\dot{m} / \text{kg/s}$	9.18	1.54
Thermal power	$P / \text{kW}$	372	

Table 5.4: Design specifications of the shell-and-plate regenerator.

		Hot Side (MM, vapor)	Cold Side (MM, liquid)
Inlet Temperature	$T_{in} / ^\circ\text{C}$	227	92
Outlet Temperature	$T_{out} / ^\circ\text{C}$	120	185
Mass flow rate	$\dot{m} / \text{kg/s}$	1.54	
Thermal power	$P / \text{kW}$	315	

Table 5.5: Main design features of the shell-and-plate primary heat exchanger.

Number of Plates	Grouping		Plates Pitch / mm	Total Area / m <sup>2</sup>	Pressure Drop / kPa <sup>+</sup>	
	Hot Side (Shell Side)	Cold Side (Plate Side)			Hot Side (Shell Side)	Cold Side (Plate Side)
120	1 × 19 + 2 × 20 SM	3 × 20 PM	3	10.97	22.8	3.26

<sup>+</sup> Calculated.

The pump moves the liquid from the back of the regenerator to the outlet of the cold side located on the top of the plate side. The vapor enters and exits the shell side. Despite the lower thermal duty, the regenerator requires an overall heat transfer area about 2.5 times larger than that of the primary heat exchanger, due to the relatively low heat transfer coefficient of the vapor flowing in the hot side. As the plate geometry is identical to that of the primary heat exchanger, such a larger heat transfer area is achieved by increasing the number of plates (270 vs. 120), see Tab. 5.6. The shell material is carbon steel and the plate material is 316L stainless steel.

The effective area per plate is 0.0929 m<sup>2</sup>, which, if multiplied by 268, gives a total area of 24.92 m<sup>2</sup>. The calculated hot-side pressure drop is 25.6 kPa and that of the cold side is 7.13 kPa. The plate grouping is more complicated if compared to that of the primary heat exchanger. The 270 plates are subdivided to form 134 channels on the shell side (working fluid vapor) and 135 channels on the plate side (working fluid liquid). The

shell side features 4 U-shaped passes, which allows both fluid inlets and outlets to be connected to the same side, therefore the unit can be disassembled for maintenance without disconnecting the heat exchanger from the fluid entry and exit pipes. The pipes are grouped with a  $2 \times 33 + 2 \times 34$ SM arrangement, where SM stands for Shell Material. There is only one channel type with an average medium plate distance of 3 mm. The plate side is formed by 135 channels, divided into 8 passes, resulting in a grouping of  $1 \times 16 + 7 \times 17$ PM, where PM stands for Plate Material. The relative arrangement of the fluid streams is cross-flow and the calculated correction factor for the logarithmic mean temperature difference is 0.906.

Equations for counter-current heat exchangers are applicable since the calculated number of transfer units (NTU) is sufficiently low, e.g.,  $NTU < 5$  [148, Pg. 41]. Table 5.6 reports the plate type combination of the regenerator. The calculated mean temperature difference in design conditions is 31.1 K with a  $K$  value of  $409 \text{ W}/(\text{m}^2 \cdot \text{K})$  and a net empty weight of 787 kg. The internal volume of the hot side is  $94.1 \text{ dm}^3$ , while the cold side is  $43.8 \text{ dm}^3$ . The external dimensions excluding flanges are  $475 \times 1165 \text{ mm}$  ( $D \times L$ ).

Table 5.6: Plate type combination of the regenerator. For reasons explained in Sec. 5.6 the regenerator was replaced after the commissioning activities. The number of passes on the plate/cold side was increased from 8 to 12 resulting in the new plate grouping  $9 \times 11$ PM +  $3 \times 12$ PM. Consequently, the pressure drop on the cold side increased to 20.57 kPa.

Plate Combin.	Grouping		Number of Plates	Total Area / $\text{m}^2$	Pressure Drop / $\text{kPa}^+$	
	Hot Side (Shell Side)	Cold Side (Plate Side)			Hot Side (Shell Side)	Cold Side (Plate Side)
SM-PM	$2 \times 33$ SM + $2 \times 34$ SM	$1 \times 16$ PM + $7 \times 17$ PM	270	24.92	25.6	7.13

<sup>+</sup> Calculated.

## CONDENSER

The condenser is a *Alfa Laval Compabloc CP20-82* fully welded plate heat exchanger without interplate gaskets providing a large heat transfer area within a very compact space, see Fig. 5.7. It is composed of a pack of AISI 316 L stainless-steel plates stacked in a frame. The CP20 denomination means it features square plates of approx.  $200 \times 200 \times 0.8 \text{ mm}$  ( $L \times H \times T$ ). The thermal data used to design the condenser are summarized in Tab. 5.7. The fluid enters and leaves the channels through holes at the corner of the plates.

Open and blind holes define the path of the fluids through the different channels. The cross-flow configuration and the internals of the condenser are shown in the exploded view of Fig. 5.7. The plates are corrugated with a pattern designed to enhance heat transfer, but the manufacturer does not disclose the specific geometry. The effective area per plate is  $0.061 \text{ m}^2$ , which, if multiplied by 80 gives a total heat transfer area of  $4.88 \text{ m}^2$ . The estimated hot-side pressure drop is 1.24 kPa and that of the cold side is 7.54 kPa on the cold side. Table 5.8 reports the plate combination. The 80 plates are divided into 40 channels with 1 pass in the working fluid side and 40 channels with 4 passes in the cooling water side. This gives a final grouping of  $1 \times 40$  M and  $3 \times 10 +$

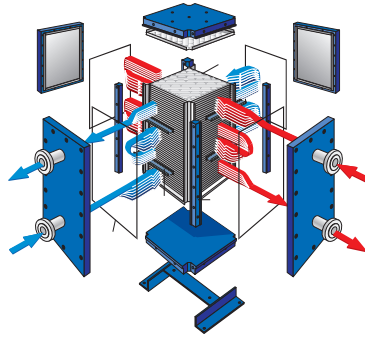


Figure 5.7: Exploded view of the *Alfa Laval* brazed-plate *Compacbloc* condenser of the ORCHID, showing the cross-flow arrangement determined by the plates configuration. Image courtesy of *Alfa Laval*.

1 × 11 M. The average plate distance of a channel is 5 mm. The condenser is the component which limits how quickly the ORCHID can undergo the start-up and shut-down procedures. According to the specifications of the manufacturer, the temperature rate of change must not exceed 1 °C/ min and the pressure build-up rate must not exceed 1 bar/ min. These precautions avoid thermal shocks or unnecessary stress, thus prolong the life of the unit. The design mean temperature difference is 58.0 K. The empty weight is 462 kg and the internal volume of the hot side is 24.8 dm<sup>3</sup>, while the cold side is 23.1 dm<sup>3</sup>. The external dimensions excluding flanges are 613 × 445 × 305 mm (H × W × L).

Table 5.7: Design specifications of the *Compacbloc* CP20-82 condenser.

Thermal Data		Hot Side (MM)	Cold Side (Glycol/Water)
Inlet Temperature	$T_{in} / ^\circ\text{C}$	122	30
Outlet Temperature	$T_{out} / ^\circ\text{C}$	78.2	50
Mass flow rate	$\dot{m} / \text{kg/s}$	1.54	4.52
Thermal power	$P / \text{kW}$		377.5

Table 5.8: Plate type combination of the condenser.

Plate Combination	Grouping		Number of Plates	Total Area/m <sup>2</sup>	PressureDrop/kPa <sup>+</sup>	
	Hot Side	Cold Side			Hot Side	Cold Side
M-M	1 × 40 M	3 × 10+ 1 × 11 M	80	4.9	1.24	7.54

<sup>+</sup> Calculated.



## AIRCOOLER

The ORCHID heat exchanger providing refrigeration to the water of the condenser is an *Alfa Laval* tube-and-fin single-row dry cooler (*Alfablue BDMSE803DD45 CR Feet ICM*), see Fig. 5.8. The tubes are made of copper and the fins of aluminum. Three fans are placed in a single row and their diameter is 800 mm. The rated capacity of the aircooler is  $415 \text{ kW}_{\text{th}}$  and the external dimensions are  $5705 \times 1495 \times 900 \text{ mm}$  (L×H×D), while the dry weight is 752 kg. The thermal and coil data are listed in Tab. 5.9. The design has been obtained by assuming  $20^\circ\text{C}$  as the air temperature and pure water as the heat transfer fluid. However, during actual operation a water/glycol mixture 41%<sup>5</sup> is used to prevent freezing when the air temperature is below zero during the winter.

Table 5.9: Design specifications of the tube-and-fin aircooler.

		Inlet	Outlet
Glycol/water temperature	$T_{\text{Glycol,water}} / ^\circ\text{C}$	50	29
Glycol/water pressure drop	$\Delta P / \text{kPa}$		31
Glycol/water volume flow rate	$\dot{V}_{\text{Glycol,water}} / (\text{m}^3/\text{h})$		17.5
Nominal thermal power	$Q_{\text{th}} / \text{kW}_{\text{th}}$		415
Air temperature	$T_{\text{air}} / ^\circ\text{C}$		20
Fin Spacing	$x_{\text{fin}} / \text{mm}$		2.1
Surface	$S / \text{m}^2$		1230.6
Number of tube circuits	-		45
Internal Volume	$V / \text{l}$		107



Figure 5.8: Photograph of the *Alfablue BDMSE803DD45 CR Feet ICM* dry single-coil aircooler. The photograph shows the single row three fan arrangement. Image courtesy of *Alfa Laval*.

## OIL HEATER

Figure 5.9 shows an isometric view of the thermal energy source of the ORCHID. It is a *WTE 10-10-400-2-B HTT* electric heater. Ten 40 kW rods provide a maximum of  $400 \text{ kW}_{\text{th}}$  to a thermal oil loop. The maximum flow temperature of the selected thermal oil, Therminol VP1, is  $400^\circ\text{C}$ , which is circulated by a magnetically driven hermetic centrifugal

<sup>5</sup>The fluid *EUROL COOLANT -26* is prediluted for frost protection down to  $-26^\circ\text{C}$ . In fact, it is an antifreeze MEG + inhibitors at 41 vol % in water. The total volume used was 120 litres.

pump. The design rotational speed is 2900 RPM and the motor is rated at 11 kW. The design pressure ratio of the orifice plate used to regulate the flow is 0.36, resulting in a constant volume flow rate of  $40 \text{ m}^3/\text{h}$ . A 500 litre buffer vessel (expansion tank) stores the fluid charge and allows for volumetric expansion due to temperature increase. The unit is skid-mounted in a standard twenty-foot container (6.1 m long  $\times$  2.44 m wide), see Fig. 5.10. The heater is controlled with a continuous temperature PI controller which is an integral part of the design due to its ability to control the supply temperature TT016 with a high tolerance.

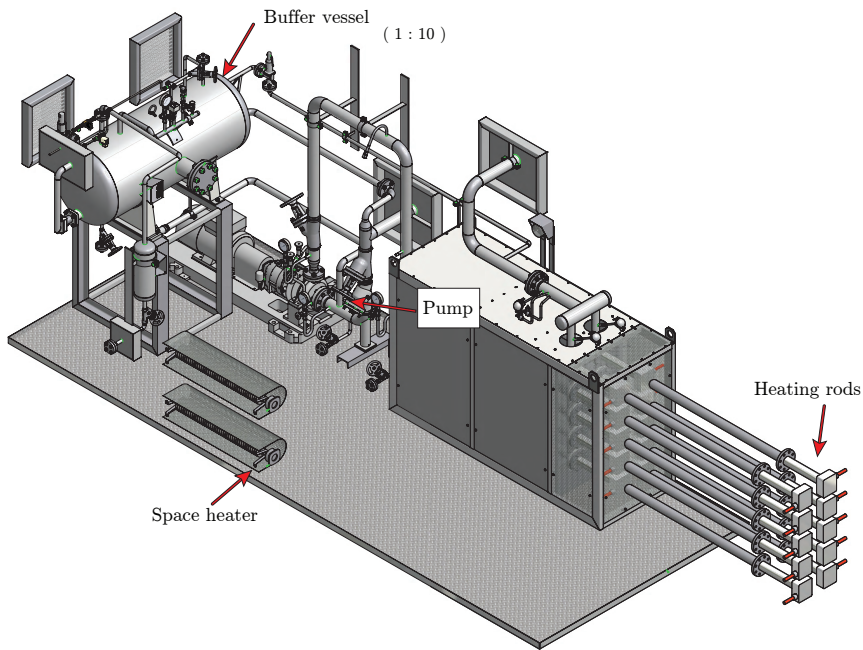


Figure 5.9: An isometric view of the WTE 10-10-400-2-B HTT electric oil heater. Image courtesy of HTT energy.



Figure 5.10: A photograph of the *WTE 10-10-400-2-BHTT* electric oil heater mounted in a container outside the Propulsion and Power Lab at Delft University of Technology. The aircoolers are located on top of the container.

## 5.5. INSTRUMENTATION, DATA ACQUISITION & CONTROL

Similarly to an ORC power plant, the ORCHID is monitored and controlled by means of a set of sensors and actuators governed by a data acquisition & control system (DAQ&C) connected to a personal computer, which records and visualizes all the main process variables and provides the interface to the operator, see Fig. 5.11 and Fig. 5.12. The architecture is therefore that of a supervisory control and data acquisition (SCADA) system in which the PC does not perform any automatic control function, but is only used for monitoring, data logging and operator interface.



Figure 5.11: The control and monitoring station of the ORCHID. The computer monitors display graphical user interfaces of the ORCHID CODAQ software.

### 5.5.1. DATA ACQUISITION AND CONTROL SYSTEM

The controller and data acquisition functions are performed by a *National Instruments compactRIO 9067*, an industrial-grade real-time-capable controller with a processor and a field-programmable gate array (FPGA) with slots for seven I/O modules. The controller is connected via an Industrial Ethernet link to the SCADA PC (Intel(R) Xeon(R) CPU W-2223 @ 3.6 GHz Turbo and 32 Gb of RAM) running the Windows 10 operating system. The system runs the ORCHID Control and Data Acquisition (CODAQ) human machine interface (HMI) program developed with the *National Instruments LabVIEW 2016* software suite.

Figure 5.12 shows a scheme of the instruments, connections and data acquisition and control hardware equipping the ORCHID, which, together with the P&ID of Fig. 5.2, provides a rather complete overview of the system and its configuration. Table 5.10 lists the modules installed in the slots of the *compactRIO* controller and their characteristics. The signals connected to these modules are shown in Tab. 5.11 and 5.12, which reports also a list of all the digital and analog instruments and actuators.

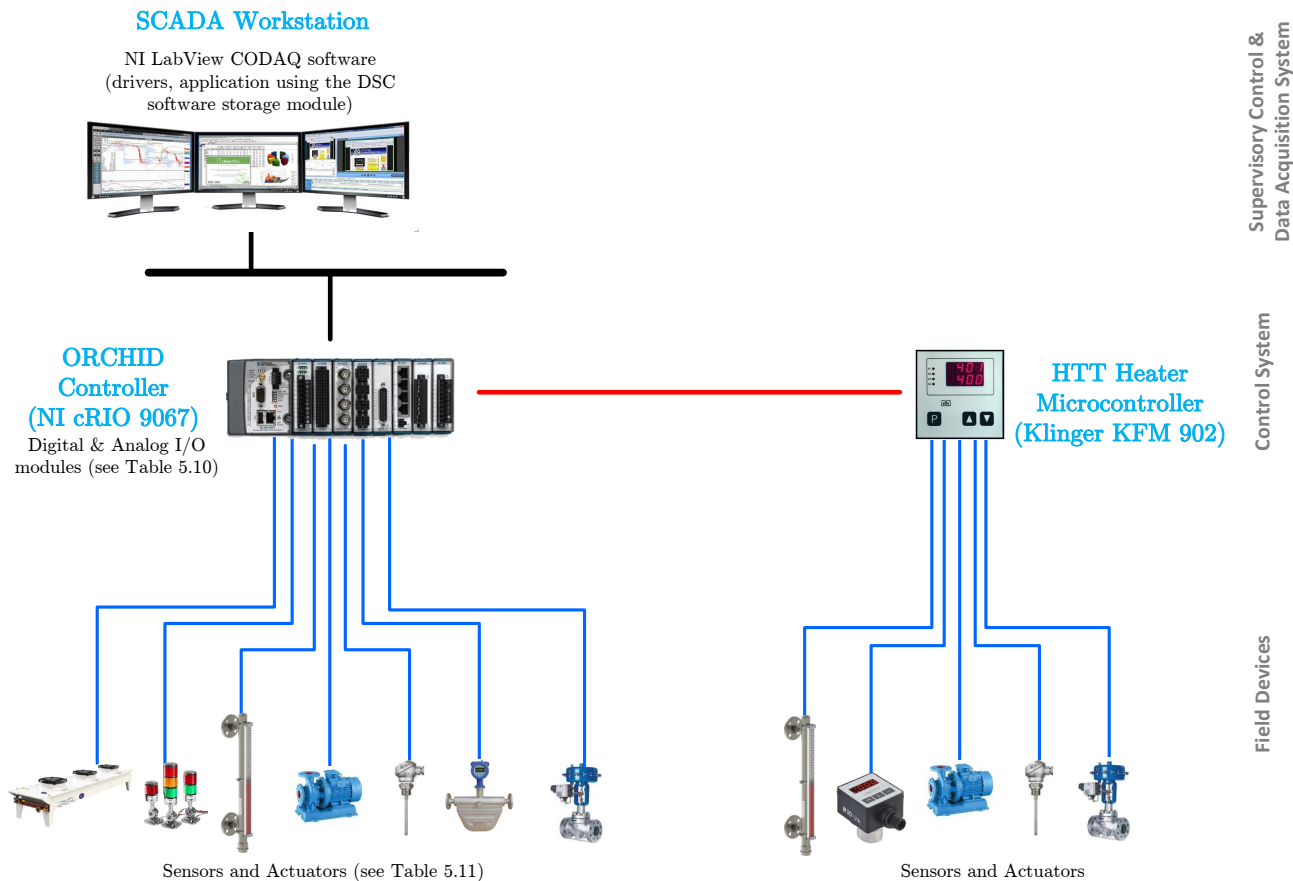


Figure 5.12: Overall architecture of the SCADA system of the ORCHID. —: Industrial Ethernet; —: Profibus; —: FieldBus. The FieldBus input/output signals connecting the controller interfaces to sensors and actuators are 4-20 mA (analog), 0 - 10 V (analog and digital).

Table 5.10: The *National Instruments compactRIO* controllers and the installed modules. All the A/D converters feature a digital resolution of 24 bit.

Analog					
Model	# of modules	Type	Range	Channels	Description
NI9208	3	Current Input	4-20 mA	16	Sensor & valve position feedback
NI9266	1	Current Output	4 - 20 mA	8	Valve actuation
NI9264	1	Voltage Output	0 - 10 V	16	Fan & pump frequency control
Digital					
Module	Number	Type	Range	Channels	Description
NI9375	1	Input + Output	-	16 + 16	Liquid level, alarms, & pump enable
Profibus					
Module	Number	Type	Range	Channels	Description
NI-PB	1	Digital input + output & Analog input + output	-	-	Heater operation (remote start, set-point)

In addition, the compactRIO controller connects to the controller of the *HTT* electrical furnace, a *Klinger KFM 902*, via a *compactRIO Profibus* interface module (*NI 781352-01*), linked to an external *Klinger KFM 99spde* Profibus adapter. In this way the ORCHID operator can issue the main commands to the *HTT* electrical heater. The four basic commands are: 1) start (heater ON), 2) stop (heater OFF), 3) change the set-point temperature, and 4) receive the value of the setpoint temperature together with other safety-related messages. This communication with the *HTT* heater is integrated into the general control logic managing normal and abnormal operation, see Sec. 5.5.3. Finally, the speed of the three fans of the air cooler can be set by adjusting the frequency drive of the electric motors by means of 0 – 10 V signals issued by an analog output module (*NI9264*) of the *compactRIO* controller, thus the aircooler control is also integrated into the general control system of the ORCHID.

Figure 5.13 shows the main operator interface of the ORCHID CODAQ *LabView* program. The interface shows a simplified P&ID on the left hand side and a virtual control panel on the right hand side, providing graphical information about the process states and access to the settings of the control loops. Moreover, the operator can actuate the various control actions (startup, shutdown and testing) by clicking the appropriate virtual button. The user can login either as *supervisor* or as *operator*. The supervisor can change the settings of the control loops and access the control panel for manual operation, therefore modifying the input to all controllable devices. A secondary operator interface displays trend charts (real-time or historical) of the main process variables, thanks to the *LabVIEW Datalogging and Supervisory Control Module (DSC module)*. The operator can alter the units and the range of the displayed process variables. To monitor the process, the operator can also display a real-time  $T - s$  chart reporting all the thermodynamic states of the organic Rankine cycle process by clicking on a virtual button

on the main operator interface. Another button on the same interface visualizes a panel reporting all the pressures measured by the *Scanivalve* of the nozzle test section.



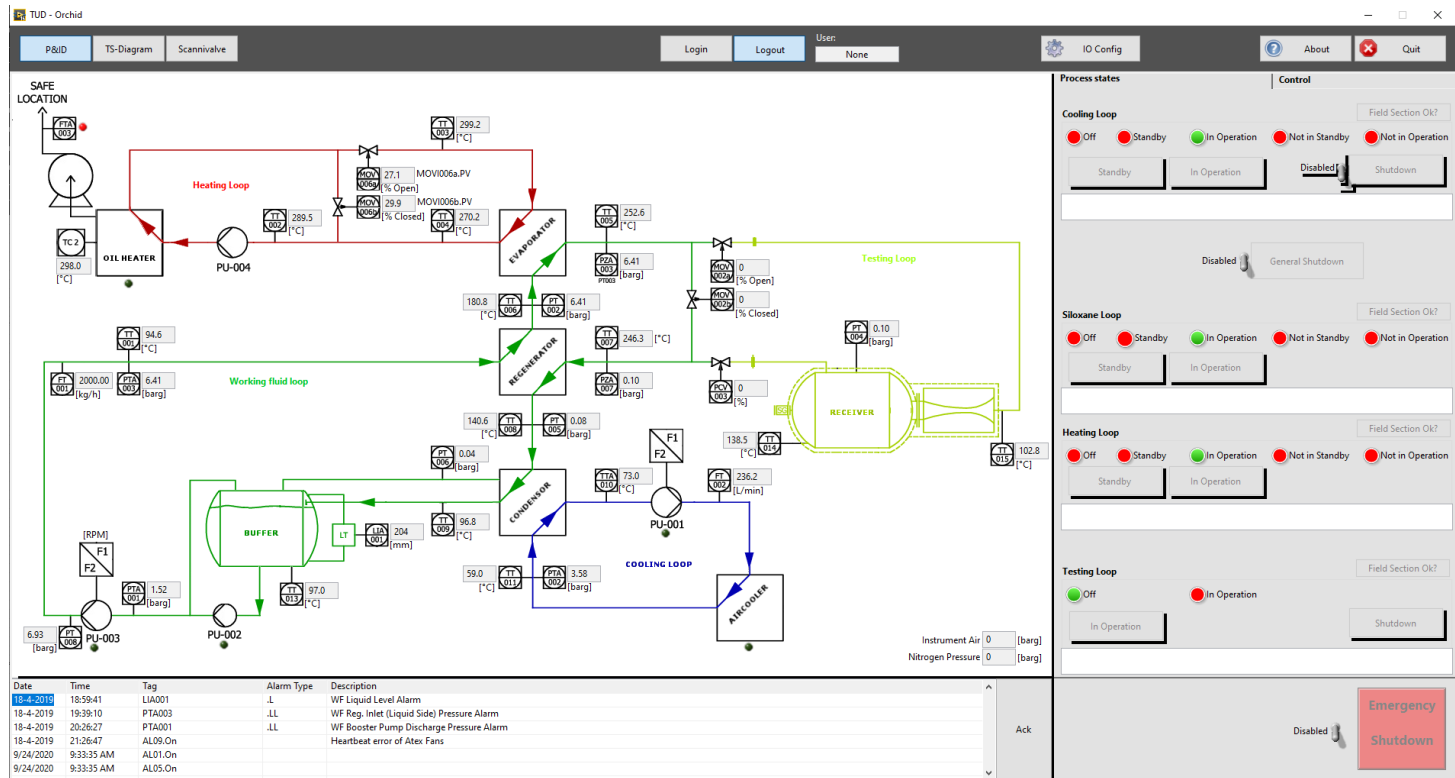


Figure 5.13: The main operator panel of the ORCHID CODAQ software.



### 5.5.2. INSTRUMENTATION

The ORCHID is equipped with a variety of process sensors and actuators, which are listed in Tab. 5.11 and 5.12 and treated in some detail in the following.

#### PRESSURE INSTRUMENTS

Besides five *WIKA 232.50* analog Bourdon tube pressure indicators for visual monitoring, one *WIKA CPG1500* precision digital pressure gauge, and ten *WIKA UPT 20* pressure transmitters<sup>6</sup> are installed to measure the pressure in the low and high pressure parts of the working fluid loop of the ORCHID, and in the cooling loop. The range of these instruments varies and depends on the expected minimum and maximum pressure to which they can be exposed in normal operation. The ranges are [0, 16] barg, [−1, 5] barg and [0 – 40] barg. The measured values, for all of them except the analogue indicators, are transmitted via a 4–20 mA signal to a 16-channel 24-bit A/D compactRIO input module (NI9208). The tags of all pressure instruments together with their full scale range and factory-certified accuracy are listed in Tab. 5.11, and are also reported on the P&ID of Fig. 5.2.

#### TEMPERATURE INSTRUMENTS

The temperature indicators for visual inspection are *WIKA S5550* bimetallic thermometers, and their location is indicated on Fig. 5.2 with the tags listed in Tab. 5.11. Recordings of all the main process temperatures are performed by means of fourteen *WIKA TR10* resistive thermometers (RTDs). The measured values are transmitted via a 4–20 mA signal to another 16-channel 24-bit A/D compactRIO input module (NI9208). Similarly to the pressure transmitters, also the range of the temperature transmitters varies depending on the expected minimum and maximum value to which they can be exposed to in normal operation. The ranges are [0, 150] °C, [−10, 400] °C, [0, 300] °C, [−20, 200] °C and [0, 350] °C. All these temperature sensors are equipped with thermowells, apart from those with tag TT013 and TT014, see Tab. 5.11 and Fig. 5.2, which are located at the inlet and outlet of the nozzle test section and whose metallic sensor tip is mounted directly into bored holes. This way, their response time is shorter, a useful feature for gasdynamic experiments.

The accuracy of the resistive thermometers is Class A or higher according to the EN 60751 standard. The full scale accuracy is defined by the total measurement uncertainty, estimated with a confidence level of 95 % and is affected by the intrinsic performance of the instrument, the measurement uncertainty of the reference instrument, the long-term stability of the sensor, and the influence of ambient conditions. These temperature transmitters are highly accurate, e.g., Class AA ( $\pm 0.1 + 0.0017|T|$  °C) and Class A ( $\pm 0.15 + 0.002|T|$  °C). The tags of all the temperature transmitters together with their full scale range and factory-certified accuracy are listed in Tab. 5.11, and are also reported on the P&ID of Fig. 5.2.

---

<sup>6</sup>The measurement principle is as follows: a diaphragm isolates the process side from the measuring cell. The internal space between this diaphragm and the pressure measuring cell is completely filled with a system fill fluid. The pressure is transmitted from the measured medium/process by the elastic diaphragm into the system fluid and from there to the measuring element. The measuring cell is made of stainless steel 316L (1.4404).

## FLOW RATE INSTRUMENTS

The working fluid mass flow rate is measured using a *Krohne OPTIMASS 6400C* Coriolis mass flow meter, while the cooling loop volume flow rate is measured using a *Blancett B2800* turbine flow meter. Both instruments provide 4–20 mA output signals which are connected to one of the two *compactRIO NI9208* modules.

## CONTROL VALVES

The three pneumatic equal-percentage gate valves needed to realize the bypass of the nozzle test section are *Schubert & Salzer GS-8021/24/26*. The linear percentage gate valves controlling the mass flow of the fluid being heated in the primary heat exchanger are *Schubert & Salzer GS-8021/24/26*. The valves are actuated by a 4 – 20mA current signal issued by an analog output module (NI9266) of the *compactRIO 9067*. Feedback of the set-point value of the valve position is obtained by means of the analog input module (NI9208). The main characteristic of the valves and their tags are reported in Tab. 5.12 and their location can be identified in Fig. 5.2.

## FREQUENCY DRIVES

The motor speed of the working fluid feed pump is controlled with a *Siemens SINAMICS G120* frequency drive coupled with a *Siemens CU240B-2* control unit. The motor speed of the cooling loop is controlled with a *Kolmeks NC406* frequency drive. The set-point of the of the feed pump, aircooler fans' and cooling pump speed can be set by means of 0 – 10 V signals issued by the analog output module (NI9264) of the *compactRIO* controller. Only the feedback of the feed pump speed set-point value is obtained by means of an analog input module (NI9208). The main characteristic of the frequency drives and their tags are reported in Tab. 5.12.

### 5.5.3. CONTROL STRATEGY AND IMPLEMENTATION

#### OBJECTIVES

The control system of the ORCHID must satisfy three main objectives. The first objective is to manage the start-up and shut-down of the set-up by performing an appropriate sequence of procedures until the required operating conditions are reached. Both the start-up and shut-down processes must be fully automated due to the long required time to reach the design conditions, and for safety reasons. The goal of the controlled start-up process is to reach the operating conditions of the planned experiment safely and by complying with the specifications of the equipment in terms of pressure and thermal stresses. Conversely, the aim of the controlled shut-down procedure is to reach operating conditions corresponding to a mild temperature of the working fluid, also complying with the specifications of the equipment in terms of pressure and thermal stresses, such that all rotating machinery can be stopped and the setup can then reach ambient conditions by means of passive cooling.

The second objective is to maintain the value of temperature, pressure and mass flow rate at the inlet of the nozzle test section, and the backpressure in case of the turbine test section, within a narrow range. These values were prescribed based on the operating conditions and working fluid designated for the commissioning of the ORCHID, namely siloxane MM. Specifically, the temperature should be maintained within  $\pm 0.5$  °C, the

Table 5.11: Process sensors of the ORCHID and associated Type B measurement uncertainties.

Temperatures				
Type	Company/Brand, Model & Quantity	Tag	FS Measuring Range / °C <sup>◇</sup>	Uncertainty, $U_B / \pm ^\circ\text{C}^*$
Bimetallic thermometer (Analogue Display)	WIKA S5550 × 3	TI02, TI03, TI04	-20 – 100	Class 1
RTD	WIKA TR10-C × 2	TT013, TT001	0 – 150	Class AA
RTD	WIKA TR10-C × 4	TT002, TT003, TT004, TT016	-10 – 400	Class A
RTD	WIKA TR10-C × 4	TT005, TT007, TT008, TT009	0 – 350	Class A
RTD	WIKA TR10-C × 1	TT006	0 – 300	Class A
RTD	WIKA TR10-H/T32.1S × 2	TT014, TT015	0 – 300	Class A
RTD	WIKA TR10-C × 2	TT011, TTA010	-20 – 200	Class A
Pressures				
Type	Instrument & Quantity	P&ID Tag Name	FS Measuring Range / barg <sup>◇</sup>	Uncertainty, $U_B / \pm \% ^*$
C (Analogue Display)	Pressure Indic. (232.50) × 2	PI02, PI03	0 – 10	1
C (Analogue Display)	Pressure Indic. (232.50) × 3	PI04, PI05 PI06	-1 – 0.6	1
UPT20	Pressure Trans. (UPT 20) × 1	PTA002	0 – 16	0.1
UPT20	Pressure Trans. (UPT 20) × 3	PT004, PT005 PT006	-1 – 5	0.1
UPT20	Pressure Trans. (UPT 20) × 1	PZA007	0 – 6	0.1
C (Digital Display)	WIKA CPG1500 × 1	PI06	-1 – 0.6	0.1
UPT20	Pressure Trans. (UPT 20) × 5	PT002, PZA003 PT008, PTA001 PTA003	0 – 40	0.1
Mass Flow				
Type	Instrument & Quantity	P&ID Tag Name	FS Measuring Range / kg/hr <sup>◇</sup>	Uncertainty, $U_B / \pm \% ^*$
Coriolis	Mass Flow Trans. (OPTIMASS 6400 C) × 1	FT001	420 – 5580	0.1
Volume Flow				
Type	Instrument & Quantity	P&ID Tag Name	FS Measuring Range / l/min <sup>◇</sup>	Uncertainty, $U_B / \pm \% ^*$
Turbine	Volume Flow Trans. (Blancett B2800) × 1	FT002	56.9 – 682	1

\* Full scale accuracy (Type B expanded uncertainty ) is defined with a coverage factor of  $k = 2$ . This is mentioned as *absolute accuracy* in the WIKA documentation.

◇ Electrically connected sensors transmit an output signal of 4 – 20 mA to the NI9208 module. This signal is then scaled to the corresponding FS range of the sensor in the ORCHID CODAQ software. The indicator/display pressure/ temperature sensors do not transmit any electrical signal.

Table 5.12: Actuators of the ORCHID.

Control Valves					
Type	Model	Tag	Full Scale Range / %	Input Signal / mA	Output Signal / mA
Diaphragm / Pneumatic	GS-8021/24/26	GS-002a	0 – 100	4 – 20	4 – 20
Diaphragm / Pneumatic	GS-8021/24/26	GS-002b	0 – 100	4 – 20	4 – 20
Diaphragm / Pneumatic	GS-8021/24/26	GS-006a	0 – 100	4 – 20	4 – 20
Diaphragm / Pneumatic	GS-8021/24/26	GS-006b	0 – 100	4 – 20	4 – 20
Diaphragm / Pneumatic	GS-8021/24/26	GS-003	0 – 100	4 – 20	4 – 20
Frequency Drives					
Type	Model	Tag	Full Scale Range / %	Input Signal / V	Output Signal / mA
Electrical VFD	<i>Siemens SINAMICS G120</i> Controller ( <i>CU240B-2</i> )	FC1	0 – 100	0 – 10	4 – 20
Electrical VFD	NC406 Controller	FC2	0 – 100	0 – 10	-
Electrical VFD	Master Controller CBMx	FC-FN003-005	0 – 100	0 – 10	-

pressure and the mass flow rate at the inlet of the nozzle test section within  $\pm 0.5$  % of the set point, and the value of the backpressure within  $\pm 0.01$  bar. These values were specified based on an estimate of what could be achieved with state-of-the-art process equipment and control [248].

Finally, the third objective of the control system is to ensure operational safety and to avoid that the equipment operates in conditions which would shorten its lifetime. The objective is therefore to comply with equipment operation specifications provided by the manufacturers. Apart from over-pressure in any part of the setup, see Tab. 5.1, the other stringent requirement is related to the heat exchangers and is that the maximum temperature gradient with respect to time to which they are subjected remains within a prescribed value. This limitation is due to maximum thermal expansion or contraction that the welding can withstand or to the different thermal elongation of the plates with respect to the casing. The most critical component with respect to this requirement is the condenser (1 °C/ min).

## IMPLEMENTATION

Given the stated objectives, the chosen controlled variables are four: the working fluid mass flow rate, the temperature at the outlet of the primary heat exchanger, the pressure of the working fluid in the condenser and the backpressure of the test section.

Due to the limited size of the working fluid loop, hence to the relatively small inertia, it was preferred to control the working fluid mass flow at the outlet of the feed pump rather than the pressure at the inlet of the nozzle. Its value is then determined by the

flow characteristic of the orifice plate on the bypass, the nozzle or of the turbine.

The selected manipulated variables are: the rotational speed of the motor of the feed pump, the opening of the interlocked valves on the thermal oil loop which regulates the mass flow rate delivered to the primary heat exchanger, the rotational speed of the pump motor pressurizing the water/glycol loop, and the opening of the backpressure valve of the nozzle test section.

In order to set the temperature at the outlet of the primary heat exchanger, the temperature difference between the thermal oil and the working fluid could be adjusted by modulating the oil temperature set point of the electric heater controller, instead of regulating the thermal oil mass flow rate entering the primary heat exchanger. However, modulating the oil mass flow rate was preferred because it arguably allows a faster response of the system. Similarly, the working fluid pressure in the condenser is regulated by adapting the water/glycol flow rate rather than adjusting its temperature by changing the air coolers' fan speed.

For simplicity, the four controlled variables are regulated with four single-input/single-output control loops, see Figure 5.2, implementing a proportional-integral (PI) feedback mechanism. The reduction of time-response provided by the derivative action was deemed unnecessary. The proportional and integral constants were set according to the Ziegler-Nichols method [417] and were adjusted during the commissioning phase, see Tab. 5.13. The regulation logic is coded in a series of VI programs running on the compactRIO. The control loops are:

1. The FICA001 control loop regulates the mass flow rate of the working fluid where the controlled variable is the frequency of the drive of the feed pump motor (FC01), and the process or set-point variable is the mass flow rate (FT001). In addition, variable FT001 is monitored and might trigger an alarm on the screen of the operator or the automated shut-down procedure if its value during normal operation drops below 150 kg/h.
2. The TICA001 control loop sets the working fluid temperature at the outlet of the primary heat exchanger (TT005). The controlled variables are the position of the interlocked valves actuating the bypass line of the thermal oil loop (MOV006a and MOV006b). The setpoint variable may trigger the shut-down procedure if its value is larger than 300 °C.
3. The PICA002 control loop stabilizes the condensing pressure of the working fluid in the condenser (PT006) by regulating the rotational speed of the cooling loop pump. The controlled variable is the frequency of the drive of the feed pump motor of water/glycol loop (FC02). PT006 triggers the automated shut down procedure if its value exceeds 2.5 bar.
4. The PICA001 control loop adjusts the expansion ratio of the nozzle by varying the pressure drop in the throttling valve downstream of the nozzle receiver. This additional controller is needed because the action of the control loop that regulates the condensing temperature of the working fluid is too slow for the purpose of setting the expansion ratio over the test section, due to the relatively high thermal inertia of the condenser and of the cooling water circuit. The controlled variable is thus

the position of the PCV003 valve which enables to finely tune the backpressure of the test section (PT004). The alarm event is raised if the value of PT004 is larger than 20 bar, which might happen in case of excessive closing of the valve.

In addition to the alarm events defined within the four control loops, other process variables are monitored and can trigger warnings, alarm or a shutdown event depending on the severity, see Tab. 5.14.

During normal operation, therefore in order to maintain planned experimental conditions, control loops FICA001, TICA001 and PICA001 are active, while PICA001 is activated only when required by a particular experiment. For example, this regulation is used to control the nozzle flow regime such that a normal shock is formed in the divergent part of the nozzle.

Table 5.13: Constants of the four PID controllers, determined on the basis of the ORCHID design operating conditions.

		P	I	D
FICA001	working fluid mass flow controller	0.0005	0.0163	0
PICA001	test section backpressure flow controller	0.0005	0.0163	0
PICA002	Condensing pressure controller	0.0005	0.05	0
TICA001	Evaporation temperature controller	0.125	0.1	0

Table 5.14: Alarms associated with the control loops. Four alarm levels are defined: high-high (HH), high (H), low (L), low-low (LL). Letter A stands for an alarm event signaled on the main ORCHID CODAQ window, while S indicates that the alarm event triggers the automated shutdown procedure.

Cooling circuit				
	Action and Value			
	HH	H	L	LL
PTA002	A, 4 barg	-	-	A + S, 0.2 barg
PTA006	A + S, 1.5 barg	-	-	-
TTA010	A + S, 100 °C	-	-	-
FTA002	-	-	A,100 l/min	-
Siloxane circuit				
	Action and Value			
	HH	H	L	LL
PTA001	-	-	-	A + S, 0.5 barg
PTA003	-	-	-	A + S, 1 barg
PZA003	A + S, 22 barg	-	-	-
PZA007	A + S, 3.5 barg	-	-	-
PTA006	A + S, 1.5 barg	-	-	-
TTA013	-	A, 140 °C	-	-
FTA001	-	-	-	A + S, 150 kg/h
LIA001	A+S,90%	-	A,30%	A + S, 20%
Heating circuit				
	Action and Value			
	HH	H	L	LL
TT016	A, 300 °C	-	-	-
General				
	Action and Value			
	HH	H	L	LL
PTA010	A + S, 160 barg	A, 30 barg	-	A + S, 10 barg
PTA009	-	-	A + S, 3 barg	-

The cold start up procedure is semi-automatic and consists of the following sequence:

1. First the ORCHID control system sends a signal request to the building safety system which then enables the fans of the ATEX enclosure. The start-up sequence (and normal operation) continues only if the fans' watchdog signal is received by the control system.
2. The cooling loop pump (PU001) and fans (FN003-006) are turned on, at the same time, at the rotational speed prescribed by the operator.
3. The circulation of the working fluid is started by first turning on the booster pump (PU002) and then the feed pump (PU003) at a constant rotational speed set by the operator. The test section is kept isolated from the working fluid loop.
4. The operator sets discharge temperature of thermal oil pump (TC2) to a certain value, normally 75 °C, and the electric heater is started up. The thermal oil flows only in the primary heat exchanger bypass line.
5. The PICA002 control loop is activated.
6. The FICA001 control loop is activated.
7. The operator selects the working fluid temperature at the outlet of the primary heat exchanger (TT005) and the TICA001 control loop is activated. This causes the valves regulating the thermal oil flow delivered to the primary heat exchanger to progressively open. The set point of the thermal oil temperature (TC2) is progressively increased with a prescribed ramp in order to avoid excessive thermal stresses in the heat exchangers.
8. The working fluid is gradually delivered to the nozzle test section by first opening valve PCV003 and then by opening MOV002a. The actuation of this valve is synchronized with that of MOV002b, which is progressively closed. The actuation of MOV002a and MOV002b follows a prescribed ramp in order to avoid excessive pressure fluctuation in the working fluid loop.

The sequence of the shut-down procedure is the inverse of the start-up sequence. Two automated shut-down procedures are programmed: the emergency sequence is fast and is triggered by alarm events, while normal shut down is the same in terms of sequence and is activated by the operator after normal operation. The normal shut down procedure complies with all the specified heating and cooling rates of the heat exchangers. In particular, if the cooling mass flow rate is abruptly interrupted, it may lead to an exceedingly fast temperature rise in the condenser. Therefore, the cooling loop must be the last to be turned off.



## 5.6. COMMISSIONING

For the commissioning of the setup, which is the process of ensuring that all sub-systems and components of the installation are designed, installed, and operated according to the requirements defined in the design phase, different tests or process runs were executed. For the sake of brevity, only two tests are here discussed and are listed in Tab. 5.15. Each process run showcases the start-up, the steady-state operation, and the shut-down of the ORCHID, but they differ for the specific process conditions achieved during steady-state operation. Notably, the operating conditions targeted in the first process run, i.e. PR.020-BP.001, correspond to those chosen for the design point of the MM turbine while the process conditions of the second test are those required by the nozzle experiments, see Sec. 4.9.3. Since the turbine test section has not been constructed yet, the expansion ratio characteristic of the turbine design is achieved by circulating the flow on the bypass line and regulating the valve (MOV002b) on the same line. To distinguish among the different process runs, these are labeled with the letter PR followed by: i) a number indicating the progressive enumeration of the operational cycles, from start-up to shut-down, undergone by the facility, ii) the acronym NT or BP depending on whether the flow is circulated through the nozzle test section or just the bypass line, and finally iii) a number enumerating the experiments carried out in the given process run.

Table 5.15: Targeted operating conditions of the commissioning test runs.

Test Run	Date	Maximum temperature TT005/°C	Evaporation pressure PZA003/bar	Back pressure PT004/bar	Condensation pressure PT006/bar	Mass flow rate FT001/kg/h
PR.020-BP.001	3/15/2019	275	21	-	0.3	600
PR.025-NT.002	4/25/2019	252	19.1	2.1	1	4122

The PR.020-BP.001 test run regarding the turbine test section is reported first, because this test case is more appropriate for the discussion of the start-up and shut-down procedure of the balance of plant, as the vapor flow is circulated only through the bypass line. The analysis of PR.025-NT.002 mainly focuses on the operational phases characteristic of the nozzle test section. Moreover, given the much larger working fluid mass flow rate with respect to PR.020-BP.001, this experiment is aimed at demonstrating that the balance of plant can safely operate in proximity of its design limits in terms of thermal loads and vapor mass flow rate. In this regard, it is important to mention that the nozzle used in PR.025-NT.002 features a throat area of  $150 \text{ mm}^2$  ( $H = 7.5 \text{ mm}$ ,  $W = 20 \text{ mm}$ ) instead of  $200 \text{ mm}^2$ , which was the specified design value, see Section 4.5.

The reason thereof is that, during preliminary process runs preceding PR.025-NT.002, it was concluded that the performance of the regenerator does not match the specified design requirements. Consequently, it was not possible to achieve the combination of vapor flow rate ( $1.55 \text{ kg/s}$ ) and thermodynamic conditions originally chosen as design point of the nozzle. Fig. 5.14 depicts the profile of the de Laval nozzle installed during the PR.025-NT.002 test run.

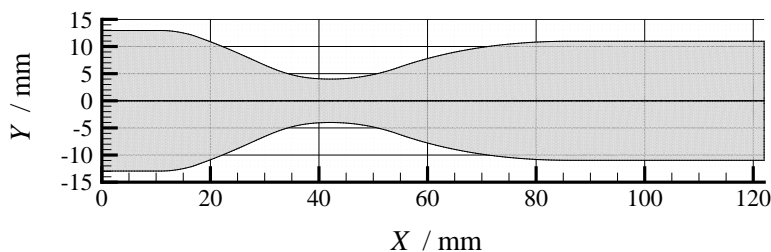


Figure 5.14: 2-D profile of the de Laval nozzle adopted in PR.025-NT.002. Designed for the conditions specified in Tab. 6.1.

### 5.6.1. VALIDATION OF OPERATION

Before the facility can be operated, leakage tests must be conducted to check the tightness of the working fluid loop. The tightness was characterized in terms of the average leak rate [266],

$$Q = \frac{\Delta p \cdot V}{\Delta t},$$

where  $V$  is the internal volume,  $1.29 \text{ m}^3$  for the working fluid circuit of the ORCHID, and  $\Delta p$  is the pressure variation measured after a time interval  $\Delta t$ , i.e., three days for all the commissioning tests.

It is possible to distinguish among three different types of leakage tests:

1. the working fluid loop is pressurized with air and the pressure is monitored over time by means of the pressure indicator on the vacuum line (PI006). The test is carried out before the working fluid is introduced into the main circuit, and thus it was performed only during the early stages of the commissioning to spot the main leakage locations. It requires up to 1.5 hours before steady conditions are reached and measurements can be recorded.
2. A vacuum pump is activated to remove the incondensable gases from the working fluid loop until a constant value of pressure, compatible with the vapor pressure of MM, is reached. After the vacuum pump is turned off, the pressure rise is recorded. This test is conducted before each process run as a safety measure. The leakage rate is then calculated with an internal empty volume of  $0.829 \text{ m}^3$  (given a working fluid charge of 460 l). If the tightness of the working fluid loop proves to be unsatisfactory, the leak locations are identified through a helium leak detection test.
3. A helium leak detector (*Pfeiffer ASM 340*) is used in two different modes of operation, namely, in vacuum or spray mode and in sniffing mode [294]. In sniffing mode, the circuit is slightly pressurized with helium and the detector probe is used to sniff helium from possible leakage locations, like flanges, valves, etc. Such a test can be conducted also when the working fluid has been already charged into the circuit. For this reason, it is performed each time the main working fluid loop undergoes maintenance. In the vacuum or spray mode, instead, the helium detector

is connected to the circuit through a flange and works as a vacuum pump. The working fluid loop is therefore brought to medium vacuum ( $< 1$  mbar). Helium is then sprayed around the locations where the leakage is suspected. If this is the case, part of the sprayed helium is sucked into the circuit and, after a certain time it can be detected by the instrument.

During the tests with the helium detector in spray mode (medium vacuum), values of the leak rate  $Q$  lower than  $3 \times 10^{-4}$  mbar·l/s were recorded. The tightness of the working fluid loop was deemed satisfactory if the leakage rate was approximately  $1.2 \times 10^{-2}$  mbar·l/s.

#### PR.020-BP.001

Since the turbine test section was not built yet at this stage of the research program, the process conditions typical of mini-ORC turbine testing were achieved by circulating the vapor through the bypass line. Moreover, since this was one of the first test runs, as a precautionary measure, the pressure and temperature at the evaporator outlet targeted in the experiment were limited, respectively, to 21 bara and 275 °C in place of 22 bara and 300 °C as prescribed by the design conditions of the turbine test section. Lower pressure and temperature allow to keep a larger safety margin with respect to i) the thermal stability limit of MM (300 °C according to Preissinger & Bruggemann [305]), and, ii) to the maximum design pressure of the loop (25 bara).

Figure 5.15 reports the evolution of the main process variables of the ORCHID during the PR.020-BP.001 process run.<sup>7</sup> In particular, Fig. 5.15a reports the working fluid temperature at the evaporator outlet (TT005), the temperature of the thermal oil in the electric heater (TT016), and the temperature at the exit of the condenser (TT009). Figure 5.15b shows the evolution of the evaporation pressure (PZA003), the condensing pressure (PT006), and the regenerator exit pressure (PT005). Figure 5.15c illustrates the variation over time of the mass flow rate of the working fluid downstream of the main pump (FT001), and the volume flow rate of the cooling water (FT002).

The initial part of the start-up phase consists in the sequential activation of the ATEX ventilation, aircoolers, cooling loop pump, booster and main pump. With reference to Fig. 5.15, these components have already reached their operational set point at the initial time, i.e., 13:30. The start-up procedure continues then with the heating of the working fluid. First, the control valves of the heating loop, i.e., MOV006a/b, are actuated to direct part of the thermal oil flow to the primary heat exchanger. The set-point specified for the position of the valve actuators is 40 %, see Fig. 5.16.

Once this operation is concluded, the temperature of the thermal oil in the electric heater is gradually increased by 3 °C/min until it reaches the set-point value of 300 °C. With reference to Fig. 5.15a, this condition is reached at about 15:30. The slope of the thermal oil temperature ramp is limited to prevent a spike of thermal stresses in the heat exchangers. Especially in the condenser the average operating temperature cannot vary with a rate exceeding 1 °C/min according to the manufacturer. This is the main constraint preventing a shorter duration of the ORCHID start-up and, to a lower extent, of the shut-down.

<sup>7</sup>Unless otherwise indicated, a process run or operational cycle was always executed from cold conditions, e.g., the facility was off-line for more than 24 h.

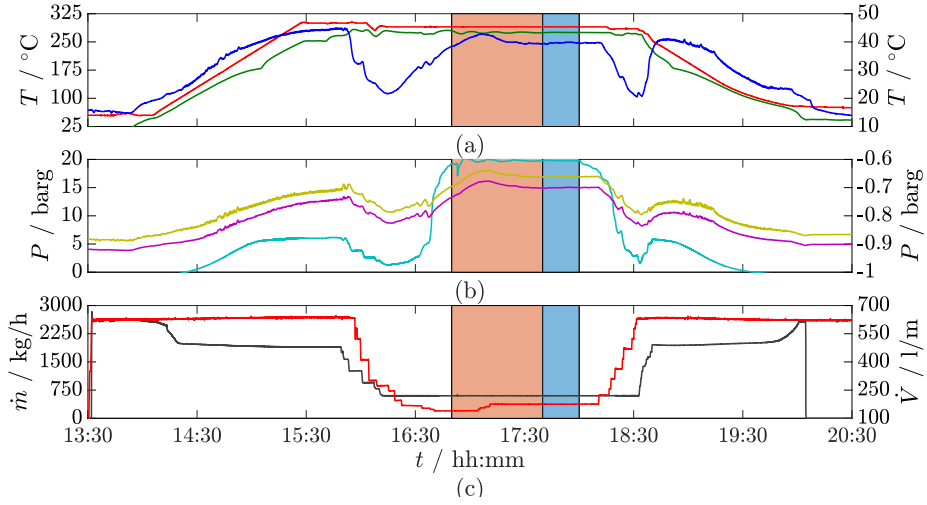


Figure 5.15: Recording of some process variables during the PR.020-BR.001 test run. The time interval highlighted with the orange box indicates the settling time, while the time interval highlighted with the blue box indicates the period in which the process can be considered at steady state according to the criteria reported by Woodland *et al.* [409]. (a) Left axis: Thermal oil supply temperature of the electric heater (— TT016); Primary heat exchanger outlet temperature of the working fluid (— TT005); Right axis: condenser outlet temperature of the working fluid (— TT009). (b) Left axis: evaporator pressure (— PZA003); right axis: regenerator outlet pressure (vapor side) (— PT006), and condensing pressure (— PT005). (c) Left axis: mass flow rates of the working fluid (— FT001); right axis: volume flow rate of the cooling water (— FT002).

Right after the ramp-up of the thermal oil temperature is concluded, the TICA001 controller is activated to maintain TT005, i.e., the temperature of the fluid leaving the primary heat exchanger, at 275 °C, see Fig. 5.16. The start-up phase is therefore over and the process conditions can be adjusted according to the requirements of the experiment. For example, Figure 5.15c shows that at about 16:00 the cooling circuit pump and the main pump flow rates were manually step-wise reduced. Once the values of these process variables are close to the desired values for the experiment, the FICA001 and PICA002 controllers were activated in order to maintain a working fluid flow rate of 600 kg/h (0.17 kg/s) and a condensation pressure of 0.3 bara. In order to set the evaporation pressure of the working fluid to 21 bara, the opening of the MOV002b valve on the bypass line was adjusted manually. The final actuator position corresponds to 70 % of the valve stem travel.

At about 17:00, the operating conditions envisaged for turbine testing were reached. A settling period of approximately 30 minutes to 1 hour, indicated in Fig. 5.15 by the orange box, was required to let the process conditions stabilize. The blue box in the same figure highlights the period of operation during which the process was deemed at steady-state.

A comparison between the actual and the desired performance of the setup is discussed in Section 5.6.2, while Tab. 5.17 summarizes the uncertainties associated with

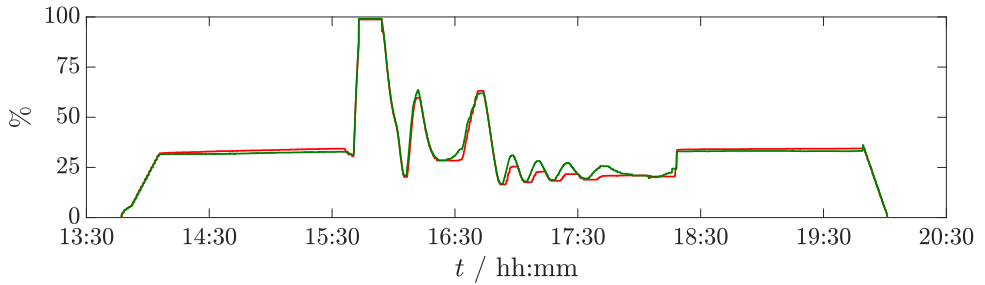


Figure 5.16: Actual position over time of the heating loop control valves (— MOV006a & — MOV006b) during the PR.020-BP.001 test run. The fail-safe positions of MOV006a and MOV006b are *closed* and *open*, respectively. Therefore, for MOV006a, the 0 % position implies that the valve is closed, while the 0 % position for MOV006b implies that it is open.

the measured process conditions. The temperature, pressure, and mass flow rate of the vapor at the outlet of the primary heat exchanger were therefore proven to be adequately stable for turbine testing, because the relative amplitude of the fluctuations of these process variables remained within  $\pm 0.6\%$  during the time frame highlighted by the blue boxes in Fig. 5.15.

During the commissioning, special attention was devoted to monitoring the working fluid sub-cooling in the buffer vessel. It is worth recalling that, to maintain a sufficient degree of sub-cooling in the condensate, valve V009 must be closed to ensure that there is liquid in the second pass of the condenser. The vapor balancing line (C4 in Fig. 5.2) that was designed in order to equalize the pressure in the second pass of the condenser with that of the buffer vessel should maintain the condensate in the buffer vessel in a sub-cooled liquid state. Figure 5.17 compares the variation over time of TT013, i.e., the temperature of the liquid inside the buffer vessel, against the saturation temperature of the working fluid, calculated based on the condensing pressure recorded by PT006. The temperature difference remains approximately 15 °C. A similar trend was observed in all other process runs, including PR.025-NT.002, despite the higher thermal load of the condenser in this experiment. Due to the higher thermal load, the difference between the estimated condensing temperature and TT013 reduces to about 8 °C. However, given that the ORCHID was operated during the PR.025-NT.002 test run close to its operational limits in terms of thermal capacity and vapor flow, it can be argued based on the commissioning tests that: i) the working fluid is sufficiently sub-cooled in the condenser in all operating conditions, and ii) the use of the vapor balancing line allows the condensate inside the buffer vessel to remain in a sub-cooled liquid state.

Once the experiment was concluded, the setup was shut down according to a two-step procedure. First the controllers FICA001 and PICA002 were deactivated and the working fluid and cooling water mass flow rate were returned to the values they had at the end of the start-up phase because a larger mass flow rate in the primary heat exchanger allows to cool it more rapidly. The TICA001 controller was also disabled and the position of the actuators of the valves MOV006a/b was put back to 40 %. The progressive opening of the MOV002b bypass valve led to a quick reduction of the working fluid

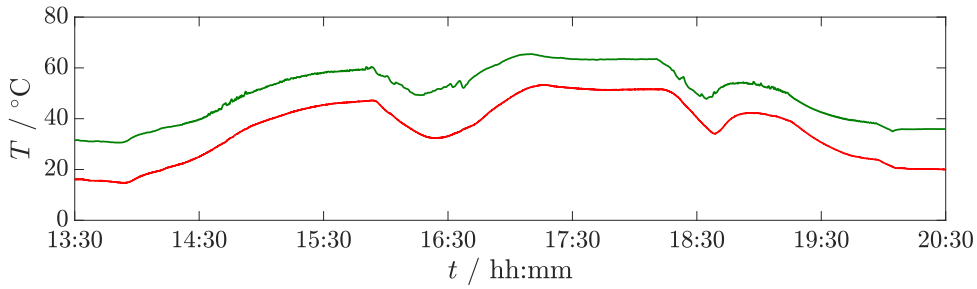


Figure 5.17: Saturation temperature corresponding to ( — PT006 ) and the temperature of the condensate inside the buffer vessel ( — TT013 ).

pressure, which was only partially compensated by the increase in the mass flow rate. Afterwards, at about 18:30 the automated shut-down procedure was initiated. Figure 5.15a shows that the set-point of the thermal oil temperature in the electric heater was decreased at an almost constant rate of 3 °C/min until reaching a final value of about 50 °C. The working fluid circulating in the loop cooled down as a result of the lower thermal power input and of the unchanged cooling power in the condenser. In this operational phase, the pressure in the working fluid circuit decreased as well, but with a lower rate. When the working fluid has reached a temperature at the outlet of the primary heat exchanger that is deemed safe, e.g., 150 °C, the valve regulating the thermal oil supply to the same heat exchanger, MOV006b, can be fully closed and the main pump and the booster pump can be stopped. In the PR.020-BP.001 process run, the working fluid was cooled down to approximately 50 °C, see TT005 in Figure 5.15a. Finally, after a proper time lag, the cooling pump and the aircoolers fans could be also turned off.

#### PR.025-NT.002

The PR.025-NT.002 test run was conducted to: i) assess the performance of the ORCHID if operated close to its upper operational limits in terms of working fluid mass flow rate and thermal capacity, and ii) verify the stability over time of the nozzle inlet and outlet conditions. Fig. 5.18 displays the variation in time of the main process variables of the entire process run PR.025.

From Fig. 5.18 it is apparent that the nozzle test section was opened twice during this commissioning test: the nozzle is opened first (experiment NT.001) between the period 10:50 - 11:40 and then a second time (experiment NT.002) between 11:48 - 12:15. The time intervals highlighted in orange indicate when the vapor flow rate was redirected from the bypass to the nozzle TS and the consequent settling period. The blue-colored time-frames point out when the measurement acquisition in the de Laval nozzle was performed under steady flow conditions. In the first experiment NT.001, schlieren images of the supersonic flow in the nozzle were recorded, while in the experiment NT.002 the electronic pressure scanner was activated to characterize the static pressure variation along the nozzle. These measurement techniques were not applied simultaneously to simplify the related troubleshooting in this early testing phase of the ORCHID.

The negative spikes in the signal of PZA003, see Fig. 5.18b, occur in correspondence

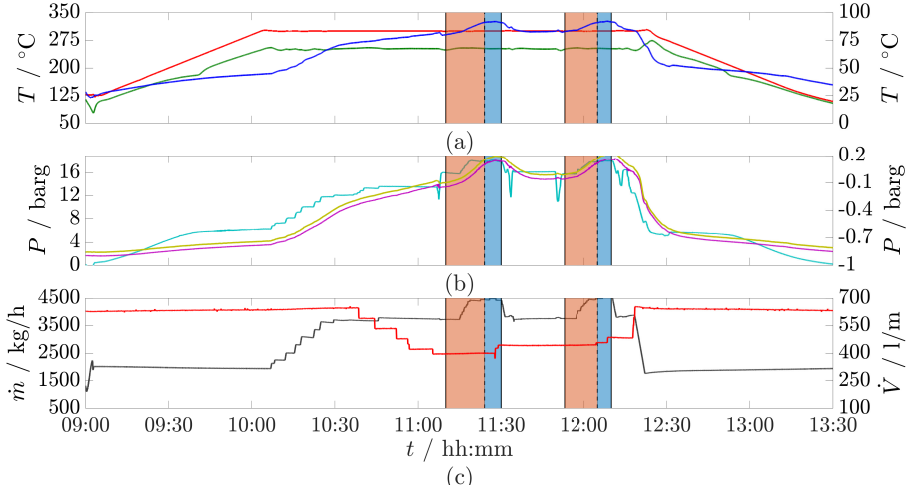


Figure 5.18: Recording of some process variables during the PR.025-NT.002 test run. The time interval highlighted with the orange box indicates the settling time, while the time interval highlighted with the blue box indicates the period in which the process can be considered at steady state according to the criteria reported by Woodland *et al.* [409]: (a) Left axis: Thermal oil supply temperature of the electric heater (— TT016); Primary heat exchanger outlet temperature of the working fluid (— TT005); Right axis: regenerator outlet temperature of the working fluid (— TT009). (b) Left axis: evaporator pressure (— PZA003); right axis: condenser outlet temperature (vapor side) (— PT006), and condensing pressure (— PT005). (c) Left axis: mass flow rates of the working fluid (— FT001); right axis: volume flow rate of the cooling water (— FT002).

with the opening and closing of the nozzle test section. The amplitude of these pressure fluctuations would be even larger, however the orifice plate on the bypass line provides some mitigation as expected. Another measure adopted to damp such pressure variations is to initially regulate the mass flow rate of the main pump such that its value is lower than the value required by the experiment. Successively the set point of the mass flow rate FT001 is adjusted to the target value, see the ramp-wise trait in the corresponding signal within the orange boxes in Fig. 5.18.

The measured liquid mass flow rate (FT001) corresponding to the total inlet temperature and pressure at the design conditions of the nozzle (4527.3 kg/h) is 10 % higher than the theoretical value (4122 kg/h, see Tab. 5.15). The discrepancy might be due to leakage through the bypass valve or to the thermal dilation of the nozzle, which enlarges the throat area.

Figure 5.19 displays the variation in the position of the PCV003 and MOV002a valves during experiment NT002 as a showcase regarding the regulation of the opening and closing of the test section. The primary control valve, PCV003, is first moved to a fully opened position at a rate of 20 % of the travel per minute. Then, the MOV002a nozzle inlet valve is completely opened at a rate of 40 % of the travel per minute. Similarly, MOV002b is closed at the same rate. Figure 5.20a shows the recording of the evaporation pressure PZA003 and of the nozzle receiver PT004 corresponding to the opening sequence of these valves. The total pressure at the inlet was not directly available because

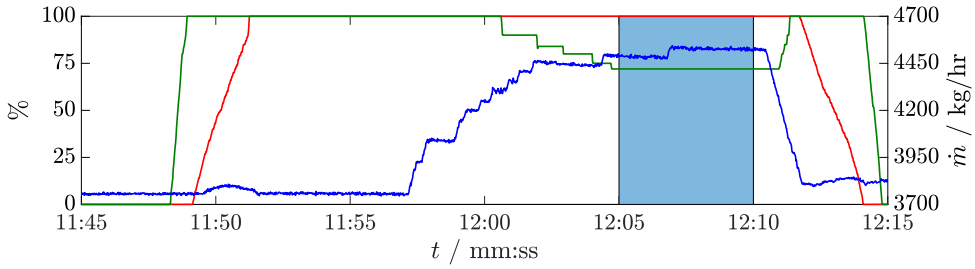


Figure 5.19: Position of the nozzle TS inlet valve (— MOV002a) and of the primary control valve (— PCV003). Mass flow rate of the working fluid loop (— FT001).

it is measured by the Scanivalve, which could not be utilized at the time of these experiments because it was not yet commissioned. Therefore, the total pressure at the inlet of the nozzle test section was calculated by subtracting the pressure drop  $\Delta P$  over the MOV002a valve, the pipe line and the settling chamber from the measured evaporation pressure. The estimation of pressure drop,  $\Delta P = 0.7$  bar, was obtained during previous trial process runs. As the measured evaporation pressure was  $P = 19.06$  bara, the estimated pressure at the inlet of the nozzle was therefore  $P_0 = 18.36$  bara. The value of PT004 increases after opening the PCV003 valve to match the regenerator inlet pressure (PZA007), while the negative spikes recorded by the PZA003 pressure transmitter occur during the actuation of the MOV002a/b valves.

Figure 5.20b reports the total temperature in the settling chamber (TT015) and the temperature in the receiver (TT014) during the NT002 experiment. As the vapor enters the nozzle test section, the values recorded by the two temperature sensors rise. The trends reported in this chart as well as those of the PZA003 and PT004 pressure sensors, allow to evaluate the high level of stability of the inlet and outlet conditions of the nozzle test section, see the lines within the blue boxes in Fig. 5.18. The uncertainty analysis related to the stability of the experimental conditions is treated in Section 5.6.2.

It can therefore be concluded that the operation of the ORCHID is successful as it complies with the prescribed control narrative, see Sec. 5.5.3: the test rig can be safely operated according to the conceived procedures regarding startup, shutdown and testing. Moreover, the process conditions are compatible with the thermal stability characteristics of the working fluid: three samples of MM were retrieved to perform a column gas chromatographic analysis which revealed that the level of thermal decomposition of the fluid is negligible with respect to the planned experiments.

Fig. 5.21 and Table 5.16 show that the fluid composition of a reference sample (Sample A) taken from the barrels of working fluid before the setup was charged, and that of two samples taken after the PR.020-BP.001 and PR.025-NT.002 process runs, is the same, to a large extent. Table 5.16 summarizes the chromatogram results, i.e., retention time, the percentage height and area of the peaks. The peaks in samples B and C which are not present in sample A may indicate small traces of cutting, machining or pump lubricating oil, or decomposition products.



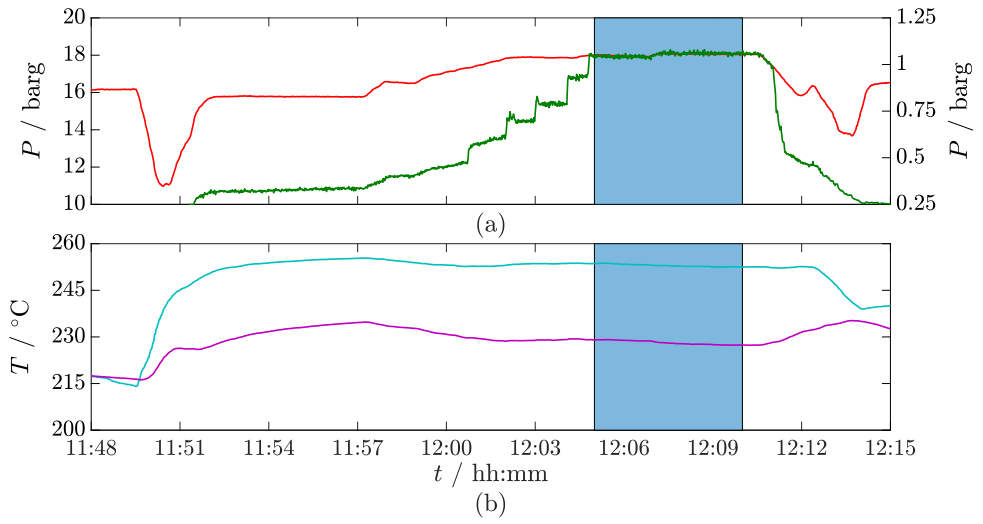


Figure 5.20: Recording of some process variables during the PR.025-NT.002 test run: **(a)** Left axis: Pressure of the evaporator ( — PZA003 ); Right axis: receiver ( — PT004 ). **(b)** Temperature of the nozzle TS SC inlet ( — TT015 ) and the receiver ( — TT014 ).

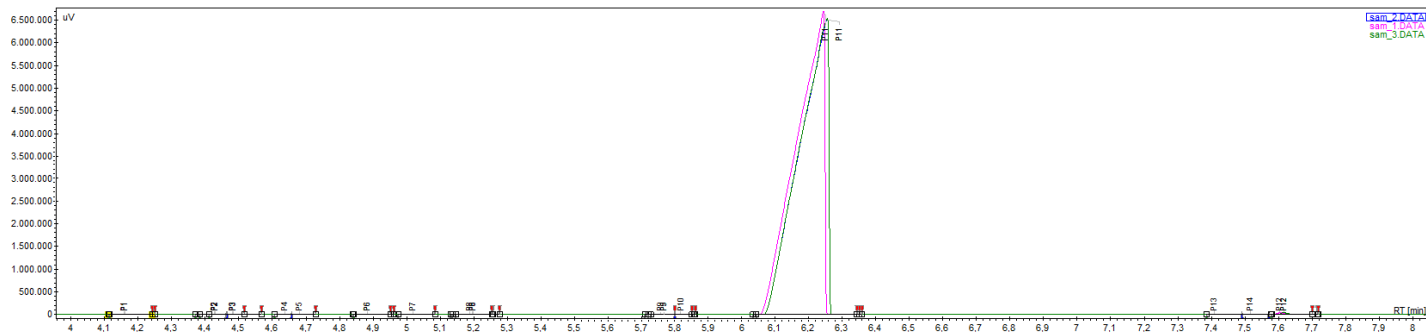


Figure 5.21: Screenshot of the chromatogram obtained with the *Galaxie Chromatography Workstation* software related to the samples of siloxane MM taken from the barrel before the working fluid loop is charged ( Sample A, — ) and after two process runs ( Samples B, —, and C, — ). The corresponding data are reported in Tab. 5.16. Sample B was taken after experiment PR.20-BP.001 (2019.03.15). Sample C was taken after the commissioning experiments (2019.04.25). A *Agilent FactorFour VF-5ms* GC was used. The temperature temporal profile of the head space analysis was:  $T = 50\text{ }^{\circ}\text{C}$  (5 min)  $\rightarrow 160\text{ }^{\circ}\text{C}$ ,  $10\text{ }^{\circ}\text{C}/\text{min}$ ;  $160\text{ }^{\circ}\text{C} \rightarrow 220\text{ }^{\circ}\text{C}$ ,  $20\text{ }^{\circ}\text{C}/\text{min}$ ,  $220\text{ }^{\circ}\text{C}$  (8 min); carrier gas: He at 40 kPa; incubation:  $220\text{ }^{\circ}\text{C}$  (8 min) ; syringe:  $115\text{ }^{\circ}\text{C}$ ; sample size:  $500\text{ }\mu\text{l}$ ; injection: Split, 1:10,  $T_{\text{injector}} = 250\text{ }^{\circ}\text{C}$ ; detector: FID,  $T_{\text{detector}} = 290\text{ }^{\circ}\text{C}$ .

Table 5.16: Results of the gas chromatographic analysis of the three MM samples, see also Fig. 5.21.

Peak	Sample A			Sample B			Sample C		
	Time / min:sec	Height / %	Area / %	Time / min:sec	Height / %	Area / %	Time / min:sec	Height / %	Area / %
P1	-	-	-	04:10	0.04	0.01	04:10	0.08	0.01
P2	04:26	0.07	0.02	04:26	0.14	0.03	04:26	0.11	0.02
P3	-	-	-	04:29	0.03	0.01	04:29	0.06	0.02
P4	-	-	-	-	-	-	04:38	0.03	0.01
P5	-	-	-	-	-	-	04:41	0.09	0.02
P6	-	-	-	04:53	0.09	0.02	04:53	0.20	0.04
P7	-	-	-	-	-	-	05:01	0.04	0.01
P8	05:11	0.03	0.01	05:12	0.09	0.02	05:12	0.16	0.04
P9	05:46	0.03	0.01	05:46	0.03	0.01	05:46	0.04	0.01
P10	-	-	-	-	-	-	05:49	0.01	0.00
P11	06:14	99.15	99.78	06:16	98.93	99.75	06:16	98.52	99.65
P12	07:36	0.13	0.13	07:37	0.65	0.15	07:37	0.65	0.15
P13	07:25	0.03	0.03	-	-	-	-	-	-
P14	07:31	0.02	0.02	-	-	-	-	-	-

### 5.6.2. RESULTS WITH UNCERTAINTIES

Figure 5.22 shows the temperature entropy diagrams of MM and a comparison between the thermodynamic cycle of the ORCHID that was specified during the design phase, see Sec. 4.9.3, and that was realized during the commissioning phase. The comparison shows that i) the thermal duty of the regenerator is considerably lower than its design value and, ii), that the maximum cycle temperature achieved during the test aimed at the commissioning of the operating conditions for the turbine test section was prudentially kept at a lower value (275 °C vs. 300 °C). However, the supercritical conditions were successfully achieved.

The insufficient performance of the regenerator was investigated. Fouling in the heat exchanger was excluded following an inspection of the inner surfaces with a boroscope, which revealed that they were perfectly clean as expected. It was therefore concluded that the most likely cause of the lower thermal duty delivered by the regenerator was a design flaw: the manufacturer overestimated the vapor-side heat transfer coefficient. A new regenerator was therefore put into production and it has been installed at the time of this writing.

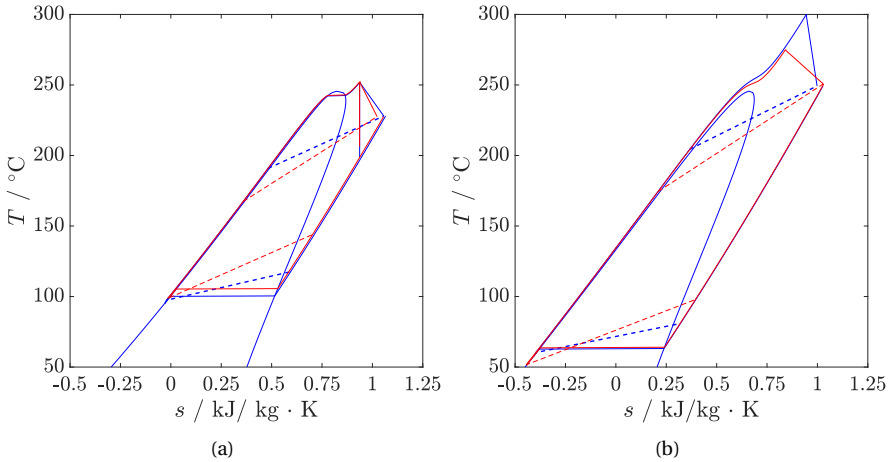


Figure 5.22: Thermodynamic cycles in the  $T-s$  diagram of MM corresponding to the operating conditions of the ORCHID resulting from its design (—) and obtained from fluid states measured during the commissioning phase (—). **(a)** thermodynamic cycles corresponding to the operating conditions of the design and of the commissioning of the nozzle test section (PR.025-NT.002). **(b)** thermodynamic cycles corresponding to the operating conditions of the design and of the commissioning of the turbine test section (PR.020-BP.001). The values identifying the saturation line of MM and the states of the fluid determining the thermodynamic cycle were calculated with the in-house fluid property estimation program FLUIDPROP [93]. The values of thermodynamic variables identifying the states of the fluid at the inlet and outlet of each component were computed using as an input for the state estimation the average of the measured temperatures and pressures over a statistically significant number of samples, see Tab. 5.17 and 5.18.

### METHOD FOR THE EVALUATION OF MEASUREMENT UNCERTAINTY

The International Organization for Standardization (ISO) [194] recommends categorizing uncertainty components associated to measurements as *Type A* or *Type B*, depending

on the method of evaluation. Type A uncertainties are those that are evaluated by means of series of repeated measurements and result therefore in the evaluation of the standard deviation. Type B uncertainties are those that are not evaluated by means of statistical analysis of a series of observations. The probability distribution function in this case is assumed, based on scientific knowledge, technical datasheets or previous measurement data.

For example, in the case of the measurement of the condensing pressure of the ORCHID, uncertainties associated to uncontrolled fluctuations and/or disturbances, which are therefore random errors (unpredictable, non-reproducible) are evaluated as Type A uncertainties. It is therefore calculated as the standard deviation of the data recorded over a period of time in which the process is deemed at steady state. The measurement is affected also by a calibration uncertainty and an uncertainty due to signal conditioning and the analog to digital (A/D) conversion. These uncertainties are evaluated as Type B, therefore information about the calibration error is taken from the calibration certificate of the instrument and the uncertainty of the signal conditioning and A/D conversion system (CompactRIO controller) is evaluated based on information reported on the specification sheets of the electronic equipment.

The adopted nomenclature related to uncertainty evaluation is consistent with the PTC 19.1-2005 ASME standard [12]. Measurement uncertainties have been quantified using the methods outlined by Moffat [262] and Abernethy *et al.* [1]. The *standard uncertainty*  $u$  is the estimated standard deviation of a measurement or an error source in the measurement chain. The *expanded uncertainty*  $U$  is the uncertainty associated with a measurement or error source, with the desired level of confidence and is calculated as  $U = k \cdot u$ . If the distribution associated to the standard uncertainty is normal,  $k$  is in the range 2–3, where 2 defines an interval with a level of confidence of 95 %, while 3 defines an interval with a level confidence greater than 99 %. If a measurement is affected by multiple error sources, the overall uncertainty, the *combined uncertainty*, is calculated by propagating through the measurement chain the uncertainty associated with the individual error sources.

## TYPE A UNCERTAINTIES

In order to quantify the mean and standard deviation (Type A *standard* uncertainty) of the values recorded by the measuring instruments equipping the balance of plant of the ORCHID, reference datasets acquired while the setup was in operation were selected. These datasets refer to periods in which the operating conditions of the setup were deemed at steady state. The steady state identification process is reported in App. D.

The selected datasets were those pertaining to experimental run PR.020-BP.001 and to experimental run PR.025-NT.002 because they are representative of typical operating conditions for the ORCHID. PR.020-BP.001 is representative of the process conditions envisaged for turbine test section experiments, albeit in this case the dense vapor of the working fluid was routed to the bypass, while PR.025-NT.002 for nozzle test section experiments.

In order to compute Type A *expanded uncertainties*, the second order moments of the process variables of interest are first determined and then a coverage factor of 2 is

applied to the standard deviation resulting in an expanded uncertainty value with a 95 % confidence interval. Table 5.17 and Tab. 5.18 list the Type A expanded uncertainties and means related to the PR.020-BP.001 and PR.025-NT.002 experimental runs, respectively.

The Type A uncertainties affecting the measurements of the flow rates are much larger if compared with those related to the PR.020-BP.001 experimental run. In case of the fluctuations of the working fluid mass flow rate, this can be explained by the increased frequency of the pulsation of the feed pump associated with a larger mass flow rate. A similar explanation might apply to the larger fluctuations of the cooling water, albeit the pump in this case is centrifugal.

Table 5.17: Averages and Type A expanded uncertainties of the process variables for the PR.020-BP.001 experimental run (turbine test section). Values are computed over the reference period 17:20 - 18:00 at 1 Hz, i.e., 2400 samples. Refer to Fig. 5.2 to identify the instruments by their tags.

Temperatures					
Tag	$\bar{T} / ^\circ\text{C}$	$U_{\text{Type A}} / \pm ^\circ\text{C}^*$	Tag	$\bar{T} / ^\circ\text{C}$	$U_{\text{Type A}} / \pm ^\circ\text{C}^*$
TT001	51.73	0.51	TTA009	39.63	0.42
TT002	286.32	0.27	TTA010	41.05	0.53
TT003	290.99	0.11	TT011	34.93	0.55
TT004	272.05	1.71	TT013	51.76	0.89
TT005	275.00	1.31	TT014	N.A.	N.A.
TT006	174.57	0.56	TT015	N.A.	N.A.
TT007	250.87	1.29	TT016	290	0.00
TT008	97.65	0.32	-	-	-
Pressures					
Tag	$\bar{P} / \text{barg}$	$U_{\text{Type A}} / \pm \text{bar}^*$	Tag	$\bar{P} / \text{barg}$	$U_{\text{Type A}} / \pm \text{bar}^*$
PTA001	0.88	0.042	PT005	-0.66	0.008
PT002	19.77	0.110	PT006	-0.66	0.008
PTA002	2.65	0.017	PZA007	-0.074	0.00
PTA003	19.76	0.110	PT008	19.97	0.110
PZA003	19.78	0.11	PTA010	160.96	0.45
PT004	N.A.	N.A.	-	-	-
Flow Rates					
Tag	Avg. Flow rate	$U_{\text{Type A}} / \pm^*$			
FT001	600.01	1.00 kg/h			
FT002	175.11	0.44 l/s			

\* Coverage factor  $k = 2$ . The reported values are the absolute expanded uncertainties associated to the Type A errors.

Table 5.18: Averages and Type A expanded uncertainties of the process variables for the PR.025-NT.002 experimental run (nozzle test section). Values are computed over the reference period 12:07 - 12:10 at 1 Hz, i.e., 180 samples. Refer to Fig. 5.2 to identify the instruments by their tags.

Temperatures					
Tag	$\bar{T}$ / °C	$U_{\text{Type A}}$ / $\pm$ °C *	Tag	$\bar{T}$ / °C	$U_{\text{Type A}}$ / $\pm$ °C *
TT001	98.75	0.77	TTA009	91.84	0.39
TT002	283.82	0.13	TTA010	51.87	0.64
TT003	301.42	0.08	TT011	34.42	0.47
TT004	277.55	0.57	TT013	100	0.65
TT005	252.31	0.41	TT014	227.71	0.59
TT006	167.50	0.09	TT015	252.70	0.32
TT007	225.89	0.75	TT016	300	0
TT008	143.89	0.38	-	-	-
Pressures					
Tag	$\bar{P}$ / barg	$U_{\text{Type A}}$ / $\pm$ bar *	Tag	$\bar{P}$ / barg	$U_{\text{Type A}}$ / $\pm$ bar *
PTA001	1.57	0.036	PT005	0.21	0.013
PT002	18.08	0.03	PT006	0.21	0.013
PTA002	2.76	0.03	PZA007	0.36	0.011
PTA003	18.08	0.03	PT008	20.04	0.037
PZA003	18.06	0.03	PTA010	159.95	0.15
PT004	1.06	0.014	$P_0$ <sup>+</sup>	17.36	-
Flow Rates					
Tag	Avg. Flow rate	$U_{\text{Type A}}$ / $\pm$ *			
FT001	4527.3	11.2 kg/h			
FT002	470.32	28.38 l/s			

\* Coverage factor  $k = 2$ . The values reported are the absolute expanded uncertainties associated to the Type A errors.

<sup>+</sup> The total pressure at the nozzle inlet  $P_0$  is calculated from the measurement of the PZA003 sensor, i.e., by subtracting the estimated pressure drop between the primary heat exchanger outlet and the nozzle inlet,  $\Delta P = 0.7$  bar, from the value measured by PZA003 sensor, that is 18.06 barg.

## TYPE B UNCERTAINTIES

The uncertainty related to the measurement instruments and to the A/D conversion, which includes signal conditioning, is calculated as

$$U_{\text{Type B}} = \sqrt{U_{\text{instrument}}^2 + U_{\text{A/D}}^2}, \quad (5.2)$$

where  $U_{\text{instrument}}$  is the expanded systematic uncertainty of a sensor and  $U_{\text{A/D}}$  is the expanded uncertainty due to the analog to digital converter and related signal conditioning. Values of  $U_{\text{instrument}}$  for all the instruments of the ORCHID balance of plant are reported in Tab. 5.11. The expanded uncertainty  $U_{\text{A/D}}$  was calculated assuming a confidence level of 95 %, where the *combined standard uncertainty*  $u_{\text{A/D}}$  results from the combined effect of the following types of non-idealities affecting the operation of an A/D converter: 1. offset error, 2. gain error, 3. input noise, and 4. integral non-linearity. Uncertainties in A/D conversion equipment are classified as a Type B if the A/D system noise can be considered negligible. A recommended way of calculating the combined standard uncertainty [194] is to take the residual sum of squares (RSS) of the maximum values of all individual standard uncertainties assuming no correlation exists. The combined standard uncertainty due to the A/D converter is therefore

$$u_{\text{A/D}} = \sqrt{u_{\text{gain}}^2 + u_{\text{offset}}^2}, \quad (5.3)$$

where  $u_{\text{gain}}$  is the gain error uncertainty and  $u_{\text{offset}}$  is the offset error uncertainty. The integral non-linearity term and the noise term are not included in Eqn. 5.3 as their effect is minimal, see Refs. [26, 52]. For normal environmental temperatures like those of the laboratory hall and inside the control cabinet where the signal conditioning and A/D conversion modules are located, the departure from the nominal value of the gain is commonly called *gain error uncertainty* and is specified as

$$u_{\text{gain}} = \frac{\delta_{\text{gain}} \cdot X}{100},$$

where  $\delta_{\text{gain}}$  is the gain uncertainty in percentage of the full scale value and  $X$  is the measured value. Similarly, the offset component of the A/D conversion uncertainty is defined as

$$u_{\text{offset}} = \frac{\delta_{\text{offset}} \cdot R}{100},$$

where  $\delta_{\text{offset}}$  is the offset uncertainty in percentage of the full scale value and  $R$  is the range — the reading span for which the device is configured. At the time of the ORCHID commissioning, the measurement chain of the pressure and temperature sensors was not calibrated.<sup>8</sup> In particular, no information on the signal conditioning part was available other than the specification sheets of the DAQ equipment. The uncertainty values reported by the manufacturer are known to be excessively conservative due to liability implications, therefore were not deemed meaningful in the context of this uncertainty analysis. The calibration of the entire measurement chain of all the sensors is planned to occur in the near future. For this reason, the total expanded uncertainty was not evaluated, and it will be estimated once the data from the calibration is available.

<sup>8</sup>The sensors themselves, however, were used within the time-frame of their recommend calibration period.



## TOTAL EXPANDED UNCERTAINTIES

The total expanded uncertainty of each measurement is calculated as

$$U = \sqrt{U_{\text{Type A}}^2 + U_{\text{Type B}}^2}, \quad (5.4)$$

where  $U$  is the total expanded uncertainty,  $U_{\text{Type B}}$  is defined in Eqn. 5.2 and  $U_{\text{Type A}}$  results from the statistical analysis of the measured values. The values of the total expanded uncertainty of all the measured variables of the ORCHID balance of plant and for the two experimental runs PR.20-BP001 and PR.25-NT.001 are listed in Tab. 5.17 and 5.18. The uncertainties related to the PR.20-BP001 experimental run are deemed representative of turbine test runs, while those related to the PR.25-NT.001 experimental run are deemed representative of nozzle test runs.

## 5.7. CONCLUSIONS AND OUTLOOK

The ORCHID was conceived to perform both fundamental gas dynamic experiments regarding non-ideal compressible fluid dynamics, and testing of high-speed mini organic Rankine cycle turbines. Gas dynamic experiments are aimed at the validation of CFD software to be used for design and performance evaluation of system components, while the testing of fully instrumented mini turbines will provide experimental information for the development of design guidelines.

The setup implements a recuperated high-temperature cycle that supplies hot dense vapor to two test sections. Only the supersonic nozzle test section with optical access has been realized so far, while the turbine test bench is being designed. The working fluid selected for the initial experimental phase is siloxane MM, however the setup was designed to operate with a variety of working fluids belonging to different chemical families. The thermal energy source is an electric heater rated at 400 kW<sub>th</sub>, the maximum temperature of the thermal oil is 400 °C, and the maximum working fluid pressure is 25 bar. The condenser is indirectly cooled by an air cooler, via a water/glycol loop. A special diaphragm pump guarantees very stable operating conditions at set point. Experimental conditions can be maintained continuously for a long time, and can span a large range of temperature, pressure and mass flow rate. The thermodynamic state of the fluid at the inlet of the test sections can be saturated, superheated or supercritical.

The facility was successfully commissioned. The envisaged controlled operation was validated, therefore startup, stable operation and shutdown were repeatedly and safely carried out. Moreover, here two typical commissioning test runs are documented. One test run was intended to characterize the operating conditions typical of a supersonic nozzle experiment, therefore  $1.257 \pm 0.003$  kg/s (Type A) of dense organic vapor of MM was kept at  $T = 252.7 \pm 0.4$  °C (Type A) and  $P = 18.36 \pm 0.03$  bara (Type A) at the inlet of the test section. The other commissioning run was intended to achieve the design conditions for the turbine test bench. In this case the mass flow rate was  $0.1666 \pm 0.0003$  kg/s (Type A) while the thermodynamic state at the inlet of the test section was that corresponding to  $T = 275.0 \pm 1.3$  °C (Type A) and  $P = 20.78 \pm 0.11$  bara (Type A).

The design value of the working fluid mass flow rate could not be achieved at the operating conditions corresponding to nozzle experiments because the regenerator did not perform according to the design specifications (lower heat duty). A redesigned regener-

ator has been installed. Moreover, a working fluid mass flow rate larger than 1.4 kg/s is associated with high vibration and noise of the main pump, hence the mass flow rate of the planned experiments will always be limited to values lower than 1.4 kg/s, also once the new regenerator will be in operation. Moreover, there is a mismatch between the measured mass flow rate and the calculated sonic value due to either the incomplete sealing of the bypass valve or the increase of the nozzle throat area when the flow is at high temperature. A vapor mass flow meter has been installed upstream the nozzle test section and the throat height will be measured during the experiments based on calibration information obtained in cold conditions.

## ACKNOWLEDGEMENTS

The author is grateful to Steve van Herk for his help with the detailed design of the nozzle test section, and to Jos van Meurs for the realization of the nozzle pressure measurement chain and auxiliary systems. Furthermore, we extend our gratitude to Henk-Jan Siemer for his invaluable technical expertise and his persistence and efforts during the construction of the ORCHID. A special and warm mention goes to Paul Straatman. Paul's expertise in the process industry led to a robust plant design. Finally, Peter Batenburg and Gert-Jan Berends. The control narrative was initially developed by Johan Konz, but later revised by Peter Batenburg, which allowed the refinement of many critical details. The implementation into LabVIEW was made by Naiara Arellano and Gert-Jan Berends. Naiara was delightfully persistent in obtaining the required software specifications from various manufactures. Her efforts were greatly appreciated. Gert-Jan's impeccable coding skills made the safe and controlled operation of the facility possible.



# 6

## DESIGN AND COMMISSIONING OF THE NOZZLE TEST SECTION

Contents from:

Head, A. J., Beltrame, E., de Servi, C., and Colonna, P. Experimental Investigation of Complex Flow Structures in a Steady High Speed Expansion of the Organic Vapor MM. Experiments in Fluids (TO BE SUBMITTED)

### ABSTRACT

This chapter provides a description of the hardware, methods and results leading to the commissioning of the ORCHID nozzle test section and related instrumentation aimed at supplying accurate data for the validation of flow solvers capable of simulating non ideal compressible fluid dynamic (NICFD) flows. In particular, it treats the specifications of initial NICFD experiments which, at this stage of the research, target only inviscid phenomena. Moreover, it describes in detail the supersonic nozzle, the pressure and optical measurement systems and the devised experimental procedure. The first schlieren imaging experiments and the recording of static pressure profiles are also reported and they provide sufficient information for the commissioning of the device.

A series of schlieren photographs displaying Mach waves in the supersonic flow of the dense vapor of siloxane MM were obtained and are documented here for two experiments, namely, for inlet conditions corresponding to a stagnation temperature and pressure of  $T_0 = 252\text{ }^{\circ}\text{C}$  and  $P_0 = 18.4\text{ bara}$ , and to a back pressure of 2.1 bara. Furthermore, static pressure values were measured along the expansion path for operating conditions given by  $T_0 = 252\text{ }^{\circ}\text{C}$  and  $P_0 = 11.2\text{ bara}$  at the nozzle inlet and by a back pressure of 1.2 bara. The two inlet conditions of the fluid correspond to a compressibility factor of  $Z_0 = 0.58$  and  $Z_0 = 0.79$ .

The digital processing of the schlieren images allowed to estimate multiple angles formed by the Mach waves stemming from the upper and lower nozzle surfaces because

of the infinitesimal density perturbations generated by the, albeit small, roughness of the metal surfaces. These values are related to the local Mach number by a simple equation. These Mach number values together with the values of the static pressure along the top and the bottom profile of the nozzle were used for a first assessment of the capability of evaluating NICFD effects occurring in dense organic vapor flows by comparison with the results of CFD simulations. The outcome of the comparison was satisfactory.

It can thus be inferred that the nozzle test section has been commissioned and it is ready for experimental campaigns in which its full potential will be exploited. For example, in terms of measurements accuracy, repeatability, operational flexibility and suitability for other measurement techniques and other flow types.

## 6.1. INTRODUCTION

The computer simulation of compressible flows is critical for a large variety of scientific studies and engineering purposes. CFD codes have reached a remarkable level of accuracy because of the availability of a vast amount of accurate experimental data which could be used for verification and validation purposes [328]. The validation of a flow solver is defined as *the process of determining the degree to which a model is an accurate representation of the real world from the perspective of the intended uses of the model* [7], see also Oberkampf & Roy [280]. The validation of CFD software is therefore based on the availability of many and accurate experimental flow datasets.

CFD codes are at the core of the development of advanced technologies involving compressible flows, like airplanes and aero engines, rockets, and gas turbines, to name a few. Fluid dynamic experiments providing data for *code quality assurance* purposes [252] can be grouped into 1) experiments aimed at generating paradigmatic flows or certain physical phenomena, see, e.g., Refs. [282, 327, 392]; and, 2) *validation* experiments aimed at providing detailed measurements with uncertainties, which allow to improve the design of components in specific engineering applications, like, for instance, turbomachinery, see [125] and [406, p. 311], thus often requiring complex geometries and challenging operating conditions. Furthermore, there have been coupled CFD and experimental research efforts regarding research on hypersonic vehicles with the primary goal of improving simulation capabilities and wind tunnel experimentation: In the early nineteen nineties Sandia National Laboratories set up a conjoint effort which improved the confidence and accuracy in both the wind-tunnel measurements and computational aerodynamic predictions [279, 394].

However, all this body of work deals, to an almost complete extent, with aerodynamics or classical and ideal gas dynamics. Section 2.2 reviews the first experiments employing shock tubes and vapor tunnels which generated the first measurements of properties of NICFD flows. However, these data are insufficient in terms of quantity and quality for the validation of modern CFD software. Section 2.4.2 provides an outlook of the NICFD setups that were recently realized and of the associated first experiments. Some of these experiments are starting to generate fluid dynamic data of sufficient accuracy for the validation of NICFD-capable flow solvers.

The ORCHID has been conceived and realized to provide, in analogy to what has been done for classical and ideal gas dynamics, both accurate experimental data for paradigmatic NICFD benchmark flows and, in a second phase of the research, measure-

ments for turbomachinery operating partly in the NICFD regime.

This chapter describes the initial commissioning of the ORCHID nozzle test section consisting in the generation of supersonic flows of dense organic vapors, and in the first measurements which demonstrate the capability of obtaining accurate data for the validation of the simulation of inviscid flows with CFD codes. In particular, datasets have been generated for: i) the total conditions at the inlet and outlet of the planar nozzle, ii) the static pressure along the profile, and, iii), thanks to schlieren imaging, Mach lines over the entire length of the divergent part of the nozzle. All these quantities are very sensitive to NICFD effects because of the influence of both volumetric and caloric thermodynamic properties of the fluid.

At the time of this writing, preparations for experiments aimed at generating flow fields involving exemplary shock waves produced by a diamond immersed in the supersonic flow are almost completed. The prediction of the angle of shock waves is of particular interest for the design of transonic and supersonic turbomachinery like ORC turbines and supercritical CO<sub>2</sub> compressors. Furthermore, the optical access of the nozzle will be used in experiments focused on the direct measurement of the velocity field and possibly other primary quantities characterizing both inviscid and viscous aspects of the flow.

This chapter is structured as follows. The design of preliminary commissioning tests for inviscid flows are discussed in Sec. 6.2, while the modular nozzle test section is described in Sec. 6.3. The measurement chains used to obtain the pressure fields and to perform schlieren imaging are discussed in Sec. 6.4, 6.5 and 6.6. Section 6.7 details the experimental procedure, while the operating conditions, the stability of the flow and its symmetry are treated in Sec. 6.8. The results of the first experiments and the outcome of the post-processing of the digital images to obtain information on the Mach field of the flow are presented and discussed in Sec. 6.9. Section 6.9.3 presents a comparison between the CFD prediction and measured data. Final remarks and suggestions for further investigations conclude this chapter, see Sec. 6.10.

## 6.2. SPECIFICATIONS OF THE COMMISSIONING EXPERIMENT

Starting from the study documented in Ch. 4, specifications for experiments aimed at the initial commissioning of the nozzle test section were conceived. A preliminary validation of a CFD software with the results, such as the ones resulting from these experiments, is treated as an exercise, but with synthetic data, in Ch. 7.

Siloxane MM was selected as the working fluid. In this first phase of the research, measurements targeted only inviscid flow phenomena, in analogy with what is typical for the commissioning of conventional wind tunnels. It was therefore decided to perform total pressure and temperature measurements at the inlet and outlet of the nozzle, static pressure measurements along the nozzle profile, and Mach number estimations based on schlieren images. According to the findings documented in Ref. [361], and differently from what is described in Sec. 4.5, it was determined that initially, and for simplicity, no protruding elements were to be inserted within the divergent part of the nozzle, and that instead the Mach number distribution over the divergent part of the nozzle would be estimated based on the detection of Mach lines stemming from the upper and lower surfaces of the planar nozzle.

Table 6.1: Envisaged specifications for the commissioning experiment, see also Fig. 6.1. The working fluid is siloxane MM.

Fluid	$T_{1,t}$ / °C	$P_{1,t}$ / bara	$Z_{1,t}$	$P_2$ / bara	$M_2$	$\dot{m}$ / kg/h
MM	252	18.4	0.56	2.1	2	4122

Mach waves,  $\mu$ , form in the divergent part of the nozzle because of infinitesimal density perturbations originating from the roughness of the upper and lower metal surfaces of the planar nozzle, see e.g. Ref. [312, Sec. 4.2], and appropriately tuned schlieren imaging equipment is sensitive enough to detect them as darker lines. This technique was already used in the similar pioneering experiments of Spinelli *et al.* [361], who demonstrated that this method for the direct estimation of the local Mach number can be accurate in case of NICFD flows, given the strong density gradient variation over the supersonic expansion. The angle  $\mu$  formed by the Mach line with the local flow angle with respect to the axis of the nozzle depends only on the value of the Mach number according to the relation [374, Ch. 9]

$$M = \frac{1}{\sin \mu},$$

therefore the local Mach number can be obtained directly from the measurement of  $\mu$ .

Variables which would allow for a more direct validation of the models implemented in compressible flow solvers are density and specific internal energy, as these are most often the primary variables of the conservation equations at the basis of these models. However, the measurement of the local density in a supersonic vapor flow is rather challenging and internal energy cannot be measured directly. Static pressure and Mach number are calculated by means of a thermodynamic model, which in turn is a critical sub-model of any NICFD-capable flow solver. Pressure is a so-called primary volumetric thermodynamic property of the fluid, while the Mach number is a secondary and thermal property. Both variables are sensitive with respect to NICFD effects, see Ref. [156, 361]. For these reasons, pressure and Mach number were deemed meaningful quantities for the validation of the inviscid features of NICFD flows.

The operating conditions of the commissioning experiments were chosen starting from the design considerations reported in Sec. 4.5.1, and Sec 4.8.1, thus starting from the nozzle preliminary design described in Sec. 4.9.1. However, the original nozzle geometry has been adapted for a smaller throat area owing to the reasons specified in Sec. 5.6. The main objective remained to obtain sufficiently large non-ideality for a supersonic and isentropic flow through the nozzle. The operating conditions planned for the commissioning experiment are summarized in Tab. 6.1.

The process corresponding to the expansion in nominal conditions (the operating conditions for which the designed nozzle is adapted) is shown in the  $T - s$  diagram of the fluid in Fig. 6.1(a). The nozzle profile obtained with the method of characteristics for these conditions, see Sec. 5.6, is shown in Figure 6.1(b). The highly non-ideal quality of the envisaged flow is made evident by the constant  $Z - 1$  lines in both Figure 6.1(a) and Figure 6.1(b).

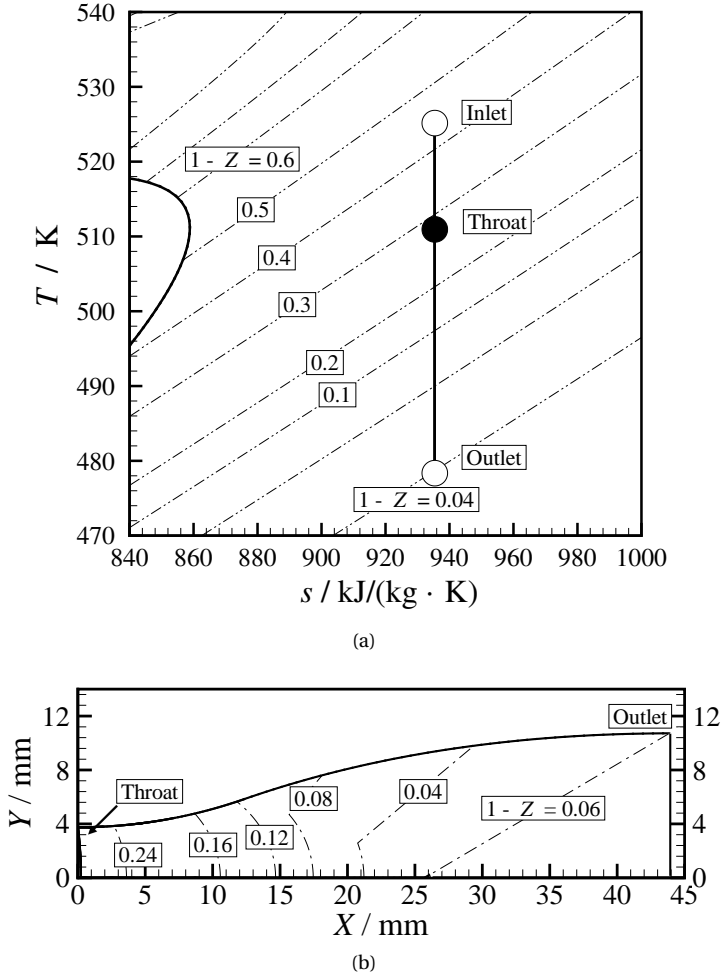


Figure 6.1: Envisaged commissioning experiment: supersonic flow through the nozzle (nozzle B). The specifications of the experiments are reported in Tab. 6.1. (a)  $T-s$  diagram showing the isentropic expansion with contours of  $1-Z$  (---). (b) The nozzle profile (Profile B) was generated with a program implementing the method of characteristics, see Ref. [163] and Sec 4.5. The contours of  $1-Z$  are obtained with the same computer program. Fluid properties are estimated with an in-house program [93] implementing the multiparameter equation of state model documented in Ref. [231].



Even if the planned measurements were based on standard gasdynamics measurement techniques, a number of technical problems due to the operation of the nozzle in the NICFD regime make this type of experiment very challenging. The dense vapor is at high temperature, and adiabatic experimental conditions can be obtained only if cold spots on any of the containing surfaces are avoided. A local decrease of temperature can also cause condensation, because the operating conditions of interest for NICFD experiments are those of a vapor that is only slightly superheated. On the contrary, hot spots are also to be avoided because the operating conditions are close to the so-called thermal stability limit of organic compounds, i.e., the temperature at which the rate of decomposition of the molecules becomes large, see, e.g., Refs. [62, 289, 305]. At high temperature, sealing is always problematic, and, in addition, it is of paramount importance because many organic working fluids are flammable. All these aspects were considered also for the realization of the test section, of the measurement systems and of the experiments which are treated in the following.

## 6.3. THE NOZZLE TEST SECTION

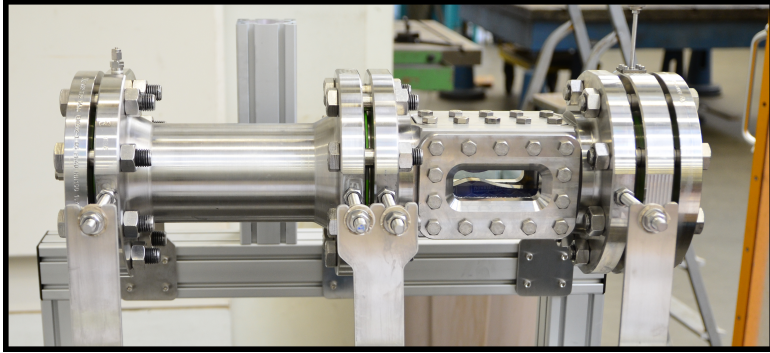
The nozzle test section, Fig. 6.2(a), is modular and formed by three compartments, namely, the settling chamber, the nozzle housing and the receiver, complemented by the Scani-valve pressure scanner, see the top left of Fig. 6.2(b).

### 6.3.1. SETTLING CHAMBER

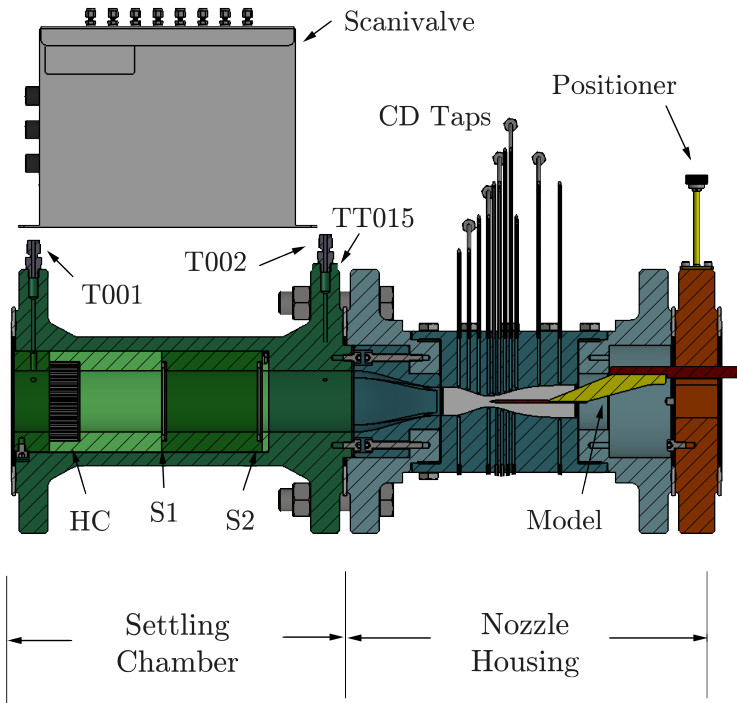
The settling chamber contains flow conditioning devices, i.e., one set of honeycombs and two sets of screens, in order to reduce the turbulence of the flow. The accuracy of all measurements and the comparison to models depend on knowing the values of the intensity and of the turbulence length scale [383]. Wind tunnels can normally achieve values of turbulence intensity as low as 0.02 to 0.05 % of the mean speed [121], which has remained relatively constant over the past 60 years [286]. These values can be controlled by optimizing the honeycomb and screen geometric parameters.

In order to achieve values of turbulence in line with current wind tunnel expertise, best practices have been followed for the design of the settling chamber, see Refs. [31, 251, 302]. The value of the diameter of the settling chamber is calculated starting from the nozzle throat area  $A_{th}$ : the cross-sectional area of the settling chamber  $A_{SC}$  must be such that area contraction ratio  $A_{SC}/A_{th}$  is a value between 6 and 12, although a larger value is acceptable so long as the resulting velocity does not fall below approx. 2 m/s. The length of the settling chamber should then be calculated as  $L_{SC} = 1.5 \cdot D_{SC}$  [170]. The calculated mass flow required to choke the nozzle is 1.15 kg/s, and the related MM vapor density is 122 kg/m<sup>3</sup>, see Tab. 5.15 and 6.1. The resulting bulk velocity in the settling chamber is therefore approximately 4 m/s. If the design operating condition or the fluid changes, thus requiring a different nozzle profile and throat area, then the modularity of the nozzle test section allows the diameter and length of the settling chamber to be changed accordingly.

Honeycombs for wind tunnels are available in different shapes and sizes for the purpose of aligning the flow with the axis of the test section and to break up the large-scale flow unsteadiness. The cells of a honeycomb reduce the mean or fluctuating variations



(a)



(b)

Figure 6.2: The nozzle test section **(a)** The realised design before being assembled into the ORCHID. **(b)** Its CAD representation. The settling chamber contains the honeycombs (HC) and two screens (S1 and S2). Taps T001 and T002 are located in the flanges of the settling chamber and correspond to the measuring ports of the Scanivalve  $P_{SV001}$  and  $P_{SV002}$  (if a non-symmetric measurement configuration is chosen). Temperature transmitter TT015 is located on the same plane as T002. The nozzle housing contains the contraction channel, the planar de Laval nozzle and the model support system. The remaining pressure taps are located in the converging diverging channel (CD). The positioner is used to axially translate (future) installed models.

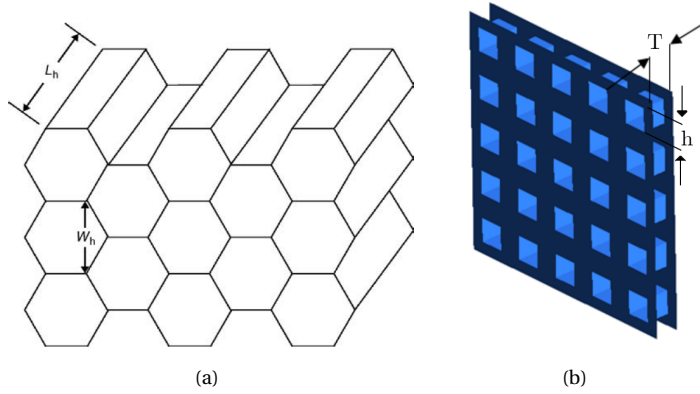


Figure 6.3: Simplified representation of the flow-conditioning devices within the settling chamber. **(a)** The honeycomb. **(b)** An isometric view of a screen with square holes. Sketches taken from Ref. [47].

in the transverse velocity. However, the honeycomb has little effect on the stream-wise velocity because the pressure drop through a honeycomb is small, therefore screens are also needed. With reference to Fig. 6.3(a), honeycombs with cells featuring a ratio between the length  $L_h$  and the diameter  $W_h$  of 7 to 10 and with roughly 150 cells per settling chamber diameter have been shown to provide the best performance, see Refs. [68, 251].

Honeycombs of varying geometry can be mounted in the settling chamber of the ORCHID by means of a capsule insert which can be easily removed. A honeycomb from ANDER Technologies was chosen and is installed at the inlet of the settling chamber. It has a ring diameter of 70 mm, a foil thickness of 0.05 mm, a cell size of 3.2 mm, a length of 25.4 mm and is formed by approximately 160 cells. The complete geometry is reported in App. A.1.

The achievement of a final uniform velocity distribution requires the addition of screens [304]. Screens make the flow velocity profiles more uniform by imposing a pressure drop and thus reduce the boundary layer thickness. In the settling chamber the screens are placed after the honeycombs with the mesh aligned perpendicularly to the flow direction [31] since honeycombs placed downstream of screens often result in an increase of the turbulence level [251]. Typically, wind tunnel screens are made of metal wires interwoven to form square or rectangular meshes, see Fig. 6.3(b). This reduces the size of turbulent eddies in such a way that turbulence with a small length scale rapidly decays after the screen, thus before reaching the nozzle or the test section where the measurements take place.

The mesh, see Fig. 6.3(b), is usually defined in terms of two parameters, namely

- the pressure drop coefficient  $K = f_1(\sigma, Re, \theta) = \Delta p / q$ , where  $\sigma$  is the screen open-area ratio,<sup>1</sup>  $Re$  is the Reynolds number,  $\theta$  is the flow incidence angle, measured from the normal to the screen,  $\Delta p$  is the pressure drop through one screen and

<sup>1</sup>For square mesh screens this is defined as  $\left(1 - \frac{T}{h}\right)^2$ .

$q = \frac{1}{2} \rho v^2$  is the dynamic pressure; and,

- the deflection coefficient,  $\alpha = f_2(\sigma, K, \theta)$ .

Normally several screens are placed in series, each with a small  $K$  (typical values range between 0.57 and 1.5) [251] and with an open-area ratio or mesh porosity in the range 60 – 70 % [302].  $K$  and  $\alpha$  can be determined according to one of the expressions documented in the literature: one commonly adopted is  $K = \frac{C(1-\sigma)}{\sigma^2}$  where  $C$  is a constant [251]. This expression is either obtained from the correlation of experimental data and the geometry of the screen or by measuring the pressure drop and speed of the flow [121]. The total number of screens and thus the total  $K$ -value depends on the turbulence level requirements and these values should be as low as possible to avoid misinterpretations when reading measurement data [251]. The remaining geometry specifications of the screens, e.g., the wire diameter and mesh width have been selected based on a literature survey and by calculating the geometries for  $K$ -values obtained from literature.

The mesh density of the screens should change depending on their location: it has been shown [68, 121] that lower values of the testing channel turbulence can be obtained by varying porosity of the screens placed in series, with the coarsest screen being closest to the inlet of the settling chamber, and the finest screen being closest to the outlet. The positioning of the two screens in the settling chamber of the ORCHID is reported in Fig. 6.2(b). The selection and the configuration of the screen is in accordance with the recommendations documented in Ref. [251]. The installed screens are of the spring steel mesh type, are mounted on a ring, and were obtained from *Kabel-Zaandam*. The first screen has the following characteristics: ring diameter of 70 mm, mesh width of 1.4 mm  $\times$  1.4 mm (L  $\times$  H) and wire thickness of 0.4 mm. The characteristics of the second screen are: ring diameter of 70 mm, mesh width of 0.37 mm  $\times$  0.37 mm (L  $\times$  H) and wire thickness of 0.1 mm. The meshes can easily be swapped by removing the internal capsule if a different turbulence intensity level is desired. Figure 6.2(b) also shows the positions the two wall pressure taps (T001 and T002), which are used to determine the total pressure drop over the settling chamber. In particular, the total pressure is measured by tap T002 with the Scanivalve device on port  $P_{SV001/2}$ <sup>2</sup> and the total temperature is measured with temperature transmitter TT015. The influence of the honeycomb and of the screen geometry on the flow conditions and thus on the turbulence level of tunnels operating with on an organic fluid is a topic worthy of investigation since, to the author's knowledge, it has only been briefly documented in Ref. [316].

Flow quality, e.g., bulk flow turbulence intensity can be determined with wind tunnel calibration techniques, see Ref. [301]. Hot wire anemometry, PIV or high frequency pressure transducers are normally used to quantify turbulence levels in the settling chamber or in the test section. However, at this stage of the research, the characterization of the turbulence level of the nozzle test section has not been pursued yet and will be investigated in the future.

<sup>2</sup>The Scanivalve port number will change depending on the valve configuration, see Tab. 6.2.

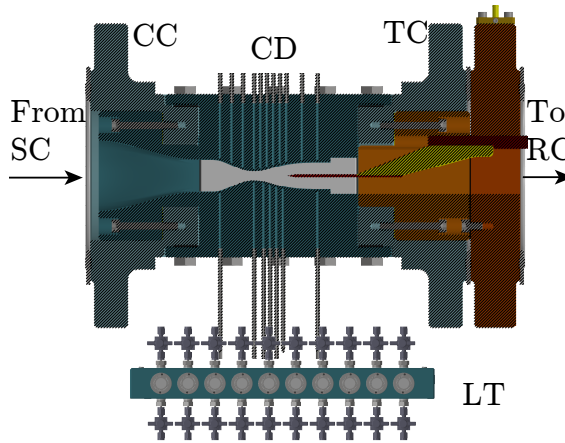


Figure 6.4: Cross-section of the nozzle housing; SC: settling chamber; CC: contraction channel; CD: converging diverging nozzle; MSC: model support compartment; PT: pressure taps; LT: liquid traps; RC: Receiver. The MSC can accommodate simple geometrical objects such as a diamond protruding through the outlet of the converging-diverging nozzle.

### 6.3.2. NOZZLE HOUSING

Figure 6.4 shows the CAD drawing of the vertical cross-section of the nozzle housing compartment and its modules, namely, the contraction channel, the converging-diverging nozzle, the model support compartment and the instrumentation. The nozzle housing is thermally insulated with jackets, see Fig. 6.6.

Aside from providing the geometrical transition from a circular to a rectangular channel, the contraction channel increases the mean flow speed, while reducing mean velocity variations and reduces the relative turbulence level, see, e.g. Refs. [250, 267]. The main design variable influencing the performance of the contraction channel is the area contraction ratio between the inlet and the outlet of the channel, and this is 12. The length of the contraction channel is  $L = 1.25 \cdot D_{in}$  and is based on previous designs [170]. The channel profile follows a polynomial curve.

The converging diverging nozzle module consists of two equal and removable profiles fitted in an enclosure. The shape of the channel can therefore be altered, if, for example, the working fluid is changed and thus a different nozzle must be inserted. The two vertical sides of the nozzle module host transparent windows providing optical access. The windows were supplied by *Crystran* (fused silica,  $W \times H \times D = 120 \pm 0.25 \text{ mm} \times 60 \pm 0.25 \text{ mm} \times 40 \pm 0.1 \text{ mm}$ ). The thickness was specified by assuming a safety factor of 4, thus, with a design pressure of 25 bar, the windows can withstand 55 bar at temperatures up to 400 °C. As for the optical characteristics, the flatness is  $\lambda/2$  over a length of 25 mm, the wavefront distortion is  $\lambda/4$ , the surface quality is 60/40 (scratch/dig) and the parallelism is lower than 10 arc secs. The nozzle profile was designed considering MM as the working fluid and half of the resulting divergent portion is shown in Fig. 6.1(b) and 6.5. The spatial coordinates of the nozzle profile obtained for the nominal operating conditions are reported in App. B.

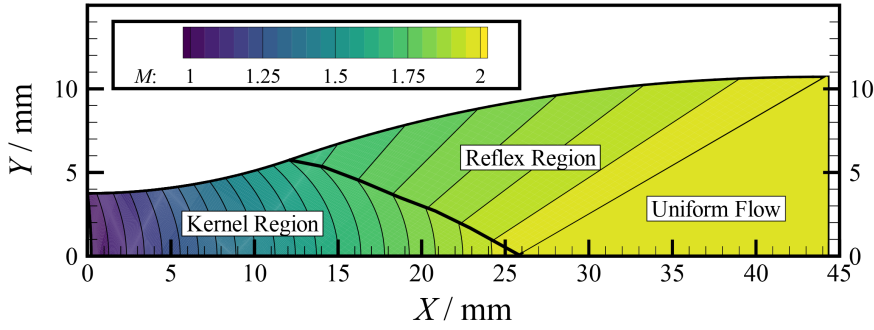


Figure 6.5: Upper part of the diverging portion of nozzle B as designed with the method of characteristics for the MM working fluid and with nominal total inlet conditions corresponding to  $T_0 = 252\text{ }^\circ\text{C}$ ,  $P_0 = 18.4\text{ bar}$  and with a back pressure of 2.1 bar ( $M_{\text{exit}} = 2.0$ ). The nozzle profile is created with a program implementing the method of characteristics, see Ref. [163], with Mach number contours plotted using the same program. Fluid properties are estimated with an in-house program [93] implementing the multiparameter equation of state model documented in Ref. [231].

The inlet pipe before the settling chamber and after the nozzle housing is electrically traced. However, in order to prevent excessive thermal losses and thus condensation in the nozzle test section, a thermal insulating jacket surrounding both the settling chamber and the nozzle housing had to be added.

### 6.3.3. RECEIVER

The receiver is connected to the outlet of the nozzle housing. It is a low-pressure vessel where the high kinetic energy of the vapor at the outlet of the nozzle is partially dissipated, leading to an increase in the fluid temperature. Figure 6.7 shows the cross-section of the receiver.

The receiver and the pipe connecting the receiver to the balance of plant are electrically traced in order to prevent vapor condensation. A glass window at the back of the receiver allows optical access for the application of PIV to the measurement of the flow within the test section by means of a sheet of light axially aligned with the nozzle axis.

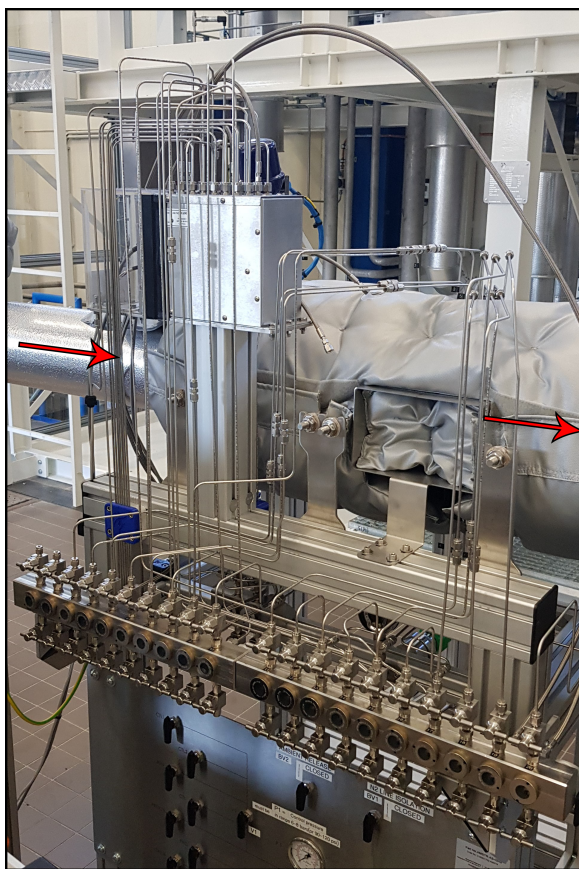


Figure 6.6: The nozzle housing, covered with thermal insulation, together with the *Scanivalve* measurement system. The red arrows indicate the flow direction.

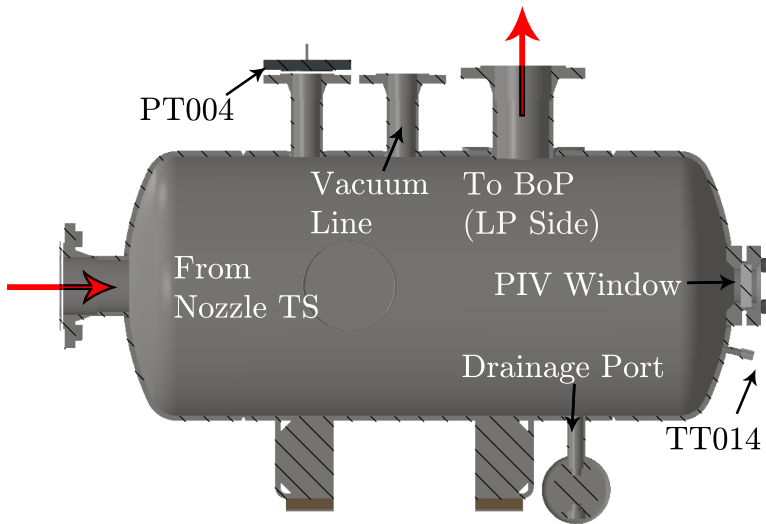


Figure 6.7: The vertical cross-section of the receiver. The pressure and temperature inside this low pressure vessel are measured with the PT004 and the TT014 transmitters. Optical access for laser light from the back is provided by a circular window (PIV window). The vessel is also fitted with a vacuum line and a liquid drainage valve. Red arrows indicate the vapor flow direction at the inlet and outlet. There is a flange on the backside which is used to perform maintenance or to mount/ unmount models, if necessary.



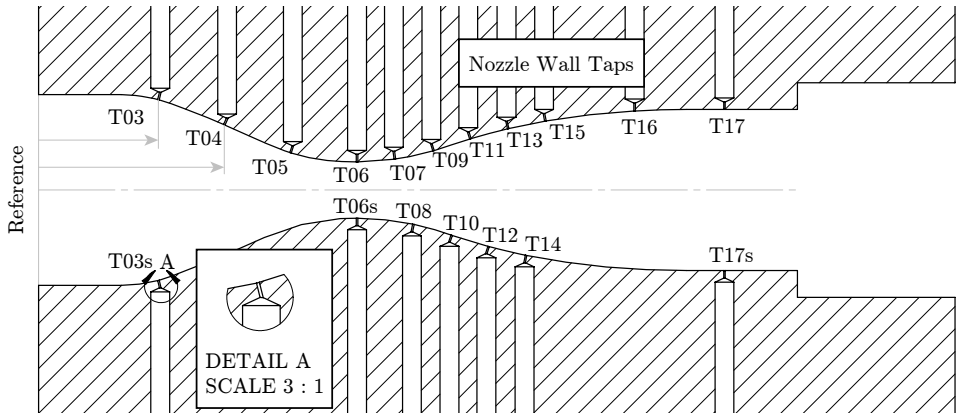


Figure 6.8: A cross-section of the planar nozzle showing the positioning of the eighteen pressure taps. The horizontal location is determined with the distance from a reference point on the axis at the inlet of the nozzle. The distances of the taps from the reference point are listed in Tab. 6.2. Three taps are symmetrically aligned and are indicated by the letter s. Detail A shows that the opening of each tap is perpendicular to the nozzle profile wall.

## 6.4. TOTAL AND STATIC PRESSURE MEASUREMENTS

Pressure measurements are performed with a system consisting of *Wika UPT 20* pressure transmitters and a *Scanivalve DSA3218* pressure scanner. These are also briefly described in Sec. 5.5.2. The DSA3218 is a stand-alone digital pressure scanner which can accept up to 16 pneumatic inputs (ports  $P_{SV}001$  to  $P_{SV}016$ ) where each input is connected to a discrete pressure transducer. In particular, it incorporates 16 temperature compensated piezoresistive pressure transducers with a pneumatic calibration valve, RAM, 16 bit A/D converter, and a microprocessor in a compact self contained module. It is a network-ready, Ethernet pressure scanning module. The pressure sensors are grouped according to their full scale specification, namely 34.5 barg ( $P_{SV}001 - 003$ ), 17.2 barg ( $P_{SV}004 - 009$ ), and 6.8 barg ( $P_{SV}010 - 016$ ).

The pressure measurement system is used to estimate i) the total pressure at the inlet and outlet of the nozzle housing,<sup>3</sup> with two wall taps positioned in the settling chamber whose signal is measured with the Scanivalve, see Tab. 6.2, and, ii) the static pressure along the nozzle profile, see Fig. 6.8, also measured with the Scanivalve. The *WIKA UPT 20* transmitter (PT004) is used to measure pressure in the receiver, see Fig. 6.7.

Figure 6.2(b) shows the two taps, T001 & T002, in the settling chamber located at the first and second flange and the eighteen taps situated along the upper and lower nozzle profiles giving a total number of twenty. The taps were obtained by boring 0.2 mm diameter holes perpendicular to the profile surface, and afterwards, by drilling a 2.5 mm hole from the top mounting surface, see detail A in Fig. 6.8. Eighteen 1/16 inch Swagelok tubes are braze welded to the top surface of the nozzle profile and separately routed, together with the two tubes connected to the taps of the settling chamber, underneath the nozzle test section to small chambers equipped with sight glasses, i.e., the liquid

<sup>3</sup>In this case the static and total pressure are approximately the same as the flow velocity is low.

Table 6.2: Position of the pressure taps and configurations of the Scanivalve (tap-scanivalve port connections).

Nozzle Wall Tap Number	Axial Coordinate / mm	Scanivalve Port Number Normal Config.	Scanivalve Port Number Sym. Config.
T001	n.a. <sup>*</sup>	P <sub>SV</sub> 001	P <sub>SV</sub> 001
T002	n.a. <sup>@</sup>	P <sub>SV</sub> 002 <sup>⊙</sup>	-
T003s	15.96	-	P <sub>SV</sub> 002 <sup>⊙</sup>
T003	15.96	P <sub>SV</sub> 003	P <sub>SV</sub> 003
T004	24.72	P <sub>SV</sub> 004	P <sub>SV</sub> 004
T005	33.55	P <sub>SV</sub> 005	P <sub>SV</sub> 005
T006	42.4 <sup>+</sup>	P <sub>SV</sub> 006	P <sub>SV</sub> 006
T006s	42.4 <sup>+</sup>	-	P <sub>SV</sub> 007 <sup>◀</sup>
T007	47.44	P <sub>SV</sub> 007 <sup>◀</sup>	-
T008	49.90	P <sub>SV</sub> 008	P <sub>SV</sub> 008
T009	52.57	P <sub>SV</sub> 009	P <sub>SV</sub> 009
T010	55.01	P <sub>SV</sub> 010	P <sub>SV</sub> 010
T011	57.5	P <sub>SV</sub> 011	P <sub>SV</sub> 011
T012	59.91	P <sub>SV</sub> 012	P <sub>SV</sub> 012
T013	62.53	P <sub>SV</sub> 013	P <sub>SV</sub> 013
T014	64.89	P <sub>SV</sub> 014	P <sub>SV</sub> 014
T015	67.47	P <sub>SV</sub> 016 <sup>◇</sup>	-
T016 <sup>□</sup>	79.35	-	-
T017s	91.3	-	P <sub>SV</sub> 016 <sup>◇</sup>
T017	91.3	P <sub>SV</sub> 015	P <sub>SV</sub> 015

<sup>\*</sup> The first tap is located upstream of the honeycomb in the first flange of the settling chamber.

<sup>@</sup> The second tap is located downstream of the last screen in the second flange of the settling chamber.

<sup>+</sup> Location of the throat.

<sup>⊙</sup> A three-way valve (V<sub>SV</sub>18) allows to switch between T002 and T003s.

<sup>◀</sup> A three-way valve (V<sub>SV</sub>19) allows to switch between T007 and T006s.

<sup>◇</sup> A three-way valve (V<sub>SV</sub>20) allows to switch between T015 and T017s.

<sup>□</sup> T016 is not used.

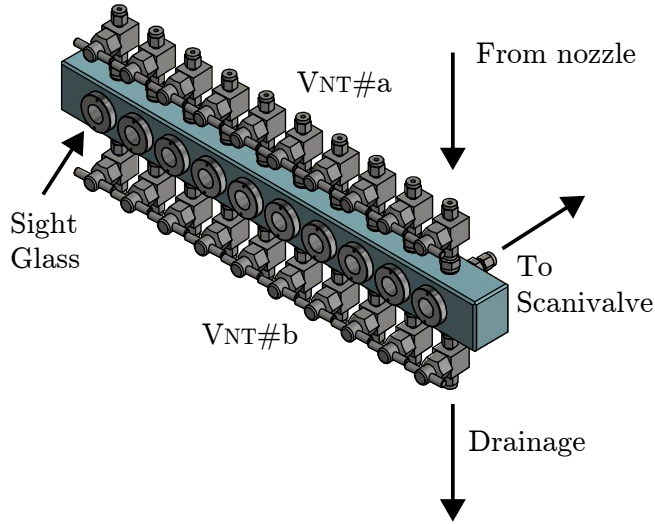


Figure 6.9: The assembly of the liquid traps (only one segment containing ten sight glasses is shown). The valve  $V_{NT\#a}$  isolates the process from the *Scanivalve* should the user observe condensate forming in one of the sight glasses. Valve  $V_{NT\#b}$  allows to drain the liquid during operation.

traps (see Fig. 6.9 for the liquid traps assembly and Fig. 6.6 showing the position of the assembly relative to the nozzle test section).

The liquid traps were conceived to protect the sensors of the *Scanivalve* from liquid resulting from the condensation of the organic vapor. The sight glasses allow to check if condensation occurs in the lines while acquiring pressure data. The liquid trap is provided with two manual ball valves:  $V_{NT\#a}$  to isolate the process from the *Scanivalve*, and  $V_{NT\#b}$  to drain the individual parts of the tap circuits, should condensate form inside the liquid trap. Figure 6.10 shows a simplified P&ID of the assembly formed by the nozzle test section, the DSA3218 scanivalve and the liquid traps, whereas Fig. C.1 shows the complete P&ID with the tube circuit.

In order to allow verifying that the flow inside the nozzle is symmetric, three taps (T003s, T006s and T017s in Fig. 6.8) are positioned along the lower profile in locations which are symmetrical with respect to taps in the upper profile. The three-way valves  $V_{SV}018/019/020$  (Fig. C.1) allow to easily switch from a normal measuring configuration to the symmetric configuration. The spatial resolution of the normal measuring configuration is higher since the taps, apart from the ones designated with an s, are arranged in a zig-zag pattern, e.g., located in a different axial position with respect to the top and bottom profiles, see Fig. 6.8.

## 6.5. TEMPERATURE MEASUREMENTS

The nozzle test section is equipped with two *WIKA TR10-C* resistance temperature detectors (RTD). The first, TT015, is located in the second flange of the settling chamber

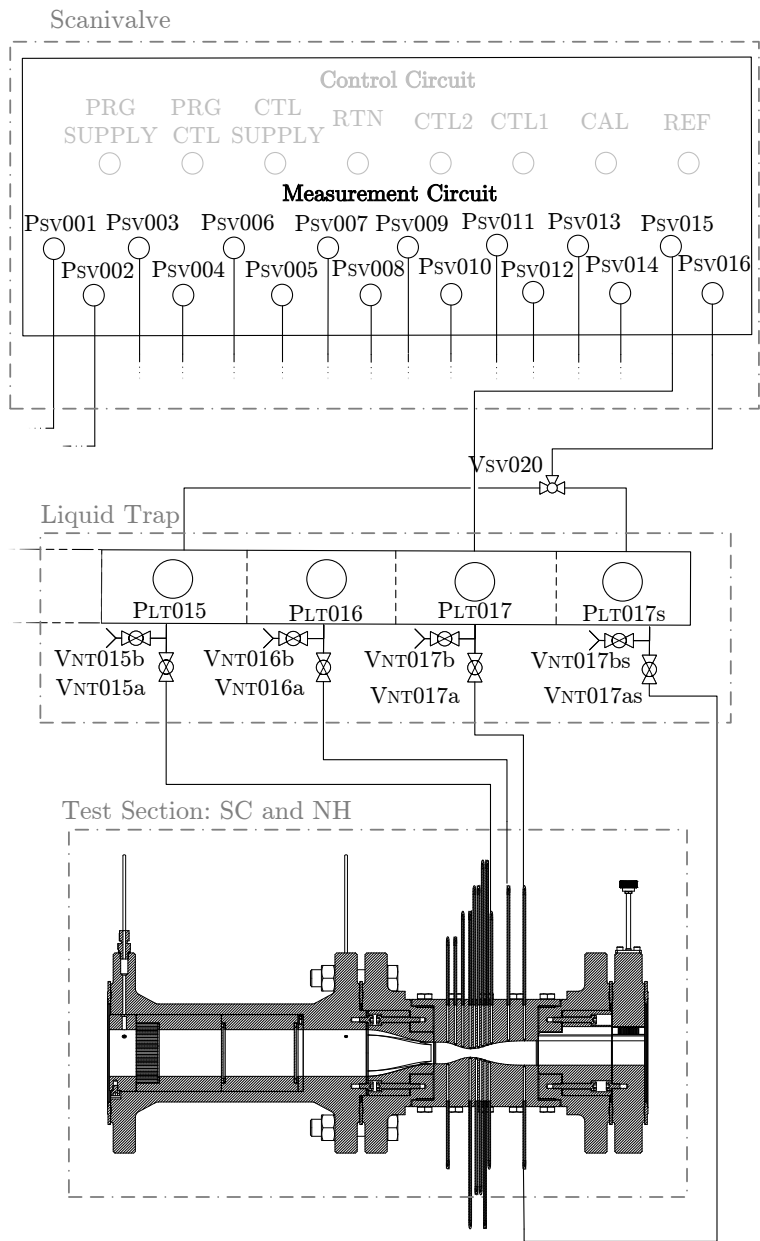


Figure 6.10: Simplified Piping & Instrumentation Diagram (P & ID) of the assembly formed by the nozzle test section, the DSA3218 Scanivalve and the liquid traps. Only one three-way valve Vsv020 is shown for clarity. Fig. C.1 shows the complete system, including the routing for all twenty pressure taps and Tab. 5.3 details the legends and symbols for the process equipment.

and the other, TT014, is located near the PIV sight glass in the receiver, see the P&ID in Fig. 5.2 and/or the positions in Figs. 6.2 and 6.7. These temperature transmitters measure within the range of 0–300 °C, and their corresponding electrical output is a 4 – 20 mA current signal. They are directly connected to a 24-bit A/D input module (NI9208) of the compactRIO controller. Unlike the other RTD equipping the ORCHID balance of plant, these two sensors do not feature thermowells so as to achieve a faster response time.

## 6.6. SCHLIEREN IMAGING

The schlieren method is an optical technique for visualizing the gradient of density in a transparent medium. The name of this technique derives from the German word "schliere" (plural schlieren), which means "inhomogeneous regions/medium". It is based on the variation of the light intensity due to variation in the refractive index of the medium, which in turn is caused by density gradients in the fluid. Schlieren imaging can therefore be used to estimate the density gradient in a flow.<sup>4</sup> Here, the foundations of schlieren imaging is briefly treated to illustrate the theoretical background and to show that, in case of a dense vapor flow of complex organic molecules, the resulting flow images are much more sensitive to density gradients if compared to air flows or ideal gas flows of simple molecules in general.

The geometric theory of light refraction within a *schliere* is briefly recalled, see Ref. [353, App. 6]. Since the vapor of siloxanes is sufficiently transparent, see Sec. 3.2, here the component of the refractive index related to light absorption is not treated, thus those frequencies/ wavelengths of light near the absorption frequency  $\nu_i$  of the vapor. The refractive index  $n$  is a complex number and the imaginary part is related to the absorption of light through the vapor [258], which is therefore neglected.

The speed of light in a given medium  $c$  is related to the speed of light in a vacuum,  $c_0 = 2.99792458 \times 10^8$  m/s, through the index of refraction  $n$ , which is defined as

$$n \equiv \frac{c_0}{c}. \quad (6.1)$$

With reference to Fig. 6.11, in order to predict the observable density variation pattern in a recording plane one may determine the deflection angles  $\epsilon_x$  and  $\epsilon_y$  at the end of the test object for each light ray. It can be demonstrated, see Refs. [353, 399] and Goldstein & Kuehn [154, p. 377–397], that optical inhomogeneities refract or bend light rays in proportion to their gradients of refractive index in an  $x, y$ -plane. The resulting ray curvature is then given by

$$\frac{\partial^2 x}{\partial z^2} = \frac{1}{n} \frac{\partial n}{\partial x} \quad \text{and} \quad \frac{\partial^2 y}{\partial z^2} = \frac{1}{n} \frac{\partial n}{\partial y}. \quad (6.2)$$

For a small angles, Eqn. 6.2 is valid for the entire light path through the test object. Assuming the entering angle is zero, integrating once Eqn. 6.2 gives the components of the angular ray deflection in the  $x$  and  $y$  directions as

<sup>4</sup>The absolute value of the density can also be obtained, provided a reference value is available. However, for accurate quantitative evaluation, other optical techniques such as interferometry are chosen because they are based upon the precise measurement of fringe pattern distortion instead of a less precise measurement of change in photographic contrast [353, p. 265].

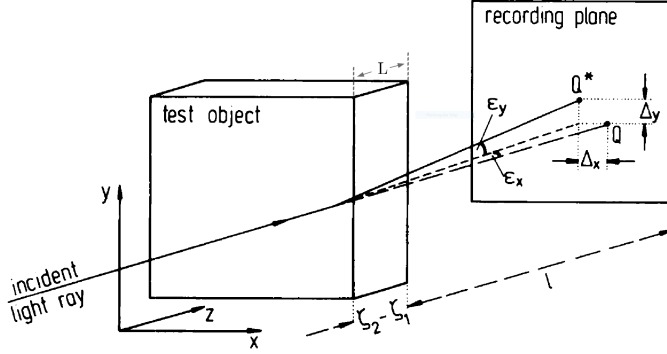


Figure 6.11: Simplified representation of the deflection of a light ray through an inhomogeneous test object in which the density varies and its effect on a recording plane at distance  $l$  from the point-like light source. Taken from [258].

$$\epsilon_x = \frac{1}{n} \int_{\zeta_1}^{\zeta_2} \frac{\partial n}{\partial x} \partial z \quad \text{and} \quad \epsilon_y = \frac{1}{n} \int_{\zeta_1}^{\zeta_2} \frac{\partial n}{\partial y} \partial z. \quad (6.3)$$

where  $\epsilon_x$  and  $\epsilon_y$  are the angles at the exit of the test object. For two-dimensional schlieren of extent  $L$  along the optical axis, these relations become

$$\epsilon_x = \frac{L}{n_0} \frac{\partial n}{\partial x} \quad \text{and} \quad \epsilon_y = \frac{L}{n_0} \frac{\partial n}{\partial y}, \quad (6.4)$$

where  $n_0$  is the refractive index of the medium surrounding the test object, commonly air. These expressions provide the mathematical foundation of the schlieren technique. Moreover, Eqns. 6.2, 6.3 and 6.4 show that light rays are always bent toward the region of higher  $n$ . It can also be shown that, for gases and vapors, a region in space in which  $n$  is higher corresponds to a region of higher density  $\rho$ .

Figure 6.12 shows a typical two-lens schlieren system, which consists of a light source, condensing lens, slit, collimating lens ( $L_1$ ) and a schlieren head ( $L_2$ ) [353], knife-edge, and camera. The lamp, condenser lens, slit and lens  $L_2$  produce a collimated light beam illuminating the vapor flow enclosed in the test section. The schlieren head focuses the image of the light source on the face of the so-called knife, namely a sharp-edged opaque object mounted on an adjustable stand. The knife-edge cuts off part of the light-source image passing through the test section, thus reducing the light intensity illuminating the photographic plate. The purpose of the knife is therefore to allow the adjustment of the system sensitivity to density gradients in the vertical and horizontal directions. A horizontal knife-edge configuration is sensitive to vertical density gradients in the flow, while a vertical knife-edge configuration is sensitive to horizontal gradients.

The system sensitivity can be adjusted in several ways and the regulation method can be explained by analyzing the relationship between the relative light intensity distribution and the density. Following the analysis treated in Merzkirch [258, p. 135] and with reference to Fig. 6.13 the relative light intensity distribution in the recording plane is determined as follows. Let  $a_K$  be the reduced height of the light source image where  $a_0$

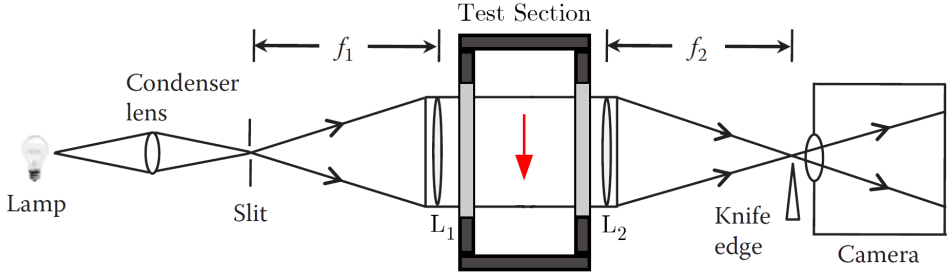


Figure 6.12: Schematic of a two-lens schlieren optical system. The red arrow indicates the flow direction. Adapted from Ref. [261, Fig. 7.13].

and  $b_0$  represent the undisturbed image projected on the face of the knife-edge. In the absence of any disturbance in the test section, the light intensity  $I$  arriving at any point  $(x, y)$  of the photographic plane is constant, and the uniform illumination is given with sufficient accuracy by

$$I(x, y) = I_0 \cdot \frac{a_K \cdot b_0}{f_c^2},$$

where  $I_0$  is the intensity (luminance) of the light source, i.e., the general background intensity level, and  $f_c$  is the focal length of the camera lens, see Fig. 6.12.

In the presence of a disturbance in the test section the light rays are deflected by an angle  $\epsilon$ . The corresponding image of the light source formed by these rays on the plane of the knife-edge is shifted by distances  $\Delta a$  and  $\Delta b$ . The shifts are perpendicular and parallel to the knife-edge, see Fig. 6.13(b). If  $\epsilon_y$  is the vertical component of the deflected ray  $\epsilon$ , and  $f_2$  is the focal length of the schlieren head then  $\Delta a \approx \epsilon_y f_2$ . The light intensity in  $(x, y)$  is then changed by

$$\Delta I = I_0 \cdot \frac{\Delta a}{a_K}.$$

The photographic process allows one to estimate the relative light intensity changes, i.e., contrast changes rather than absolute values of light intensity; therefore,

$$\frac{\Delta I}{I_0} = \frac{\Delta a}{a_K} = \epsilon_y \cdot \frac{f_2}{a_K}, \quad (6.5)$$

where  $\Delta I = I_d - I_0$  is the change in light intensity on the recording screen with respect to the light source intensity  $I_0$  [353].  $I_d$  is the intensity associated with the deflected light ray. Substituting the ray deflection defined by Eqn. 6.3 into 6.5 results in

$$\frac{\Delta I}{I_0} = \frac{f_2}{a_K} \int_{L_1}^{L_2} \frac{1}{n} \cdot \frac{\partial n}{\partial y},$$

which, with two-dimensional schlieren of extent  $L$  along the optical axis, see Fig. 6.11, this becomes

$$\frac{\Delta I}{I_0} = \frac{f_2}{a_K} \cdot \frac{L}{n_0} \cdot \frac{\partial n}{\partial y}. \quad (6.6)$$

With this geometrical arrangement of the schlieren system, the  $y$  component of the refractive index gradient can be measured. Turning the knife-edge by 90 degrees around the optical axis makes the system sensitive to the displacement  $\Delta b$ , see Fig. 6.13(b), and one measures the  $x$  component of the intensity gradient. If an appropriate relationship between the refractive index and the density is known then Eqn. 6.6 can be used to obtain a relation between the variation in light intensity and density.

Several mathematical and empirical models describe the relationship between the refractive index  $n$  and density  $\rho$  in both liquids and gases. The Lorentz–Lorenz definition [241, 242] of molar refraction [50],

$$A = \frac{M}{\rho} \frac{n^2 - 1}{n^2 + 2} \quad (6.7)$$

results in an explicit relation between molecular constants, properties of the fluid and the refractive index.  $M$  is the molar mass of the substance and  $\rho$  is its density.

The empirical Gladstone–Dale equation in the abbreviated form

$$n - 1 = K \cdot \rho, \quad (6.8)$$

is valid for air and gases of simple molecules [258]. This relation is valid in the assumption that the refractive index maintains a value approaching unity, i.e.,  $n \rightarrow 1$ . The Gladstone–Dale coefficient  $K$ , is determined experimentally and is approx.  $2.3 \times 10^{-4} \text{ m}^3/\text{kg}$  for air at standard conditions, given visible illumination.

Equation 6.8 shows that  $n$  in this case is only weakly dependent on  $\rho$ . For example, a large change in air density, e.g., a variation of two orders of magnitude, would cause a negligible change in  $n$ . Conversely,  $n - 1$  in air at the standard temperature and pressure is only 0.000292. Therefore, in order to optically detect small gas density variations in air, sensitive equipment is necessary.

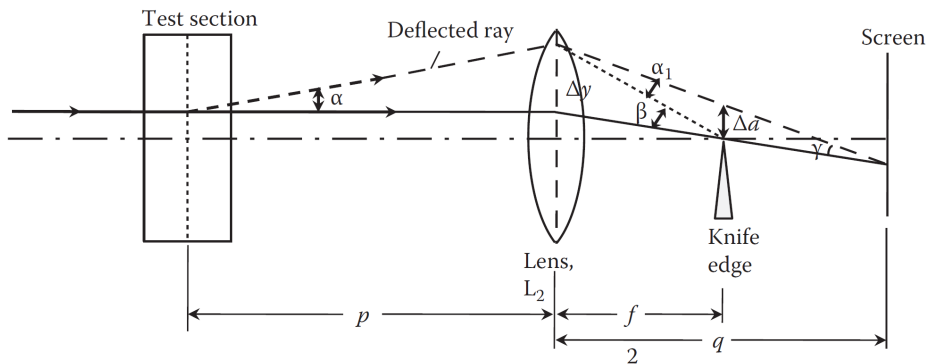
For gases made of simple molecules, the Gladstone–Dale coefficient may vary roughly from 0.1 to  $1.5 \text{ m}^3/\text{kg}$  [258, 353]. Values of  $K$  for gaseous substances other than air, e.g.,  $\text{N}_2$ , He,  $\text{H}_2\text{O}$ ,  $\text{CO}_2$ ,  $\text{CH}_4$ ,  $\text{SF}_6$ ,  $\text{CF}_4$  [61] or mixtures of different chemical constituents, can be found in Refs. [258] and [238].

For gases formed by more complex molecules, therefore also for siloxane vapors and other complex organic compounds, the Gladstone–Dale relation does not hold because the refractive index cannot be assumed to feature a value approaching unity. However, the refractive index of these fluids can be determined if the molar refraction  $A$  is known, either because it has been measured, or because it can be estimated with methods based on the concept of *additivity of bond refractions* [395].

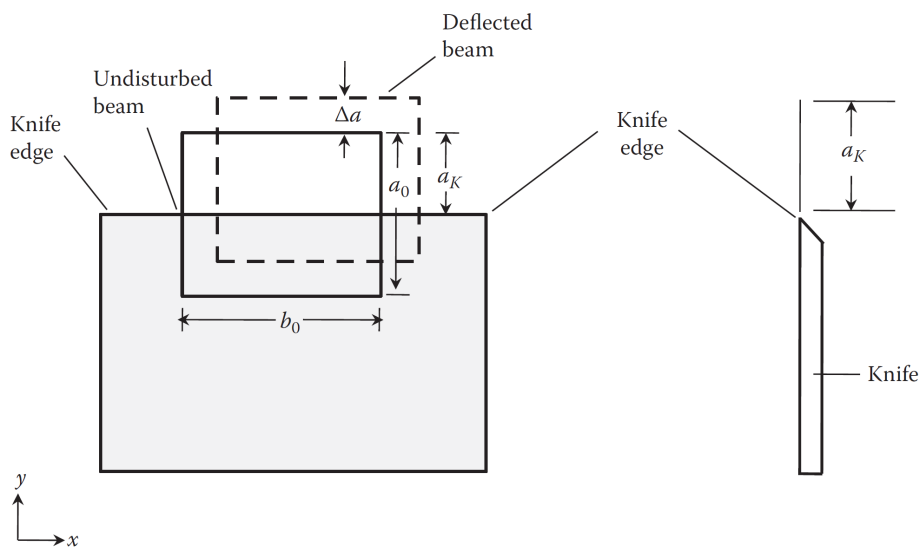
Equation 6.7 can be inverted to obtain the refractive index as a function of density, molar refraction and molar mass, resulting in

$$n = \sqrt{\frac{1 + 2A \cdot \rho / M}{1 - A \cdot \rho / M}}. \quad (6.9)$$





(a)



(b)

Figure 6.13: (a) The deviation of an optical ray at a knife-edge. (b) Deflected beams at the knife-edge. Taken from [261, Fig. 7.14].

Table 6.3: Refractivity data for the atomic bonds linking the atoms of siloxanes.

Atomic Group	Group Molar Refractivity/ $\text{cm}^3 \text{mol}^{-1}$	Reference
Si – O	1.75	[395]
Si – CH <sub>3</sub>	7.57	[395]

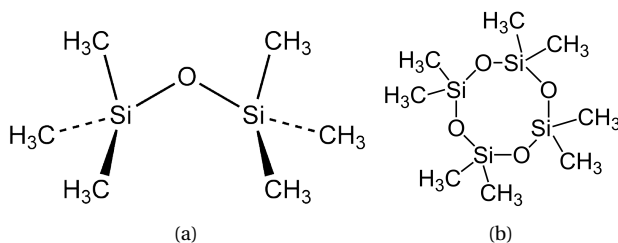


Figure 6.14: The stereo structural formulas of a linear and cyclic siloxane. **(a)** hexamethyldisiloxane (MM). **(b)** octamethylcyclotetrasiloxane (D<sub>4</sub>).

The molar refractivity  $A$  can be measured experimentally. However, its value is not available for all the molecules of interest in engineering applications. As common with many molecular properties, also the molar refractivity can be obtained with theoretical methods based on the *additive contribution* assumption with an acceptable error. For the case of the refractive index, the contributions are given by the atomic bonds forming a molecule. The same bond can form different molecules. The molar property of interest can be obtained by summing the contributions of the various type of atomic bonds present in the molecule. If the refractivities of atomic bonds present in the molecule are known, one can therefore calculate the molar refractivity as [113, 395]

$$A = \sum_i R_i \quad (6.10)$$

where  $R_i$  is the contribution to the molar refractivity of atomic bond  $i$ .

### 6.6.1. REFRACTIVE INDEX OF DENSE SILOXANE VAPORS AND ITS INFLUENCE ON SCHLIEREN FLOW VISUALIZATION

Warrick [395] and Sauer [342] adopted the bond contribution method, see Eqn. 6.10, to estimate the molar refractivity of organo-silicon compounds; siloxanes belong to this category of substances. The bond contribution method is convenient for siloxanes, since many of the bond refractivities of organosilicon compounds are known. In case of siloxanes, the bond refractivities of both Si–CH<sub>3</sub> and Si–O<sub>2</sub> are available, see Tab. 6.3, and siloxanes are composed by atoms linked various combinations of these two bond types. Figure 6.14 shows the chemical structure of two siloxanes, a linear (MM) and a cyclic (D<sub>4</sub>) polymer.

The molar refractivity of D<sub>4</sub> was determined experimentally and is reported in Tab. 6.4, where also the value calculated with Eqn. 6.10 is reported. The table lists also the small

Table 6.4: Experimental and calculated values of the molar refractivities  $A$  for  $D_4$  and MM vapors.

Fluid	Chemical formula	$A_{\text{observed}} / \text{cm}^3 \text{mol}^{-1}$	Reference	$A_{\text{calculated}} / \text{cm}^3 \text{mol}^{-1}$	Relative deviation / %
$D_4$	$[(\text{CH}_3)_2\text{SiO}]_4$	74.60*	[191, 395]	74.56	-0.03
MM	$\text{O}[\text{Si}(\text{CH}_3)_3]_2$	-	-	48.92	-
Air	-	6.66	[258]	-	-

\* Reported in Ref. [395] as cyclic dimethylsiloxane tetramer.

percentage relative deviation between the experimental and the calculated value. Such small difference provides confidence in the value of molar refractivity calculated for MM, which has not been measured, and whose calculated value is also reported in Tab. 6.4.

Molar refractivity is weakly dependent on light wavelength, and all the values reported in Tab. 6.4 are for light of wavelength close to 527 nm. Hence, these values should not change for almost all wavelengths in the visible spectrum [258]. The molar refractivity of vapors is also weakly dependent on temperature [15, 138]. According to Fainberg & Miller [138] the effect of temperature on molar refractivity can be of the order of 0.005–0.02 % per degree centigrade for organic vapors in the range 0–40 °C, resulting in a molar refractivity variation of less than 0.1 %. Furthermore, following Born & Wolf [50, p. 93] in the case for air at 14.5 °C, a pressure increase from 1 to 40 bar results in an increase of molar refractivity of less than 1 %. For the experimental studies conducted with  $\text{CO}_2$  Besserer & Robinson [37], Michels & Hamers [259] have determined a similar effect on the refractive index [37, 259] by varying temperature and pressure. In accordance with Liu & Daum [238], molar refractivity is thus assumed to be independent of light wavelength, temperature and pressure for the flows of dense organic vapors treated here. Furthermore, Born & Wolf [50, p. 94] and Malik [245, p. 25] report that changes of thermodynamic state have very minor influences on the value of the measured molar refractivity.

The additivity of the bond contribution method also implies that molar refractivity increases with the number of bonds in the molecule, thus, within the same family of fluids, it increases with the molecular weight and complexity of the molecule. The dependence of the refractive index on molar refractivity, see Eqn. 6.9, is such that also the refractive index increases with the number of bonds in the molecule. Consequently, the molar refractivity of dense organic fluids is substantially larger than that of mixtures of simple molecules such as air. In addition, the refractive index increase with density.

The following simple exercise illuminates the reason why a less sensitive optical system is needed when the fluid is comprised of complex molecules. Consider three isentropic expansions of air, MM, and  $D_4$  corresponding to an outlet nozzle Mach number of approximately 2. Giepmans [152, p. 68] conducted an experiment with air in the supersonic windtunnel TST-27 (TU Delft Aerodynamics Laboratory) at total conditions 278 K and 2.7 bara, and a back pressure of 0.6 bara — resulting in density values 3.4–0.7 kg/m<sup>3</sup>. The second isentropic expansion pertains to the conditions specified in Tab. 6.1 for the fluid MM resulting in a density variation of 120–3 kg/m<sup>3</sup>. The third isentropic expansion pertains to conditions specified in Tab. 4.5 for the fluid  $D_4$  resulting in the density variation 150–7 kg/m<sup>3</sup>. The density is then normalized by means of the inlet stagnation

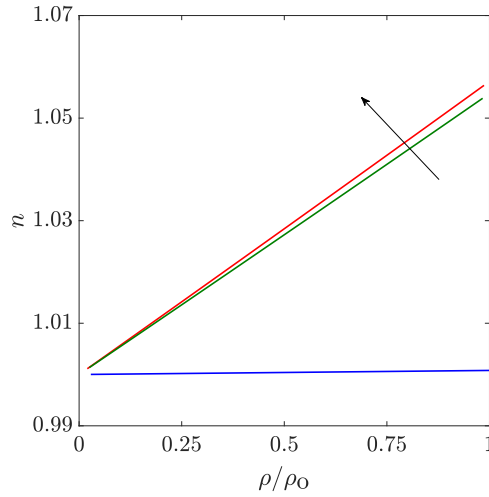


Figure 6.15: The refractive index  $n$  vs. normalised density  $\rho/\rho_0$  for  $D_4$  (—), MM (—), and air (—) and for ranges of densities typical supersonic expansions for which the refractive index is calculated with Eq. (6.9).

density corresponding to those isentropic supersonic expansions.

Figure 6.15 shows the variation of the refractive index  $n$  with nondimensional density. The refractive index is computed with Eqn. 6.9 by substituting the calculated molar refractivity from Tab. 6.4 and the density ranges defined above.

It can therefore be inferred that the variation of light intensity through a dense organic vapor is much larger than that through air for comparable density changes, thus much less optical sensitivity is needed in order to obtain schlieren images of dense organic vapor flows compared to that needed for air flows. Conversely, for a given quality of the optical equipment, a much higher contrast of the schlieren image can be obtained if the fluid of the observed flow is a dense organic vapor.

### 6.6.2. THE SELECTED LAYOUT OF THE SCHLIEREN SYSTEM

Figure 6.16 shows the schematic of the general layout of the schlieren system. Figure 6.17 is a photograph showing the schlieren arrangement from the outside of the ventilation cabinet of the ORCHID. All of the hardware elements, e.g., light source, lenses, mirrors and camera are mounted on three separate rigid structures which ensure the correct alignment of all components. The LED light source and the camera are situated outside the ventilation hood since they are non-ATEX compliant equipment.

The simple z-type two-lens configuration was chosen instead of the more complex and costly configuration in use in modern wind tunnels because i) it provides sufficient resolution given that is used to visualize flows of dense vapors and, as treated in Sec. 6.6, in this case the sensitivity to density gradients is much higher than in air flows, ii) the visualization space of interest, namely the space determined by the dimensions of the nozzle window shown in Fig. 6.2(a), is rather small ( $100 \times 60$  mm).

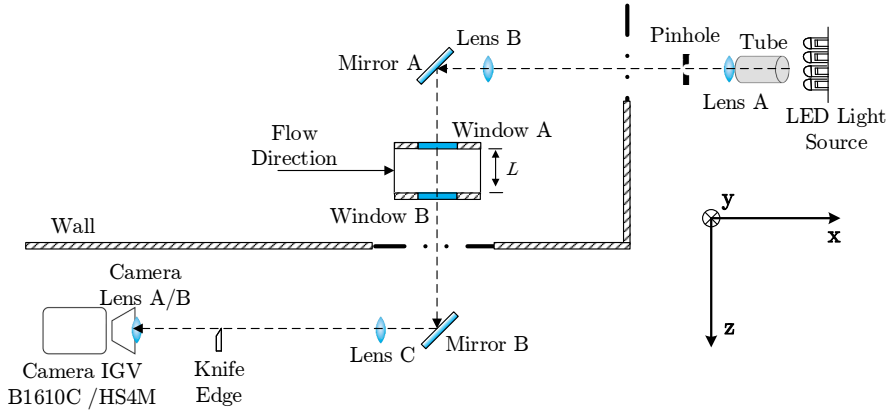


Figure 6.16: Birds-eye schematic view of the schlieren lay-out used for visualising the flow in the ORCHID nozzle test section: a simple lens-type setup with two flat mirrors.

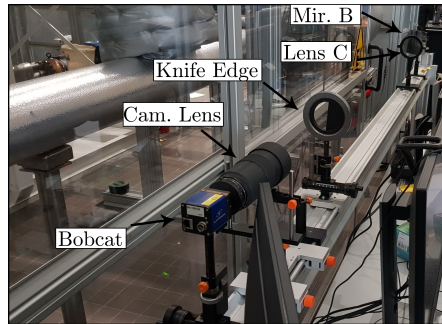


Figure 6.17: Photograph of part of the optical configuration of the z-type schlieren measurement chain. The camera, knife-edge, lens C and mirror B are shown outside the ventilation cabinet mounted behind the operator desk. Mirror A and Lens B are located inside the ventilation cabinet. The pinhole, Lens A, tube and LED source are also located outside the ventilation cabinet close to the door (not shown in this figure but is shown on the right-hand side of Fig. 6.16).

## LIGHT SOURCE

The LED illumination source (Fig. 6.16) is located outside the ventilation hood. A *cold white* mounted LED from *Thorlabs* (Model: MCWHLP1) with driver (Model: LEDD1B) provides continuous uncollimated light with a typical output power of 2350 mW if driven at a current of 700 mA. In all experimental runs the continuous light source was used at the maximum possible intensity. This ensured that measurements could be taken at the highest possible acquisition rates and shutter speeds, if necessary.

A tube is placed around the light source and the condensing lens which has a focal length of 150 mm, see lens A in Fig. 6.16. The light from the LED source is then focused onto the pinhole. The maximum pinhole aperture was limited to 2 mm, however, it is possible to switch to smaller diameters, e.g., minimum of 0.2 mm if a higher degree of sensitivity to density gradients is necessary. The hardware is grouped on the same beam structure and is located outside the ventilation hood, see top right of Fig. 6.17.

## PRIMARY LENSES AND MIRRORS

The light beam from the pin hole, which is placed at the focal point and thus collimated by the Achromatic<sup>5</sup> lens B (116 mm diameter,  $f = 1524.7$  mm), is redirected through the nozzle test section by mirror A. Mirrors A/B are flat with a surface accuracy of  $4 - 6 \lambda$  with enhanced aluminum coating. The dimensions of both flat mirrors are  $127 \times 178$  ( $L \times H$ ) mm and are based on the minimum dimensions of the nozzle and part of the testing channel. These two flat mirrors are used to finely adjust the direction of the light beam towards lens C, which is identical to lens B. A beam structure within the ventilation hood and next to the nozzle test section supports lens B and mirror A.

The light from lens C is refocused to form an inverted image of the source at the knife-edge. The inverted image is then projected onto the charge-coupled device (CCD) sensor of the digital camera by means of an independent standing lens or a Nikon camera lens. Figure 6.17 shows the third (and biggest) beam structure which supports Mirror B and Lens C together with the camera system.

## CAMERA

A high-frequency-acquisition camera with on-board image memory storage was used to assess the start-up phase of the experiment and the steadiness of the flow. A camera with a lower image acquisition rate was used to record steady flow images on an external hard drive for a much longer time in order to achieve meaningful statistics.

The high-speed camera is a *LaVision Imager Pro HS4M*, with a maximum resolution of  $2016 \times 2016$  pixels delivering a maximum frame rate of up to 1279 frames per second. The pixel size is  $11 \times 11 \mu\text{m}$  and it has a shutter speed/exposure time ranging between  $1.5 \mu\text{s}$  and 40 ms. The camera used for steady-flow schlieren images is a *BOBCAT IGV-B1610* equipped with a single 16-bit CCD. Its image resolution is  $1628 \times 1236$  pixels delivering a maximum frame rate of up to 25 frames per second. The pixel size is  $4.4 \mu\text{m}$  and it has a shutter speed/exposure time ranging between  $5 \mu\text{s}$  and 59 ms. Two different Nikon camera lenses (A and B) were used to capture the sections of flow field of interest. Lens A has a focal length of 105 mm and lens B has a focal length of 180 mm. The focal

<sup>5</sup>Optical properties are more or less independent of the wavelength of the light and thus the chromatic aberration effect is minimized.

Table 6.5: Characteristics of the imaging system.

Variable	HS4M	IGV-B1610C (Bobcat)
Maximum		
Resolution / pixel	2016 × 2016	1628 × 1236
Pixel Size, $\Delta_{\text{pix}} / \mu\text{m}$	11 × 11	4.4 × 4.4
Frame Rate / fps, Hz	1279 (2240 <sup>+</sup> )	25 <sup>*</sup>
Shutter Speed	1.5/1,000,000 to	1/200,000 to
(Exposure Time) / s	4/100	1/17

<sup>+</sup> Overclocked at full resolution.

<sup>\*</sup> At full resolution.

length of lens B was increased with a *lens doubler* <sup>6</sup> which allowed to target smaller regions of the flow field. The camera is supported on the beam structure, see Fig. 6.17, or by a tripod. All the image data are transferred via a CAT-5 cable to a PC solely dedicated to image acquisition and processing.

## 6.7. EXPERIMENTAL PROCEDURE

The ORCHID processes must first be gradually started as described in Sec. 5.6 and the target operating conditions of the nozzle achieved. Once the operating conditions have stabilized around the values of total inlet pressure and temperature chosen for the experiment, a settling period of approximately one hour has to pass by before redirecting hot dense vapor to the nozzle test section. Provided that the test section was insulated and preheated the night before to sufficiently high temperature (say 180 °C for NICFD experiments with MM), around twenty minutes are required to stabilize the temperature before an experimental campaign can be conducted.

The experimental procedures to record flow images using the schlieren technique and to acquire pressure field data are described separately, but they may be conducted simultaneously. However, operating the Scanivalve, which still requires some manual handling, while in the dark to perform schlieren imaging is challenging. Therefore, first measuring the pressures and then acquiring flow images might be preferable, if highly stable flow is observed. Provisions like covering the schlieren setup with screens will be implemented in the near future to facilitate the synchronous measurements of the pressure and Mach fields.

### 6.7.1. PRESSURE FIELD MEASUREMENTS

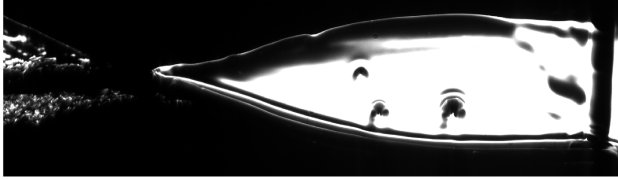
Pressure field measurements are to be carried out first, because they are directly connected with operating the nozzle in the wanted gas dynamic and thermodynamic conditions. These measurements must be complemented by experimental data on the inlet and outlet nozzle temperatures and on the mass flow rate.

Preliminary flow observations with the schlieren measurement chain allow to verify if supersonic conditions have been reached in the nozzle and if the fluid is a dry vapor, before pressure measurements are carried out. The nozzle must be sufficiently pre-warmed in order to prevent excessive condensation during the initial stages of the

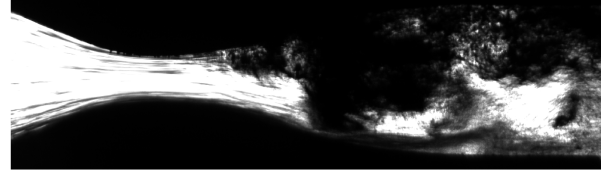
<sup>6</sup> A 2x teleconverter increases the apparent focal length of a lens by two.

opening of the inlet and outlet control valves (MOV002a and PCV003 in Fig. 5.2). Furthermore, due to the inability of gate-valves to perfectly seal against the flow direction, liquid tends to reside in the receiver during the ORCHID start-up sequence and fluid condensate forms on the windows of the nozzle test section during the opening of the valves, thus the nozzle must be operated for some time to allow all the liquid to evaporate. Figure 6.18 shows a typical nozzle starting process.

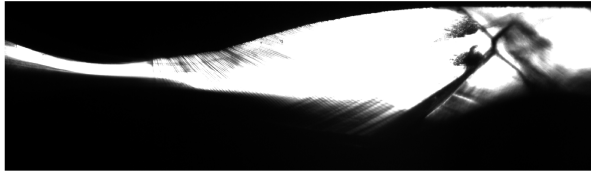




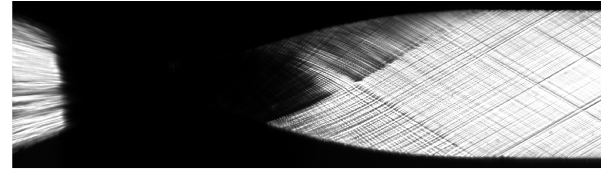
(a) Before nozzle startup, no-flow condition. Due to large liquid spots, or other inhomogeneity, images like this cannot be used for calibration.



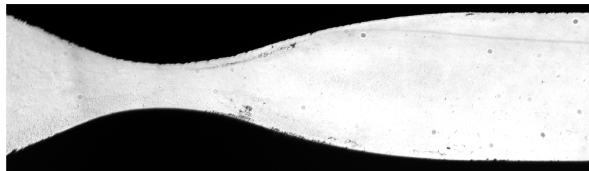
(b) Fluid condensation during the nozzle startup, immediately before the nozzle inlet valve is opened. A turbulent fluid/vapor mixture is transported downstream, as a result of the temperature difference between the core vapor flow and the pipe at the outlet of the nozzle.



(c) Propagation of an oblique shock train towards the nozzle exit. The flow is asymmetric, owing to the shock-fluid interaction at the bottom half of the nozzle.



(d) Underexpanded fully supersonic flow of dry vapor.



(e) No-flow condition, right after an experimental campaign has ended. This type of image is used for calibration.

Figure 6.18: Nozzle starting process (and no-flow conditions) visualized with the schlieren measurement chain in experiment PR.024-NT.001 (Date: 24-04-2019). The fluid is siloxane MM with total conditions  $TT015 = 252\text{ }^{\circ}\text{C}$ ,  $P_{SV001} = 18.0\text{ bara}$ , a back pressure of  $PT004 = 1.5\text{ bara}$ , and flow rate  $FT001 = 4170\text{ kg/h}$ . The *LaVision High Speed HS4M* camera was used to image the flow. The knife-edge orientation is vertical, frame rate is 150 fps at an exposure time of  $900 \times 10^{-6}\text{ s}$ . The cropped resolution is  $2016 \times 616$ . Pinhole dimensions are  $\varnothing\ 0.2\text{ mm}$ .

Appendix C.3 describes the detailed procedure to operate the Scanivalve. The scanivalve system is configured differently depending from the locations where the pressures are to be measured, see Sec. 6.4. First, the symmetry of the flow about the mid horizontal plane must be verified and the specific three-way valve configuration is described in Sec. C.3.5. Flow field uniformity is essential to reducing Type A uncertainties. Afterwards, the pressure along the nozzle can be recorded, by appropriately setting the related scanivalve configuration.

A general outline of the pressure measurement procedure is as follows:

1. The DSA3218 pressure scanner is pre-warmed one hour before measuring in order to ensure the module becomes thermally stabilized;
2. Given that the tubes leading to the ports are initially filled with liquid, these lines are purged with  $N_2$ , see Sec. C.3.2 for more details. Liquid purging ensures that the measuring ports are not blocked by, e.g., dust, metal filaments, tracer particles, and minimises the risk of damaging the transducers while measuring. Additionally, the presence of condensate in the lines is unwanted since it does not allow to correctly measure the flow pressure;
3. Vapor is then redirected over the nozzle until the wanted process conditions are reached. The operator must wait a further twenty minutes so that temperatures inside the nozzle become sufficiently constant. This pause is particularly important in case of a first start from cold conditions;
4. The pressure lines are purged again in order to remove any condensate which may have accumulated during the nozzle starting phase, and which is therefore visible through the sight glass of the liquid trap, see Fig. 6.9. The liquid is ejected back into the flow, and this can be checked because the liquid level in the trap must decrease. This procedure normally lasts approximately 10 seconds.
5. A quick-zero adjustment is performed and the recording of pressures can begin immediately. Simultaneous flow visualization can be performed at this stage of the pressure measurements procedure.
6. Periodic purging and zero-offset corrections must be made, depending on the duration of the pressure recording. For example, if the measurement lasts more than 3 minutes condensate starts to form in liquid traps.
7. Once the measurement campaign is over, the DSA3218 pressure scanner is returned to the initial state.

### 6.7.2. FLOW IMAGING FOR MACH FIELD ESTIMATION

A flow imaging campaign is prepared by first correctly tuning/aligning all elements of the optical system and by selecting the proper camera, camera settings and lenses.

Normally, the light source is operated at the maximum possible intensity, so that, together with a small pinhole aperture, the highest degree of sensitivity to the flow density gradients can be obtained. The flat mirrors must also be aligned carefully in order to

ensure that no image blurring occurs due to out-of-plane misalignment, which might arise, for example, because the floor of the lab is not perfectly flat.

Once MOV002a is fully opened and the temperature stabilized, the controller PICA002 is initialized in order to set the back pressure of the nozzle (PT004) to the desired value. After steady conditions are achieved, and no condensation is detected, flow images can be recorded with a suitable camera and the correct configuration of the schlieren equipment.

The steadiness of the flow can be assessed first using the *HS4M camera* with various acquisition frequencies, namely, 25, 60 and 500 Hz. These tests revealed that in this type of steady experiments aimed at quantifying time-invariant quantities of the flow, the lowest image acquisition frequency of 25 Hz is appropriate, and allows to achieve statistical convergence of the measured quantities, given that the flow is sufficiently steady. For steady flow experiments it is therefore advisable to use the *BOBCAT IGV-B1610 camera* at a sampling rate of 25 Hz, even if the image resolution is slightly lower. Using the *HS4M camera* entails a much larger data transfer to the connected computer which poses additional problems, without a meaningful improvement of the measured information.

The field of view acquired by the camera can be adjusted by properly selecting its lenses. The resolution of the camera CCD must also be carefully selected in order to comply with the storage constraint of the connected computer. In case of Mach field measurements, the number of acquired images can be determined based on the value of average and of the variance of the mid-line Mach number value in order to ensure statistical convergence.

A calibration image must be recorded whenever any component of the schlieren system is adjusted. The calibration image is taken at the end of an experimental campaign, after the vapor is redirected over the bypass and there is no flow through the nozzle, see Fig. 6.18(e). The calibration image is used in the image pre-processing stage in order to remove background noise from the image sequence. In addition, this image is used to identify the nozzle walls and thus the location of the throat.

### 6.7.3. ESTIMATION OF THE LOCAL MACH NUMBER

The post-processing procedure and tools used to obtain the local Mach number exploit the relation between the Mach number and the inclination of the Mach lines appearing in the schlieren images, namely

$$M = \frac{1}{\sin \mu}, \quad (6.11)$$

see Ref. [374, Ch. 9] for theoretical aspects.

The geometrical representation of the Mach lines, which allows to compute the angle formed by the line and the axis of the nozzle, is obtained by detecting the edges of the Mach lines within the schlieren image. This is accomplished by identifying the boundaries of the lines by detecting discontinuities in brightness. This procedure is known as *image binarization* and the result is a digital image containing 1's at the location where edges are detected and 0's elsewhere. The original 8-bit grayscale image is therefore converted into a black-and-white image, thus reducing the information related to the 256 level of gray of the original image to the binary information of the processed image.

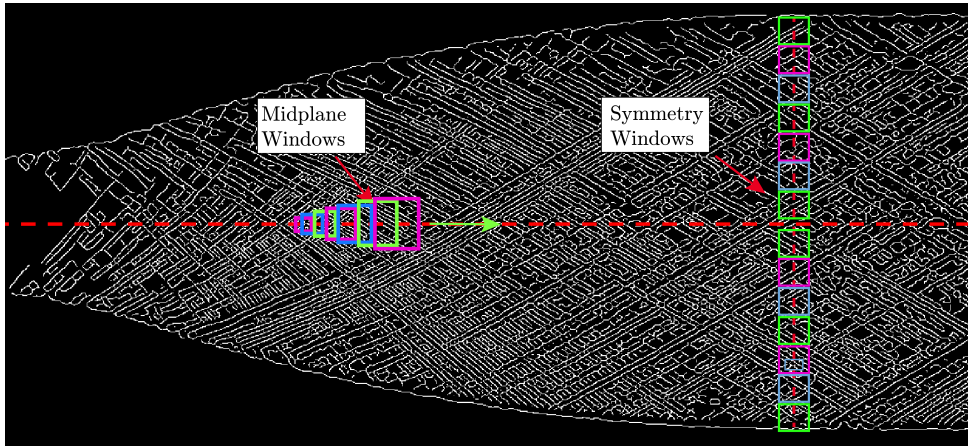


Figure 6.19: A binarised image obtained from a schlieren photograph shot during the NT.001 test. Several so-called *interrogation windows* along the mid- and symmetry planes are highlighted in colors. The windows are used to discretize the flow domain. For clarity, the size of the windows is larger than those used for post-processing.

The method adopted to detect Mach lines within the schlieren image of the supersonic flow consists in the application of two main image processing algorithms as follows:

- first the Canny algorithm is applied to the digital image. It is used to identify the edges in the image based on the computation of the intensity gradients with respect to a given threshold. This results in a binary image formed by black lines of variable thickness over a white background. The accuracy of the Canny algorithm depends on the correct setting of the threshold which is selected based on the uniformity of the image luminosity, see Fig. 6.19. Given that the luminosity of the nozzle-flow schlieren image is not uniform and that the Mach lines become curved in the kernel region, the image of the nozzle field is decomposed into several sub-images centered on the nozzle axis;
- subsequently, the Hough transform [122] is applied to reduce all the variable-thickness lines to lines of constant pixel thickness, by processing all the edges identified by the Canny algorithm in a given sub-window.

Other line detection algorithms can be employed together with the Hough transform to obtain the mathematical representation of Mach lines, however, Beltrame [35] and Maini & Aggarwal [244] recommend the use of the Canny algorithm if the image of the flow field is comprised of a complex pattern of densely packed lines. More in detail, the Hough transform [239] determines for each pixel of the image if a straight line with a specific orientation  $\theta$  and distance from the origin  $r$  may pass through that pixel. The result of this process is a two-dimensional matrix called an *accumulator* which ranks the different lines based on the number of pixels they fit. The number of columns and rows of the matrix is a function of the resolution set by the user to discretize, respectively, the

inclination  $\theta$  and the distance from the origin  $r$  of the lines. The higher the resolution, the larger the matrix. The cell in the matrix with the highest value represents the combination of  $\theta$  and  $r$  which best fits the edges determined by the Canny algorithm, thus identifying a candidate Mach line.

In order to ensure the detection of a Mach line and not a random number of collinear points, only the line with the highest value in the accumulation matrix and with a length above a specified threshold is marked as Mach line. For this reason and the fact that the Mach lines tend to curve as the distance from the nozzle mid-plane increases, the binary image returned by the Canny algorithm is decomposed into several sub-images, also called *interrogation windows*, which are partially overlapping and are centered on the longitudinal axis of the nozzle. Furthermore, the midplane windows' dimensions decrease in size as the lines become more curved, e.g., in the kernel region. The minimum window size is selected such that the line curvature is not detectable in the pixel-discretized domain, namely the maximum line curvature must be lower than the angular resolution. In the considered experiments, this was achieved by specifying a window height to nozzle height ratio equal to 0.15. In each interrogation window, a local and instantaneous value of the  $\mu$  angle is calculated and its corresponding flow Mach number is determined according to the Eqn. 6.11.

Figure 6.19 shows the interrogation windows along the midplane and a series of windows at the exit of the nozzle. For this experiment, the interrogation windows size along the midplane, (rows  $\times$  columns) ranges from  $45 \times 50$  (throat region) to  $60 \times 70$  pixels (nozzle exit). The windows at the exit are equidistantly spaced from the nozzle axis to the walls, and are of equal dimensions ( $60 \times 70$  pixels). To verify the symmetry of the flow, two Mach lines per window are detected, one above and one underneath the midplane. The flow is deemed symmetric if the difference between the average angles of the Mach lines, in those complementary windows, are smaller than the total expanded uncertainty associated with the angle estimation, see Sec. 6.9.5.

The calculation of statistical quantities related to the Mach angles is achieved by processing a multitude of consistent sets of sub-images derived from the many schlieren images recorded over a test run. The minimum number of images needed to ensure that there is enough data to calculate meaningful statistical quantities is calculated with the criteria outlined in [194, App. C]. The statistical significance is achieved by verifying that the mean and standard deviation of the measured quantities remain approximately constant as the sample number increases. For both the NT.001 and NT.002 test runs, the number of images required to obtain the average Mach number satisfying the statistical convergence criteria was approx. 900. Given the acquisition frequency of the camera, i.e. 25 Hz, this corresponds to the analysis of 40 s of flow history. The convergence of the statistical quantities cannot be obtained if the flow is unsteady. Thus, the schlieren images recording is activated only if certain experimental conditions are met, as described in Sec. 6.7. The Mach line angle extraction procedure was implemented in a general-purpose mathematical programming environment [386]. For more details, the reader is referred to [35].

Figure 6.20 shows a schlieren image of the diverging part of the supersonic nozzle obtained during the NT.001 test run, together with segments of the Mach lines computed with the image post-processing procedure. The Mach segments are highlighted in green

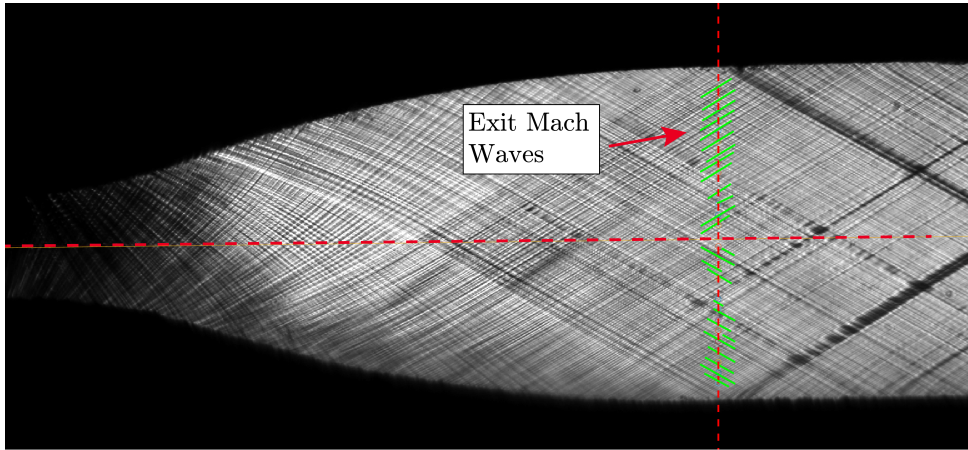


Figure 6.20: A schlieren photograph obtained during the NT.001 test. Mach line segments at a cross section of the nozzle exit region obtained with the image processing procedure are indicated in green. The angle with the nozzle axis is  $\mu = 30.1^\circ$ , therefore the Mach number along the section identified by the dashed red line is  $M = 2$ . The flow is therefore uniform and symmetric with respect to the midplane of the nozzle.

and their angle with respect to the axis of the nozzle is constant, indicating the the flow is uniform over the section of the nozzle represented by the vertical dashed red line. Furthermore, the Mach segments are symmetric with respect to the axis of the nozzle, thus the flow is symmetric with respect to the midplane. The calculated value of the Mach angle is  $\mu = 30.1^\circ$  therefore, upon substitution into Eqn. 6.11, the corresponding Mach number over the cross-flow section is  $M = 2$ .

Figure 6.28 displays another example related to the estimation of the Mach number over relevant locations within the nozzle flow, namely along the axis in the diverging region. Also in this case, the segments of the Mach lines obtained with the image processing procedure are superimposed to the first image of the dataset recorded during the test run. Figure 6.28(a) is related to the diverging portion of the nozzle and to data recorded during the NT.001 test. Thirty-two values of the Mach angle were computed along the midplane. The averaged values of the Mach angles reduce in magnitude as flow expands. Figure 6.28(b) is an example of how higher resolution can be achieved if the field of view is restricted to the portion of nozzle closer to the throat. Data were recorded during the NT.002 test.

## 6.8. OPERATING CONDITIONS OF THE COMMISSIONING EXPERIMENTS

As it was not possible to obtain information regarding the commissioning of the nozzle test section and related measurement system with one single experimental campaign at the specified operating conditions described in Sec. 6.2, two main sets of experiments were conducted, each aimed at a specific commissioning aspects. With reference to Tab. 6.6, the operation of the nozzle and the pressure measurement system were tested

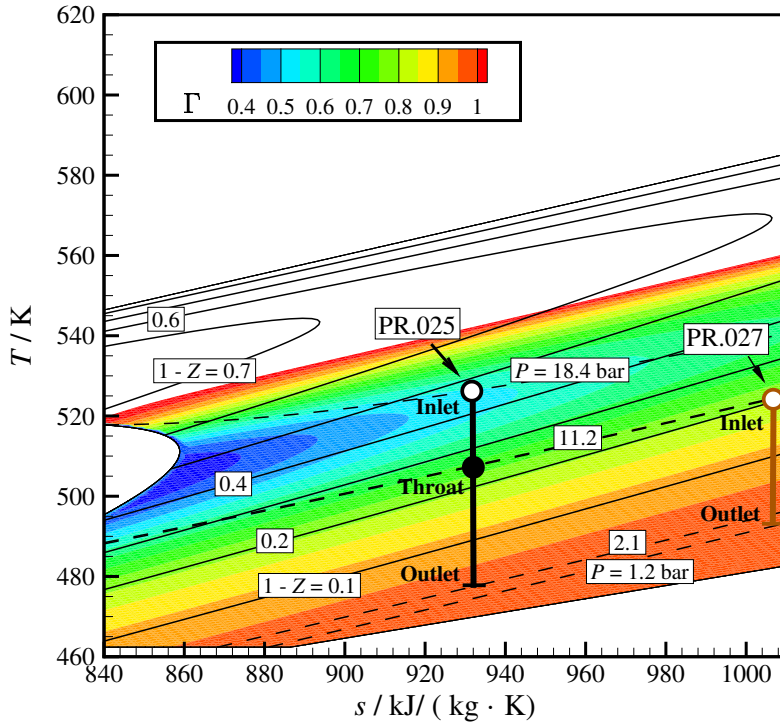


Figure 6.21:  $T-s$  diagram for MM showing contours of the fundamental derivative  $\Gamma$ , the complement of the compressibility factor  $Z$  (—), and isobars (---). The two isentropic expansions correspond to experiments PR.025-NT.001 ( $P_0 = 18.4$  bara) (see Fig. 6.5 for the corresponding nozzle design.) and PR.027-NT.001 ( $P_0 = 11.2$  bara). All values are calculated with an in-house program for fluid properties estimation [93], and using the thermodynamic model documented in Ref. [231].

during process run PR.027, while the commissioning of the schlieren system was performed during process run PR.025. Data related to the nozzle operating conditions for these two experiments are reported in Tab. 6.6 and Fig. 6.21 displays the thermodynamic states identifying the related expansion processes.

### 6.8.1. PRESSURE FIELD: PROCESS RUN PR.027

This experimental campaign was composed of two tests, named NT.001 & NT.002. The second test was conducted to ensure the experiment could be reproduced. Furthermore, the experiment was run twice to understand the response times during purging and the times elapsed to reach steady state. These tests were executed at a lower pressure ratio than that of the nozzle design pressure ratio because of concerns related to proper functioning of sealing and instrumentation. Once correct operation is verified at lower pressure, design conditions can be set with lower risk of failure. A secondary objective of these experiments was also determining the amount of time needed to reach steady



Table 6.6: Summary of the parameters defining the operating conditions of the commissioning experiments.

Exp. Run	Purpose	Date	Tot. temp. TT015 / °C	Evap. press. PZA003 / bara	Tot. press. $P_{SV001}$ / bara	Back press. PT004 / bara	M. flow FT001 / kg/h
PR.025- NT.001&2	schlieren	25-04 2019	252	19.1	18.4 <sup>+</sup>	2.1	4400
PR.027- NT.001&2	p. meas.	13-05 2019	252	11.9	11.2	0.9	2920

<sup>+</sup> The total pressure  $P_0$  is calculated by subtracting from the value of PZA003 the pressure drop across the pipe lines leading up to the nozzle test section and the devices inserted into the settling chamber, which was estimated in previous trial experiments, because the Scanivalve pressure scanner was not activated for this experiment.

operating conditions, and establishing a procedure for the purging of the liquid traps of the pressure lines (duration and frequency).

The evaporation pressure (PZA003) was 11.9 bara, the evaporation temperature (TT005) was 252 °C, the mass flow rate of MM 2920 kg/h (0.81 kg/s). The total conditions in the settling chamber were  $P_0 = 11.2$  bara and  $T_0 = 252$  °C, corresponding to a reduced pressure  $P_r = 0.57$ , and to a reduced temperature  $T_r = 1.02$ . The measured back pressure was  $P_b = 0.9$  bara and it was set to obtain approximately the same expansion ratio as in the other commissioning experiments.

## 6.8.2. SCHLIEREN: PROCESS RUN PR.025

Also this experimental campaign was made of two experiments, NT.001 & 2, for repeatability and in order to test the possibility of achieving higher spatial resolution in the flow area where non ideal effects are more prominent, close to the nozzle throat. The operating conditions were those that were designed, see Sec. 6.8. The total pressure at the inlet was not directly available because it is measured by the Scanivalve, which could not be utilized at the time of these experiments because it was not yet commissioned. Therefore, the total pressure at the inlet of the nozzle test section was calculated by subtracting the pressure drop  $\Delta P$  over the MOV002a valve, the pipe line and the settling chamber from the measured evaporation pressure. The estimation of pressure drop,  $\Delta P = 0.7$  bar, was obtained during previous trial process runs. As the measured evaporation pressure was  $P = 19.1$  bara, the estimated pressure at the inlet of the nozzle was therefore  $P_0 = 18.4$  bara. The total temperature was  $T_0 = 252$  °C. In terms of reduced variables, pressure and temperature were  $P_r = 0.95$  and  $T_r = 1.02$ . The back pressure was  $P_b = 2.1$  bara.

## 6.9. RESULTS

### 6.9.1. PRESSURE FIELD, PR.027

Condensate had formed in the pressure lines during previous operation of the setup, due to the difference between the temperature of the equipment of the balance of plant and that of the nozzle test section. All sixteen of the measurement taps were carefully purged and visually checked during the process. In addition, schlieren visualization was performed on jets of liquid expelled by the nitrogen flow before the setup was started,



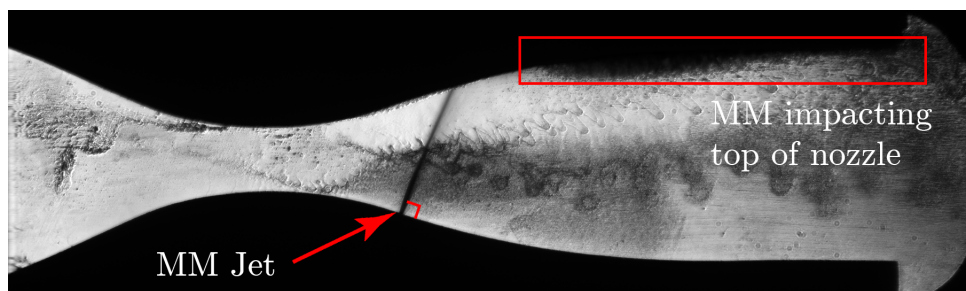


Figure 6.22: Schlieren image of the purging of liquid MM through one of the pressure taps by means of pressurized  $N_2$ , before the starting of the setup. Flow in the nozzle is therefore at rest. As expected, the orifice is perpendicular to the nozzle surface, to the qualitative degree that is possible to ascertain with this method.

in order to verify that the axis of the pressure taps is perpendicular to the nozzle profile surface, see Fig. 6.22.

Figure 6.23a shows the recording of several relevant process variables over the period of time in which the process run was conducted, thus encompassing both the nozzle tests NT.001 and NT.002. The process run lasted approximately two and half hours. The periods in which dense MM vapor was flowing through the nozzle can be deduced by the opening of the two valves MOV002a and PCV003 (the valves were completely open between time 11:46:00 and 12:16:00 and between 13:34:00 and 13:46:00). The intervals are displayed with more resolution in Fig. 6.24. NT.001 took place at time 12:02:30, for six minutes, while NT.002 at 13:40:37, until 13:43:04 for two minutes and 27 seconds. Pressures along the nozzle profile were recorded with a frequency of 25 Hz.

The nozzle test runs were conducted when the values of the evaporation pressure (PZA003), the total inlet pressure  $P_{SV001}$ , temperature (TT015) and mass flow (FT001) were sufficiently steady. A settling period of twenty minutes was sufficient to reach an indicated fluctuation ( $2\sigma$ ) around the average value of less than a  $\pm 0.43^\circ\text{C}$  for temperature TT014, a fluctuation of  $\pm 0.0051$  bar for pressure PT004 and fluctuation of  $\pm 2.52$  kg/h for mass flow rate FT001, see Tab. 6.11. The reference periods used to calculate the means and standard deviations were selected based on the analysis reported in App. D. Both the fluctuations of temperatures and pressures at the inlet and outlet of the nozzle satisfied the steady state criteria defined by Woodland *et al.* [409]. After steady flow conditions were obtained, the pressure lines were purged, and this is indicated by the spike in the PT004 line reported in Fig. 6.24, at the time just preceding the start of the nozzle test NT.001 and NT.002 highlighted in the chart.

The steady state condition was not met for NT.002, thus the statistical quantities related to the pressure measurements along the nozzle were calculated only for NT.001. The experiment NT.002 is shorter because 1. small leakages started to form around the nozzle window owing to a gasket failure, and 2. at the time of the experiment it was unknown how long a test campaign should be run in order to generate a sufficient amount of data to obtain statistically relevant quantities.

Figure 6.25 shows the recording of the sixteen pressure values along the nozzle profile over the period in which NT.001 and NT.002 took place. The exact tap location can

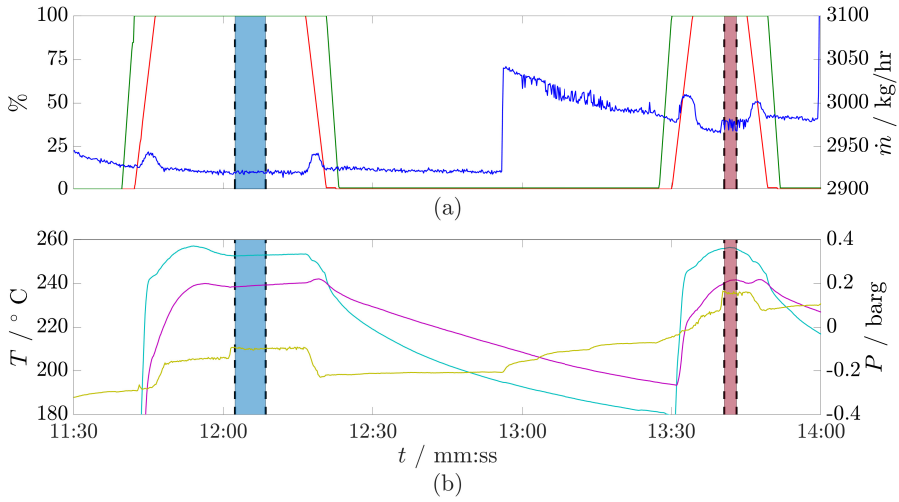


Figure 6.23: Recording of relevant process variables for the nozzle test NT.001 (■) and NT.002 (■) pressure experiments occurred during process run PR.027. The periods of the two experiments are highlighted with shaded color areas. **(a)** The percentage aperture (position) of the nozzle inlet valve MOV002a (—) and of the primary control valve PCV003 (—) can be read on the left axis. The value of the MM mass flow rate FT001 (—) can be read on the right axis. **(b)** The values of the total inlet temperature TT015 (—) and of the receiver temperature TT014 (—) can be read on the left axis, while the receiver pressure PT004 (—) can be read on right axis.

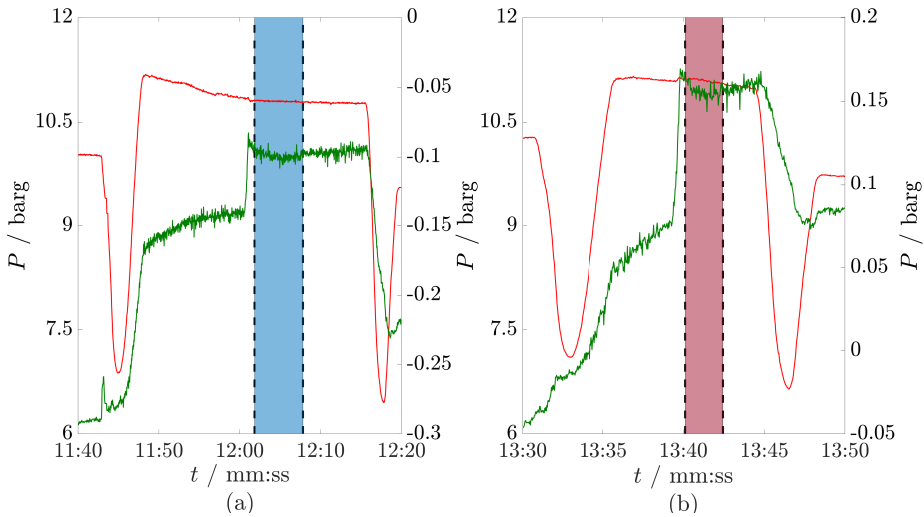


Figure 6.24: Enlargement of Figure 6.23. Nozzle TS time series pressure data for test run PR.027-NT.001&2 where the colored areas, NT.001 (■) and NT.002 (■), show the period where the Scanivalve measurements were acquired. Evaporation pressure PZA003 (—) on the left axis and receiver/ nozzle back pressure PT004 (—) on the right axis: **(a)** First opening of the nozzle NT.001 **(b)** Second opening of the nozzle NT.002.

be determined by cross-referencing Tab. 6.2 and Fig. 6.8. Figure 6.25 shows that the pressure signals are affected by a different time response, resulting from different tube lengths; the longest transient is that related to  $P_{SV005}$  and lasts approx. 1 min and 50 seconds. The reference period used to calculate the means and standard deviations of the static pressure field were selected based on the analysis reported in App. D. The convergence of the statistical quantities obtained from the experimental results has to satisfy the criteria discussed in [194, App. C]. This is achieved by verifying that the mean and standard deviations of the measured quantities remain approximately constant as the sample number increases. Figures 6.24 and 6.25 show that in experiment NT.001 the nozzle operating conditions and the pressure field along the surface of the nozzle is steady after time 03:04 for a period of approximately 3 minutes and 4 seconds. The statistical quantities are summarized in Tab. 6.11. These conditions are deemed sufficiently steady for the envisaged experiments.

Figure 6.26 shows the recordings of the measured pressures, nondimensionalized with respect to the nozzle inlet pressure, versus the position along the nozzle, nondimensionalized with respect to the nozzle throat height. The plot also reports the results of the RANS CFD simulation of the expansion, and is discussed in detail in Sec. 6.9.3. The measurements uncertainty estimation is described in Sec. 6.9.4 and 6.9.5. The final average values in experiment NT.001 were  $\bar{P}_0$  ( $\bar{P}_{SV001}$ ) = 11.22 bara,  $\bar{T}_0$  (TT015) = 252.87 °C, TT014 = 239 °C, and  $\bar{P}_b$  (PT004) = 0.901 bara. The remaining means of the reported data are listed in Tab. 6.11.

The symmetric pressure taps at the inlet (T001 and T002) and at the throat (T006 and T007), measured the same average values, see Fig. 6.26. However, symmetric tap pair at the outlet measured different average pressure values, namely  $\bar{P}_{SV016}$  = 2.33 bar and  $\bar{P}_{SV015}$  = 1.09 bar. The difference of 1.24 bar is likely owed to liquid MM which was not completely purged from that pressure line. The line leading up to the scanivalve port  $P_{SV016}$  is longer than the other lines and is located on the bottom of the nozzle profile. This line is therefore the lowest location of the entire pressure measurement system and thus it is where the condensate can accumulate more easily. It can be concluded that a longer purging time is necessary to completely remove the liquid.

### 6.9.2. MACH FIELD, PR.025

The two tests that were carried out during this process run were devoted to the validation of the procedure devised in order to estimate the spatial distribution of the Mach number over the nozzle flow field using schlieren images. The operating conditions for this experiment are reported in Tab. 6.6 and App. B provides details on the nozzle geometry, see nozzle B.

The BobCat IGV-B1610 camera was used, mounted at the end of the beam structure shown in Fig. 6.17, with a Nikon lens (focal length = 105 mm) for the NT.001 test, and with a Nikon lens (focal length = 180 mm) together with lens doubler for the NT.002 test, in order to obtain a higher resolution, but limited to the nozzle throat region. This camera features a CCD chip of  $1624 \times 1236$  pixels. The raw images were recorded in 8-bit grayscale (256 different intensities, i.e., shades of gray) tiff format.

For the NT.001 experiment, the images were cropped in the wall-normal direction to  $1386 \times 644$  pixels, while for the NT.002 experiment to  $1624 \times 800$  pixels. The schlieren

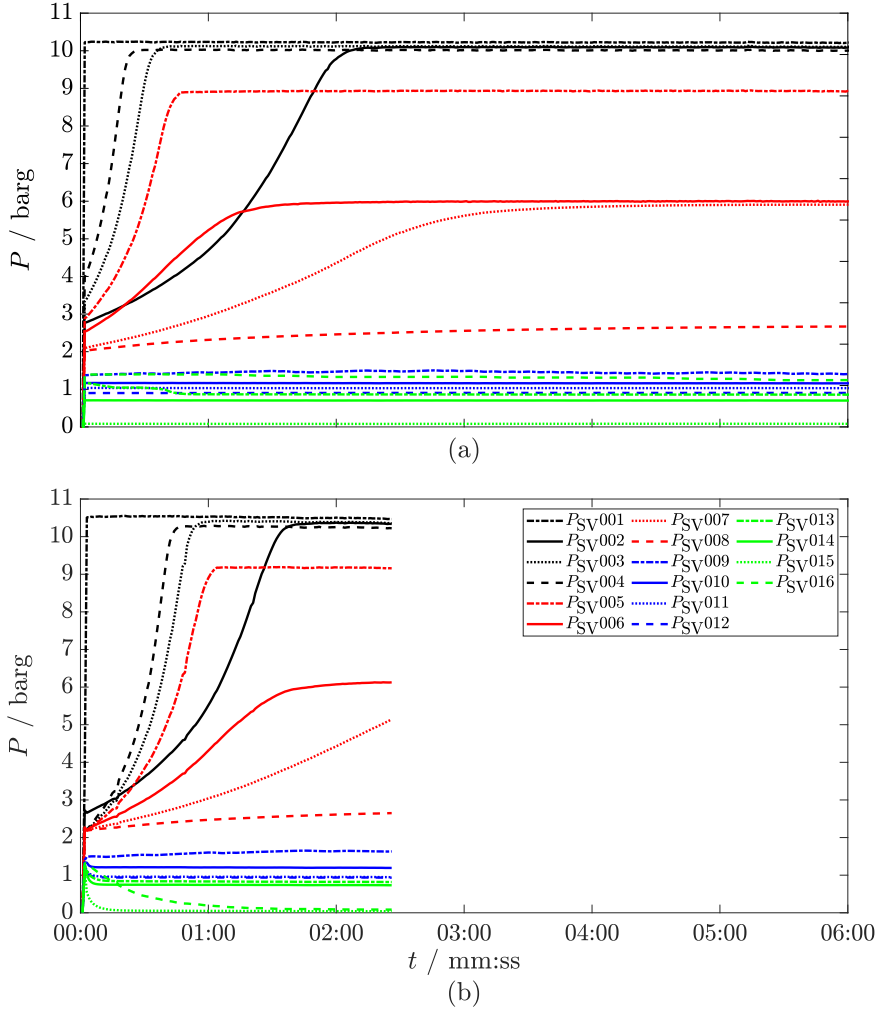


Figure 6.25: Recording of pressure values along the nozzle during the commissioning tests: **(a)** NT.001 process run. **(b)** NT.002 process run. The *Scanivalve* port numbers are listed in Tab. 6.2. Each port is equipped with its own pressure transducer.

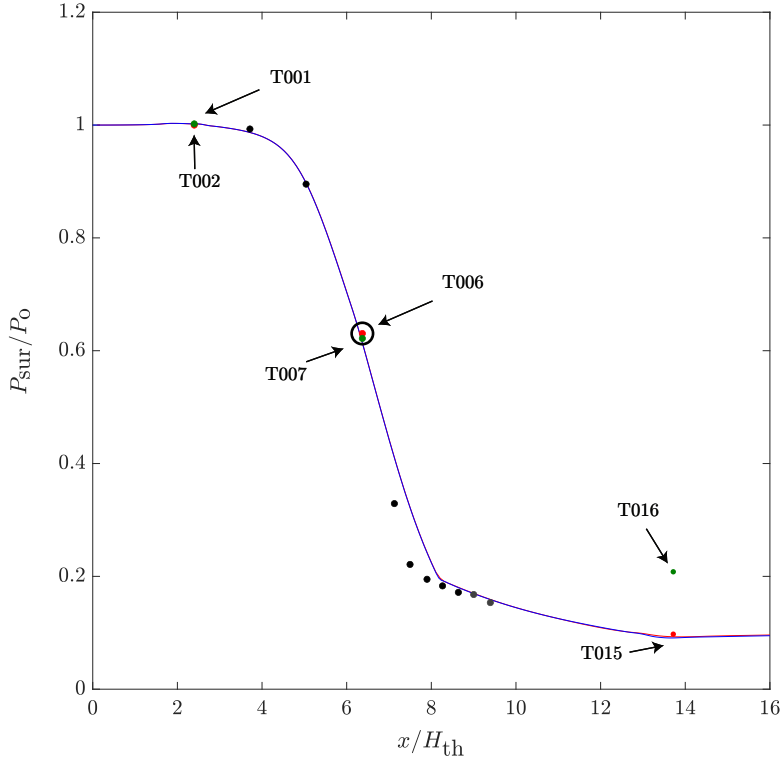


Figure 6.26: Values of the average static pressure  $P_{\text{sur}}$  along the nozzle surface measured during the PR.027-NT.001 test (■). The horizontal coordinate is the distance from the nozzle inlet and is nondimensionalized with the throat height,  $H_{\text{th}} = 6.66$  mm. The average static pressure values are nondimensionalized with the value of the total pressure at the inlet of the nozzle  $P_0 = 11.2$  bar. The evaluation of the indicated expanded uncertainty is described in Sec. 6.9.3. (—) RANS and (—) EULER simulation of the expansion (details on the calculation in Sec. 6.9.3). The black empty circle indicates the nozzle throat position. The pressures measured at taps (T001, T002, T006, T007, T015, T016) are located in the same axial position and those are indicated by the solid colored red and green circles. The axial location of the taps can be determined with Tab. 6.2.

images were acquired during time intervals in which the flow conditions match the stability criteria described in defined in Sec. D.1. For both tests (NT.001/2) the final average values of the boundary conditions were  $P_0 = 18.36$  bar,  $T_0 = 252.2$  °C,  $TT014 = 242.2$  °C, and  $P_b = 2.06$  bar. During the NT.001 and NT.002 tests, approximately 2,000 images were recorded a rate of 25 Hz, therefore for approximately 1 minute and 20 seconds. The number of images was sufficient in both cases to estimate the Mach number along the midplane. For both NT.001 and NT.002 the Mach number was determined according to the procedure reported later in this section. After the image acquisition phase, the valves MOV002a and PCV003 were closed and a calibration image taken. The information related to the camera settings in summarized in Tab. 6.7.

Figure 6.27 shows three exemplary schlieren images taken during experiments the NT.001 and NT.002 test runs. Figure 6.27(a) displays the NT.001 calibration image, namely,

Table 6.7: Summary of the *BOBCAT IGV-B1610* camera settings for the experiments.

Test	NT.001	NT.002
Field of View	Diverging section	Nozzle Kernel Region
Frame rate / fps	24.75	24.75
Exposure time / s	Determined by (frame) rate. = $1/24.75^+$	Determined by (frame) rate. = $1/24.75^+$
Cropped Resolution / px $\times$ px	1386 $\times$ 644	1624 $\times$ 800

<sup>+</sup> The maximum limit. The camera automatically selects the exposure time from the frame rate with 1/fps (internal camera register controlled). The exposure time resides in the interval specified in Tab. 6.5.

the photograph of entire diverging section of the nozzle once there was no more flow through the nozzle after completion of the experiment. Figure 6.27(b) shows an image of the MM dense vapor flow field at the prescribed operating conditions, see Tab. 6.9. Experiment NT.002 was conducted with a field of view limited to the kernel region of the nozzle which is shown in Fig. 6.27(c).

In both Figure 6.27(b) and Fig. 6.27(c), Mach lines originating from the roughness and grooves along the profile surface are clearly visible. At these conditions, it is difficult to obtain a high level of resolution in the throat region, which therefore appears more uniformly darker. As already documented in Ref. [95], this is due to large density change of the fluid over this region, caused by the large compressibility of the flow, which in turn causes light deviation to exceed the schlieren system measuring range.

The darkening of the image can be explained from the schlieren principle (see Sec. 6.6 and, in particular, Eqn. 6.6). It is known that the visualization of horizontal density gradients results in darker shades if the density increases (compression and shock waves), and in lighter shades if the density decreases (expansion and fans) [353]. In this case, the darker regions at the throat are due to a rapid decrease in density. This causes the light rays to deflect to such an extent that the source image completely departs from the knife-edge. Towards the exit of the nozzle the derivative of density with respect to the spatial coordinate  $x$  decreases and thus so does the change in image contrast. This results in data which can be measured by the adopted schlieren configuration.

Several steps are required before the images can be processed with the line detection algorithms to estimate the local Mach number. First, the commercial image processing software supplied with the high-speed camera system (LaVision Davis software version 8.3.0 [229]) was used to align every image of the sequence with the first recorded schlieren image in order to compensate for the shift and rotation caused by vibrations in the test section. Then, the image background noise, e.g., artefacts such as spots on the camera CCD chip or on the window pane of the nozzle test section were removed from each image forming the entire dataset. This was accomplished by subtracting the calibration image from each image in the dataset [353].<sup>7</sup> Finally, image properties such

<sup>7</sup> Each image comprises a matrix of data about the brightness/intensity value of each pixel. Image subtraction is a process in which the intensity value associated with each pixel of an image is subtracted from the intensity value of the corresponding pixel of another image.

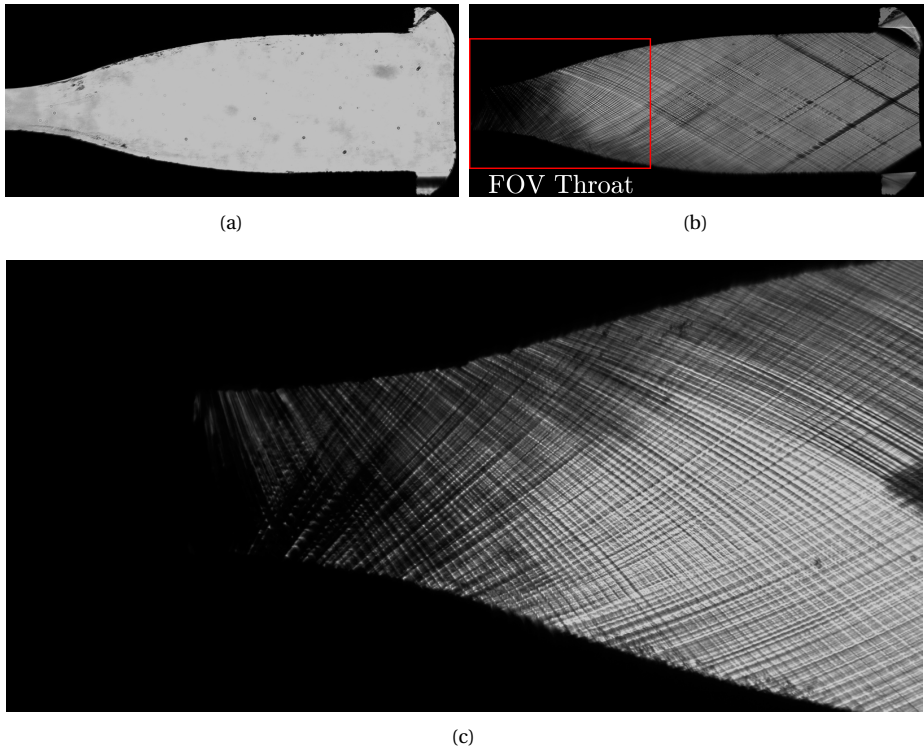


Figure 6.27: Exemplary schlieren images of the supersonic flow of dense MM vapor expanding through the ORCHID nozzle taken during the PR.025 process run. **(a)** Calibration image taken after the NT.001 test. **(b)** Image of the diverging section taken during the NT.001 test. **(c)** Image of the throat region (boxed in red in b) taken during the NT.002 test.

as contrast were optimised before the further image processing aimed at the detection of the Mach lines.

Figure 6.29 shows the plot of the Mach numbers (computed from measured Mach angles) versus the position along the nozzle nondimensionalized with the throat height related to the NT.001 experiment. The plot also reports the results of the CFD simulations of the expansion, which are discussed in detail in Sec. 6.9.3. The measurements uncertainty estimation is described in Sec. 6.9.5. The means and total expanded uncertainties of the reported data are listed in Tab. 6.12.

### 6.9.3. SIMULATIONS

The validation of the commissioning experiments consists of the quantitative evaluation of the measurement uncertainty and of a comparison with the results of CFD simulations.

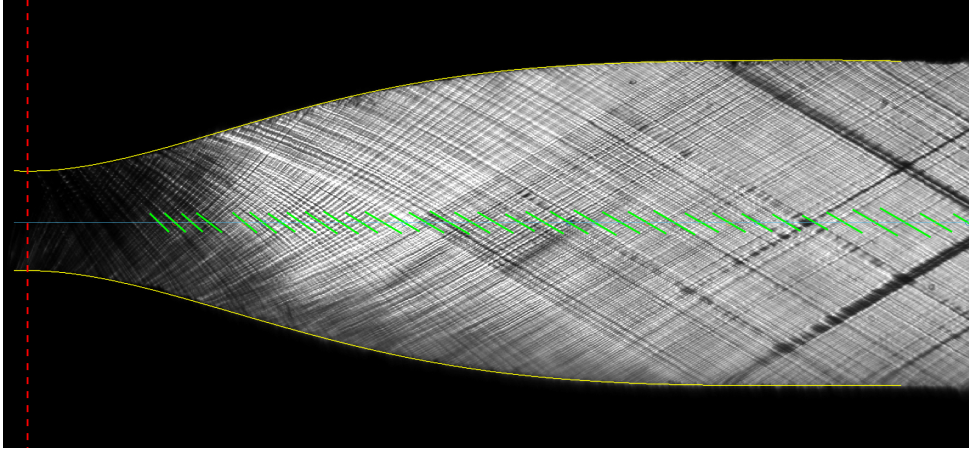
#### METHOD

Steady-flow two-dimensional Reynolds averaged Navier-Stokes (RANS) simulations of the supersonic expansions of dense MM vapor were carried out with the open source SU2 flow solver [132]. The code is also capable of modeling compressible flows affected by NICFD effects [390, 391]. In addition, two-dimensional Euler simulations were carried out to confirm that the difference in the simulation results is very small. The thermo-physical properties of MM were computed by coupling SU2 with a in-house thermo-physical property library [93]. In particular, thermodynamic property values were calculated using the model based on the iPRSV cubic equation of state [368], while the transport property model is the one of Chung [73]. Turbulence effects have been modeled with the Shear-Stress Transport (SST) closure [256].

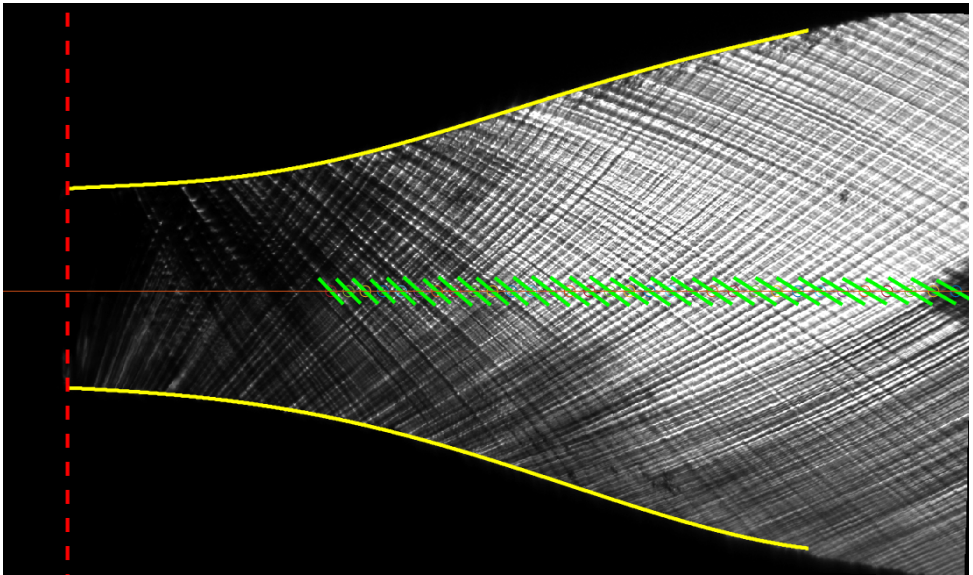
The computational domain, half of the nozzle with symmetry conditions along the mid plane, was meshed with an unstructured grid of tetrahedrons. The throat height considered to design the nozzle with the method of characteristics was 7.5 mm. The value set for the simulated geometry was measured and was 6.7 mm. The difference between the two values is due to the compression of the gaskets of the nozzle housing. As an effect of the translation of the nozzle profiles, the nozzle inlet height is 23.1 mm, and the nozzle outlet height 20.7 mm. The mesh cells have been clustered such that  $y^+ < 1$  along the nozzle walls.

The procedures outlined in Ref. [10] were followed to ensure grid independence, thus to minimise the related numerical error. In particular, a grid convergence study based on the methods presented in Refs. [25, 70] was performed. Variables that are key to the objective of the simulation study, i.e., static pressure and Mach number, were used for the assessment. An unstructured mesh of 10,000 core elements was sufficient to obtain results unaffected by grid size. The Euler implicit time marching scheme was adopted for smooth convergence, and the CFL number was set to 20.0. The convective fluxes are discretized using a Roe scheme [332] with the Venkatakrishnan limiter [387]. The computation was initialized with the free-stream conditions and solved using a weighted least squares numerical method for spatial gradients. The residuals for the Euler simulations were converged to machine-level accuracy, while for the viscous simulations the residuals were reduced by six orders of magnitude. The CFD simulations were performed with





(a)



(b)

Figure 6.28: In green, Mach line segments identified with the post-processing algorithm, superimposed to the first schlieren image. The nozzle domain has been discretized along the  $x$  axis with 32 windows. Each window is populated by a Mach line. **(a)** schlieren photograph obtained during the NT.001 test. **(b)** schlieren photograph obtained during the NT.002 test. The field of view is smaller, therefore the resolution of the image is higher if compared to that of **(a)**.

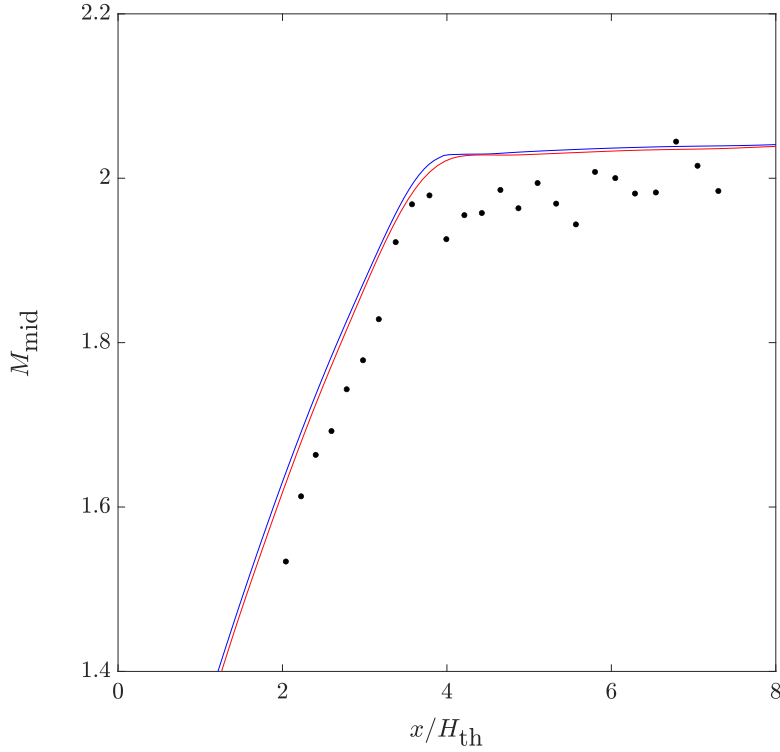


Figure 6.29: Experimentally derived Mach numbers along the midplane (•) from the nozzle throat to the outlet vs values obtained with CFD simulations (— RANS, — Euler) (details on the calculation in Sec. 6.9.3). The position along the midplane is given as distance from throat nondimensionalized with the throat height,  $H_{th} = 6.66$  mm. Values refer to the PR.025-NT.001 test run. The throat is the reference point and the first measurement starts at  $mid(x)/H_{th} = 1.94$  ( $M_{avg} = 1.53$ ) and ends at 7.2 ( $M_{avg} = 1.98$ ). The domain has been discretised into 25 windows.

Table 6.8: Boundary conditions of the simulation of the PR.027-NT.001 test run. Taken from the average experimental values resulting from the analysis in Sec. 6.9.1.

Total inlet pressure, PV002 / bara	11.2
Total inlet temperature, TT015 / °C	252.2
Static outlet pressure, PT004 / bara	0.9

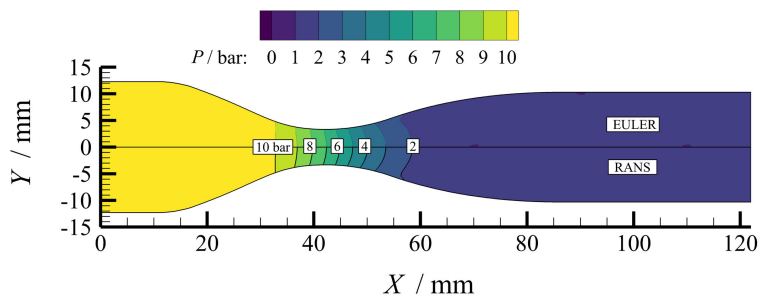


Figure 6.30: Pressure contours along the supersonic nozzle calculated with the SU2 code using the operating conditions of the PR.027-NT.001 experimental run as boundary conditions, see Tab. 6.8. The upper side of the figure displays results calculated by solving the RANS equations, while the lower side displays the results of the Euler simulation. Thermodynamic properties of the MM working fluid are obtained with a model based on the iPRSV cubic equation of state [368], while the transport property values needed for the RANS simulations are calculated with the Chung's model [73]. Both models are implemented in the FluidProp library [93]. N.B. The profiles have been translated in order to satisfy a throat height of 6.66 mm.

a workstation equipped with an Intel i7-8750H (2.21 Ghz, 6 cores) and lasted approximately 10 minutes.

#### SIMULATION OF THE PR.027-NT.001 TEST RUN

The boundary conditions for the simulation are reported in Tab. 6.8 and are those of the experiment reported in Sec. 6.9.1. Figure 6.30 shows the computed pressure field along the nozzle. The values of the calculated static pressure along the nozzle at locations corresponding to the positions of the pressure taps is reported in Fig. 6.26, which shows that the trend of the measured and calculated values is very similar. The comparison provides a qualitative validation of the measurements, as the simulation model is based on first-principle equations, and on validated thermophysical property models.

#### SIMULATION OF THE PR.025-NT.001 TEST RUN

Analogously, the boundary conditions imposed for this simulation are listed in Tab. 6.9. Figure 6.31 shows the predicted Mach number contours along the supersonic nozzle. The computed Mach numbers can be compared with the values obtained from the schlieren images in Figure 6.28. Also in this case, the juxtaposition of values obtained from measurements and computed values provides a satisfactory qualitative validation of the experiments.

Table 6.9: Boundary conditions of the simulation of the PR.025-NT.001 test run. Taken from the average experimental values in Tab. 6.12.

Total inlet pressure, PV002 / bara	18.36
Total inlet temperature, TT015 / °C	252.2
Static outlet pressure , PT004 / bara	2.1

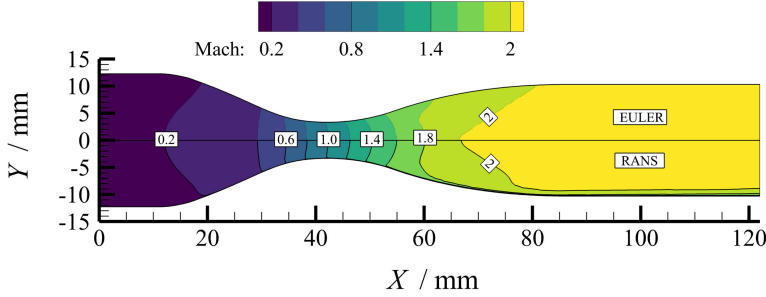


Figure 6.31: Mach contours along the supersonic nozzle calculated with the SU2 code using the operating conditions of the PR.025-NT.001 experimental run as boundary conditions, see Tab. 6.9. The upper side of the figure displays results calculated by solving the RANS equations, while the lower side displays the results of the Euler simulation. Thermodynamic properties of the MM working fluid are obtained with a model based on the iPRSV cubic equation of state [368], while the transport property values needed for the RANS simulations are calculated with the Chung's model [73]. Both models are implemented in an in-house fluid property estimation software [93]. N.B. The profiles have been translated in order to satisfy a throat height of 6.66 mm.

## 6.9.4. TEMPERATURE AND PRESSURE MEASUREMENT UNCERTAINTIES

The uncertainty analysis is based on the method described in Sec. 5.6.2.

### TEMPERATURE

It is assumed that the temperatures measured by the probes in the settling chamber and receiver are approximately equal to the total temperature because i) the difference between the total and static value is within the total uncertainty of the instrument, ii) in any case the contribution to the total value of the kinetic energy of the flow is very small and iii) to a certain extent accounted for by its dissipation on the probe surface. The total temperature measurements at the inlet of the nozzle and in the receiver, tagged as TT014 and TT015 in Fig. 6.7 and Fig. 6.2, respectively, are obtained with *WIKA TR10-C PT100* sensors. The 4 – 20 mA signals are connected to a 24-bit analog to digital (A/D) input module (*NI9208*) installed in a *compactRIO* controller. The measured data are recorded and stored using the *ORCHID CODAQ LabVIEW* program in the *Datalogging and Supervisory Control Module (DSC module)* database, with a time step equal to 1 s. A logging dead-band filter<sup>8</sup> with a threshold of 1 % is used to eliminate noise from the data. The measurement uncertainty associated to the sensor is evaluated as Type B based on information in the data sheet. These temperature transmitters feature high accuracy, as they

<sup>8</sup>Data is only recorded if the percentage difference between the new value and the previous value equals or exceeds the dead-band threshold.

Table 6.10: Type B absolute uncertainties associated with the *DSA 3218 Scanivalve* pressure scanner.

Tag	Full scale range / bara	$U_B/\pm\text{bar}^*$
P <sub>SV</sub> 001-003	35.5	0.0172
P <sub>SV</sub> 004-009	18.2	0.0086
P <sub>SV</sub> 010-016	7.8	0.0035

\* Coverage factor of  $k = 2$ .

are categorized as Class A, therefore their full scale accuracy is  $\pm(0.15 + 0.002 |T| \text{ } ^\circ\text{C})$ , see the EN 60751 standard.

In order to quantify the contributions of Type A uncertainties for experiments PR.025-NT.001 and NT.002 and for experiment PR.027-NT.001, first a period of time in which the process can be considered at steady state was identified, based on the steady-state detection method of Kim *et al.* [210] together with the threshold criteria defined by Woodland *et al.* [409], see App. D. Then the standard deviations of the measurements were calculated and expanded with a coverage factor of 2, see Tables 6.11 and 6.12. For experiment PR.025-NT.001&2 these are TT015 =  $\pm 0.085 \text{ } ^\circ\text{C}$  (Type A) and TT014 =  $\pm 0.10 \text{ } ^\circ\text{C}$  (Type A) and for experiment PR.027-NT.001 these are TT015 =  $\pm 0.21 \text{ } ^\circ\text{C}$  (Type A) and TT014 =  $\pm 0.43 \text{ } ^\circ\text{C}$  (Type A).

## TOTAL AND STATIC PRESSURE

The system pressure is measured with two *WIKA UPT 20* pressure transmitters<sup>9</sup> and the data along the expansion with a pressure scanner. The *Scanivalve DSA3218* 16-channels pressure scanner is equipped with piezo-resistive sensors, signal conditioning, 16 bit D/A conversion and data buffering in one single module.

The full scale values of the 16 sensors are different and are 34.5 barg for channels 13 to 16, 17.2 barg for channels 7 to 12 and 6.9 barg for channels 1 to 6. The sensors are calibrated down to a vacuum and up to 110 % of the full scale. However, the nominal accuracy is not guaranteed beyond the full scale value and below 10 % of the full scale.

Measurement uncertainties have been quantified using the methods outlined by Mofat [262] and Abernethy *et al.* [1]. The Type B uncertainty associated with the *Scanivalve* system is equal to 0.05 % of the full scale of the sensors, see Tab. 6.10 for the absolute values, and they include the uncertainty associated to the A/D conversion.

Table 6.11 and 6.12 report mean values and uncertainties also for the pressure measurements. For the experiment PR.027-NT.001, the reported mean values and associated uncertainty of the nozzle inlet and outlet pressure are PZA003 =  $11.791 \pm 0.041$  bara (Type A) and PT004 =  $0.901 \pm 0.0051$  bara (Type A). As for the pressures measured with the *Scanivalve*, the mean values and related total expanded uncertainty are summarized in Tab. 6.11. During the test run PR.025-NT.001 the *Scanivalve* was not operated, therefore only the values of Type A uncertainty for the variables characterizing the operating conditions of the nozzle are listed in Tab. 6.12.

<sup>9</sup>The measurement principle is as follows: a diaphragm isolates the process side from the measuring cell. The internal space between this diaphragm and the pressure measuring cell is completely filled with a system fill fluid. The pressure is transmitted from the measured medium/process by the elastic diaphragm into the system fluid and from there to the measuring element. The measuring cell is made of stainless steel 316L (1.4404).

Table 6.11: Experimental mean values and related uncertainties for the PR.027-NT.001 test. Data refer to 300 samples over the period 12:03:30 - 12:08:30 (test-date: 13-05-2019). For the measurements related to the nozzle inlet and outlet, only Type A expanded uncertainties could be evaluated. The Scanivalve pressure values and related total expanded uncertainties are also shown in Fig. 6.32.

Operating conditions			
	Tag	Mean Value	$U_{\text{Type A}}^*$
Nozzle inlet temp.	TT015 / °C	252.87	$\pm 0.21$
Receiver temp	TT014 / °C	239	$\pm 0.43$
Mass flow rate	FT001 / kg/h	2920.8	$\pm 2.52$
Evaporator pressure	PZA003 / bara	11.79	$\pm 0.041$
Receiver pressure	PT004 / bara	0.901	$\pm 0.0051$

Scanivalve pressures					
Tag	$\bar{P}$ / bara	$U$ / bara *	Tag	$\bar{P}$	$U$ / bar *
$P_{\text{SV}001}$	11.22	$\pm 0.0192$	$P_{\text{SV}009}$	2.45	$\pm 0.0280$
$P_{\text{SV}002}$	11.09	$\pm 0.0192$	$P_{\text{SV}010}$	2.16	$\pm 0.00878$
$P_{\text{SV}003}$	11.11	$\pm 0.0185$	$P_{\text{SV}011}$	2.03	$\pm 0.00352$
$P_{\text{SV}004}$	11.01	$\pm 0.0186$	$P_{\text{SV}012}$	1.90	$\pm 0.00357$
$P_{\text{SV}005}$	9.93	$\pm 0.0106$	$P_{\text{SV}013}$	1.86	$\pm 0.00433$
$P_{\text{SV}006}$	6.99	$\pm 0.0118$	$P_{\text{SV}014}$	1.70	$\pm 0.0035$
$P_{\text{SV}007}$	6.90	$\pm 0.0156$	$P_{\text{SV}015}$	1.08	$\pm 0.00368$
$P_{\text{SV}008}$	3.65	$\pm 0.0178$	$P_{\text{SV}016}$	2.30	$\pm 0.0379$

\* Coverage factor  $k = 2$ .

Figure 6.32 shows the values of the static pressure along the supersonic nozzle measured during the PR.027-NT.001 experiment, together with the corresponding total uncertainty bars.

Notice that the average and total expanded uncertainty of  $P_{\text{SV}016}$  is larger when compared to  $P_{\text{SV}015}$ , which is most likely owed to liquid trapped in the line, which was not purged correctly during the purging process.

The total expanded uncertainty of the nozzle inlet pressure measurements (Scanivalve) ( $P_{\text{SV}002}$ ) is an order of magnitude smaller if compared to that of the evaporation pressure measurement (PZA003). This is because the accuracy of the sensor is higher and because the pressure fluctuations at the inlet of the nozzle are dampened by the screens and honeycombs of the settling chamber.

Moreover, the total expanded uncertainty of the pressure measurements (Scanivalve) decreases for lower pressures because the Type A uncertainty is almost constant as it is associated with the process fluctuations, while the Type B uncertainty decreases with the measured pressure due to the increased accuracy at lower full scale levels.

### 6.9.5. UNCERTAINTY OF THE MACH NUMBER ESTIMATIONS

As described by Oberkampf & Roy [280], there are several aspects related to experiments in wind tunnels which may contribute to uncertainties in flow field measurements. These error sources are, generally, identified based on experience and wind tunnel calibration procedures [108, 263, 278], and may originate from the operational conditions of the facility, the test section geometry, the adopted measurement technique and instruments,

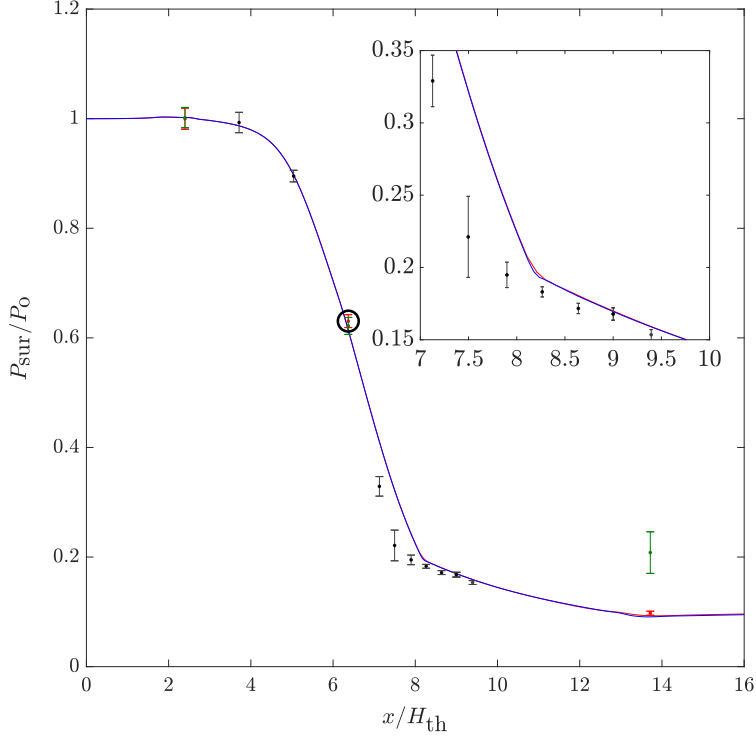


Figure 6.32: Static pressure values measured along the two-dimensional ORCHID supersonic nozzle during the PR.027-NT.001 experimental run together with the related total expanded uncertainty bars, see Tab. 6.11. The nozzle operating parameters for this experiment are  $P_0 = 11.22 \pm 0.0192$  bara,  $T_0 = 252.9 \pm 0.69$  °C, and  $P_b = 0.9 \pm 0.01$  bara. The uncertainty in the total pressure is including Type A and B since it is measured by the Scanivalve while the back pressure is only of Type A since it belongs to the ORCHID BoP. The pressure is non dimensionalized with the average value of the total pressure at the inlet  $P_0 = 11.2$  bara and the axial coordinate with the throat height  $H_{th} = 6.66$  mm. The circle indicates the throat position. Static pressures resulting from the RANS simulation (—) and the Euler simulation (—). The details of the calculation are reported in in Sec. 6.9.3. The pressure at the inlet, at the throat and the outlet was measured by two pressure taps, therefore the uncertainty bars are indicated with different colors. The axial location of the taps can be determined with Tab. 6.2.

Table 6.12: Experimental mean value and related Type A expanded uncertainties of the operating conditions for the PR.025-NT.001. Data are related to 360 samples over the period 11:24 - 11:30 (test-date: 25-04-2019). Refer to Fig. 5.2 to identify the instruments by their tags.

	Tag	Mean Value	$U_{\text{Type A}}$
Nozzle inlet temp.	TT015 / °C	252.6	$\pm 0.085$
Receiver temp	TT014 / °C	226.3	$\pm 0.10$
Mass flow rate	FT001 / kg/h	4481.8	$\pm 11.37$
Evaporator pressure	PZA003 / bara	19.16	$\pm 0.0349$
Total pressure <sup>+</sup>	$P_0$ / bara	18.46	—
Receiver pressure	PT004 / bara	2.043	$\pm 0.0148$

\* Coverage factor  $k = 2$ .

+ The total pressure at the nozzle inlet  $P_0$  is calculated from the measurement of the PZA003 sensor, i.e., by subtracting the estimated pressure drop between the primary heat exchanger outlet and the nozzle inlet,  $\Delta P = 0.7$  bar, from the value measured by PZA003 sensor, that is 19.16 bar.

as well as the post processing tools. References [3, 8] discuss how to quantify error sources associated with wind tunnel testing and reduce the corresponding uncertainties. The information reported in these articles, together with Ref. [194] which provides general guidelines for assessing measurement uncertainty, were used to identify, characterise and quantify all the uncertainty sources concerning the operating conditions of the ORCHID nozzle test section and the schlieren measurement chain.

More in detail, the sources of error which contribute to uncertainties in the measurements of the Mach angle  $\mu$  may be categorized into two main groups. The first category comprises the error sources that influence the flow uniformity and quality within the nozzle test section, while the second category pertains to the measurement technique, as well as the algorithms used in the post processing stage.

The errors sources that might affect the flow in the ORCHID nozzle are

1. periodic fluctuations in the total inlet conditions and back-pressure of the nozzle test section, due to the control system and the hardware, such as the volumetric pump which imposes flow pulsations.
2. incorrectly designed and installed flow conditioning devices [280];
3. changes in environmental conditions during the course of an experiment [280];
4. geometrical imperfections, e.g., poorly machined wall contours of the axisymmetric contraction section, the nozzle profile and the test channel [280, 312];
5. misalignment of the nozzle profiles, which may influence the nozzle area distribution [3, 8];
6. boundary layer development along the nozzle profile walls, which influences the area distribution [3, 8, 182];

Once the flow is at steady state, variations in the operating conditions of the test section, e.g., in the back-pressure PT004 or the total inlet temperature TT015, see the



expanded uncertainties reported in Tab. 6.12, can be only of the random type, though a certain periodicity is observed in the measurements, probably due to the fluctuations in the circuit caused by the volumetric pump, which cannot be completely eliminated by the flow damper and the internal volumes of the heat exchangers and the settling chamber. The result of this fluctuation is a variation over time in the flow features within the test section, which affects the quality of the measurements. A similar effect on flow quality might be expected from changes in environmental conditions and geometrical imperfections due to the manufacturing process. The lab hall in which the ORCHID is installed is equipped with a finely controlled thermal management system, thus systematic effects on the flow patterns in the nozzle test section are excluded. The same consideration applies to the effect of geometrical imperfections, as the machining accuracy nowadays available is extremely high. On the other hand, a misalignment of the upper and lower nozzle profiles may have detrimental consequences on the experimental accuracy. The nozzle is made from two equal and removable profiles. When mounted these profiles can be, unintentionally, axially misaligned such that they do not complement each other symmetrically. However, the assessment of flow symmetry conducted in Section 6.7.3 and complemented by the study of static pressures in Section 6.9.1 reveals that the flow field can be considered uniform. Thus, the uncertainty associated with an incorrect installation or manufacturing of the nozzle profiles are arguably low.

The error sources related to the measurement chain include

1. possible misalignments in the optical system, as well as the finite and discrete resolution of the camera sensor [35, 353]; and,
2. approximations adopted in the post-processing algorithms used for Mach line extraction from the schlieren images [35], such as the pixel-to-meter conversion ratio used to rescale the image into the physical domain, which depends on the effective throat height of the nozzle measured before the experiment [3, 8, 35].

The uncertainty in the estimated Mach line angle  $\mu$  or in the flow Mach number, which originates from the error sources affecting the flow uniformity as well as from possible misalignments in the optical system, are evaluated as Type A uncertainty based on the standard deviation of the samples returned by the Mach line extraction algorithm and assuming a 95 % confidence level. This uncertainty contribution is defined as  $U_{\text{Type A}, \mu}$  or  $U_{\text{Type A}, \text{Mach}}$  depending on the response quantity of interest.

Regarding the post-processing algorithm, it is possible to distinguish between the uncertainty related to the position at which the Mach line angle is estimated  $U_x$  and the uncertainty related to the angle itself  $U_\mu$ .

The nondimensional position along the nozzle where the Mach line angles are estimated  $\bar{x}$  is uncertain and is

$$\bar{x} = \frac{(x_{\text{th}, \text{pix}} - x_{\text{pix}})}{H_{\text{th}, \text{pix}}}. \quad (6.12)$$

The throat height  $H_{\text{th}, \text{pix}}$  and throat location  $x_{\text{th}, \text{pix}}$  (in pixels) are calculated based on the nozzle profile that can be detected from the calibration image used for schlieren data post-processing.  $x_{\text{pix}}$  is the coordinate of the evaluated Mach line. Translating the

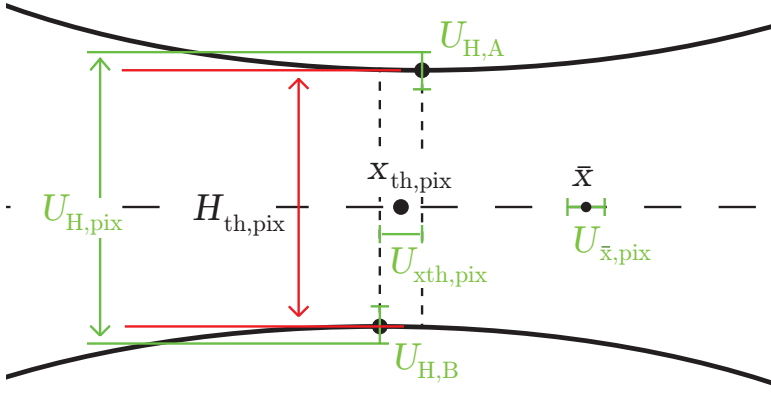


Figure 6.33: Sketch of the nozzle indicating throat height and coordinates related to the uncertainty evaluation of the throat location.

nozzle throat position to the origin, and subsequently flipping the coordinate system is necessary for post processing purposes and comparisons against the simulations.

Figure 6.33 shows a sketch of the nozzle together with the variables used to calculate the position uncertainty  $U_{\bar{x}}$ . The lines representing the nozzle profiles are fitted with a polynomial function, and the two points featuring horizontal tangent are identified. As the two points are not vertically aligned, the throat location is taken as the arithmetic average of the distances of the two points from the nozzle inlet. The throat height is the vertical distance between the two points. The uncertainty associated with the throat height is then

$$u_{H,\text{pix}} = u_{H,A} + u_{H,B}, \quad (6.13)$$

where  $u_{H,A}$  and  $u_{H,B}$  are the standard deviations associated with the polynomial fitting of the upper and lower lines. Similarly, also the axial position of the nozzle throat location  $U_{x_{\text{th}},\text{pix}}$  is uncertain and is

$$U_{x_{\text{th}},\text{pix}} = |x_A - x_B| + 0.5 \quad (6.14)$$

$x_A$  and  $x_B$  are the  $x$  coordinates along the wall polynomials at the local minimum and maximum of the upper and lower walls. The addition of 0.5 represents the round off error due to pixel discretization.

The total expanded uncertainty associated with the non-dimensionalized coordinates  $\bar{x}$  where the Mach line angles are measured,  $U_{\bar{x},\text{pix}}$ , is then

$$U_{\bar{x},\text{pix}} = \bar{x} \cdot \sqrt{\left(\frac{U_{H,\text{pix}}}{H_{\text{pix}}}\right)^2 + \left(\frac{U_{x_{\text{th}},\text{pix}}}{x_{\text{th},\text{pix}}}\right)^2}. \quad (6.15)$$

Moreover, as described in Sec. 6.7.3, the line extraction procedure selects a single Mach line in each interrogation window to minimize the chances of selecting a spurious set of collinear points in the image. The selected line is *a priori* assumed passing through

the center of the related interrogation window. It follows that the actual position of the line can be anywhere along the horizontal dimension of the window. The corresponding uncertainty is indicated as *discretisation uncertainty*  $U_{\Delta x}$ . Assuming a 100 % confidence level and a uniform probability distribution for the exact location of the extracted Mach line within the interrogation window,  $U_{\Delta x}$  is equal to half of the interrogation window width. Finally, the total expanded uncertainty associated with the position of a Mach line angle can be calculated as

$$U_x = \sqrt{U_{\Delta x}^2 + U_{x,\text{pix}}^2}. \quad (6.16)$$

The uncertainty associated with the estimation of the Mach angle or flow Mach number by means of the post-processing algorithm is referred to as  $U_\mu$  which is comprised of the Mach angle *extraction uncertainty* and a Type A uncertainty contribution, which is the computed standard deviation of the measured quantities.

The Mach angle extraction uncertainty  $U_{\text{ext},\mu}$  consists of two main contributions, i.e., the uncertainty associated with the image resolution  $U_{\text{ir}}$  and the uncertainty due to the Mach line angle discretization assumed in the Hough transform implementation  $U_{\text{Hough}}$ .

As  $U_{\text{ir}}$  and  $U_{\text{Hough}}$  are statistically independent from one another,  $U_{\text{ext},\mu}$  is estimated as

$$U_{\text{ext},\mu} = \sqrt{U_{\text{ir}}^2 + U_{\text{Hough}}^2}. \quad (6.17)$$

$U_{\text{Hough}}$  is equal to half of the discretization step of the line angle  $\Delta\mu$  considered in the accumulator of the Hough transform, see Section 6.7.3.  $U_{\text{ir}}$  corresponds to the angular resolution within a given interrogation window with a 95% confidence level that results from the pixel resolution. The finite number of pixels of the image inherently introduces an approximation on the line angle, which tends to increase the shorter the Mach lines [35]. The angular resolution is equal to the arctangent of the inverse of the detected line length. The length of the detected Mach lines varies from one image sample to another due to changes in brightness, disturbances in the flow, numerical approximations, and other random effects. Moreover, as the size of the interrogation windows is not constant, the minimum angle that can be identified varies along the expansion process.  $U_{\text{ir}}$  is, then, determined for each interrogation window by calculating the average angular resolution and adding to this term two times the line length standard deviation propagated through the angular resolution equation, namely

$$\begin{aligned} \overline{\Delta\mu_{\text{ir}}} &= \overline{\arctan \frac{1}{L}}, \\ U_{\text{ir}} &= \overline{\Delta\mu_{\text{ir}}} + \frac{2\sigma_L}{1 + \overline{L}^2} \end{aligned} \quad (6.18)$$

where  $\overline{L}$  is the average length of a detected Mach line in the interrogation window of interest.

Similarly, the uncertainty on the flow Mach number  $U_{\text{ext},\text{Mach}}$  can be evaluated by propagating the uncertainty on the Mach line angle through Eq. 6.11. It results that

$U_{\text{ext,Mach}}$  is a function of the corresponding uncertainty in the estimation of the Mach line angle  $U_{\text{ext},\mu}$  and the Mach number itself, i.e.,

$$U_{\text{ext,Mach}} = M\sqrt{M^2 - 1}U_{\text{ext},\mu}. \quad (6.19)$$

The factor  $M\sqrt{M^2 - 1}$  is derived by evaluating the derivative of the Mach number with respect to the Mach line angle  $\left| \frac{dM(\mu)}{d\mu} \right|$  [35]. Equation 6.19 implies that the uncertainty on the flow Mach number increases from the throat to the exit of the nozzle.

#### TOTAL EXPANDED UNCERTAINTIES

The total expanded uncertainties of the Mach line angle or Mach number can be expressed as

$$U_\mu = \sqrt{U_{\text{Type A},\mu}^2 + U_{\text{ext},\mu}^2 + 2\rho \cdot U_{\text{Type A},\mu} \cdot U_{\text{ext},\mu}} \quad (6.20)$$

and

$$U_{\text{Mach}} = \sqrt{U_{\text{Type A,Mach}}^2 + U_{\text{ext,Mach}}^2 + 2\rho \cdot U_{\text{Type A,Mach}} \cdot U_{\text{ext,Mach}}} \quad (6.21)$$

where  $\rho$  is the Pearson correlation coefficient between the two error sources, due to the statistical dependence between the uncertainty contributions estimated as Type A and the uncertainty associated with the Mach line extraction algorithm. The flow Mach number distribution obtained from the schlieren images taken during the experimental runs reported Sec. 6.8 are displayed in Figs. 6.34 and 6.35 with the corresponding uncertainty bars.

#### 6.9.6. EXPERIMENTAL DATA WITH UNCERTAINTY VS SIMULATIONS

Figure 6.34 shows the midline Mach number distribution along the nozzle axial coordinate  $x$ , normalized by the nozzle throat height  $H_{\text{th}}$  for the PR.025-NT.001 test run.  $x$  is equal to zero at the geometrical throat of the nozzle. The value of Mach numbers are obtained by averaging values estimated with the post-processing procedure detailed in Sec. 6.7.3. The vertical bars refer to total expanded uncertainties of the estimated Mach numbers (See Eqn. 6.21), while the horizontal bars refer to the uncertainty of the locations at which the Mach numbers were estimated (See Eqn. 6.16). The chart reports also Mach numbers resulting from RANS and Euler simulations.

The values of flow Mach number obtained with the CFD simulations are within the uncertainty bars of the values estimated from experimental data, except from a few corresponding to locations closer the throat. Both a vertical and a horizontal offset of the values estimated from experimental data with those obtained from simulations can be observed. The reason might depend on the uncertainty affecting the estimation of the throat size and position, which affects not only the Mach value estimations but also the simulations. The throat height was measured after the tests, once the metal parts reached ambient temperature. Thermal expansion during the tests alters this value, though the magnitude of the alteration is currently unknown. The position of the throat

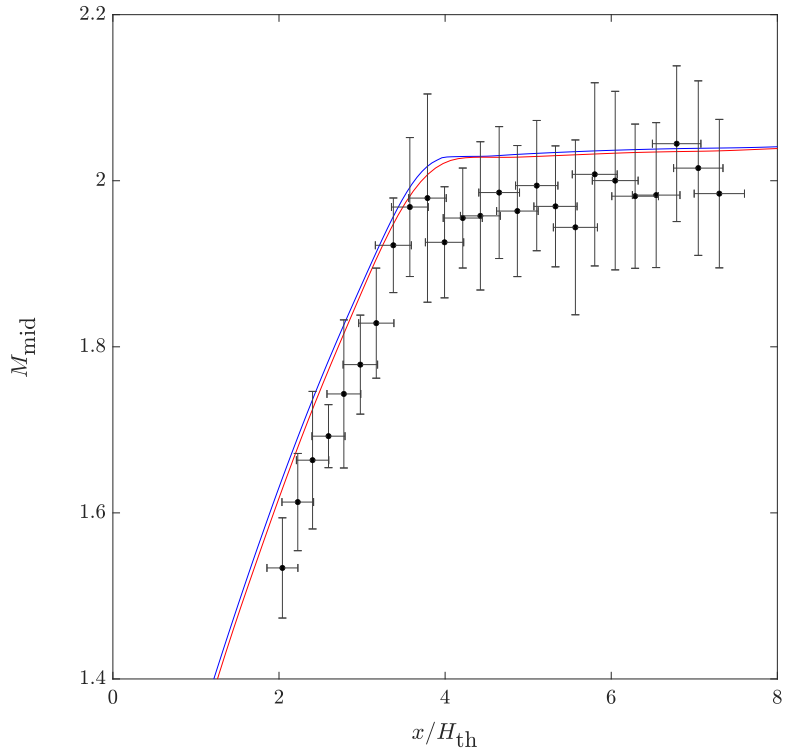


Figure 6.34: Estimated Mach numbers with corresponding uncertainty bars along the midplane (•) from the nozzle throat to the outlet vs. values obtained with CFD simulations (— RANS, — Euler) for the PR.025-NT.001 test run (details on the calculation in Sec. 6.9.3). See Fig. 6.28(a) for more details.

was estimated based on the analysis of schlieren images and its location may be different from that of the geometrical throat. Moreover, the simulations do not account for 3D effects, such as the boundary layer development over the glass windows, which causes a reduction in the nozzle flow area.

The total expanded uncertainty on the Mach number increases towards the nozzle outlet. This occurs despite the value of the uncertainty  $U_{\text{Type A, Mach}}$  is almost constant, and it reaches the highest values close to the nozzle throat where lines are less visible and the quality of the images decreases. Also the uncertainty associated to the Mach line angles  $U_{\text{ext},\mu}$  does not vary significantly, at least as long as the images are sharp and the brightness level is constant. The total uncertainty of the estimated Mach number is therefore larger towards the outlet of the nozzle because, in accordance with Eq. 6.19, its value is amplified by the value of the Mach number itself.

As described in Sec. 6.9.2, another test run was performed in order to acquire schlieren images with higher resolution closer to the throat by properly reducing the field of view. The average estimated Mach number together with the corresponding total expanded uncertainty is shown for thirty points starting at  $x/H_{\text{th}} = 1.27$  and ending at  $x/H_{\text{th}} = 4.32$  in Fig. 6.35. Values of the Mach number could not be obtained for locations in proximity of the throat owing to extreme light ray deflections, arising as a consequence of the density gradients in the flow, exceed the currently configured schlieren system measuring range, see Sec. 6.9.2. The effect of the increased spatial resolution is the reduction of the total expanded uncertainty, as the angular resolution is improved.

The predicted Mach numbers match reasonably well with the experimental results, in particular at the beginning of the supersonic expansion. The difference between the average estimated flow Mach number and the RANS prediction at position  $x/H_{\text{th}} = 1.27$  is less than 0.6 %. The maximum deviation is 4.4 % and occurs at position  $x/H_{\text{th}} = 3.54$ . Figure 6.35 shows also that the RANS simulation predicts lower values for the flow Mach number along the nozzle if compared to the values calculated with the Euler simulations. The differences between the results obtained with the two numerical simulations are, however, very small.

## 6.10. CONCLUSIONS AND RECOMMENDATIONS

This chapter describes all the activities leading to the commissioning of the two-dimensional supersonic nozzle of the ORCHID for the characterization of inviscid steady flows of dense vapors expanding partially in the non ideal compressible fluid dynamic regime. More in detail, the specifications for the conditions of paradigmatic experiments are first treated. Then, the detailed design and realization of the nozzle test section is reported, followed by the account of the pressure and temperature measurement system. The total temperature is measured at the inlet of the nozzle, while the total pressure is measured at the inlet and the outlet of the nozzle, and static pressures are measured by means of fifteen pressure taps along the upper and lower nozzle profile. These measurements can be used together with the estimation of the local Mach number for the validation of CFD codes. Values of the flow Mach number along the nozzle are estimated starting from information on the Mach lines originating from the metal surfaces of the the upper and lower profile obtained from schlieren images. The schlieren technique is briefly recalled and the adopted schlieren measurement chain is illustrated. The description

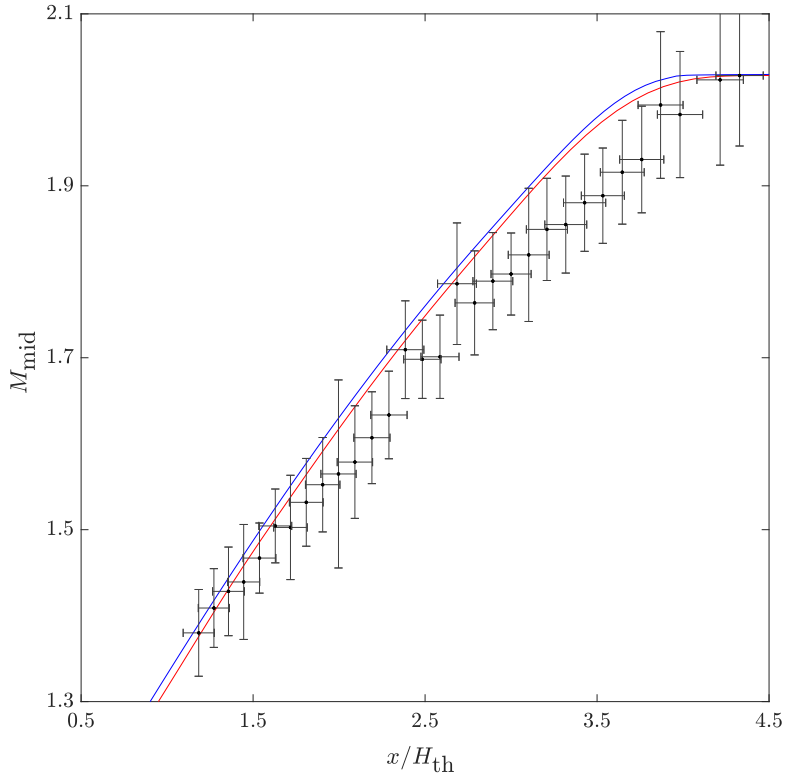


Figure 6.35: Estimated Mach numbers with corresponding uncertainty bars along the midplane (•) for a portion of the nozzle in proximity of the throat vs values obtained with CFD simulations (— RANS, — Euler) for the PR.025-NT.002 test run (details on the calculation in Sec. 6.9.3). See Fig. 6.28(b) for more details.

of the experimental procedure precedes the treatment of the two sets of commissioning experiments in which the working fluid is dense vapor of siloxane MM, one aimed at obtaining pressure measurements and one aimed at the estimation of the local flow Mach number over the flow field. The results of these experiments were validated, namely, values of pressure, and Mach number along the nozzle were compared to the results of CFD simulations first, in order to gain confidence regarding the observed trends, and then fully characterized in terms of experimental uncertainty.

The work and results described here allow to draw several conclusions related to exemplary experiments carried out with the vapor of siloxane MM expanding from non-ideal thermodynamic conditions. It can be argued that these conclusions have more general validity, and are applicable to any similar NICFD experiment with other fluids and other operating conditions. In summary, the following observations hold:

1. static pressure measurements along the nozzle profile are affected by a relative total expanded uncertainty in the order of  $\frac{0.0192}{11.22} \cdot 100 = \pm 0.17\%$ . The issues related to the possible condensation of the working fluid in the tubes of the Scanivalve measurement system have been solved with a liquid purging system;
2. a method for the estimation of the local Mach number from information on Mach lines displayed in schlieren images of the flow has been devised and successfully applied. The computed Mach number values corresponding to expansions featuring an outlet Mach number in the range 1.5 – 3 are affected by an uncertainty which increases with the value of the Mach number. For example, for an expansion with an outlet Mach number of 2, the absolute expanded uncertainty varies from  $\pm 0.04$  closer to the throat, to  $\pm 0.1$  in the divergent part of the nozzle. This is due to the progressively larger contribution of the angular resolution component of the uncertainty;
3. a certain discrepancy between experimental and simulated values of pressure and Mach number exist. The cause of this discrepancy will be further analyzed, but a first hypothesis is that the thermal elongation of the metal parts when the nozzle is at high temperature causes a significant increase of the throat aperture;
4. the ORCHID nozzle test section has been successfully commissioned, because it can be argued that experiments with it can provide pressure and Mach number data related to NICFD flows which are sufficiently accurate for the systematic validation of CFD codes to be used for engineering purposes.

The experience gained with these commissioning activities points to a number of recommendations for the improvements of these kind of experiments, that is

1. an additional pressure sensor should be added and located in the settling chamber. The sensor must be independent from the Scanivalve pressure measurement system, so that experiments aiming at estimating local flow Mach numbers can be carried out without operating the Scanivalve system, thus avoiding related complications;



2. a mass flow meter should be added at the inlet of the nozzle test section. This avoids the uncertainty on the value of the mass flow due to the possible leakage over the bypass valve;
3. large density changes in the kernel region are a characteristic of dense organic vapor expansions, which cause light rays to exceed the schlieren system measuring range. The schlieren components can be tuned for smaller field of views of the flow field. For example, the focal length of the schlieren head (lens C in Fig. 6.16) can be adjusted and, together with a gradient based filter, it would allow to achieve the optimal change in image contrast for a given light source intensity.
4. the size of the throat should be accurately measured while the nozzle is in operation. This can be achieved by marking the throat height with two points on the upper and lower profiles. Then the schlieren calibration image is used to determine the height to pixel ratio and another schlieren image, taken when the nozzle is in operation, is used together with the obtained ratio to determine the height of the throat in hot operating conditions. The width of the throat can be measured with a suitable displacement sensor, e.g., a Confocal CL-3000 WW optical instrument.

## ACKNOWLEDGEMENTS

The author would like to express their gratitude to Nando Timmer for his suggestions concerning wind tunnel design methods, Steve van Herk for his help in the realization of the nozzle test section and Jos van Meurs for his help realising the pressure measurement system. The author would also like to thank Ferdinand Schrijer for his help tuning the schlieren measurement chain and his suggestions concerning the uncertainty quantification in the post processing stages. Additionally, gratitude is extended to Fabio Beltrame who implemented the methods and developed the post processing tools under the author's guidance.

# 7

## TOWARDS THE VALIDATION OF CFD SOLVERS FOR NON-IDEAL COMPRESSIBLE FLOWS

Contents partly from:

Head, A. J., Iyer, S., de Servi, C., Pini, M.: Towards the validation of a CFD solver for non-ideal compressible flows. *Energy Procedia* 129, 240–247 (2017).

### ABSTRACT

The availability of experimental gas dynamic data concerning the fluids and the flow conditions of interest for the design of turbomachinery whose fluid dynamics is affected by non-ideal compressible fluid dynamics (NICFD) effects is very limited [163]. Therefore, CFD tools used for the fluid dynamic design of these components cannot be validated against reliable measurements. To bridge this gap, new experimental facilities are currently being built, such as the ORCHID which was under construction at the time of this writing [179].

The availability of proper experimental datasets is not, however, the sole requirement for validating a CFD code. Another important requirement is the definition and application of an appropriate validation methodology. This chapter documents the first steps of the development of a method for the systematic validation of CFD solvers capable of simulating non-ideal compressible flows. In particular, the proposed procedure is based on the application of an industry-standard validation method for software code credibility assessment to the case of dense vapor flows of organic compounds. Furthermore, the validation exercise is performed to 1. understand the main uncertainties involved in the validation process; 2. refine the *design of experiment*; and, 3. assess the adequacy of the

validation procedure itself. The exercise is limited to determining how the uncertainties in model inputs, e.g., fluctuations in boundary conditions and thermodynamic property models influence the overall accuracy of NICFD simulations. The assessment of other sub-models is left for a successive phase of this research program.

A numerical procedure based on uncertainty quantification analysis has therefore been conceived. Synthetic datasets are used to investigate the validity of this procedure, because at the time of this writing actual experimental data were not available yet. The validation exercise confirms the applicability of the proposed method, but also points out that the adopted validation metrics should be complemented with additional statistical indicators. The error sources in the designed experiment are identified and all the uncertainties are adequately quantified.

## 7.1. INTRODUCTION

The need for adopting a systematic Verification and Validation (V&V) methodology for code quality assurance is a topic well documented in the literature [280, 281, 329, 336]. The American Institute for Aeronautics and Astronautics (AIAA) and the American Society of Mechanical Engineers (ASME) were the first to publish V&V guidelines for CFD computer programs [7, 25]. According to these references, *validation* is the process of determining by statistical means the degree of confidence with which a model is an accurate representation of the physical phenomena of interest in its domain of applicability. In other words, since models as well as measurements are consistent with reality only within a certain level of approximation, their comparison cannot be accomplished without first identifying and quantifying the uncertainty sources which affect both the model and the measurements. The predictive capability of the model can then be assessed by statistical tests or appropriate metrics, taking into account the uncertainty range associated to each single physical observation and the corresponding model calculation.

As estimating the uncertainty of measurements and of computer simulations strongly depends on the characteristics of the experiments and the model, the adopted validation method has to be tailored to the problem at hand. Therefore, the work documented in this chapter is related to the first steps of the development of a systematic method for the validation of a CFD flow solver for non-ideal compressible flows. A validation framework has been developed to assess the influence of the accuracy of the fluid thermodynamic model on the results of flow simulations, one of the main sources of uncertainty related to the physical sub-models, the others being the boundary conditions of the experiment, the turbulent model and the transport properties. Due to the lack of suitable experimental data at the time of this writing, a synthetic dataset was generated and used to demonstrate the validity of the procedure.

The chapter is structured as follows. Sec. 7.2 introduces the adopted validation approach and metrics. The validation test cases, namely the experiments envisaged at the time of this writing are briefly treated in Sec. 7.3, while the simulation model and the Uncertainty Quantification (UQ) method used to estimate the uncertainty in the CFD code predictions is described in Sec. 7.4. Finally, the validation assessment is exemplified in Sec. 7.7.

## 7.2. VALIDATION OF A CFD CODE FOR NICFD SIMULATIONS

The validation metrics and procedure adopted in this work to compare flow measurements against model predictions are those first considered by Coleman & Stern [82] and Eça *et al.* [131]. The following treatment is adapted from the code validation process documented in Oberkampf & Roy [280, Sec. 6.4].

The first metric is the *validation comparison error*

$$E = S - D, \quad (7.1)$$

where  $S$  is the numerical prediction and  $D$  is the experimental value of the considered system response quantity (SRQ). The error in the numerical prediction value is the difference between  $S$  and the true value  $T$ , i.e.,  $\delta_S = S - T$ . Similarly, the error in the experimental value  $D$  is  $\delta_D = D - T$ . Equation 7.1 can now be expressed as

$$E = S - D = (T + \delta_S) - (T + \delta_D) = \delta_S - \delta_D. \quad (7.2)$$

Therefore, the validation comparison error  $E$  deriving from the simulation and the experiment. The relevance of the experimental error sources can be assessed and the associated uncertainty interval estimated by the techniques reported in Refs. [12, 81, 194, 202]. The errors of the numerical predication  $\delta_S$  can be expressed as follows

$$\delta_S = \delta_{\text{num}} + \delta_{\text{input}} + \delta_{\text{model}}, \quad (7.3)$$

where  $\delta_{\text{num}}$  is the error due to the numerical procedure adopted to solve the equations,  $\delta_{\text{input}}$  is the error in the simulation result due to imperfect knowledge of code inputs (fluid properties, flow geometry and/or boundary conditions), and  $\delta_{\text{model}}$  is the error due to the modelling assumptions and approximations (e.g., the choice of the thermodynamic model used to close the system of conservation equations).

The  $\delta_{\text{num}}$  term includes three different components: the round-off error, the iterative error and the discretization error. There are well-established methods to assess the relevance of these individual components and to estimate an uncertainty interval where the numerical error is contained. The round-off error and the iterative error can be considered negligible when compared to the discretization error, provided that double precision values for the variables are used in the code and that the numerical solution is sufficiently converged according to well established practices. Discretization errors also become negligible with increasing grid-refinement [329] and the procedures described by Celik *et al.* [70] can be adopted to assess their relevance.

The input error  $\delta_{\text{input}}$  term arises from a combination of errors related to the simulation input parameters. The Monte Carlo method, or more efficient methods such as stochastic collocation (SC), can be used to estimate the effect of  $\delta_{\text{input}}$  on the SRQ. Finally,  $\delta_{\text{model}}$  cannot be estimated with a rigorous methodology. For this reason, the ASME [25] V&V Standard and Oberkampf & Roy [280] indicate that the primary objective of the validation process is to estimate a range within which the simulation modelling error  $\delta_{\text{model}}$  is contained. Therefore, the comparison error can be rewritten by combining Eqn. 7.2 and 7.3

$$E = \delta_{\text{model}} + \delta_{\text{num}} + \delta_{\text{input}} - \delta_D.$$

Finally, rearranging the equation, results in

$$\delta_{\text{model}} = E - (\delta_{\text{num}} + \delta_{\text{input}} - \delta_{\text{D}}). \quad (7.4)$$

The *standard uncertainties* corresponding to these errors are  $u_{\text{num}}$ ,  $u_{\text{input}}$ ,  $u_{\text{D}}$ . These uncertainties correspond to an estimate of the standard deviation of the parent distribution.

The second validation metric is the *validation standard uncertainty*  $u_{\text{val}}$  and is defined as an estimate of the standard deviation of the parent distribution of the combination of errors ( $\delta_{\text{num}} + \delta_{\text{input}} - \delta_{\text{D}}$ ). If all three errors are independent it follows,

$$u_{\text{val}} = \sqrt{u_{\text{num}}^2 + u_{\text{input}}^2 + u_{\text{D}}^2}. \quad (7.5)$$

The goal of the procedure is then to estimate the interval  $[E - u_{\text{val}}, E + u_{\text{val}}]$  that contains the modeling error  $\delta_{\text{model}}$ . The model needs to be improved if  $|E| \gg u_{\text{val}}$ . However, if  $|E| \leq u_{\text{val}}$  then the model is capable of predicting the physics of the problem under investigation with sufficient accuracy. It is common practice to assess if the modelling error falls within an expanded uncertainty interval defined as  $U(y) = k \cdot u(y)$ , where  $k$  is the coverage factor [12, 274] and corresponds to a 95 % confidence interval.

## PHYSICAL SUBMODELS

The total uncertainty related to quantities predicted by a CFD code originate from the uncertainties  $U_{\text{input}}$  attributed to its computational sub-models and the uncertainties  $U_{\text{num}}$  associated to the numerical procedure. Considering the physical phenomena occurring in the applications of interest, namely turbomachinery operating with dense organic vapors as working fluids, three predominant sub-models can be identified and necessitate an uncertainty assessment: the turbulence model, and the fluid transport and thermodynamic property models [280]. Each computational sub-model features fitting or material-dependent closure parameters. For example, fluid thermodynamic models based on equations of state may need the critical point properties as one of the inputs, and they are affected by uncertainties.

If the process being modeled encompasses many interacting physical phenomena, the validation process is generally hierarchical: a validation test is performed for each sub-model of the CFD code on the basis of relatively simple experiments. In this case the first sub-model needing assessment is the thermodynamic model of the fluid, since it is impossible to define validation experiments for the turbulence and transport properties sub-models which do not require the use of a fluid thermodynamic model.

## 7.3. ENVISAGED VALIDATION EXPERIMENTS

Chapter 6 documents the first experimental campaign performed with the ORCHID nozzle test section, i.e., flow visualizations of a supersonic expansion through a converging diverging nozzle aiming at investigating flow patterns in a NICFD flow. A similar experiment, but in this case featuring a slender object, e.g., a wedge protruding axially in the diverging part of the nozzle is envisaged as a validation test case, especially regarding the predictive capabilities of the code for accurately computing shock wave angles.

The schlieren technique can be used to detect shock waves generated by a body in a supersonic flow [182], and models/obstacles of varying geometry – e.g., slender pins, and instrumented wedge or diamond shapes – can be used.

Figure 7.1(a) shows the diverging section of the ORCHID nozzle and the contours of  $1 - Z$  resulting from the nozzle designed with the MoC, see Sec. 4.5.1. For this study therefore the nozzle geometry termed *profile A*, see Sec. 5.6, was adopted. Fig. 7.1(b) shows the process representation in the  $Ts$  diagram of the fluid, also with  $1 - Z$  contours. The value of  $1 - Z$ , where  $Z = p(\rho RT)^{-1}$ , provides an indication of the departure of the volumetric characteristics of siloxane MM from those of an ideal gas. The volumetric non-ideal effect is more pronounced in the initial part of the expansion ( $Z_{\text{inlet}} \approx 0.55$ ), while at the nozzle exit fluid properties relation and variation approaches that of the ideal gas ( $Z \approx 0.95$ ).

While it would be attractive to generate shock patterns close to the throat where the effect of non ideal fluid thermodynamic properties is stronger, this appears to be difficult due to blockage effects induced by the inserted obstacle [111, 351]. However, since the flow characteristics are influenced by the expansion upstream, shock patterns generated and imaged at the exit of the nozzle are also deemed meaningful for NICFD validation purposes, as shown in Sec. 7.7. Moreover, the measurement of the variation of static pressure along the nozzle can be recorded and it provides additional validating information.

## 7.4. UNCERTAINTY QUANTIFICATION (UQ) FRAMEWORK

An uncertainty quantification (UQ) framework is required to calculate the model uncertainties of the system response quantities as function of the uncertainties of the input variables  $U_{\text{input}}$ , i.e.  $[S - U_{\text{input}}, S + U_{\text{input}}]$  with a 95 % confidence level. The UQ framework developed within this work comprises a non-intrusive Monte Carlo method coupled to a flow model for the evaluation of the SRQs. In the present validation study, the selected SRQs are an array of shock-wave angles  $\vec{\beta}$  and the pressure distribution along the center axis of the nozzle  $\vec{p}$ , as they are the physical quantities most sensitive to the uncertainties of the thermodynamic model. These SRQs can also be easily measured.

The SRQs are in turn calculated via two successive flow computations. First, a steady two-dimensional inviscid solution of the flow field in the nozzle (advection scheme second order accurate) is obtained using a commercial solver [23]. The domain is a half-nozzle and a symmetry condition is imposed along the mid plane.

Successively, the properties of the shock discontinuity are determined by applying the so-called jump conditions, evaluated by means of the integral equations. The shock wave inclination  $\beta$  is calculated by first obtaining the undisturbed static flow quantities, e.g., pressure, density, Mach number and velocity, at the exit of the nozzle along the centerline from the simulation results, and then by solving the jump conditions for an arbitrary flow turning angle imposed by the obstacle, e.g., the semi-aperture angle of the wedge  $\theta$ , see the top left of Fig. 7.2 [157].

This approach assumes that conditions to the left and to the right of the steady shock are nearly constant. At the exit of the nozzle the flow conditions are uniform and thus uncertainties attributed to the calculation of fluid properties across a shock-wave with

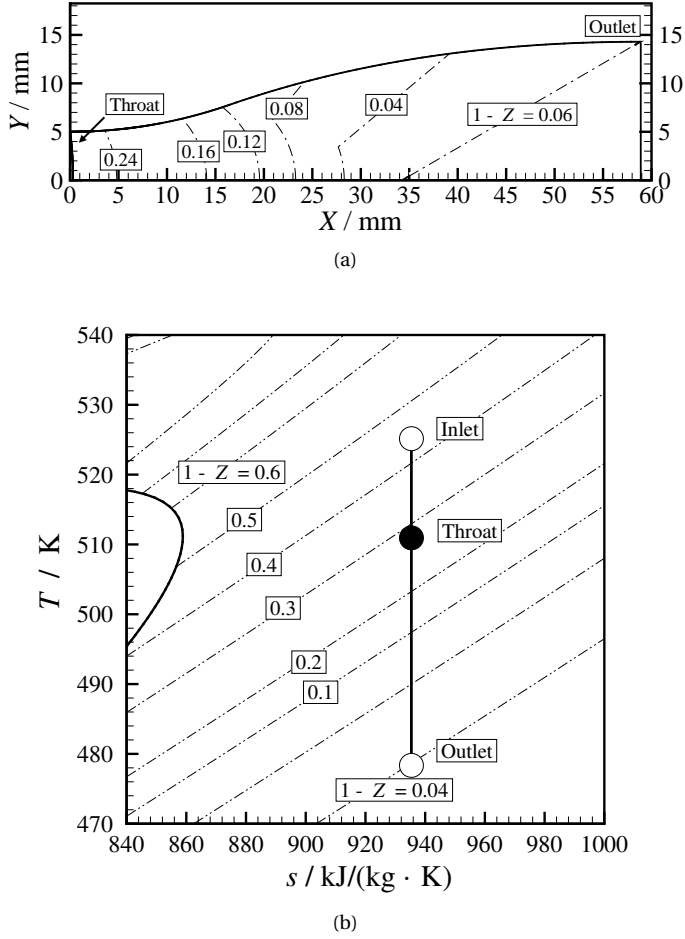


Figure 7.1: Supersonic flow of dense MM through a de Laval nozzle (Profile A), see Tab. B.1. n.b. only the diverging part is shown. The specifications of the flow experiment are reported in Table 6.1. (a) Upper half of the nozzle displaying contours of  $1 - Z$  (---) in the flow passage. The nozzle profile was generated with a program implementing the method of characteristics, see Ref. [163] and Sec 4.5.  $1 - Z$  lines were obtained with the same computer program. (b)  $T-s$  diagram of siloxane MM showing the isentropic expansion and contours of  $1 - Z$ . Fluid properties are estimated with an in-house program [93] implementing the multiparameter equation of state model documented in Ref. [373].

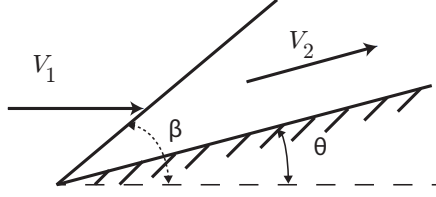


Figure 7.2: A wedge immersed in a supersonic flow, generating a shock wave.  $\beta$  is the shock angle,  $\theta$  is the semi-aperture angle of the wedge, 1 identifies the pre-shock conditions and 2 the post-shock conditions.

the jump conditions are negligible. Furthermore, in the envisaged experiment, the interrogation windows of the schlieren imaging will be restricted to the immediate vicinity of the wedge tip such that the wave geometry can be resolved with sufficient accuracy.

Figure 7.3 summarizes the flowchart of the calculation method to propagate the uncertainties of the closure coefficients of the thermodynamic model and of the boundary conditions (BCs) through the CFD simulation and the steady shock wave solver. The uncertainty of the input parameters are propagated through the numerical model via a Monte Carlo method [2]. The Monte Carlo calculation is initialized with 2500 samples distributed within the design space by means of a Latin Hypercube procedure. Figure 7.4(a) and Fig. 7.4(b) show the convergence results for two system response quantities which required the largest number of samples to converge.

## 7.5. MODEL UNCERTAINTIES

Two sources of model input uncertainties are considered in this preliminary study: the input data of the fluid thermodynamic model and the boundary conditions of the flow simulation. The vector of the model input uncertainty is listed in Table 7.1. The values of the input parameters are forward-propagated through the UQ numerical framework.

The thermo-physical properties of the siloxane MM have been computed via a look-up table approach, in which the thermodynamic property values are calculated with an in-house program [93]. The adopted thermodynamic model is based on the iPRSV cubic volumetric equation of state [293, 368, 371]

$$p = \frac{RT}{v - b} - \frac{a}{v^2 + 2bv - b^2},$$

where,

$$a = \left( \frac{0.457235 R^2 T_{cr}^2}{p_{cr}} \right) \alpha$$

and,

$$b = \left( \frac{0.077796 RT_{cr}}{p_{cr}} \right).$$

The  $a$  parameter uses the  $\alpha$  function proposed by Soave [355],



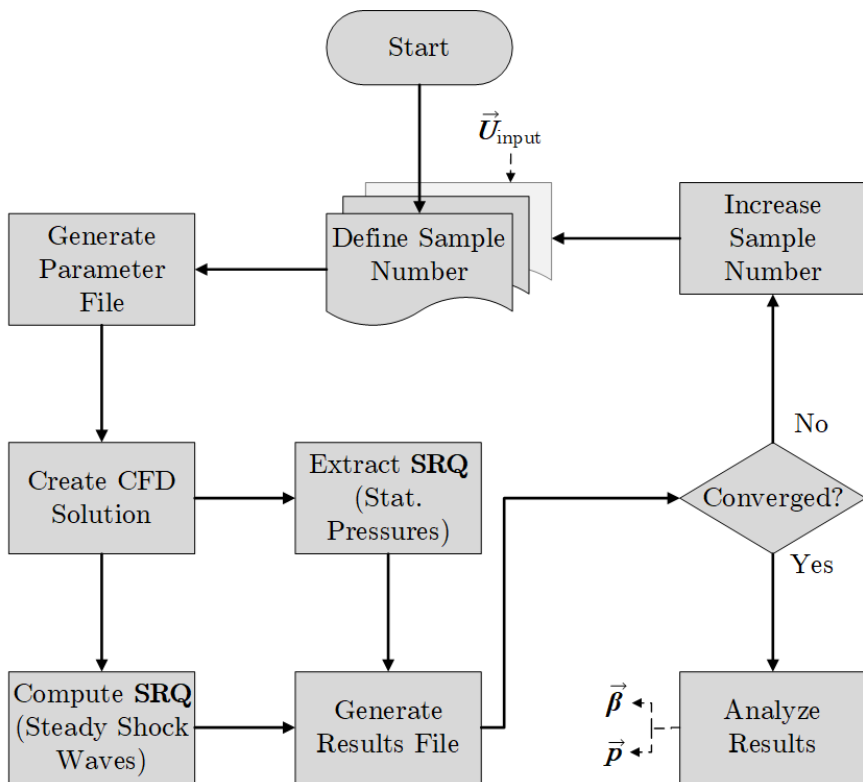
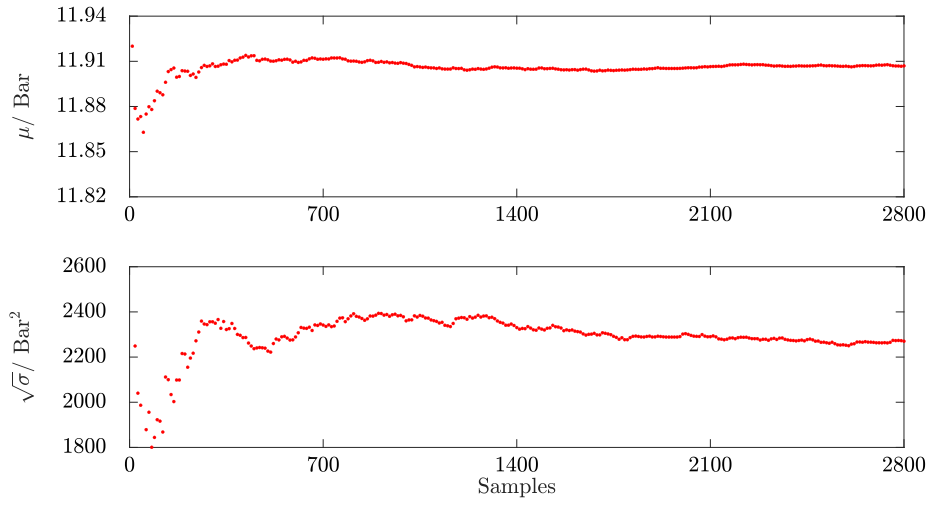
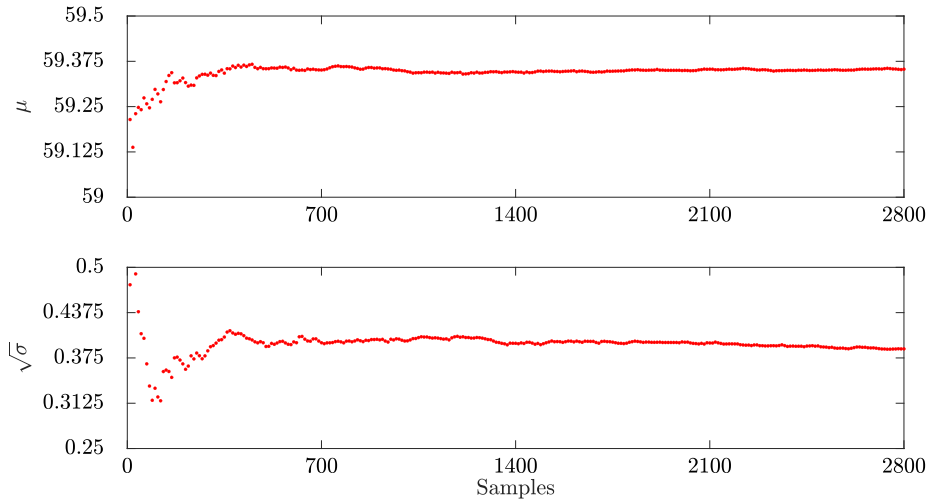


Figure 7.3: Simplified flowchart of the UQ calculation method.



(a)



(b)

Figure 7.4: Uncertainty quantification calculation: convergence plots of the first and second order moments of exemplary system response quantities. (a) static pressure at the throat; (b)  $\theta = 33^\circ$  at  $x = 56$  mm downstream from the throat.

$$\alpha = \left[ 1 + \kappa \left( 1 - \sqrt{\frac{T}{T_{\text{cr}}}} \right) \right]^2$$

with,

$$\kappa = \kappa_0 + \kappa_1 \left[ \sqrt{\left( A - D \left( \frac{T}{T_{\text{cr}}} + B \right) \right)^2 + E + A - D \left( \frac{T}{T_{\text{cr}}} + B \right)} \right] \sqrt{\frac{T}{T_{\text{cr}}} + C}.$$

and,

$$\kappa_0 = 0.378893 + 1.4897153\omega - 0.17131848\omega^2 + 0.0196554\omega^3,$$

where

$$\omega = -\log_{10}(p_r^{\text{sat}}) - 1, \text{ at } T_r = 0.7 \quad (7.6)$$

$A$ ,  $B$ ,  $C$ ,  $D$ , and  $E$  are constants set at 1.1, 0.25, 0.2, 1.2, and 0.01 respectively.  $\kappa_1$  is a parameter which is fitted to experimental vapor pressure data and is fluid dependent. The critical point values are physical properties affected by uncertainty, the uncertain difference between the measured value and the real value. The acentric factor and the  $\kappa_1$  are fitting parameters for which also an uncertainty of a different nature can be defined. This is the difference between the value and the best-fit value, which is unknown because it depends on the experimental data and their uncertainty. It is therefore assumed that the acentric factor and  $\kappa_1$  parameters are affected by a uniform uncertainty of  $\pm 5\%$  around the value obtained by fitting the model on the values of experimental saturated pressure data. Here the uncertainty of critical properties and of fitting parameters are all termed as *uncertainty*, and their values are reported in Tab. 7.1.

A study conducted by Iyer [197] concluded that the acentric factor and the  $\kappa$  parameter have negligible influence on the values of the system response quantities for the operating conditions of interest and thus were not considered in the uncertainty quantification exercise. The validity of this assumption has been checked by repeating the simulations systematically with values  $\kappa$  and  $\omega$  within the assumed uncertainty range. No significant contribution from these parameters to the output system responses was observed.

The complete thermodynamic iPRSV model is formed by the volumetric equation of state complemented by a fourth order polynomial function of the temperature for the ideal gas isobaric heat capacity in the form

$$C_p^{\text{ig}} = \eta_1 + \eta_2 T + \eta_3 T^2 + \eta_4 T^3. \quad (7.7)$$

The coefficients in Eqn. 7.7 are valid over the range  $273.15 \leq T \leq 673.15$  K and, for this exercise and for the sole purpose of testing the UQ framework, are assumed uniformly distributed with an arbitrary variation of  $\pm 15\%$  around the values resumed in Tab. 7.1. The values of these  $\eta$  coefficients are determined by means of fitting the polynomial expression on experimental data, see Ref. [90].

Table 7.1: Total expanded uncertainty of the input data of the thermodynamic model of MM and of the boundary conditions for the flow simulation. The distribution of the uncertainty is assumed uniform for all the fluid model parameters and boundary conditions of the flow solver.

Parameter	Nominal value	% uncertainty
<b>iPRSV thermodynamic model [77]</b>		
$T_c$ / K	245.45	$\pm 3^*$ [335]
$P_c$ / bar	19.40	$\pm 5^*$ [335]
$\omega$	0.42	$\pm 5^+$
$\kappa_1$	-0.05	$\pm 5^+$
$\eta_{01}$ / kJ/(k mol · K)	51.89	$\pm 15^+$
$\eta_{02}$ / kJ/(k mol · K)	$741.34 \times 10^{-3}$	$\pm 15^+$
$\eta_{03}$ / kJ/(k mol · K)	$-416.10 \times 10^{-6}$	$\pm 15^+$
$\eta_{04}$ / kJ/(k mol · K)	$70.00 \times 10^{-9}$	$\pm 15^+$
<b>Boundary Conditions (BC)</b>		
$T_0$ / °C	252.00	$\pm 0.2^+$
$P_0$ / bar	18.40	$\pm 0.5^+$

\* Experimental. + Assumed.

In order to quantify the influence of the variation of the polynomial coefficients on the response quantities, Bills [45] conducted a UQ study using the stochastic collocation and variance based decomposition method. It was concluded that the variation of the polynomial coefficients based on the values of the Sobol indexes is negligible, therefore these coefficients were not further considered in this study.

The other source of model input uncertainty originates from fluctuations in the stagnation values of temperature and pressure at the inlet of the nozzle, and these were selected as boundary conditions for the CFD simulations. The magnitude of these uncertainties were estimated based on the root sum square of the systematic and random uncertainties. The random uncertainty was assumed to be equal to the sensor accuracy. The model uncertainties are listed in Tab. 7.1. The probability density function of the uncertain parameters is assumed to be uniform due to the limited available data. The only value arbitrarily assumed as deterministic is the static nozzle back pressure, fixed at 2.1 bar. Such values guarantees the attainment of a clean supersonic flow within the nozzle for all admissible values of inlet total pressure, in agreement with what observed in actual experiments.

The numerical uncertainty  $U_{\text{num}}$  is made up of round-off, iterative and discretization error terms. The round-off error can be ignored providing double precision variables are used in the code. The iterative error is also neglected since solutions are converged to RMS residual levels of the order of  $10^{-8}$ . Furthermore, it was also ensured that the iterative error was reduced of at least three orders of magnitude below the discretization error, similarly to what is recommended in Refs. [128–130].

A mesh independence study was performed on seven grids varying between 3000 to 110,000 elements. To assess the contribution of the discretization error, a grid convergence study based on the procedure described in Refs. [25, 70] was performed. Specifically, the Richardson extrapolation method together with the Grid Convergence Index

approach of Roache [328, 329] was used to classify the importance of  $U_{\text{num}}$ . The outcome of the calculations showed that an unstructured mesh of 10,000 elements provided a sufficient balance between computational cost and uncertainty in the system response quantities, e.g., the shock angle and the static pressure. Given that  $U_{\text{num}}$  cannot be deemed negligible compared to  $U_{\text{input}}$ , see Eqn. 7.5, it is included in the calculation of  $U_{\text{val}}$ . The results are shown in Fig. 7.6 and 7.7. Both are considered to feature a 95 % confidence level.

## 7.6. PSEUDO-EXPERIMENTAL UNCERTAINTIES

Given the unavailability of actual measurements at the time of this writing, values that are expected to be representative of experimental data were generated by means of a numerical model. The thermodynamic properties of MM in this case were computed with the multi-parameter Span-Wagner model [231, 373], which is also implemented in an in-house code for thermophysical fluid properties estimation [93]. The Span-Wagner model was chosen because it is currently the most accurate model, if compared with other available thermodynamic models, like, e.g., the iPRSV thermodynamic model based on a cubic equation of state [368], also implemented in the in-house program. The results of these calculations are referred to as pseudo-experiment in the following.

Two types of uncertainties were considered, namely the uncertainties due to the fluctuations in the pseudo-experimental boundary conditions and the uncertainties related to the measurement technique. The uncertainty due to the fluctuations in the stagnation pressure and temperature at the inlet of the nozzle are random in nature, therefore Type A uncertainty according to Refs. [12, 274]. The uncertainty related to the measurement technique is of Type B, thus associated with systematic errors originating from the measurement chain. Type B uncertainties are estimated according to the well established procedure adopted for the calibration of wind tunnels [108, 263, 278].

With reference to the value of  $\beta$ , there are three predominant factors that may contribute to errors in the measurements, namely boundary layer effects on the wedge, uncertainties in the wedge model manufacturing and alignment, and errors in measuring the flow direction. According to the analytical studies of Molder [263], the boundary layer, which affects the flow turning angle  $\theta$ , causes an angular flow deviation  $U_{\text{BL}}$  of  $0.25^\circ$  in  $\beta$ . In the absence of any further information regarding the associated probability density function, this value is assumed to be uniformly distributed. The manufacturing uncertainties  $U_{\text{DF}}$  related to the wedge model were quantified by Molder [263] to be equal to  $\pm 0.1^\circ$ . Next, the uncertainty due to the model alignment  $U_{\text{FA}}$  was estimated by the same author to be equal to  $\pm 1^\circ$ .

As far as the static pressures measurements are concerned, the uncertainty  $U_{\text{SP}}$ , assumed to be uniformly distributed, is dependent on the accuracy of the adopted measuring device. The Scanivalve DSA3217 Digital Sensor Array (DSA) [343] was adopted for the ORCHID. It is a stand-alone electronic pressure scanner with an accuracy declared by the manufacturer to be equal to 0.05 % of the full scale, which varies along the expansion path.

Provided that the uncertainties are statistically independent, the overall uncertainty related to the measured values of  $\beta$  and static pressure can be computed by quadrature summation, once the uniform distributions have been transformed into equivalent

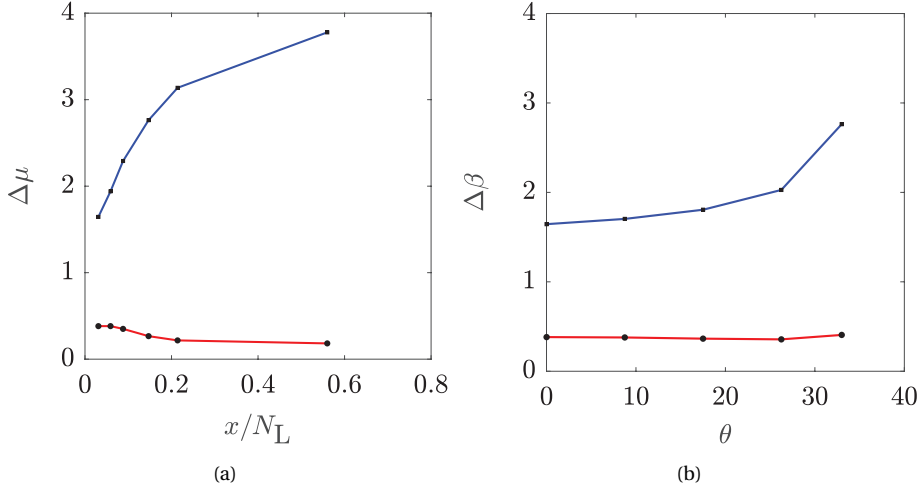


Figure 7.5: Comparison ( —  $|E|$  ) and validation ( —  $U_{val}$  ) metrics of the Mach and shock-wave angles for **(a)** Mach waves for incremented distances from the throat (reference point): 1. 3.1 mm ( $M = 1.1$ ), 2. 5.9 mm ( $M = 1.2$ ), 3. 8.8 mm ( $M = 1.3$ ), 4. 14.7 mm ( $M = 1.5$ ), 5. 21.4 mm ( $M = 1.7$ ), and 6. 56 mm ( $M = 2$ ); **(b)** Comparison (Eqn. 7.1) and validation (Eqn. 7.5) metrics of the shock-wave angle for five flow turning angles  $\theta = 0^\circ, 8.75^\circ, 17.5^\circ, 26.25^\circ, 33^\circ$  at the nozzle exit ( $M = 2$ ).

Gaussian distribution using the procedure recommended in Ref. [274]. Eventually, the overall uncertainties are given by

$$U_{c:\beta} = \sqrt{U_{BC}^2 + U_{BL}^2 + U_{DF}^2 + U_{FA}^2}$$

and

$$U_{c:p} = \sqrt{U_{BC}^2 + U_{SP}^2}.$$

The uncertainty related to a 95% confidence level is given by a final  $U_D$ , see Eqn. 7.5, which is equal to  $2U_c$  [12, 274].

## 7.7. RESULTS AND DISCUSSION

Figure 7.5(a) shows the validation comparison error  $|E|$  and the validation standard uncertainty  $U_{val}$  related to the shock wave angle  $\mu$  as a function of the simulated Mach number along the midplane of the nozzle, calculated with Eqn. 7.5 and 7.1, respectively. The results correspond to six locations along the nozzle midplane. Similarly, Fig. 7.5 shows  $|E|$  and  $U_{val}$  of  $\beta$  as a function of  $\theta$ . The displayed results refer to the exit of the nozzle.

The value of the validation comparison error  $|E|$  is lower than the value of the validation uncertainty  $U_{val}$  which, according to the validation method discussed in Sec. 7.2, means that the model predicts

1. the Mach number and thus the Mach wave angle correctly at all the locations along the nozzle midplane; and,

2. the shock wave angle adequately for all the sampled flow turning angles  $\theta$ .

Interestingly, the validation standard uncertainty  $U_{\text{val}}$  is larger for predicted  $\mu$  angles in the throat region and for  $\beta$  values close to the shock detachment angle. Such a trend indicates that the input uncertainties, which are propagated through the model, have a more pronounced effect on larger shock angles. Furthermore, the input uncertainties are more relevant when predicting system response quantities in regions in which the flow is highly non-ideal. In addition, the difference  $U_{\text{val}} - |E|$  is smaller for predicted  $\mu$  values close to the throat.

Together with a larger  $|E|$ , this suggests that the model predictions close to the throat are less accurate than those at the nozzle exit. To illustrate this aspect, the magnitude of the model uncertainty band is compared in Fig. 7.6 with the one associated to the measurements. More specifically, Fig. 7.6 shows the relation between the shock wave angle  $\beta$  and the flow turning angle  $\theta$  – i.e., the semi-aperture angle – for a diamond obstacle inserted in the flow. The uncertainty bars resulting from the calculation method are superimposed to the averaged values of both the model prediction and pseudo-measurements. The curve represents the resulting shock angles for five flow turning angles, namely,  $0.01^\circ$ ,  $8.75^\circ$ ,  $17.5^\circ$ ,  $26.25^\circ$  and  $33^\circ$  at the exit of the nozzle ( $x/L_N = 0.56$ ). The Mach wave angle is calculated with,

$$\lim_{\theta \rightarrow 0} \mu = \sin^{-1} \frac{1}{M_1} \quad (7.8)$$

at the other measurement points ( $x/L_N = 0.214, 0.147, 0.088, 0.059, 0.031$ ) along the nozzle, which indicate the distances from the throat. The relative contribution of  $U_{\text{input}}$ , i.e., the uncertainties associated with model parameters, compared to  $U_D$  (see Eqn. 7.5), namely those relative to the experiment, is approximately between 2 and 5 times larger, depending on the considered location along the nozzle. For example, the uncertainty bands of the model prediction of the Mach number increase in the flow regions more affected by non-ideal effects, e.g., the throat region. Furthermore, for a given position along the nozzle, the model uncertainty associated with the computation of the shock angle  $\beta$  gradually increases while approaching the shock detachment point, see Fig. 7.6. Finally, it is important to note that  $U_D$  remains approximately constant because the contributions from Type A uncertainties, i.e., the uncertainty related to the boundary conditions, is negligible compared to that of Type B uncertainties, i.e., instrumentation uncertainties, which is assumed constant in this validation exercise.

These results highlight that the model predictions are more uncertain in the regions where the flow non-ideality is more prominent. The thermodynamic properties sub-model could be improved, however the simulation framework can be deemed validated according to the prescribed metrics. This information is missing in the comparison between  $U_{\text{val}}$  and  $|E|$ , which must be then complemented by additional statistical indicators taking into account the extent of the uncertainty bands associated with the model predictions and the experimental value.

Figure 7.7 shows the dimensionless static pressure along the nozzle.  $P_{\text{tot}}$  is the inlet total pressure and  $L_N$  is the nozzle length for both the pseudo experiment and model predictions. Figure 7.8 shows the validation metrics  $|E|$  and  $U_{\text{val}}$  expressed in terms of dimensionless static pressure. Similarly to the shock wave angle predictions, the accuracy

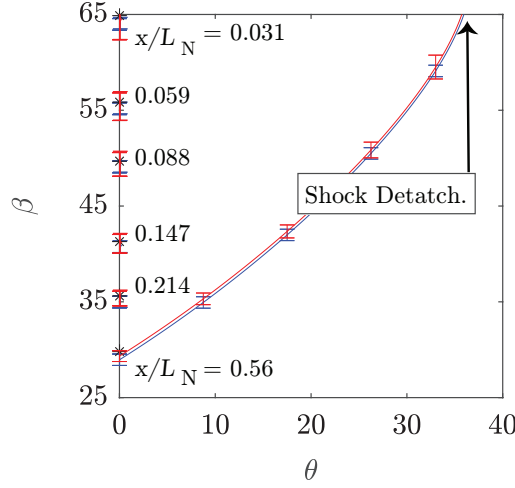


Figure 7.6: Shock wave angles diagram  $\theta - \beta - M$  reporting model iPRSV (—) and pseudo-measurement (—) uncertainties obtained with the UQ procedure.  $x/L_N$  is the nondimensional nozzle position with nozzle length  $L_N = 100$  mm. A flow turning angle  $\theta = 0$  at the measurement points  $x/L_N = 0.214, 0.147, 0.088, 0.059, 0.031$  corresponds to the flow Mach wave angle and thus to value of the Mach number at those locations along the nozzle. N.B. The throat is the reference point. The arrow indicates the point in which the shock detaches from the wedge tip.

of the model results for the static pressure is dependent on the location along the nozzle, as exemplified by the varying  $|E|$  and the difference  $|E| - U_{val}$ . The highest discrepancy occurs at the throat, while for location approaching the nozzle exit the comparison error  $|E|$  and  $U_{val}$  gradually decreases. Interestingly, the model and the pseudo experiment are in the closest agreement at the inlet; namely,  $|E|$  tends to 0. Moreover, in contrast with what is observed for  $\beta$  predictions, the error band associated to the model results is comparable in magnitude or even smaller than that expected for the measurements. This suggests that the static pressure values estimated by the model are less sensitive to uncertainties in the closure parameters of the equation of state model, or that the accuracy associate with the measurement chain is lower than that involved in measuring the shock angles. Therefore, an experiment aimed at the measurement of the shock angle is arguably more suited to assess the model validity if non-ideal gas effects are prominent.

## 7.8. CONCLUSIONS

This chapter describes a validation exercise which was performed to show how the predictive capability of a fluid thermodynamic model within an CFD solver suitable for NICFD flow simulations can be assessed by comparison with experimental data. To this end, a numerical framework based on uncertainty quantification analysis has been conceived and applied to the simulation of a supersonic nozzle expanding dense vapor of MM. Given the unavailability of experimental data at the time of this writing, pseudo-experimental data were generated for this purpose. The computed system response



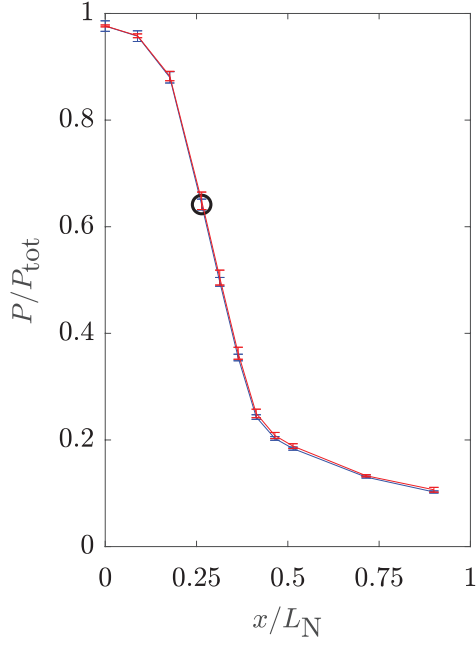


Figure 7.7: Variation of the static pressure along the nozzle midplane together with the uncertainty bands of the model results (—) iPRSV and of the pseudo-experiment (—).

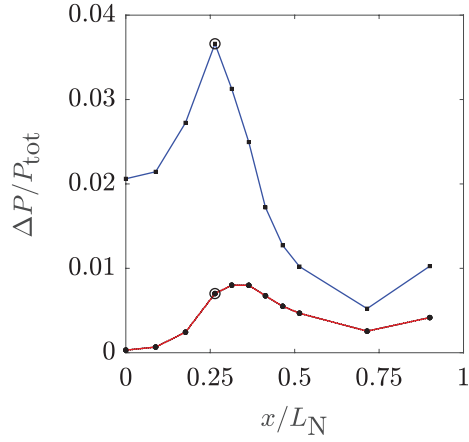


Figure 7.8: The metrics of the comparison (—)  $|E|$  and (—)  $U_{\text{val}}$ . Validation for static pressure vs. non-dimensional distance ( $x/L_N$ ) where  $L_N$  is the nozzle length along the expansion path. The eleven points correspond to the pressure taps. The circle represents the nozzle throat position. N.B. The inlet is the reference position.

quantities are the means and standard deviations of several flow and thermodynamic quantities, namely, shock wave angles and static pressures at various locations along a two dimensional de Laval nozzle.

The shock wave angle is more sensitive to the uncertainty associated with the input parameters of the thermodynamic model if compared to the static pressures. This implies that the shock wave angle is a relevant measurement for the planned CFD code validation campaign. According to the performed exercise, the flow solver predicts the Mach number and pressure with a higher degree of accuracy at the exit of the nozzle compared to the throat region, since the influence of the uncertainty of the thermodynamic model diminishes as the compressibility factor approaches one.

Finally, it can be argued that the framework and validation metrics can benefit from the introduction of additional statistical indicators taking explicitly into account the model uncertainty band. Ongoing work focuses on this aspect and on the extension of the approach to the validation of the turbulence submodels.

## ACKNOWLEDGEMENTS

The author would like to express their gratitude to Richard Dwight and Pietro Marco Congedo for their suggestions concerning code validation.



# 8

## FINAL REMARKS AND OUTLOOK

### 8.1. CLOSURE

The research described in this dissertation was motivated primarily by the need of obtaining highly accurate measurement data of paradigmatic non-ideal compressible fluid dynamic (NICFD) flows, in order to enable the quantitative validation of CFD software capable of simulating such flows for engineering and scientific purposes. The ORCHID, a unique facility conceived for this purpose, was therefore designed, realized and commissioned. The setup can generate steady-state flows of dense vapors and supercritical fluids of a variety of organic substances and is equipped with an optically accessible supersonic nozzle test section. Various commissioning experiments were performed and are documented in this dissertation, together with the detailed description of the setup and its operational procedures. In addition, another smaller setup, the NIVA, was used to assess the possibility of using the ORCHID to perform PIV with flows in the NICFD regime.

The main research question addressed by this dissertation, see Sec. 1.3, is

*How accurately can NICFD flows of dense organic vapors and supercritical fluids be simulated with current numerical tools?*

The findings of this research can be summarized as follows, by stating how other research questions cascading from the leading inquiry were answered as a result of the performed research activities.

1. *What are the key learnings from the previous studies involving NICFD theory, simulations and measurements, which can be useful for the design of the ORCHID and related experiments?*

Chapter 2 presents a historical compendium of literature describing the most relevant theoretical, numerical and experimental work in the research field of NICFD. The

theoretical development in this field of gas dynamics, dating back to the mid of the previous century, led to a conceptual infrastructure which is rather mature, though a further evolution can be expected, also because of the more recent and much needed experimental activity. The fundamental derivative of gas dynamics, a thermodynamic property of the fluid, is generally accepted as a key parameter for the evaluation of the non-ideality of gas dynamic flows.  $\Gamma < 0$  for at least a portion of the gas dynamic process is a necessary condition for the occurrence of non-classical phenomena, e.g., rarefaction shocks and compression fans. Negative  $\Gamma$  may occur only for very complex organic molecules, which are not suitable for the energy conversion systems of interest in this research program, therefore the ORCHID has been designed for substances which can be used as working fluids in power, propulsion and heat transfer systems whose flows at high reduced temperature and pressure feature  $0 < \Gamma < 1$ , therefore non ideal compressible fluid dynamic flows, excluding non-classical. Also in consideration of these previous studies, siloxane MM was chosen as the first working fluid for the ORCHID.

As typical in aerodynamics, also in the case of the study of NICFD flows, shock tubes, blow down and closed-loop tunnels were realized since the sixties. The experience related to blow-down setups, e.g., TROVA at the CREA Lab of Politecnico di Milano, the sc-CO<sub>2</sub> facility at the Gas Turbine Laboratory of M. I. T. and the R1233zd(E) facility at Imperial College London, highlighted that continuous experiments should be pursued because of the possibility of more easily obtaining the statistically significant data which are needed for CFD code validation.

The literature documenting the use of experimental setups to measure NICFD flows showed also that obtaining the static pressure along nozzle profiles or along foils is relatively easy to implement and provides accurate results. However, the working fluids adopted for those studies, SF<sub>6</sub> and CO<sub>2</sub>, cannot condense at the operating conditions of the experiments. On the contrary, the working fluids for which the ORCHID was designed can easily condense if exposed to temperature even slightly lower than those at the inlet of the nozzle test section.

Besides pressure measurements, also information on velocity, temperature and density distribution is needed for CFD code validation. Only the use of interferometry to measure the spatial distribution of density within the flow and schlieren imaging to estimate the value of the local Mach number in the diverging section of nozzle is documented in recent articles. The adoption of PIV to obtain the velocity field was considered, and a simpler experiment to evaluate its suitability was performed.

The body of scientific literature on the simulation of NICFD flows demonstrates that available RANS CFD codes coupled with modern thermodynamic models of the fluids are arguably sufficiently accurate for engineering purposes, provided that suitable numerical algorithms are employed. Previous studies demonstrated that the Roe scheme for the calculation of the fluxes and cubic or multiparameter equation of state models for the calculation of fluid properties provide a satisfactory solution to the problem of modeling NICFD flows.

2. *Which facility configuration and experiments should be designed to facilitate the means to obtain the experimental data needed for the validation of software?*

The learnings coming from the analysis of the state of the art related to experimental setups for NICFD investigations and the specific needs related to the validation of CFD codes capable of simulating NICFD flows, led to the choice of a facility capable of steady and continuous operation with a variety of working fluids. The preliminary and detailed design of the unique ORCHID is presented in Ch. 4 and 5, reporting and discussing the system and all the equipment. The desired characteristics of the setup were achieved with a rig operating according the Rankine cycle concept, and more specifically with a superheated and regenerated cycle configuration. The setup has been designed and successfully tested using MM as the working fluid, but it has been designed such that other fluids of interest for energy conversion applications can be tested, for example, MDM, MD<sub>2</sub>M, D<sub>4</sub>D<sub>5</sub>D<sub>6</sub>, pentane, cyclopentane, NOVEC649, PP2, PP80, PP90, and toluene. Its satisfactory functioning in terms of stability of operation and suitability for the desired experiment conditions is treated in Ch. 5.

Moreover, the setup was designed to accommodate two test sections, an optically accessible supersonic nozzle and an ORC turbine test bench, requiring vastly different mass flows. Experiments using the supersonic nozzle were designed to provide local flow measurements for the validation of high-fidelity CFD models. The turbine test bench is instead devoted to the characterization of the performance of the arguably most critical component of mini-ORC systems. Initially, the simplest experiment that was conceived to gather accurate data for the validation of NICFD-capable CFD codes was the supersonic isentropic expansion through a converging-diverging nozzle operating with a dense vapor and more complex flow configurations, e.g., those obtained by inserting a wedge or a needle in the diverging part of the nozzle will be studied successively.

The stability of operation over the large envelope of needed inlet test section conditions was achieved by adopting a volumetric pump, an electric heater, and a large fluid reservoir downstream of the setup condenser. A rather conventional control strategy based on few independent loops proved to be satisfactory. In the commissioning experiments, as showcase of the performance of the balance of plant, the following operating conditions were obtained. The evaporation temperatures and pressures were in the range 240 – 275 °C and 8 – 22 bar, with mass flow rates of 0.17 – 1.26 kg/s. The condensing pressures were in the range 0.3 – 1.2 bar. These measured quantities fluctuated with standard deviations in the range of  $\pm 0.21 - \pm 0.655$  °C,  $\pm 0.015 - \pm 0.055$  bar and mass flow rate of the working fluid within the range  $\pm 1.38 \times 10^{-4} - \pm 1.55 \times 10^{-3}$  kg/s.

3. *What are the most feasible and accurate measurement techniques that could be used for studying these fluid flows?*

Among all the possibilities offered by currently proven flow measurement technology, the measurement of static pressure along the nozzle and the estimate of the local Mach number based on the processing of Mach lines recorded with schlieren imaging have been proven feasible and sufficiently accurate for the assessment of the models implemented in modern NICFD-capable flow solvers, in particular the fluid thermodynamic models. Chapter 6 describes in the detail the first successful experiments, whereby the pressure and local Mach number along the two-dimensional nozzle were measured and compared to CFD simulations. In order to obtain high spatial resolution

for the measurement of the static pressure along the nozzle profile, a pressure scanner was selected instead of flash-mounted pressure transducers. The pressure scanner is connected to the pressure taps with long thin pipes, which can be purged with nitrogen to prevent the accumulation of condensate. Pressure measurements were reliable as long as the procedure described in Ch. 6 and C.3 is carefully followed.

In addition, first steps towards the implementation of PIV have been successfully accomplished and documented in Ch. 3. In this first study, it was demonstrated that the vapor is sufficiently transparent for PIV and that the tracing particles follow the flow with sufficient approximation for the estimation of the velocity field. However, due to considerations about the difficulty of managing PIV particles within the ORCHID led to the adoption of the schlieren technique for the first experiments, leaving the implementation of the PIV technique for a following phase of the project.

*4. Can all the main error sources in the designed experiment be identified and can the uncertainties be adequately quantified?*

Chapter 6 describes a systematic study aimed at identifying all the main error sources and evaluate the uncertainty of the performed pressure and Mach number measurements. In accordance with the recommendations of the international organization for standardization (ISO) the uncertainty sources associated with measurements were classified and evaluated as Type A uncertainties (those dependent on measurements statistics) and Type B (epistemic) uncertainties. Type A and B uncertainty values were used to compute the total expanded uncertainty. Static pressures were measured with total expanded uncertainties in the range of  $\pm 0.0035 - 0.028$  bar for total pressure values at the inlet of the nozzle in the range of 15 – 20 bar, and Mach numbers were estimated with total expanded uncertainties in the range of  $\pm 0.045 - 0.1$  with the highest values observed for the measurements close to the nozzle outlet where the Mach number is approximately equal to 2. It can be argued that this level of accuracy is sufficient for the validation of CFD codes to be used in engineering applications, such as the design of supersonic ORC turbines.

*5. What validation method should be adopted to assess the accuracy of NICFD-capable CFD codes?*

An NICFD-capable simulation software should be validated against a variety of test cases which cover the typical operating range of the turbomachinery of interest, various working fluids of different molecular complexity and possibly all relevant phenomena, including therefore shock waves, boundary layer, shock wave-boundary layer interaction, condensation and possibly others. The ORCHID is arguably suitable for the generation of all these types of flows, but in the time allocated for this research it was possible to commission the setup and demonstrate its capability only for experiments aimed at validating inviscid flow solvers. For this type of experiments, the repeatability and statistical significance of the measurements for the software validation have been demonstrated and discussed in Ch. 6 and 7.

In the preliminary study documented in this dissertation, the SU2 open-source code

was adopted, because it was recently extended by the TU Delft Propulsion and Power group in order to simulate NICFD flows. The code includes the generalized Roe scheme for the calculation of the advective fluxes, which previous studies demonstrated suitable for this type of flows, and can compute fluid thermodynamic properties either with a Peng Robinson model directly incorporated into the code, or by means of an external library implementing a variety of complex models.

Chapter 7 treats a preliminary and exploratory step towards the development of a validation method suitable for fluid dynamic solvers that can simulate NICFD flows. The ASME verification and validation method, an industrial standard for assessing the credibility of a software code, was tested by using computer-generated data mimicking the data that could be recorded in actual experiments, as these were not available at the time of this study. The considered model uncertainties are those associated to the parameters of the fluid thermodynamic model, e.g.,  $T_c$ ,  $P_c$ ,  $\omega$ ,  $\kappa_1$  and the coefficients of fourth order polynomial function used for the estimation of  $c_p^{\text{ig}}(T)$ . The boundary conditions of the simulation were also considered uncertain in the analysis. Uncertainties pertaining to the fluid composition were not considered at this stage of the research but should be assessed in future work.

## 8.2. FUTURE WORK AND RECOMMENDATIONS

The first improvements that should be implemented resulting from the experience acquired during the work that led to the results documented here are related to the type of experiments already carried out and to the adopted measurement techniques.

The Mach number estimation method and the measurement of the boundary conditions of the experiment are influenced by a number of identified error sources and unsatisfactory implementations, therefore, in order to improve these measurements, the following should be considered.

- The schlieren measurement chain hardware should be modified by adding a soft-edge graduated neutral-density filter, and a schlieren head with the same diameter but smaller focal length which would allow to better visualize flow regions close to the nozzle throat characterized by large changes in density. Furthermore, smaller fields of view should be imaged, especially when acquiring data in the kernel region of the expansion because it would allow to increase the spatial resolution of the measurements, hence improve on the accuracy of the estimated Mach numbers;
- a vapor flow meter should be added upstream of the nozzle test section to better predict the critical flow value. The current liquid mass flow rate measurement after the main pump may differ from the actual mass flow rate in the nozzle due to the imperfect sealing of the bypass valve when closed. A flow meter based on the Coriolis working principle is preferable because it can directly measure both mass flow and density;
- the nozzle throat dimensions during the experiments should be accurately quantified to reduce the uncertainty arising from thermal elongation at the high temperatures of operation of the nozzle. The nozzle height can be measured during



the experiments by image postprocessing and the actual value in millimeters can be estimated based on the known distance between two points in the calibration image. The nozzle width can be measured by means of an optical displacement sensor based on chromatic confocal imaging. This type of sensor can measure distances through transparent materials and fluids, therefore in principle, it can also be used to derive point-wise measurements of density.

- a pressure transmitter should be added to measure the pressure of the settling chamber of the nozzle test section. The total pressure at the nozzle inlet is currently measured through a channel of the Scanivalve pressure scanner. This device needs periodic purging to remove condensate in the pressure lines. As this operation requires manual intervention and is complicated to carry out, the measurement of the total inlet pressure is often recorded only for a short period of time. This leads to higher uncertainty in the total inlet conditions of the nozzle;
- the Mach line detection procedure used to compute the Mach number along the nozzle midplane should be improved in order to attain an even higher level of accuracy. There are several stages of the procedure which currently require an intervention of the user. The automation of these manual operations will make the experimental data postprocessing less time consuming, and, to a certain extent, more repeatable. For example, the optimal image filtering and binarization parameters should be automatically calculated. These parameters could be obtained by defining an optimization problem whose objective is to minimize the Mach number uncertainties, see Beltrame [35];
- the static pressure measurements and acquisition of schlieren images used for the quantification of the Mach number along the expansion process should and will be recorded simultaneously. This was not done during the commissioning phase, only because it was decided for a step-wise approach, in order to facilitate the learning process. Therefore, first an experimental campaign was focused solely on schlieren images, and successively another set of experiments was dedicated only to the acquisition of the nozzle pressure profile.

Once these planned improvements will be accomplished, another experimental campaign will be performed in order to record data over a large set of operating conditions, aimed at a first proper validation of the SU2 software for the case of inviscid supersonic flows in NICFD conditions. To this end, the validation method documented in Ch. 7 will also be improved and properly tested. For example, alternative and more computationally efficient sampling methods such as stochastic collocation can be adopted at the potential expense of adding additional uncertainties arising from creating surrogate models. One way of improving the validation of CFD codes will also be accomplished by generating flows with strong shocks by inserting models like a needle or a wedge in the diverging part of the supersonic nozzle.

Shock wave patterns in flows affected by NICFD effects are scientifically interesting and are relevant for the design of efficient NICFD turbomachinery because they are common in supersonic and transonic cascades, albeit unwanted, due to the relevant losses they cause. It was shown in Ch. 7 that the modeling of flows with shocks with higher

strength is very sensitive to input parameters, e.g., the stagnation conditions or the closure coefficients of the thermodynamic model. Preparations for these experiments are already underway at the time of this writing.

In addition to modifications of the current setup and instrumentation, additional measurements besides the evaluation of the Mach number and of the static pressures along the nozzle would allow for the collection of a more exhaustive set of experimental data for the validation of CFD codes for the simulation of inviscid NICFD flows. More in detail,

- in order to validate the adiabatic flow assumption, the heat flow through the metal nozzle profile could be computed by estimating the temperature at the inner surface of the nozzle profile and by measuring the temperature at a small distance from that surface by means of thermocouples.
- Two-dimensional absolute density measurements along the nozzle could be obtained with shearing interferometry, or background oriented schlieren together with a measured reference constant of integration, e.g., a reference density provided by the Coriolis flow meter [123, 135, 290] or chromatic confocal imaging [37, 290].
- Accurate velocity measurements would greatly enrich any CFD code validation method. The results of the study documented in Ch. 3 shed light on many of the possible issues related to performing PIV on flows of dense organic vapor. The LDV seeding system that the scientists at the CREALab of Politecnico di Milano designed and commissioned could inform the design and realization of a similar device for the ORCHID. The seeding could be continuous over a time interval, and this would allow to fine-tune the particle distribution. However, still a number of problems related to the contamination of the ORCHID components with seeding particles must be analyzed and solved. For example, if the tracers are not correctly filtered, they may deposit on the plates of the heat exchangers decreasing their performance or hamper the correct operation of valves and pumps. Furthermore, velocity measurement methods based on flow seeding would be affected by local variations of the refractive index as discussed in Sec. 3.2 and 6.6 and its relevance must be further assessed. A non-intrusive possibility of measuring the flow velocity may be more attractive and may be achieved by means of a filtered Rayleigh scattering (FRS) system. This technique has already been employed to measure the spatial distribution of velocity in high-speed air flows [118, 147]. Notably, the large molecules of organic vapors make this technique very sensitive because they would scatter much more light if compared to air molecules. However, the application of filtered Rayleigh scattering to measure the velocity of dense organic flows would require a specific study and customization, thus becoming itself a research topic.

The ORCHID would also be suitable for novel scientific research involving flows of other substances, including mixtures, and more complex flow configurations. Examples of other types of studies are

- the investigation of more complex flow phenomena, like boundary layer formation and evolution and laminar-to-turbulence transition. The influence of NICFD conditions and of molecular complexity on these phenomena have scarcely been studied and experimental data are at the basis of the development of numerical models. For example, Refs. [28, 29] describe a method to detect boundary layer transition in air flows with laser-interferometric vibrometry (LIV) and the study of mean values and fluctuations of the stream-wise and wall-normal velocity components with Laser Doppler Anemometry (LDA). However, a recent numerical study on the boundary layer in NICFD flows conducted by Dijkshoorn [116, Ch. 5] shows how it could prove difficult to experimentally characterize the physics inside a boundary layer along a supersonic expansion of a dense organic vapor with current optical measurement techniques. Reasons are attributed to the fact that, under the operating conditions typical of ORC expanders, the thickness of the boundary layer is too small to accurately resolve characteristics such as velocity profiles or density variations. These findings are consistent with those resulting from the measurements of Duff [123]. Micro-PIV techniques should be developed to overcome this issue.
- the experimental characterization of metastable condensing flows. This type of flows are relevant for the design and operation of components of next-generation thermal power and refrigeration systems [119, 134, 139, 158, 265, 276, 339, 352, 367, 418]. The design of these components requires the development of complex two-phase CFD tools capable of correctly modeling droplet formation. Droplets/ bubbles dispersed within an expanding flow can be characterized by shadow-based techniques, i.e., high-magnification shadow imaging. The simultaneous measurement of velocity could be attained with other flow imaging methods like particle image velocimetry (PIV) or filtered Rayleigh scattering velocimetry.

Finally, the ORCHID was designed also for another class of experiments, more directly linked to applications. A high-speed radial inflow ORC turbine has already been designed and will be realized as a part of the upcoming research titled *Airborne Energy Harvesting for Aircraft* ARENA. The envisioned work for studying the complex flow phenomena in ORC expanders will be carried out into two phases; namely, a series of validation experiments with stationary linear blade cascades, and a sequence of performance measurements / studies using the ORCHID turbine.

The first stage of the research demands for several small modifications to the nozzle test section of the ORCHID such that it can incorporate a series of linear blades, similar to those of the experiments discussed in Ref. [357, 408]. Proper measurement techniques will be selected to characterize total quantities and velocity or density distribution. Pressure measurements on blade surfaces and side walls will be recorded by means of the existing Scanivalve system.

The design and performance of the mini ORC turbine will be assessed with measurements of the mass flow rate at the inlet and of temperatures and pressures at the inlet outlet and stator-rotor interface. Measurements of the torque and rotational speed will allow to obtain performance maps [66, 219, 249]. Furthermore, velocity measurements in the turbomachine passages are envisaged for the longer term, similarly to what was

accomplished in the turbomachinery experiments described in Ref. [303, 407].

## ACKNOWLEDGEMENTS

The author would like to express his gratitude to Dominic Dijkshoorn and Bertrand Mercier for their suggestions regarding future experiments and associated measurements.





## SETTLING CHAMBER

The honeycomb used in the settling chamber of the nozzle test section is shown in Fig. [A.1](#). The diameter and honeycomb size are specified in Sec. [6.3.1](#).

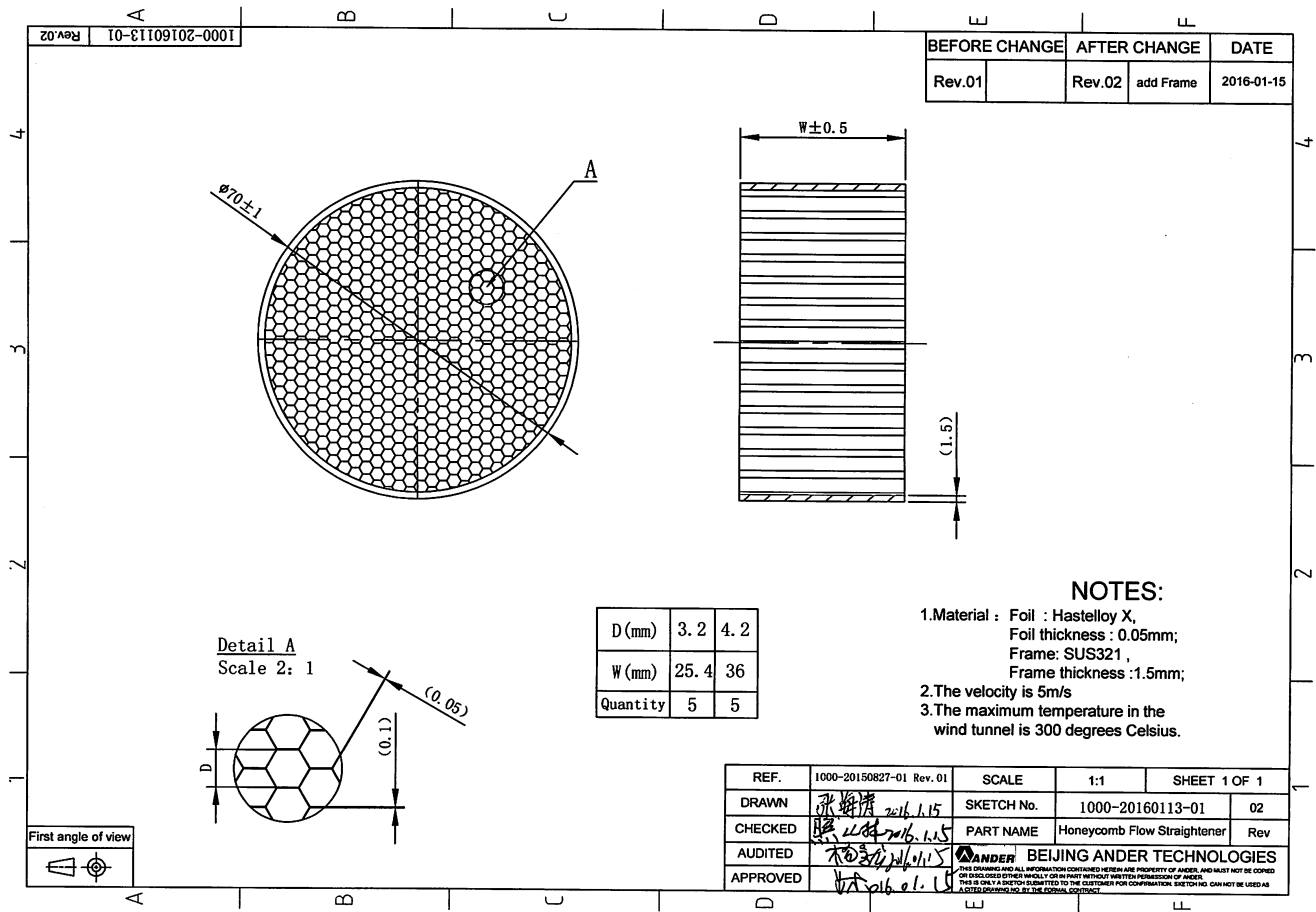






Figure A.1: Honeycomb used in the settling chamber of the nozzle test section to make the flow more uniform.

# B

## NOZZLE PROFILES AND MESHES OF THE FLOW DOMAINS FOR CFD SIMULATIONS

The coordinates of the nozzle profile are listed in Tab. [B.1](#).

Table B.1: Coordinates of the nozzle profile A and of the nozzle profile B.

Profile	Description	Original Nozzle Design Profile Data	STEP File Data
Nozzle A	Profile used in PR016		
Nozzle B	Profile used in PR025-NT001 PR027-NT001/2		

The discretised domain used for the CFD simulations documented in Sec. [6.9.3](#) is shown in Fig. [B.2](#) and [B.3](#).



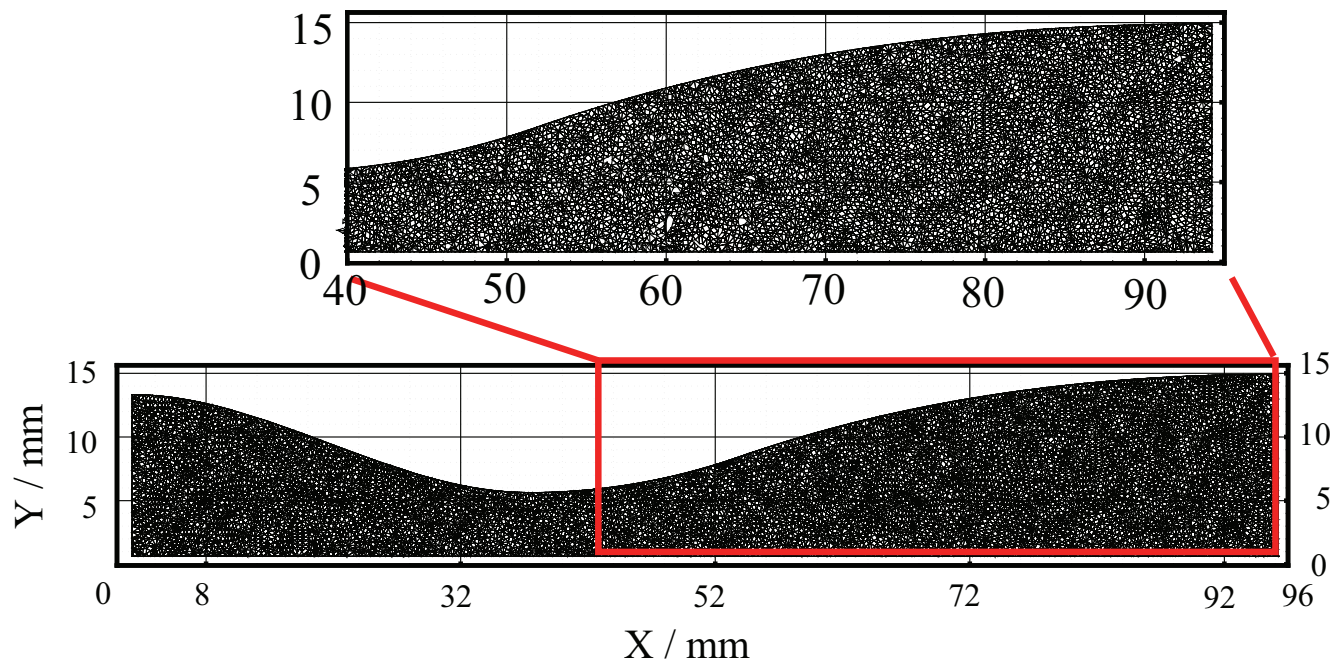


Figure B.1: Mesh used for the Euler CFD simulations of the nozzle featuring profile A. The flow core region is discretized with 10,000 tetrahedra.

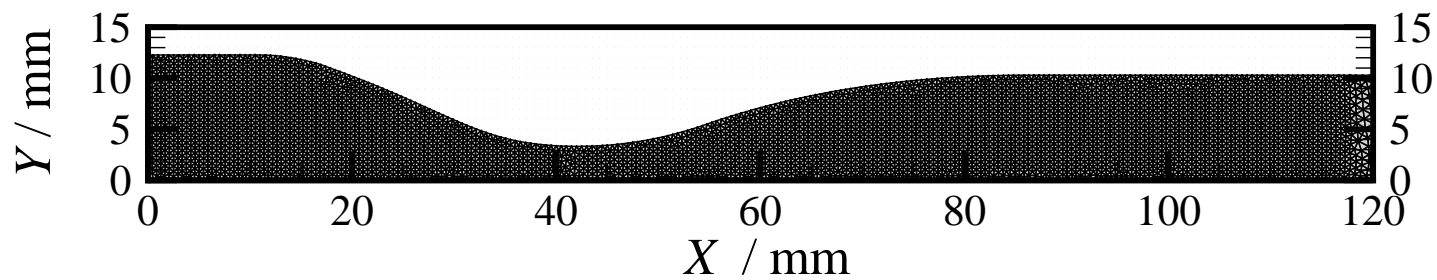


Figure B.2: Mesh used for the Euler CFD simulations of the nozzle featuring profile B. The flow core region is discretized with 15,000 tetrahedra.

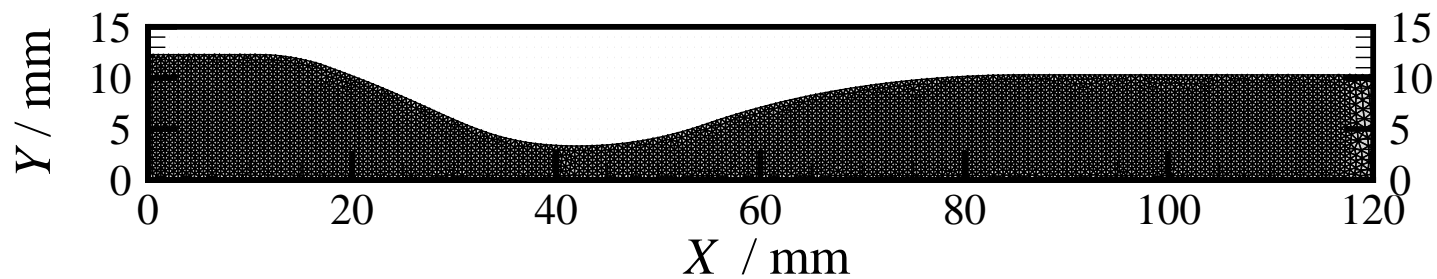


Figure B.3: Mesh used for the RANS CFD simulations of the nozzle featuring profile B. The flow core region is discretized with 15,000, while 2,000 prism elements are used to simulated the boundary layer.

# C

## SCANIVALVE PRESSURE MEASUREMENT SYSTEM

### C.1. PIPING & INSTRUMENTATION DIAGRAM

The P&ID of the pressure measurement system adopted to evaluate the static pressure along the nozzle profile (*DSA3218 Scanivalve* pressure scanner) is shown in Fig. [C.1](#). Twenty pneumatic taps are routed from the nozzle test section to liquid traps.

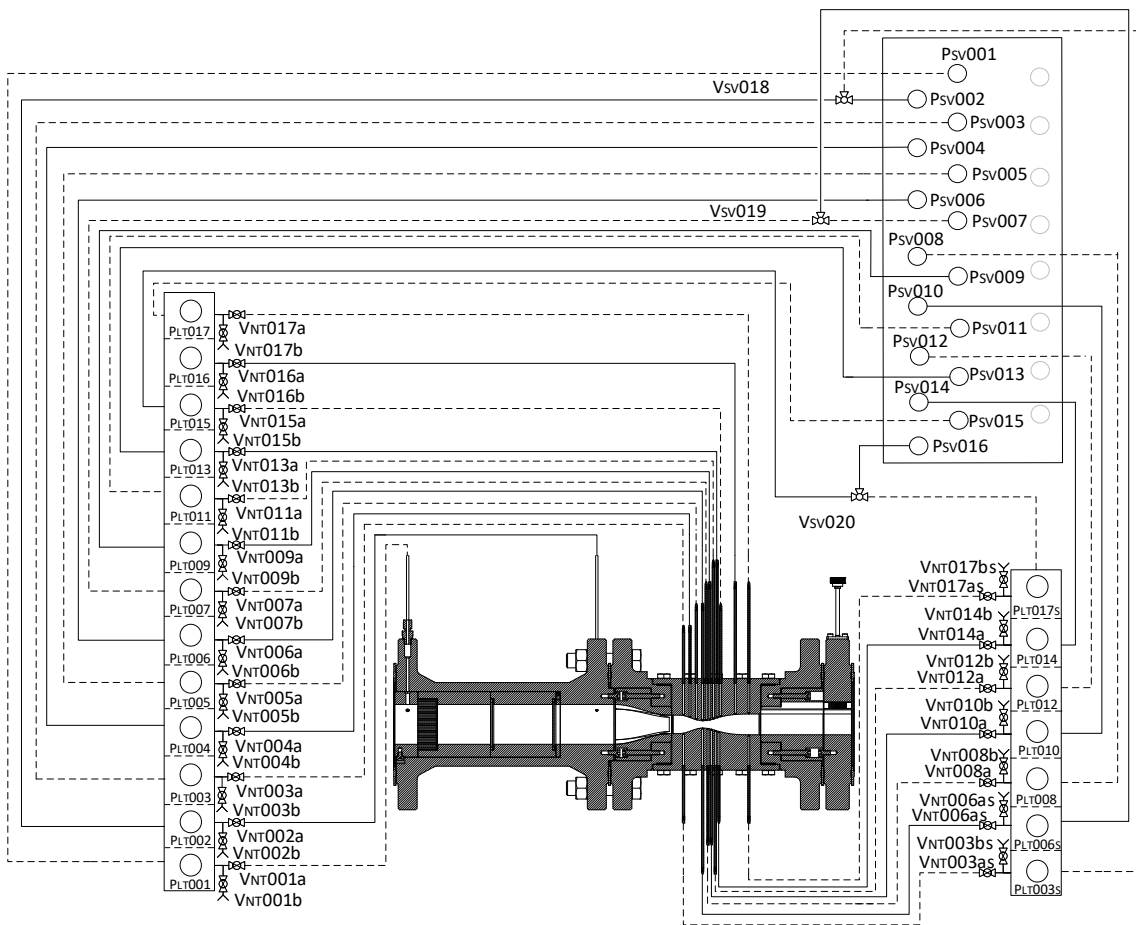


Figure C.1: Piping & Instrumentation Diagram (P&ID) of the pressure measurement system (*Scanivalve* pressure scanner) used to acquire the static pressure along the nozzle.

## C.2. PNEUMATIC CIRCUIT FOR CONTROL AND OPERATION

Aside to the measurement circuit already discussed in Sec. 6.4, a pneumatic circuit is needed to operate the *Scanivalve* DSA3218 module, see the P&ID control schematic in Fig. C.2. Actuating an internal system of valves allows to change between three operating modes, namely, *purging*, *scanning/measuring* and *zero-offset calibration*. The gas used for the pneumatic valves must be clean and dry, therefore instrument grade air or nitrogen. Since the inert gas must also be used for purging purposes aside to actuating internal valves, nitrogen was chosen. To prevent damage to the sensors due to overpressure, the nitrogen pressure is reduced with two dedicated throttling valves: the supply pressure of nitrogen for purging is 25 bar, while that for the actuation of the *Scanivalve* internal valves is in the range 6–8 bar. Figure C.2 shows the eight pressure ports and the sixteen measuring ports.

One of the ports of the control circuit is the purge supply port (PRG SUPPLY) which is used to purge the pressure measurement lines and ensures that any condensate fluid is removed. In order to avoid that the pressure sensors are damaged during purging, the sensors must be isolated from the measuring ports. This operation is accomplished by supplying nitrogen at 6–8 bar to the PRGCTL and CTL1 ports.

In the event that the module must be calibrated, which should occur once a year, then the Calibration (CAL) port provides a means to apply a known calibration pressure to a single port and have it manifolded to all of the transducers of the related pressure range. The calibration procedure must be performed by the supplier. The module has 16 sensors with three specified full scale values. During normal operation, the internal valve connected to this port is closed. The sensors of the *Scanivalve* are differential pressure sensors, measuring the difference between the ambient pressure and the pressure at the various measurement ports. The differential pressure sensors are connected to the ambient through the REF port.

## C.3. OPERATION OF THE DEVICE

Before the *Scanivalve* measurements can be started, the ORCHID should be running, the nozzle test section should be already operating and the steady operating conditions be reached. Furthermore, after turning on the DSA module, a minimum of 30 minutes before collecting data is required to allow the module temperature to become stable. It is recommended that if time allows, the warm-up period should be extended to one hour for most applications.

All the procedures must start and end with the device in a default state as described in Sec. C.3.1. When the vapor is circulating through the test section, the fluid fills the pressure lines and condensate may form, possibly filling them up to the ball valves isolating the *Scanivalve* from the process. The purging operation is, thus, the first to be performed. Afterwards, at the beginning of the experiments, it is recommended to apply the zero offset calibration procedure of the piezoresistive sensors. If data are recorded over a long period, or if condensate have filled the liquid traps, these procedures must be periodically repeated. At the end of each measurement campaign, the pressure lines must be purged and the ball valves  $V_{NT\#a}$  isolating the *Scanivalve* from the process must be closed.

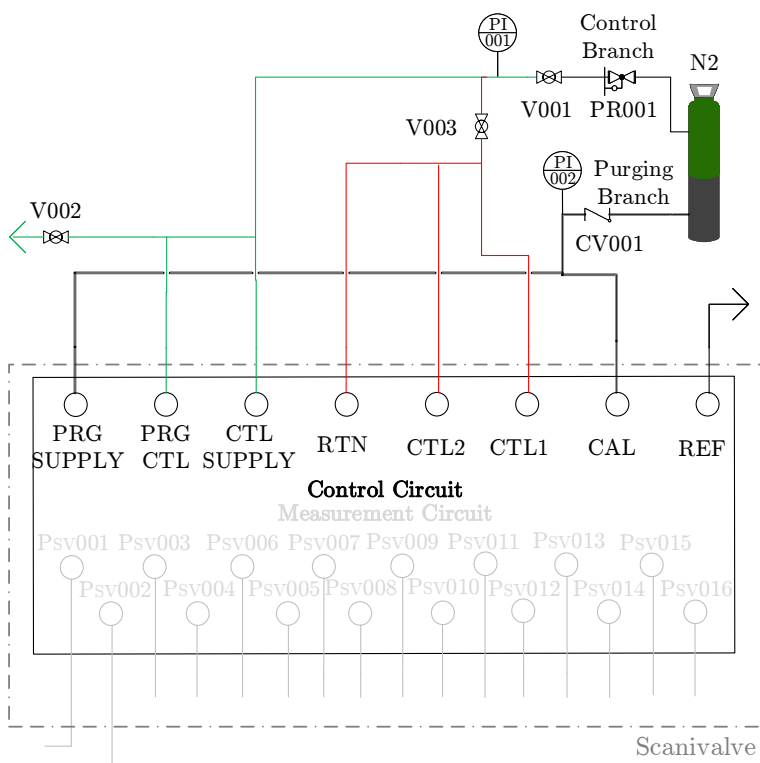


Figure C.2: Pneumatic control circuit for the actuation of the Scanivalve module. The complementary measurement circuit is shown in Fig. 6.10. See Tab. 5.3 for the legends and symbols. The incoming N2 pressure must not exceed 30 bara. The full scale value of PI001 is 10 bara and of PI002 is 30 bara.

### C.3.1. DEFAULT STATE

In the default state, all the valves of the control circuit of the *Scanivalve DSA3218* module and those on the pressure lines ( $V_{NT\#a}$ ) are closed (see Figure C.2), with the exception of V003. The pressure of the nitrogen line used to actuate the valves of the *Scanivalve DSA3218* module must not exceed 8 bar. This is achieved by manually regulating the pressure reducing valve PR001.

### C.3.2. PURGING

The pressure of the nitrogen line used for purging should always be 1 bar greater than the maximum working fluid pressure (around 23.5 bar) and should never exceed 51 bar. The steps of the procedure are as follows:

1. open the V001 valve;
2. open the CTL1, CTL2, and PRGCTL valves. The sensors are now isolated from the pressure lines;
3. open the PRG valve in order to supply the purge pressure to all lines;
4. open all valves on the pressure lines and wait for the removal of the condensate by monitoring the sight glass of the liquid traps;
5. close the PRG valve to stop the supply of nitrogen to the lines;
6. close the CTL1 and CTL2 valves. The corresponding internal valves of the *Scanivalve DSA3218* module remain in the same position;
7. close the V001 valve and open the V002 valve to vent the nitrogen line connected to the control panel;
8. open the CTL1 and CTL2 valves. The internal valves of the *Scanivalve DSA3218* module switch to the default position;
9. close the CTL1, CTL2, PRGCTL, V002 valves. The system is in a state where it can be brought back to the default state or the acquisition procedure can be started.

### C.3.3. DATA ACQUISITION

The *Scanivalve DSA3218* module is in measuring mode if all its internal valves are in their *default* state. Therefore, it must be ensured that the nitrogen line of the control circuit is not pressurized. This is achieved by

1. opening all valves used to control the *Scanivalve DSA3218* module, i.e. the CTL1, CTL2, RTN, CTL, and PRGCTL valves. The valve V003 should be already open;
2. checking the reading of the pressure indicator PI001 and if it is greater than 2 bar, then open the V002 valve;
3. closing all the valves used to control the *Scanivalve DSA3218* module, except for the V003 valve. The module is ready for data acquisition.

It is important to always monitor the liquid level in the liquid trap. In case they become completely full, they should be drained with caution by means of V00#b.



### C.3.4. ZERO OFFSET CALIBRATION

This operation must be performed once the warm up of the *Scanivalve DSA3218* module has ended, and the purge operation has been concluded. The zero offset calibration procedure must be performed every time the module is turned on, because the offset values are stored in volatile memory and due to the drift that piezoresistive sensors are prone to if exposed to temperature variations. The steps of the procedure are as follows.

1. If needed, perform steps 1 to 3 of the data acquisition procedure in order to vent the control lines;
2. close the V003 valve and open the CTL1, CTL2, and RTN valves;
3. open the V001 valve and, if needed, regulate the nitrogen pressure to a value of 6 – 8 bar;
4. open the CTL SUPPLY valve in order to inject the nitrogen;
5. execute the CALZ routine of the *Scanivalve DSA3218* module controller;
6. close the CTL1, CTL2, and RTN valves; The corresponding internal valves of the *Scanivalve DSA3218* module remain in the same position;
7. close the V001 and open the V002 valve to vent the nitrogen lines connected to the control panel. The CTL SUPPLY valve return to the default position. Close the V002 valve when this operation is concluded;
8. close the CTL SUPPLY valve; and,
9. open the V003 valve. The system is back to the default state.

### C.3.5. FLOW SYMMETRY VERIFICATION

If the flow in the nozzle is characterized by symmetry with respect to the horizontal mid-plane, the pressure measured by two pressure taps on the two opposite nozzle of the profiles must be the same, but the axial distance from the nozzle entrance must also be statistically equal.

To perform this type of experiment, the three-way valves V<sub>SV</sub>018/19/20 are actuated to connect the *Scanivalve* ports with the T003s, T006s, T017s taps, which are located on the bottom profile, see Fig. 6.8. These replace, respectively, the T002, T007 and T015 taps of the baseline valve configuration of the pressure measurement system. The three tap pairs located at equal axial distance from the nozzle inlet, and, thus, used to check flow symmetry are T003 - T003s, T006 - T006s, T017 - T017s.

## C.4. COMMISSIONING

A process run, PR.016, was conducted with the specific objective of commissioning the *Scanivalve DSA3218* module. During this experiment, only the pressure ports P<sub>SV</sub>001-002, namely the settling chamber pressure taps, were open. The other pressure ports were isolated from the process by closing the V<sub>NT</sub>003 - 017a valves and by opening the V00<sub>NT</sub>003 - 017b drainage valves. This circuit configuration allows to avoid damaging the

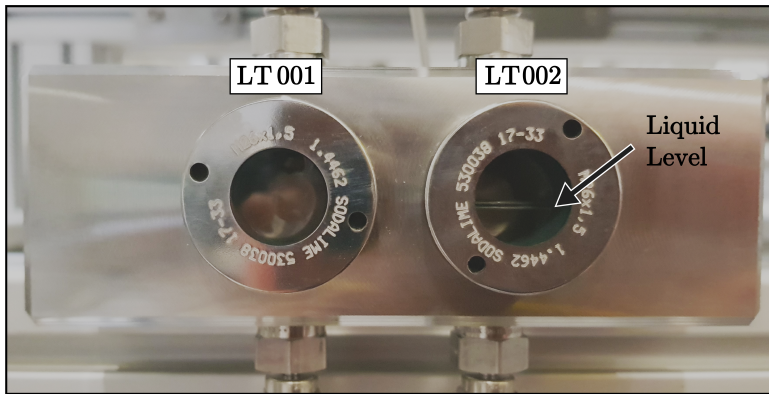


Figure C.3: Two exemplary liquid traps during a startup of the ORCHID. LT002 contains some liquid, while LT001 does not.

sensors when executing the purging operation, while still allowing to record pressures from the  $P_{SV001-002}$  ports .

During the startup phase, therefore the warm-up of the nozzle test section, condensate accumulates in the pressure lines connected to the *Scanivalve* pressure scanner. Consequently, the liquid traps slowly fill with liquid MM, as shown in Fig. C.3: in this case, the LT002 liquid trap is half-filled with liquid MM, while LT001 is not.

The purging operation takes approximately one minute, see Fig. C.4. The injection of nitrogen causes a pressure spike in the back pressure of the nozzle, PT004. During the first purge, the value recorded by PT004 increases from 0.19 to 0.32 barg and then stabilises at an average value of 0.26 barg. The liquid trap was purged from liquid a second time after a period in which the two pressures in the settling chamber were recorded because condensation continued. The increase of pressure in the receiver (PT004) due to nitrogen injection has no effect on the nozzle flow conditions because the nozzle is in over-expanded conditions. The injection of nitrogen is visible in the schlieren image of Fig. C.5.

## ACKNOWLEDGEMENTS

The design of the pressure measurement system and the operational procedures were developed and documented by Dr. Emiliano Casati. His technical notes were consulted and are at the basis of this Appendix.

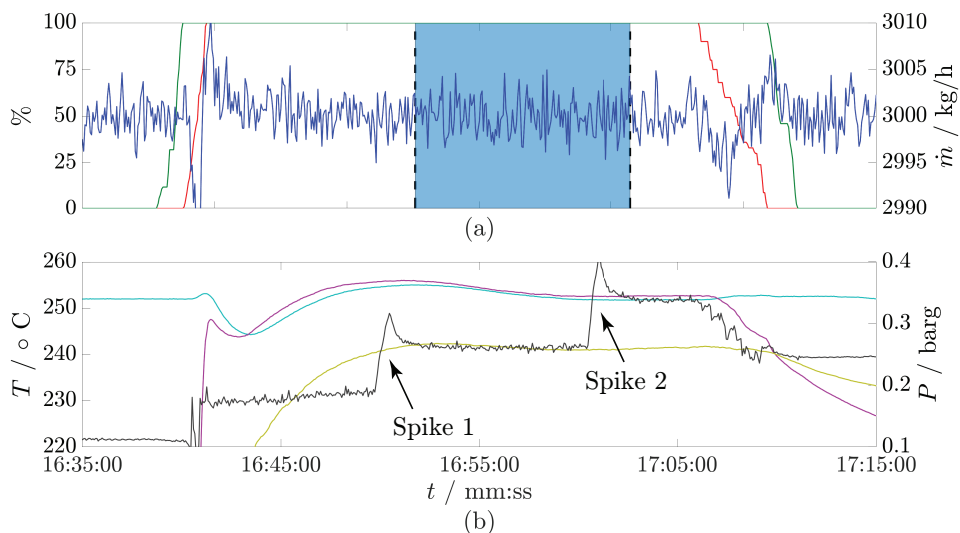


Figure C.4: Recording of several measurements taken during the PR016 process run, while testing the *Scanivale* pressure scanner. The MM vapor flow conditions were stable during the testing. The period highlighted in blue in (a) refers to the time interval in which the *Scanivale* module was in operation. (b) The two spikes in the signal of PT004 put into evidence the purging of the liquid traps by means of nitrogen injection in the lines. (a) The percentage aperture (position) of the nozzle inlet valve MOV002a (—) and of the primary control valve PCV003 (—) can be read on the left axis. The value of the MM mass flow rate FT001 (—) can be read on the right axis. (b) The values of the evaporation temperature TT005 (—) and of the total inlet temperature TT015 (—) and of the receiver temperature TT014 (—) can be read on the left axis, while the receiver pressure PT004 (—) can be read on right axis.

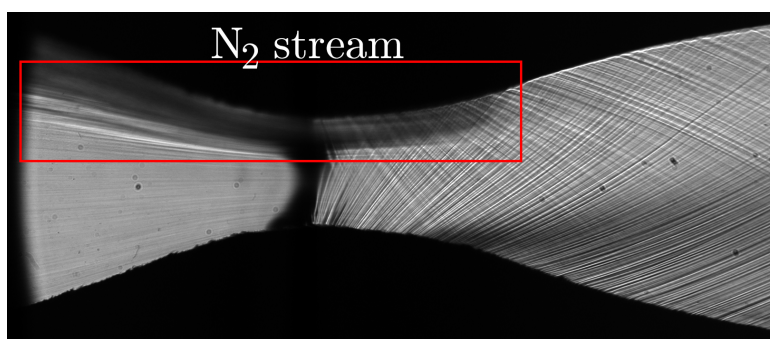


Figure C.5: Schlieren image taken during the PR.016 (16:50:00) showing a stream of N<sub>2</sub> being convected through the nozzle, and carrying liquid MM purged from the liquid traps.

# D

## ANALYSIS OF THE STEADINESS OF THE EXPERIMENTAL RUNS

Given that all the experiments described in this dissertation are based on the assumption of steady flow, the evaluation on the steadiness of the experimental conditions is of paramount importance and it can be performed by means of a systematic procedure, namely *steady-state identification*. Methods for the identification of periods in which experimental conditions are sufficiently stable for a given purpose have been reported by a number of researchers. Most of the documented techniques provide a method to select a period and corresponding data from a data set recorded during the operation of a device or setup, in which the operation can be defined as steady state according to defined criteria, and to obtain average values and related statistical parameters of relevant quantities, see, e.g., Bethea & Rhinehart [39], Jubien & Bihary [208, p. 64], Alekman [5, p. 62].

Despite the availability of these methods, most of the articles about experiments related to ORC technology do not report about the application of any of these methods for the assessment of steady state operational conditions. Woodland *et al.* [409] proposed a simple heuristic method for extracting a data set corresponding to periods of steady-state operation from the database of measurements of various process variables related to a simple Rankine cycle system employing R134a as the working fluid. Another approach is based on the so-called moving-average statistical method and is often adopted in process control [240, p. 62]. An example of the use of this method for the analysis of steady-state process variables of a residential air conditioner is reported in Kim *et al.* [210].

### D.1. STEADY STATE TIME INTERVAL DETECTION

The heuristic method described in Ref. [230], together with the Woodland *et al.* [409] criteria, have been applied to process measurements data recorded over periods of operation of the ORCHID, because of its simplicity and sufficient reliability in identifying

steady-state periods. More in detail the procedure is as follows:

- a dataset is visually inspected to qualitatively identify periods of steady operation containing at least 600 samples (10 minutes) for each of the process variables representative of the intended experiment.
- the average value of each process variable of interest obtained from the first 30 samples and the last 30 samples of the selected period is compared. If the steady state criteria defined in Ref. Woodland *et al.* [409] are met, namely that in case of a temperature measurement, the difference of the two average values is within 0.5 K, and in case of pressure and mass flow rate measurements is within 2 %, then the process is considered at steady state over the selected period.
- in order to ensure that there is enough data to calculate meaningful statistical quantities the second order moments are assessed with the criteria outlined in [194, App. C]. The statistical significance is achieved by verifying that the mean and standard deviation of the measured quantities remain approximately constant as the sample number increases.
- to assess the steadiness of periods of time following that of the initial 600 samples, the average values and the associated standard deviation of the representative process variables related to this initial time interval are used to define a statistical test: if a sample falls within the range defined as the average value plus or minus three times the standard deviation, that sample extends the steady state time window, provided that this condition holds for each of the representative process variables.

The process variables deemed representative for the assessment of steady state operation of the ORCHID were, with reference to Fig. 5.15 the evaporation temperature TT005 and pressure PZA003, the nozzle test section back pressure PT004, the condensation pressure PT006, and the working fluid mass flow rate FT001. To avoid that a positive steady state assessment is the result of a faulty measurement affected by gross error, also TT015 (settling chamber temperature of the nozzle TS), TT014 (receiver temperature), TT009 (condensation temperature), and PT005 (inlet pressure of the condensor) are tested for steadiness. If even one of these variables does not meet the steady state criterion, the considered time interval is deemed unsteady.

## REFERENCES

- [1] ABERNETHY, R. B., BENEDICT, R. P. & DOWDELL, R. B. 1985 ASME Measurement Uncertainties. *J. Fluids Eng.* **107**, 161–164.
- [2] ADAMS, B. M., BAUMAN, L. E., BOHNHOFF, W. J., DALBAY, K. R., EBEIDA, M. S., EDDY, J. P., ELDRED, M. S., HOUGH, P. D., HU, K. T., JAKEMAN, J. D., STEPHENS, J. A., SWILER, L. P., VIGIL, D. M. & WILDEY, T. M. 2014 Dakota, A Multilevel Parallel Object-Oriented Framework for Design Optimization, Parameter Estimation, Uncertainty Quantification, and Sensitivity Analysis: Version 6.1. *User Manual* SAND2014-4633. Sandia National Laboratories.
- [3] ADVISORY GROUP FOR AEROSPACE RESEARCH AND DEVELOPMENT (AGARD) 1994 Quality assessment for wind tunnel testing. *Tech. Rep.* AR-304. AGARD.
- [4] ALDO, A. C. & ARGROW, B. M. 1995 Dense Gas Flow in Minimum Length Nozzles. *J. Fluids Eng.* **117** (2), 270–276.
- [5] ALEKMAN, S. L. 1994 *Control for the Process Industries*. vol. VII, Putman Publications.
- [6] ALFEREZ, NICOLAS & TOUBER, EMILE 2017 One-dimensional refraction properties of compression shocks in non-ideal gases. *J. Fluid Mech.* **814**, 185–221.
- [7] AMERICAN INSTITUTE OF AERONAUTICS AND ASTRONAUTICS (AIAA) 1998 Guide for the Verification and Validation of Computational Fluid Dynamics Simulations. *Guide* G-077-1998. AIAA.
- [8] AMERICAN INSTITUTE OF AERONAUTICS AND ASTRONAUTICS (AIAA) 1999 Assessment of experimental uncertainty with application to wind tunnel testing. *Standard* S-071A-1999. AIAA.
- [9] AMERICAN NATIONAL STANDARD 1999 Instrumentation symbols and identification. *Standard* ANSI/ISA-5.1-2009. ISA Standards and Practices Department.
- [10] AMERICAN SOCIETY OF MECHANICAL ENGINEERS (ASME) 1993 Journal of Fluids Engineering editorial policy statement on the control of numerical accuracy. *J. Fluids Eng.* **115**, 339–340.
- [11] AMERICAN SOCIETY OF MECHANICAL ENGINEERS (ASME) 2009 Performance Test Code on Compressors and Exhausters. *Tech. Rep.* PTC 10 reaffirmed 2009. ASME.
- [12] AMERICAN SOCIETY OF MECHANICAL ENGINEERS (ASME) 2013 Test Uncertainty. *Standard* PTC 19.1 - 2018(R2018). ASME.
- [13] ANDERS, J. B., ANDERSON, W. K. & MURTHY, A. V. 1999 Transonic Similarity Theory Applied to a Supercritical Airfoil in Heavy Gases. *J. Aircr.* **36** (6), 957–964.
- [14] ANDERSON, J. D. JR. 1989 *Hypersonic and High Temperature Gas Dynamics*. McGraw-Hill.

- [15] ANDERSON, J. H. B. 1969 An experimental determination of the gladstone-dale constants for dissociating oxygen. *Phys. Fluids* **12** (5), 1–57.
- [16] ANDERSON, W. K. 1991 Numerical Study on using Sulfur Hexafluoride as a Wind Tunnel Test Gas. *AIAA J* **29** (12), 2179–2180.
- [17] ANGELINO, G., GAIA, M. & MACCHI, E. 1984 A review of Italian activity in the field of Organic Rankine Cycles. In *VDI Berichte 539 - Verein Deutscher Ingenieure. ORC-HP-technology. Working Fluid Problems. Proceedings of the International VFI- Seminar*, pp. 465–482. Zürich, Switzerland, 10-12 September: vol. 539, VDI Verlag Düsseldorf.
- [18] ANGELINO, G. & INVERNIZZI, C. 2003 Experimental investigation on the thermal stability of some new zero ODP refrigerants. *Int. J. Refrig.* **26** (1), 51–58.
- [19] ANGELINO, G., INVERNIZZI, C. & MACCHI, E. 1991 Organic Working Fluid Optimization for Space Power Cycles. In *Modern Research Topics in Aerospace Propulsion* (ed. G. Angelino, L. De Luca & W.A. Sirignano). Springer New York.
- [20] ANSOLOBEHERE, S., BEER, J., DEUTCH, J., ELLERMAN, A.D., FRIEDMAN, J., HERZOG, H., JACOBY, H., JOSKOW, P., MCRAE, G., LESTER, R., MONIZ, E. & STEINFELD, E. 2007 The future of coal: Options for a carbon-constrained world. *Study Report*. MIT.
- [21] ANSYS, INC. 2006 Ansys fluent user's guide. *Guide* Version 6.3. ANSYS.
- [22] ANSYS, INC. 2011 Ansys CFX user's manual. *Manual* release 13.0. ANSYS.
- [23] ANSYS, INC. 2017 Ansys® academic research workbench, release 17.1.
- [24] ARGROW, B. M. 1996 Computational analysis of dense gas shock tube flow. *Shock Waves* **6** (4), 241–248.
- [25] ASME 2009 Standard for Verification and Validation in Computational Fluid Dynamics and Heat Transfer. *Standard V&V20-2009*. ASME.
- [26] ATTIVISSIMO, F., GIAQUINTO, N. & SAVINO, M. 2007 Worst-case uncertainty measurement in ADC-based instruments. *Comput. Stand. & Interfaces* **29** (1), 5–10.
- [27] AZZINI, L. 2019 Numerical investigation of dense condensing flows for next-generation power units. PhD thesis, Delft University of Technology.
- [28] BADER, PASCAL, PSCHERNIG, MANUEL, SANZ, WOLFGANG, WOISETSCHLÄGER, JAKOB, HEITMEIR, FRANZ, MEILE, WALTER & BRENN, GÜNTER 2018 Experimental investigation of boundary layer relaminarization in accelerated flow. *J. Fluids Eng.* **140** (8).
- [29] BADER, PASCAL, SANZ, WOLFGANG, PETERLEITHNER, JOHANNES, WOISETSCHLÄGER, JAKOB, HEITMEIR, FRANZ, MEILE, WALTER & BRENN, GÜNTER 2016 Detecting transition in flat plate flow with laser interferometric vibrometry (LIV). In *Proceedings of ASME Turbo Expo 2016*, pp. 1–12. ASME.

- [30] BALTADJIEV, N. D., LETTIERI, C. & SPAKOVSKY, Z. S. 2015 An Investigation of Real Gas Effects in Supercritical CO<sub>2</sub> Centrifugal Compressors. *J. Turbomach.* **137** (9).
- [31] BARLOW, J. B., RAE, W. H. & POPE, A. 1999 *Low-Speed Wind Tunnel Testing*. John Wiley and Sons.
- [32] BARTOSIEWICZ, Y., AIDOUN, Z. & MERCADIER, Y. 2006 Numerical assessment of ejector operation for refrigeration applications based on CFD. *Appl. Therm. Eng.* **26** (5), 604–612.
- [33] BASSI, F., PELAGALLI, L., REBAY, S., BETTO, A., OREFICE, M. & PINTO, A. 2000 Numerical simulation of a reciprocating compressor for household refrigerators. In *International Compressor Engineering Conference*. Paper 1372.
- [34] BECKER, R. 1922 Impact Waves and Detonation. *Z. Phys* **8**, 381.
- [35] BELTRAME, F. 2020 Accuracy assessment of the SU2 flow solver for non-ideal organic vapor supersonic expansions using experimental data. Master's thesis, Politecnico di Torino.
- [36] BENDER, E. 1973 *The calculation of phase equilibria from a thermal equation of state applied to the pure fluids argon, nitrogen, oxygen and their mixtures*. Verlag C. F. Müller, Karlsruhe. 173 Seiten. Preis: DM 24.
- [37] BESSERER, G. J. & ROBINSON, D. B. 1973 Refractive indexes of ethane, carbon dioxide, and isobutane. *J. Chem. Eng. Data* **18** (2), 137–140.
- [38] BETHE, H. A. 1942 The theory of shock waves for an arbitrary equation of state. *Tech. rep.* 545. Office Sci. Res. & Dev.
- [39] BETHEA, R. M. & RHINEHART, R. R. 1991 *Applied Engineering Statistics*. CRC Press.
- [40] BEUNE, A. 2009 Analysis of high-pressure safety valves. PhD thesis, Technische Universiteit Eindhoven.
- [41] BIER, K., EHRLER, F., HARTZ, U. & KISSAU, G. 1977 Zur Berechnung von Düsenströmungen stark realer Gase. *Forsch. Ing.-Wes.* **43** (6), 175–184.
- [42] BIER, K., EHRLER, F. & NIEKRAWIETZ, M. 1990 Experimental investigation and computer analysis of spontaneous condensation in stationary nozzle flow of CO<sub>2</sub>-air mixtures. In *Adiabatic Waves in Liquid-Vapor Systems*. IUTAM Symposium.
- [43] BIER, K., EHRLER, F. & THEIS, G. 1989 Spontaneous condensation in stationary nozzle flow of carbon dioxide in a wide range of density. In *Adiabatic Waves in Liquid-Vapor Systems* (ed. Gerd E. A. Meier & Philip A. Thompson), pp. 129–141. IUTAM Symposium.
- [44] BIER, K., EHRLER, F. & THEIS, G. 1984 Comparison of spontaneous condensation in supersaturated nozzle flow of different refrigerants. In *VDI Berichte 539 - Verein Deutscher Ingenieure. ORC-HP-technology. Working Fluid Problems. Proceedings of the International VFI-Seminar*. vol. 539, VDI Verlag Düsseldorf.



- [45] BILLS, L. 2020 Validation of the SU2 flow solver for classical NICFD. Master's thesis, Delft University of Technology.
- [46] BOBER, W. & CHOW, W. L. 1990 Nonideal isentropic gas flow through converging-diverging nozzles. *J. Fluids Eng.* **112** (4), 455–460.
- [47] BOMMISETTY, R. V. N., JOSHI, D. S. & KOLLATI, V. R. 2013 Flow loss in screens: A fresh look at old correlation. *Int. J. Mech. Eng. Autom.* **3**, 29–34.
- [48] BONCINELLI, P., RUBECHINI, F., ARNONE, A., CECCONI, M. & CORTESE, C. 2004 Real gas effects in turbomachinery flows: A computational fluid dynamics model for fast computations. *J. Turbomach.* **126** (2), 268–276.
- [49] BORISOV, A. A., BORISOV, AL. A., KUTATELADZE, S. S. & NAKORYAKOV, V. E. 1983 Rarefaction shock waves near the critic liquid-vapour point. *J. Fluid Mech.* **126**, 59–73.
- [50] BORN, M. & WOLF, E. 2003 *Principles of Optics*, 7th edn. Cambridge University Press.
- [51] BORSUKIEWICZ-GOZDUR, A. 2013 Experimental investigation of R227ea applied as working fluid in the ORC power plant with hermetic turbogenerator. *Appl. Therm. Eng.* **56**, 126 – 133.
- [52] BRAUDAWAY, D. W. 2006 Uncertainty specification for data acquisition (DAQ) devices. *IEEE Transactions on Instrumentation and Measurement* **55** (1), 74–78.
- [53] BROUWER, J. M. & EPSOM, H. D. 2003 Twister supersonic gas conditioning for unmanned platforms and subsea gas processing. In *Offshore Europe, N.A. SPE-83977-MS*, p. 7. Aberdeen, United Kingdom: Society of Petroleum Engineers.
- [54] BROWN, B. & ARGROW, B. 1997 Two-dimensional shock tube flow for dense gases. *J. Fluid Mech.* **349**, 95–115.
- [55] BROWN, BRADY P. & ARGROW, BRIAN M. 1998 Nonclassical dense gas flows for simple geometries. *AIAA J* **36** (10), 1842–1847.
- [56] BROWN, B. P. & ARGROW, B. M. 2000 Application of Bethe-Zel'dovich-Thompson fluids in organic Rankine cycle engines. *J. Propuls. Power* **16** (6), 1118–1124.
- [57] BRUN, K., FRIEDMAND, P. & DENNIS, R. 2017 *Fundamentals and Applications of Supercritical Carbon Dioxide Based Power Cycles*. Woodhead Publishing.
- [58] BRYER, D. W. & PANKHURST, R.C. 1971 *Pressure-probe methods for determining wind speed and flow direction*. UK National Physical Laboratory.
- [59] BUFI, E. A. & CINNELLA, P. 2015 Efficient uncertainty quantification of turbulent flows through supersonic ORC nozzle blades. *Energy Procedia* **82**, 186–193, 70th Conference of the Italian Thermal Machines Engineering Association, ATI2015.

- [60] VAN BUIJTENEN, J. P., LARJOLA, J., TURUNEN-SAARESTI, T., HONKATUKIA, J., ESA, H., BACKMAN, J. & REUNANEN, A. 2003 Design and validation of a new high expansion ratio radial turbine for ORC applications. In *Proceedings of the Fifth European Conference on turbomachinery fluid dynamics and thermodynamics*.
- [61] BURNER, A. W. & GOAD, W. K. 1980 Gladstone-Dale constant for CF<sub>4</sub>. *Tech. Rep.* 80228. NASA.
- [62] CALDERAZZI, L. & COLONNA, P. 1997 Thermal stability of R-134a, R-141b, R-131I, R-7146, R-125 associated with stainless steel as a containing material. *Int. J. Refrig.* **20** (6), 381–389.
- [63] CAMMI, G., CONTI, C. C., SPINELLI, A. & GUARDONE, A. 2021 Experimental characterization of nozzle flow expansions of siloxane MM for ORC turbines applications. *Energy* **218**, 119249.
- [64] CASATI, E., VITALE, S., PINI, M., PERSICO, G. & COLONNA, P. 2014 Centrifugal turbines for Mini-ORC power systems. *J. Eng. Gas Turbine Power* **136** (12), 122607–1–11.
- [65] CASCI, C., ANGELINO, G., GAIA, M., FERRARI, P., GIGLIOLI, G. & MACCHI, E. 1980 Experimental Results and Economics of a Small (40 kW) Organic Rankine Cycle Engine. In *Proceedings of the Intersociety Energy Conversion Engineering Conference*, pp. 1008–1014. vol. 2, AIAA, New York.
- [66] CASEY, M. V. & FESICH, T. M. 2010 The efficiency of turbocharger compressors with diabatic flows. *J. Eng. Gas Turbine Power* **132** (7).
- [67] CASPER, J. K. 2007 *Natural Resources - Energy: Powering the Past, Present, and Future*. Chelsea House Pub.
- [68] CATTAFESTA, L., BAHR, C. & MATHEW, J. 2010 *Fundamentals of Wind-Tunnel Design*. John Wiley and Sons.
- [69] CAUSON, D. M. 1988 *A total variation diminishing scheme for computational aerodynamics*. In: Morton KW, Baines, MJ (eds) *Numerical methods for fluid dynamics III*. Clarendon Press Oxford, Oxford University Press New York.
- [70] CELIK, I. B., GHIA, U., ROACHE, P. J., FREITAS, C. J., COLEMAN, H. & RAAD, P. E. 2008 Procedure for estimation and reporting of uncertainty due to discretization in CFD applications. *J. Fluids Eng.* **130** (7).
- [71] CHANDRASEKAR, D. & PRASAD, P. 1991 Transonic flow of a fluid with positive and negative nonlinearity through a nozzle. *Physics of Fluids A: Fluid Dynamics* **3** (3), 427–438.
- [72] CHANETZ, B. & CHPOUN, A. 2001 Shock tubes and tunnels: Facilities, instrumentation, and techniques. In *Handbook of shockwaves, vol. 1*. Academic Press.

- [73] CHUNG, T. H., LEE, L. L. & STARLING, K. E. 1984 Applications of kinetic gas theories and multiparameter correlation for prediction of dilute gas viscosity and thermal conductivity. *Ind. Eng. Chem. Fundam.* **23** (1).
- [74] CINNELLA, P. 2008 Transonic flows of dense gases over finite wings. *Phys. Fluids* **20** (4).
- [75] CINNELLA, P. & CONGEDO, P. 2004 A numerical solver for dense gas flows. In *34th AIAA Fluid Dynamics Conference and Exhibit, N.A.* AIAA 2004-2137, pp. 1–12.
- [76] CINNELLA, P. & CONGEDO, P. 2007 Inviscid and viscous aerodynamics of dense gases. *J. Fluid Mech.* **580**, 179–217.
- [77] CINNELLA, P., CONGEDO, P., PEDIRODA, V. & PARUSSINI, L. 2011 Sensitivity analysis of dense gas flow simulations to thermodynamic uncertainties. *Phys. Fluids* **23** (11), 116101.
- [78] CINNELLA, P. & CONGEDO, P. M. 2008 Optimal airfoil shapes for viscous transonic flows of Bethe–Zel’dovich–Thompson fluids. *Comput Fluids* **37** (3), 250–278.
- [79] CINNELLA, P., CONGEDO, P. M., PARUSSINI, L. & PEDIRODA, V. 2010 Quantification of thermodynamic uncertainties in real gas flows. *Int. J. Eng. Syst. Model. Simul.* **2** (1-2), 12–24.
- [80] CIRRI, M., ADAMI, P. & MARTELLI, F. 2005 Development of a CFD real gas flow solver for hybrid grid. *Int J Numer Methods Fluids* **47** (8-9), 931–938.
- [81] COLEMAN, H. W. & STEELE, W. G. 2009 *Experimentation, Validation, and Uncertainty Analysis for Engineers*, 3rd edn. John Wiley and Sons.
- [82] COLEMAN, H. W. & STERN, F. 1997 Uncertainties and CFD Code Validation. *J. Fluids Eng.* **119** (4), 795 – 803, (Also “Discussion and Authors’ Closure,” Vol. 120, Sept. 1998, pp. 635–636.).
- [83] COLONNA, P., CASATI, E., TRAPP, C., MATHIJSEN, T., LARJOLA, J., TURUNEN-SAARESTI, T. & UUSITALO, A. 2015 Organic Rankine cycle power systems: From the concept to current technology, applications, and an outlook to the future. *J. Eng. Gas Turb. Power - T. ASME* **137** (10), 100801–1–19.
- [84] COLONNA, P. & GUARDONE, A. 2006 Molecular interpretation of nonclassical gas dynamics of dense vapors under the van der Waals model. *Phys. Fluids* **18** (5), 1–14.
- [85] COLONNA, P., GUARDONE, A. & NANNAN, N. R. 2007 Siloxanes: A new class of candidate Bethe–Zel’dovich–Thompson fluids. *Phys. Fluids* **19** (8), 086102.
- [86] COLONNA, P., GUARDONE, A., NANNAN, N. R. & ZAMFIRESCU, C. 2008 Design of the dense gas flexible asymmetric shock tube. *J. Fluids Eng.* **130** (3).
- [87] COLONNA, P., HARINCK, J., REBAY, S. & GUARDONE, A. 2008 Real-gas effects in organic Rankine cycle turbine nozzles. *J. Eng. Gas Turbine Power* **24** (2), 282–294.

- [88] COLONNA, P., NANNAN, N., GUARDONE, A. & VAN DER STELT, T. 2009 On the computation of the fundamental derivative of gas dynamics using equations of state. *Fluid Phase Equilib.* **286** (1), 43–54.
- [89] COLONNA, P., NANNAN, N. R. & GUARDONE, A. 2008 Multiparameter equations of state for siloxanes:  $[(\text{CH}_3)_3\text{-Si-O}_{1/2}]_2\text{-[O-Si-(CH}_3)_2]_{i=1,\dots,3}$  and  $[\text{O-Si-(CH}_3)_2]_6$ . *Fluid Phase Equilib.* **263** (2), 115–130.
- [90] COLONNA, P., NANNAN, N. R., GUARDONE, A. & LEMMON, E. W. 2006 Multiparameter equations of state for selected siloxanes. *Fluid Phase Equilib.* **244** (2), 193–211.
- [91] COLONNA, P. & REBAY, S. 2004 Numerical simulation of dense gas flows on unstructured grids with an implicit high resolution upwind Euler solver. *Int J Numer Methods Fluids* **46** (7), 735–765.
- [92] COLONNA, P., REBAY, S. & SILVA, P. 2002 Computer simulations of dense gas flows using complex equations of state for pure fluids and mixtures and state of the art numerical schemes. *Tech. Rep.* 1.0. Universita di Brescia.
- [93] COLONNA, P., VAN DER STELT, T. P. & GUARDONE, A. 2019 FluidProp (version 3.1): A program for the estimation of thermophysical properties of fluids. A computer program since 2004.
- [94] CONGEDO, P. M., CORRE, C. & CINNELLA, P. 2011 Numerical investigation of dense-gas effects in turbomachinery. *Comput Fluids* **49** (1), 290–301.
- [95] CONTI, C., A., SPINELLI, GUARDONE, A., COZZI, F., CAMMI, G. & ZOCCA, M. 2017 Schlieren visualization of non-ideal compressible fluid flows. In *12th international conference on heat transfer, fluid mechanics and thermodynamics, HEFAT2017*.
- [96] COULL, J. D. & HODSON, H. P. 2012 Predicting the profile loss of high-lift low pressure turbines. *J. Turbomach.* **134** (2).
- [97] COZZI, F., SPINELLI, A., CARMINE, M., CHELI, R., ZOCCA, M. & GUARDONE, A. 2015 Evidence of complex flow structures in a converging-diverging nozzle caused by a recessed step at the nozzle throat. In *45th AIAA Fluid Dynamics Conference*.
- [98] CRAIG, H.R.M. & COX, H.J.A. 1971 Performance estimation of axial flow turbines. *Proceedings Institution of Mechanical Engineers* **185-32/71**, 407–424.
- [99] CRAMER, M.S. & FRY, R.N. 1992 Nozzle flows of dense gases. *Physics of Fluids A: Fluid Dynamics* **5** (5), 1246–1259.
- [100] CRAMER, M. S. 1989 Negative nonlinearity in selected fluorocarbons. *Physics of Fluids A: Fluid Dynamics* **1** (11), 1894–1897.
- [101] CRAMER, M. S. 1991 Nonclassical dynamics of classical gases. In *Nonlinear Waves in Real Fluids*, pp. 91–145. Vienna: Springer Vienna.
- [102] CRAMER, M. S. & CRICKENBERGER, A. B. 1991 The dissipative structure of shock waves in dense gases. *J. Fluid Mech.* pp. 223–325.

- [103] CRAMER, M. S. & KLUWICK, A. 1984 On the propagation of waves exhibiting both positive and negative nonlinearity. *J. Fluid Mech.* **142**, 9–37.
- [104] CRAMER, M. S. & SEN, R. 1986 Shock formation in fluids having embedded regions of negative nonlinearity. *Phys. Fluids* **29**, 2181–2191.
- [105] CRAMER, M. S. & SEN, R. 1987 Exact solutions for sonic shocks in van der Waals gas. *Phys. Fluids* **30** (2), 377.
- [106] CRAMER, M. S. & SEN, R. 1990 Mixed nonlinearity and double shocks in superfluid helium. *J. Fluid Mech.* **221**, 233–261.
- [107] CRAVERO, C. & SATTA, A. 2000 A CFD model for real gas flows. In *Proceedings of ASME Turbo Expo 2020*, pp. 1–10. ASME.
- [108] CULBERSON, P.E. 1949 Calibration report on the university of Michigan supersonic wind tunnel. *Tech. Rep.* UMR0799. ARC - University of Michigan.
- [109] DAI, X., SHI, L. & QIAN, W. 2019 Review of the working fluid thermal stability for organic Rankine cycles. *Int J Therm Sci* **28** (4).
- [110] DAVIS, S. F. 1987 A simplified TVD finite difference scheme via artificial viscosity. *SIAM J. Sci. and Stat. Comput.* **8** (1).
- [111] DAYMAN, B. 1959 Prediction of blocking in the supersonic wind tunnel during an attempted start. *Tech. Rep.* JPL EP-66g. California Institute of Technology.
- [112] DE SERVI, C., TRABUCCHI, S., VAN DER STELT, T., STROBELT, F., GLOS, S., KLINK, W. & COLONNA, P. 2019 Supercritical CO<sub>2</sub> based waste heat recovery systems for combined cycle power plants. In *5<sup>th</sup> International Seminar on ORC Power Systems*. Sept 09-12.
- [113] DENBIGH, K. G. 1940 The polarisabilities of bonds - I. *Trans. Faraday Soc.* **36**, 936–948.
- [114] DETTLEFF, G., THOMPSON, P. A., MEIER, E.A. & SPECKMANN, H. 1979 An experimental study of liquefaction shock waves. *J. Fluid Mech.* **95**, 279–304.
- [115] DETTLEFF, G., THOMPSON, P. A. & MEIER, G.E.A 1976 Initial experimental results for liquefaction shock waves in organic fluids. *Arch. Mech.* **28**, 827–836.
- [116] DIJKSHOORN, D. D. 2020 Simulation of two dimensional steady state boundary layer effects applied to non-ideal gas flows. Master's thesis, Delft University of Technology.
- [117] DIXON, S. L. & HALL, C. A. 2010 *Fluid Mechanics and Thermodynamics of Turbomachinery*, 6<sup>th</sup> edn. Elsevier Inc.
- [118] DOLL, ULRICH, STOCKHAUSEN, GUIDO & WILLERT, CHRISTIAN 2017 Pressure, temperature, and three-component velocity fields by filtered rayleigh scattering velocimetry. *Opt. Lett.* **19** (42), 3773–3776.

- [119] DOSTAL, V., HEJZLAR, P. & DRISCOLL, M. 2006 High-performance supercritical carbon dioxide cycle for next-generation nuclear reactors. *Nucl. Technol.* **154** (3), 265–282.
- [120] DRIKAKIS, D. & TSANGARIS, S. 1993 Real gas effects for compressible nozzle flows. *J. Fluids Eng.* **115**, 115–120.
- [121] DRYDEN, H. L. & SCHUBAUER, G. B. 1947 The use of damping screens for the reduction of wind-tunnel turbulence. *National Bureau of Standards* **14** (4).
- [122] DUDA, RO & HART, PE 1972 Use of the Hough transformation to detect lines and curves in pictures. *Graph Image Process* **15** (1), 11–15.
- [123] DUFF, K. 1966 Non-equilibrium condensation of carbon dioxide in supersonic nozzles. PhD thesis, MIT.
- [124] DUHEM, P. 1909 On the propagation of shock waves in fluids. *Z. Phys. Chem* **69**, 169–186.
- [125] DUNHAM, J. 1998 CFD Validation for Propulsion System Components. *Tech. Rep.* AR-355. AGARD.
- [126] DURKEE, J. 2014 *Cleaning with solvents: methods and machinery*, 1st edn. William Andrew.
- [127] DURST, F., MELLING, A. & WHITELAW, J. H. 1981 *Principles and Practice of Laser-Doppler Anemometry*. Academic Press.
- [128] EÇA, L. & HOEKSTRA, M. 2006 On the influence of the iterative error in the numerical uncertainty of ship viscous flow calculations. In *26th Symposium on Naval Hydrodynamics*.
- [129] EÇA, L. & HOEKSTRA, M. 2009 Evaluation of Numerical Error Estimation Based on grid Refinement Studies with the Method of the Manufactured Solutions. *Comput Fluids* **38** (8), 1580–1591.
- [130] EÇA, L. & HOEKSTRA, M. 2014 A procedure for the estimation of the numerical uncertainty of CFD calculations based on grid refinement studies. *J. Comput. Phys.* **262**, 104 – 130.
- [131] EÇA, L., VAZ, G. & HOEKSTRA, M. 2010 Code Verification, Solution Verification and Validation in RANS Solvers. In *ASME 2010 29th International Conference on Ocean, Offshore and Arctic Engineering*, pp. 597–605.
- [132] ECONOMON, T. D., PALACIOS, F., COPELAND, S. R., LUKACZYK, T. W. & ALONSO, J. J. 2015 SU2: An open-source suite for multiphysics simulation and design. *AIAA J* **54** (3), 828–846.
- [133] EDELING, W. N., CINNELLA, P., DWIGHT, R. P. & BIJL, H. 2014 Bayesian estimates of parameter variability in the k-epsilon turbulence model. *J. Comput. Phys.* **258**, 73–94.

- [134] ELLIOT, D. G. 1982 Theory and tests of two-phase turbines. *Tech. Rep.* DOE/ER-10614-1; JPL-PUB-81-105ON: DE82013037. Jet Propulsion Lab.
- [135] ELSINGA, G. E., VAN OUDHEUSDEN, B. W. & SCARANO, F. 2005 Evaluation of aero-optical distortion effects in PIV. *Exp. Fluids* **39** (2), 246–256.
- [136] EU 2012 Consolidated version of the Treaty on the Functioning of the European Union (TFEU). *Official J. of the Eur. Union* p. 47–390, c 326.
- [137] F2CHEMICALS 2015 FLUTEC PP2. Webpage, [Perfluoromethylcyclohexane](#).
- [138] FAINBERG, A. H. & MILLER, W. 1965 Molar refractivity in fluorine-containing perhalo compounds. *J. Am. Chem. Soc.* **30** (3), 864–876.
- [139] FANGTIAN, S. & YITAI, M. 2011 Thermodynamic analysis of transcritical CO<sub>2</sub> refrigeration cycle with an ejector. *Appl. Therm. Eng.* **31** (6), 1184 – 1189.
- [140] FERGASON, STEPHEN & ARGROW, BRIAN 2001 Construction and operation of a dense gas shock tube. In *35th AIAA Thermophysics Conference*. AIAA.
- [141] FERGASON, S. H. & ARGROW, B. M. 2001 Simulations of nonclassical dense gas dynamics. In *35th AIAA Thermophysics Conference*. AIAA.
- [142] FERGASON, S. H., GUARDONE, A. & ARGROW, B. M. 2003 Construction and validation of a dense gas shock tube. *J. Thermophys. Heat Tr.* **17** (3), 326–333.
- [143] FERGASON, S. H., HO, T. L., AGROW, B. M. & EMANUEL, G. 2001 Theory for producing a single-phase rarefaction shock wave in a shock tube. *J. Fluid Mech.* **445**, 37–54.
- [144] FLATT, R. 1983 Numerical study of the unsteady flow of a real gas (methane CH<sub>4</sub>) in a pipeline. *Tech. Rep.* 1.0. Lausanne.
- [145] FLATT, R. 1985 Zur Anwendung numerischer Verfdhren der Strömungslehre in der Realgasdynamik (translation: on the application of numerical methods to the dynamics of real gases). *Forsch. Ing.-Wes* **51**, 41–51.
- [146] FLATT, R. 1986 Unsteady compressible flow in long pipelines following a rupture. *Int J Numer Methods Fluids* **6** (2), 83–100.
- [147] FORKEY, J. N., LEMPert, W. R. & MILES, R. B. 1998 Accuracy limits for planar measurements of flow field velocity, temperature and pressure using filtered Rayleigh scattering. *Exp. Fluids* **2** (24), 151–162.
- [148] FULLARTON, J. W. & VDI 2010 *VDI Heat Atlas*. Springer-Verlag Berlin Heidelberg.
- [149] GALLARINI, SIMONE 2016 Design and commissioning of a laser Dsoppler velocimetry seeding system for non-ideal fluid flows. Master's thesis, Politecnico di Milano.

- [150] GALLARINI, S., SPINELLI, A., COZZI, F. & GUARDONE, A. 2016 Design and commissioning of a laser Doppler velocimetry seeding system for non-ideal fluid flows. In *12th International Conference on Heat Transfer, Fluid Mechanics and Thermodynamics 2016*.
- [151] GELEST 2014 Hexamethyldisiloxane, MSDS. *Data Sheet* PN: SIH6115.0. Gelest, Inc.
- [152] GIEPMAN, R.H.M. 2016 Flow control for oblique shock wave reflections. PhD thesis, Delft University of Technology.
- [153] GINOSAR, D. M., PETKOVIC, L. M. & GUILLEN, D. P. 2011 Thermal stability of cyclopentane as an organic Rankine cycle working fluid. *Energy Fuels* **25** (9), 4138–4144.
- [154] GOLDSTEIN, R. & KUEHN, T. H. 1983 Optical systems for flow measurement - shadowgraph, schlieren, and interferometric techniques. In *Fluid Mechanics Measurements*. Springer-Verlag, Berlin.
- [155] GORI, G., ZOCCA, M., CAMMI, G., SPINELLI, A., CONGEDO, P. M. & GUARDONE, A. 2020 Accuracy assessment of the non-ideal computational fluid dynamics model for siloxane MDM from the open-source SU2 suite. *Eur. J. Mech. B Fluids* **79**, 109–120.
- [156] GORI, G., ZOCCA, M., GUARDONE, A., MAITRE, O.P. LE & CONGEDO, P.M. 2020 Bayesian inference of thermodynamic models from vapor flow experiments. *Comput Fluids* **205**, 104550.
- [157] GROSSMAN, B. 2000 Fundamental concepts of real gasdynamics. *Lecture Notes* No. 3. Virginia Tech.
- [158] GU, JUNJIE, WANG, SHUJUN & GAN, ZHONGXUE 2014 *Two-Phase Flow in Refrigeration Systems*. Springer New York.
- [159] GUARDONE, A. 2001 Nonclassical gasdynamics: thermodynamic modeling and numerical simulation of multidimensional flows of BZT fluids. PhD thesis, Politecnico di Milano.
- [160] GUARDONE, A. 2007 Three-dimensional shock tube flows for dense gases. *J. Fluid Mech.* **583**, 423–442.
- [161] GUARDONE, ALBERTO, COLONNA, PIERO, CASATI, EMILIANO & RINALDI, ENRICO 2014 Non-classical gas dynamics of vapour mixtures. *J. Fluid Mech.* **741**, 681–701.
- [162] GUARDONE, A., COLONNA, P. & WHEELER, A. 2017 1st international seminar on non-ideal compressible-fluid dynamics for propulsion & power. *Journal of Physics: Conference Series* **821**, 011001.
- [163] GUARDONE, A., SPINELLI, A. & DOSSENA, V. 2013 Influence of molecular complexity on nozzle design for an organic vapor wind tunnel. *J. Eng. Gas Turb. Power* **135** (4), 042307.



- [164] GUARDONE, A., VIGEVANO, L. & ARGROW, B. M. 2004 Assessment of thermodynamic models for dense gas dynamics. *Phys. Fluids* **16** (11), 3878–3887.
- [165] GUARDONE, A. & VIMERCATI, D. 2016 Exact solutions to non-classical steady nozzle flows of Bethe-Zel'dovich-Thompson fluids. *J. Fluid Mech.* **800**, 278–306.
- [166] GUARDONE, A., ZAMFIRESCU, C. & COLONNA, P. 2010 Maximum intensity of rarefaction shock waves for dense gases. *J. Fluid Mech.* **642**, 127.
- [167] GULEN, S. C., THOMPSON, P. A. & CHO, H. J. 1990 Rarefaction and liquefaction shock waves in regular and retrograde fluids with near-critical end states. In *Adiabatic Waves in Liquid-Vapor Systems: IUTAM Symposium Göttingen, 28.8.–1.9.1989*, pp. 281–290. Berlin, Heidelberg: Springer Berlin Heidelberg.
- [168] GULEN, S. C., THOMPSON, P. A. & CHO, HUNG-JAI 1994 Experimental study of reflected liquefaction shock waves with near-critical downstream states in a test fluid of large molar heat capacity. *J. Fluid Mech.* **277**, 163–196.
- [169] GUO, T., SUMNER, W. J. & HOFER, D. C. 2007 Development of highly efficient nuclear HP steam turbines using physics based moisture loss models. In *Proceedings of ASME Turbo Expo 2007*, pp. 825–833. ASME.
- [170] HAN, Y. O., GEORGE, W. K. & HJARNE, J. 2005 Effect of a contraction on turbulence. Part 1: Experiment. In *43rd AIAA Aerospace Sciences Meeting and Exhibit*.
- [171] HARINCK, J., COLONNA, P., GUARDONE, A. & REBAY, S. 2010 Influence of thermodynamic models in two-dimensional flow simulations of turboexpanders. *J. Turbomach.* **132** (1), 011001–17.
- [172] HARINCK, J., GUARDONE, A. & COLONNA, P. 2009 The influence of molecular complexity on expanding flows of ideal and dense gases. *Phys. Fluids* **21** (8), 086101.
- [173] HARINCK, J., PASQUALE, D., PECNIK, R., BUIJTENEN, JOS VAN & COLONNA, P. 2013 Performance improvement of a radial organic Rankine cycle turbine by means of automated computational fluid dynamic design. *Proc. Inst. Mech. Eng., Part A: J. Power Energy* **227** (6), 637–645.
- [174] HARINCK, J., TURUNEN-SAARESTI, T., COLONNA, P., REBAY, S. & VAN BUIJTENEN, J.P. 2010 Computational study of a high-expansion ratio radial ORC turbine stator. *J. Eng. Gas Turbine Power* **132** (5), 054501.
- [175] HARVEY, S. 2017 Centrifugal compressors in ethylene plants. *Chem Eng Prog* **113** (2).
- [176] HASSELMANN, K., REINKER, F., WIESCHE, S., KENIG, E. Y., DUBBERKE, F. & VRABEC, J. 2014 Performance Predictions of Axial Turbines for Organic Rankine Cycle (ORC) Applications Based on Measurements of the Flow Through Two-Dimensional Cascades of Blades. In *Proceedings of the ASME 2014 Power Conference*.

- [177] HAVENS, V. N., RAGALLER, D. R., SILBERT, L. & MILLER, D. 1987 Toluene stability space station Rankine power systems. *Proceedings of the 22nd Intersociety Energy Conversion Engineering Conference (IECEC)* Philadelphia, PA.
- [178] HAYES, W. D. 1958 The basic theory of gasdynamic discontinuities. In *Fundamentals of gasdynamics*. Vol. 2. Princeton University Press.
- [179] HEAD, A., DE SERVI, C., CASATI, E., PINI, M. & COLONNA, P. 2016 Preliminary design of the ORCHID: A facility for studying non-ideal compressible fluid dynamics and testing ORC expanders. In *Proceedings of ASME Turbo Expo 2016*, pp. 1–14. ASME.
- [180] HEAD, A. J. & VISSER, W. 2012 Scaling 3–36 kW microturbines. In *Proceedings of ASME Turbo Expo 2012*, pp. 1–14. ASME.
- [181] HENGWEI, LIU, ZHONGLIANG, LIU, YONGXUN, F., KEYU, G. U. & TINGMIN, Y. 2006 Characteristics of a supersonic swirling dehydration system of natural gas. *Chinese J. Chem. Eng.* **13**.
- [182] HILL, J.A.F., BARON, J.R., SCHINDEL, L.H. & MARKHAM, J.R. 1956 Mach number measurements in high-speed wind tunnels. *Tech. Rep.* AG-22. NATO.
- [183] HILL, P. G., WITTING, H. & DEMETRI, E. P. 1963 Condensation of metal vapors during rapid expansion. *J. Heat Transfer*. **85** (4).
- [184] HIRN, G. A. 1862 *Exposition analytique et experimentale de la theorie mecanique de la chaleur*. Nabu Press.
- [185] HOBBS, D.E. 1983 *A virial equation of state utilizing the principle of corresponding states*. Rensselaer Polytechnic Institute.
- [186] HOFFREN, J. 1997 Adaptation of FINFLO for real gases. *Tech. Rep.* 102. Helsinki University of Technology, Laboratory of Applied Thermodynamics.
- [187] HOFFREN, J., TALONPOIKA, T., LARJOLA, J. & SIIKONEN, T. 2002 Numerical simulation of realgas flow in a supersonic turbine nozzle engineering. *J. Eng. Gas Turbine Power* **124**, 395–403.
- [188] HUGHES, W. F. & BRIGHTON, J. A. 1999 *Schaum's Outlines Fluid Dynamics*. The McGraw-Hill Companies.
- [189] HUGONIOT, P.H. 1887 Memoire sur la propagation du mouvement dans les corps et plus spécialement dans les gaz parfaits (1e partie). *J. Ecole Polytech.* **57**, 3–97, Paris.
- [190] HUGONIOT, P.H. 1889 Memoire sur la propagation du mouvement dans les corps et plus spécialement dans les gaz parfaits (2e partie). *J. Ecole Polytech.* **58**, 1–125, Paris.
- [191] HUNTER, M. J., HYDE, J. F., WARRICK, E. L. & FLETCHER, H. J. 1946 Organo-silicon polymers. The cyclic dimethyl siloxanes. *J. Am. Chem. Soc.* **68** (4), 667–672.

- [192] INCROPERA, F. P., DEWITT, D. P., BERGMAN, T. L. & LAVINE, A. S. 2006 *Fundamentals of Heat and Mass Transfer*. John Wiley & Sons.
- [193] INOUE, NAOYUKI, KANEKO, ATSUSHI, WATANABE, HIROYOSHI, UCHIMURA, TOMOYUKI & IRIE, KIICHI 2007 Development of Electric Power Generation Unit Driven by Waste Heat (Study on Working Fluids and Expansion Turbines). In *Proceedings of ASME Turbo Expo 2007*, pp. 927–938. ASME.
- [194] INTERNATIONAL ORGANIZATION FOR STANDARDIZATION (ISO) 1993 Guide to the expression of uncertainty in measurement. *Guide 100:2008*. Joint Committee for Guides in Metrology, JCGM. Corrected and reprinted, 1995.
- [195] INVERNIZZI, C. M. 2013 Closed power cycles - thermodynamic fundamentals and applications. In *Lecture Notes in Energy*. Springer-Verlag.
- [196] INVERNIZZI, C. M. & BONALUMI, D. 2017 Thermal stability of organic fluids for organic Rankine cycle systems. In *Organic Rankine Cycle (ORC) Power Systems*, pp. 121 – 151. Woodhead Publishing.
- [197] IYER, S. 2015 Influence of thermodynamic property perturbations on nozzle design and non-ideal compressible flow phenomena. Master's thesis, Delft University of Technology.
- [198] JAFFE, LEONARD D. 1988 Review of test results on parabolic dish solar thermal power modules with dish-mounted Rankine engines and for production of process steam. *J. Sol. Energy Eng.* **110** (4), 275–281.
- [199] JARCZYK, M. & PFITZNER, M. 2012 Large eddy simulation of supercritical nitrogen jets. In *50th AIAA Aerospace Sciences Meeting including the New Horizons Forum and Aerospace Exposition*.
- [200] JASSIM, E. ANDABDI, M. A. & MUZYCHKA, Y. 2008 Computational fluid dynamics study for flow of natural gas through high-pressure supersonic nozzles: Part 1. real gas effects and shockwave. *Pet Sci Technol* **26** (15), 1757–1772.
- [201] JESPEN, TORBEN 2016 *ATEX—Explosive Atmospheres*, 1st edn. Springer International Publishing.
- [202] JOINT COMMITTEE FOR GUIDES IN METROLOGY 2008 Evaluation of measurement data - supplement 1 to the "guide to the expression of uncertainty in measurement" - propagation of distributions using a monte carlo method. *Supplement*. International Organization of Legal Metrology, jCGM 101:2008.
- [203] JONAS, O. 1998 Condensation in steam turbines - new theory and data. *American Society of Mechanical Engineers, Power Division (Publication) PWR* **33**, 205–212.
- [204] JOUGET, E. 1904 Remarques sur la propagation des percussions dans les gaz. *C.R. Acad. Sci. Paris* **138**, 1685–1688.
- [205] JOUGET, E. 1904 Sur l'onde explosive. *Ib. C.R. Acad. Sci. Paris* **139**, 121–124.

- [206] JOUGUET, E. 1901 Sur la propagation des discontinuity dans les fluides. *C. R. Acad. Sci. Paris* **132**, 673–676.
- [207] JOUGUET, E. 1904 Remarques sur la propagation des percussions dans les gaz. *C. R. Acad. Sci. Paris* **138**, Paris.
- [208] JUBIEN, G. & BIHARY, G. 1994 *Control for the Process Industries, vol. VII*. Putman Publications.
- [209] KANG, SEOK HUN 2012 Design and experimental study of ORC (organic Rankine cycle) and radial turbine using R245fa working fluid. *Energy* **41** (1), 514–524, 23rd International Conference on Efficiency, Cost, Optimization, Simulation and Environmental Impact of Energy Systems, ECOS 2010.
- [210] KIM, M., YOON, SEOK H., DOMANSKI, PIOTR A. & PAYNE, WILLIAM V. 2008 Design of a steady-state detector for fault detection and diagnosis of a residential air conditioner. *Int. J. Refrig.* **31** (5), 790–799.
- [211] KLONOWICZ, P., BORSUKIEWICZ-GOZDUR, A., HANAUSEK, P., KRYLLOWICZ, W. & BRÜGGEMANN, D. 2014 Design and performance measurements of an organic vapour turbine. *Appl. Therm. Eng.* **63** (1), 297 – 303.
- [212] KLUWICK, A. 1991 *Nonlinear waves in real fluids*. Springer-Verlag Wien.
- [213] KLUWICK, A. 2001 Handbook of shockwaves. In *Theory of shock waves: Rarefaction shocks, vol. 1*, pp. 339–411. Academic Press.
- [214] KLUWICK, ALFRED 2018 Shock discontinuities: from classical to non-classical shocks. *Acta Mechanica* **229** (2), 515–533.
- [215] KLUWICK, A. & COX, E. A. 2018 Steady small-disturbance transonic dense gas flow past two-dimensional compression/expansion ramps. *J. Fluid Mech.* **848**, 756–787.
- [216] KLUWICK, A. & COX, E. A. 2019 Weak shock reflection in channel flows for dense gases. *J. Fluid Mech.* **874**, 131–157.
- [217] KLUWICK, A. & MEYER, G. 2010 Shock regularization in dense gases by viscous-inviscid interactions. *J. Fluid Mech.* **644**, 473–507.
- [218] KREHL, P. 2001 Handbook of shockwaves. In *History of Shock Waves. vol. 1*. Academic Press.
- [219] KUNTE, H. S. & SEUME, J. R. 2015 Experimental setup of a small supersonic turbine for an automotive (ORC) application running with ethanol. In *ASME ORC2015 - 3<sup>rd</sup> International Seminar on ORC Power Systems - Brussels (BE), October 12-14*.
- [220] KURGANOV, A. & TADMOR, E. 2000 New high-resolution central schemes for non-linear conservation laws and convection laws and convection-diffusion equations. *J. Comput. Phys.* **160** (1), 241–282.

- [221] KUTATELADZE, S. S., BORISOV, AL. A. & NAKORYAKOV, V. E. 1980 Experimental detection of a rarefaction shock wave near a liquid-vapor critical point. *Sov. Phys. Dokl* **25**, 392–393.
- [222] KUTATELADZE, S. S., NAKORYAKOV, V. E. & BORISOV, A. A. 1987 Rarefaction waves in liquid and gas-liquid media. *Annu. Rev. Fluid Mech.* **19** (1), 577–600.
- [223] LACAZE, G., MISDARIIS, A., RUIZ, A. & OEFELIN, J. C. 2015 Analysis of high-pressure diesel fuel injection processes using LES with real-fluid thermodynamics and transport. *Proc Combust Inst* **35** (2), 1603 – 1611.
- [224] LAMBRAKIS, KONSTANTINE C. & THOMPSON, PHILIP A. 1972 Existence of real fluids with a negative fundamental derivative gamma. *Phys. Fluids* **15** (5), 933–935.
- [225] LANDAU, L.D. 1942 On shock waves. *J. Phys. USSR* **6**, 229–230.
- [226] LANDAU, L. D. & LIFSHITZ, E. M. 1959 *Fluid mechanics*, 1st edn. Pergamon Press.
- [227] LANG, WOLFGANG, COLONNA, PIERO & ALMBAUER, RAIMUND 2013 Assessment of waste heat recovery from a heavy-duty truck engine by means of an ORC turbo-generator. *J. Eng. Gas Turbine Power* **135** (4), 042313.
- [228] LAPPLE, C. E. & SHEPHERD, C. B. 1940 Calculation of particle trajectories. *Ind. Eng. Chem.* **32** (5), 605–617.
- [229] LAVISION INC. 2015 Davis, version 8.3.0.
- [230] LECOMPTE, S., GUSEV, S., VANSAMBROUCK, B. & PAEPE, MICHEL DE 2018 Experimental results of a small-scale organic rankine cycle: Steady state identification and application to off-design model validation. *Appl. Energy* **226**.
- [231] LEMMON, E. W., HUBER, M. L. & MCLINDEN, M. O. 2013 NIST standard reference database 23: Reference fluid thermodynamic and transport properties-REFPROP, version 9.1.
- [232] LESLIE, N. P., ZIMRON, O., SWEETSER, R. S. & STOVALL, T. K. 2009 Recovered energy generation using an organic Rankine cycle system. *ASHRAE Transactions* **115 (Part I)**, 220–230.
- [233] LETTIERI, C., SUBASHKI, G. & SPAKOVSKY, Z. 2018 Modeling near critical and supercritical fuel injection and mixing in gas turbine applications. In *Proceedings of ASME Turbo Expo 2018*, p. 16.
- [234] LETTIERI, C., YANG, D. & SPAKOVSKY, Z. 2015 An investigation of condensation effects in supercritical carbon dioxide compressors. *J. Eng. Gas Turbine Power* **137** (8).
- [235] LEUNG, J. C. & EPSTEIN, M. 1988 A generalized critical flow model for nonideal gases. *AIChE Journal* **34** (9), 1568–1572.

- [236] LEVEQUE, R. J. 2002 *Finite Volume Methods for Hyperbolic Problems*, 1st edn. Cambridge University Press.
- [237] LIU, H. W., FENG, Y. X., LIU, Z. L., GU, K. Y. & YAN, T. M. 2003 An experimental study on the dehumidification characteristics of a novel unit. In *The 10th Conference of Engineering Thermophysics Institute of Chinese Universities*, vol. 118.
- [238] LIU, Y. & DAUM, P. 2008 Relationship of refractive index to mass density and self-consistency of mixing rules for multicomponent mixtures like ambient aerosols. *J. Aerosol Sci.* **39** (11), 974–986.
- [239] LO, RONG-CHIN & TSAI, WEN-HSIANG 1995 Gray-scale Hough transform for thick line detection in gray-scale images. *Pattern Recognition* **28** (5), 647 – 661.
- [240] LOAR, J. 1994 *Control for the Process Industries*, vol. VII, no. 11. Putman Publications.
- [241] LORENTZ, H. A. 1880 Ueber die Beziehung zwischen der Fortpflanzungsgeschwindigkeit des Lichtes und der Körperdichte. *Ann. Phys.* **245** (4), 641–665.
- [242] LORENZ, L. 1880 Ueber die Refraktionsconstante. *Ann. Phys.* **247** (9), 70–103.
- [243] MACCHI, E. 1977 Design criteria for turbines operating with fluids having a low speed of sound. In *Lecture Series 100: Closed Cycle Gas Turbines*. Von Karman Institute for Fluid Dynamics, Rhode-Saint-Genèse - Belgium.
- [244] MAINI, R. & AGGARWAL, H. 2009 Study and comparison of various image edge detection techniques. *Int. j. image processing (IJIP)*.
- [245] MALIK, J. G. 1954 Interferometric studies of the refractive indices of some fluorine compounds. PhD thesis, Michigan State College.
- [246] MASQUELET, MATTHIEU M. 2006 Simulations of a sub-scale liquid rocket engine: Transient heat transfer in a real gas environment. Master's thesis, Georgia Institute of Technology.
- [247] MATHIJSEN, T. 2017 Experimental Observation of Non-Ideal Compressible Fluid Dynamics with Application in Organic Rankine Cycle Power Systems. PhD thesis, Delft University of Technology.
- [248] MATHIJSEN, T., GALLO, M., CASATI, E., NANNAN, N. R., ZAMFIRESCU, C., GUARDONE, A. & COLONNA, P. 2015 The Flexible Asymmetric Shock Tube (FAST): a Ludwig tube facility for wave propagation measurements in high-temperature vapours of organic fluids. *Exp. Fluids* **56** (10).
- [249] MCLALLIN, KERRY L., KOFSEY, MILTON G. & WONG, ROBERT Y. 1982 Cold-air performance of a 15.41-cm-tipdiameter axial-flow power turbine with variable-area stator designed for a 75-kW automotive gas turbine engine. *Technical Note*. National Aeronautics and Space Administration Lewis Research Center.

- [250] MEHTA, R. D. 1978 Aspects of the design and performance of blower tunnel components. PhD thesis, Imperial College London University: Department of Aeronautics.
- [251] MEHTA, R. D. & BRADSHAW, P. 1979 Design rules for small low speed wind tunnels. *Aeronaut. J.* **83** (827), 443–453.
- [252] MEHTA, U. B., EKLUND, D. R., PEARCE, JEFFREY A. & KEIM, NICHOLAS S. 2016 Simulation credibility: Advances in verification, validation, and uncertainty quantification. *Technical Publication* 2016–219422. Ames Research Center Moffett Field, California.
- [253] MEIER, G. E. A. & THOMPSON, P. A., ed. 1989 *Adiabatic Waves in Liquid-Vapor Systems*. International Union of Theoretical and Applied Mechanics.
- [254] MENDEZ, M. A., RAIOLA, M., MASULLO, A., DISCETTI, S., IANIRO, A., THEUNISSEN, R. & BUCHLIN, J.-M. 2017 POD-based background removal for particle image velocimetry. *Exp. Therm. Fluid Sci.* **80**, 181 – 192.
- [255] MENIKOFF, R. & PLOHR, B. J. 1989 The Riemann problem for fluid flow of real material. *Rev. Mod. Phys.* **61**.
- [256] MENTER, F. R. 1994 Two-equation eddy-viscosity turbulence models for engineering applications. *AIAA J* **32** (8), 1598–1605.
- [257] MERLE, X. & CINNELLA, P. 2015 Bayesian quantification of thermodynamic uncertainties in dense gas flows. *Reliab. Eng. Syst. Saf.* **134**, 305 – 323.
- [258] MERZKIRCH, W. 1987 *Flow Visualization*. Academic Press.
- [259] MICHELS, A. & HAMERS, J. 1937 The effect of pressure on the refractive index of CO<sub>2</sub>: The Lorentz-Lorenz formula. *Physica* **4** (10), 995–1006.
- [260] MILTENBURG, W. 2014 Plate properties and fluid distributions. A. J. Head, Personal Communication.
- [261] MISHRA, D. P. 2014 *Experimental Combustion: An Introduction*. CRC Press.
- [262] MOFFAT, R. J. 1988 Describing the uncertainties in experimental results. *Exp. Therm. Fluid Sci.* **1** (1), 3–17.
- [263] MOLDER, S. 1960 Head-on interaction of oblique shock waves. *Technical Note* 38. University of Toronto.
- [264] MONACO, J., CRAMER, M. & WATSON, L. 1997 Supersonic flows of dense gases in cascade configurations. *J. Fluid Mech* **330**, 31–59.
- [265] MOORE, M.J. & SIEVERDING, C.H. 1976 *Two-phase steam flow in turbines and separators: theory, instrumentation, engineering*. Hemisphere Pub. Corp.

- [266] MOORE, P. O. & JACKSON, C. N. 1998 Nondestructive testing handbook, vol 1. leak testing, 3rd edn. *Handbook*. The American Society for Nondestructive Testing.
- [267] MOREL, T. 1975 Comprehensive design of axisymmetric wind tunnel contractions. *J. Fluids Eng.* **97** (2), 225–233.
- [268] NANNAN, N. R., COLONNA, P., TRACY, C. M., ROWLEY, R. L. & HURLY, J. J. 2007 Ideal-gas heat capacities of dimethylsiloxanes from speed-of-sound measurements and ab initio calculations. *Fluid Phase Equilib.* **257** (1), 102–113.
- [269] NANNAN, N. R., GUARDONE, A. & COLONNA, P. 2013 On the fundamental derivative of gas dynamics in the vapor-liquid critical region of single-component typical fluids. *Fluid Phase Equilib.* **337** (15), 259–273.
- [270] NANNAN, N. R., GUARDONE, A. & COLONNA, P. 2014 Critical point anomalies include expansion shock waves. *Phys. Fluids* **26**, 021701.
- [271] NANNAN, NAWIN R., SIRIANNI, CORRADO, MATHIJSSSEN, TIEMO, GUARDONE, ALBERTO & COLONNA, PIERO 2016 The admissibility domain of rarefaction shock waves in the near-critical vapour-liquid equilibrium region of pure typical fluids. *J. Fluid Mech.* **795**, 241 – 261.
- [272] NANNAN, R. N. & COLONNA, P. 2009 Improvement on multiparameter equations of state for dimethylsiloxanes by adopting more accurate ideal-gas isobaric heat capacities: Supplementary to P. Colonna, N. R. Nannan, A. Guardone, E. W. Lemmon, *Fluid Phase Equilib.* **244**, 193 (2006). *Fluid Phase Equilib.* **280** (1–2), 151–152, short Communication.
- [273] NASSIKAS, A. A. & AKRITIDIS, C. B. 1991 Drying heat pump with supersonic separator. *Drying Technol.* **9** (4), 1105.
- [274] NATIONAL AERONAUTICS AND SPACE ADMINISTRATION (NASA) 2010 Measurement uncertainty analysis principles and methods. *Handbook* HDBK-8739.19-3. NASA.
- [275] NATTA, G. & FARINA, M. 1972 *Stereo Chemistry*. Longman Group Limited.
- [276] NICHOLS, L. R., NOZEK, S. M., WINZIG, C. H. & GOLDMAN, L. J. 1964 Experimental determination of sodium vapor expansion characteristics with inert gas injection pressure measuring technique. *Tech. Rep.* TN D-2276. NASA.
- [277] NISHIDA, M. 2001 Handbook of shockwaves. In *Shock Tubes and Tunnels: Facilities, Instrumentation, and Techniques. vol. 1*. Academic Press.
- [278] NORRIS, JOHN DE & PIERPONT, P. KENNETH 1966 Experimental performance of a conical pressure probe at Mach numbers of 3.0, 4.5, and 6.0. *Technical Note* D-3719. Langley Research Center.
- [279] OBERKAMPE, WILLIAM L. & AESCHLIMAN, DANIEL P. 1992 Joint computational/experimental aerodynamics research on a hypersonic vehicle. I - experimental results. *AIAA J* **30** (8), 2000–2009.



- [280] OBERKAMPE, W. L. & ROY, C. J. 2010 *Verification and Validation in Scientific Computing*. Cambridge University Press.
- [281] OBERKAMPE, W. L. & TRUCANO, T. G. 2002 Verification and Validation in Computational Fluid Dynamics. *Prog. in Aerosp. Sciences* **38** (3), 209–272.
- [282] OBERKAMPE, WILLIAM L., TRUCANO, TIMOTHY G. & HIRSCH, CHARLES 2004 Verification, validation, and predictive capability in computational engineering and physics. *Appl. Mech. Rev* **57** (5), 345–384.
- [283] OBERT, B. & CINNELLA, P. 2017 Comparison of steady and unsteady RANS CFD simulation of a supersonic ORC turbine. *Energy Procedia* **129**, 1063 – 1070.
- [284] OCKENDON, J. 1991 Nonequilibrium condensation in high-speed gas flows (Yuri A. Ryzhov, Ul'yan G. Pirumov, and Vladimir N. Gorbunov; V. A. Khokhrayakov, trans.). *SIAM Review* **33** (1), 159–160.
- [285] OPENCFD 2004 *OpenFOAM Programmer's Guide*.
- [286] OWEN, F. KEVIN & OWEN, ANDREW K. 2008 Measurement and assessment of wind tunnel flow quality. *Prog. Aerosp. Sci.* **44** (5), 315–348.
- [287] PACHECO, J. E., FAKHRI, S., VEZIER, C. & KOCH, J. M. 2013 LNG propane compressor performance prediction and large scale test validation. In *29th Pump Symposia*.
- [288] PAPANICOLAOU, E. & GOPALAKRISHNA, S. 1995 Natural convection in shallow, horizontal air layers encountered in electronic cooling. *Journal of Electronic Packaging* **117** (4), 307–316.
- [289] PASETTI, M., INVERNIZZI, C. M. & IORA, P. 2014 Thermal stability of working fluids for organic Rankine cycles: An improved survey method and experimental results for cyclopentane, isopentane and n-butane. *Appl. Therm. Eng.* **73** (1), 762–772.
- [290] PAXTON, D. 2016 Experimental characterization of condensation behavior for metastable carbon dioxide. Master's thesis, MIT.
- [291] PECNIK, R., RINALDI, E. & COLONNA, P. 2012 Computational fluid dynamics of a radial compressor operating with supercritical CO<sub>2</sub>. *J. Eng. Gas Turbine Power* **134** (12).
- [292] PECNIK, R., TERRAPON, V. E., HAM, F., IACCARINO, G. & PITSCH, H. 2012 Reynolds-Averaged Navier-Stokes Simulations of the HyShot II Scramjet. *AIAA J* **50** (8), 1717–1732.
- [293] PENG, DING-YU & ROBINSON, DONALD 1976 New two-constant equation of state. *Industrial & Engineering Chemistry Fundamentals* **15** (1), 59–64.
- [294] PFEIFFER VACUUM GMBH 2013 Leak detection compendium. *Tech. Rep.* 1.0. Pfeiffer.

- [295] JOURNAL OF PHYSICS: CONFERENCE SERIES, IOP PUBLISHING, ed. 2017 *Proceedings of the NICFD 2016 Seminar, 1st International Seminar on Non-Ideal Compressible-Fluid Dynamics for Propulsion & Power*, vol. 821.
- [296] PINI, M., AZZINI, L., VITALE, S. & COLONNA, P. 2019 A two-phase discrete adjoint method applied to the shape optimization of steam turbine cascades. *J. Turbomach.* **142** (11).
- [297] PINI, M., PERSICO, G., CASATI, E. & DOSSENA, V. 2013 Preliminary design of a centrifugal turbine for organic Rankine cycle applications. *J Eng Gas Turbine Power* **135**, 042312–1–9.
- [298] PINI, M., PERSICO, G., PASQUALE, D. & REBAY, S. 2015 Adjoint method for shape optimization in real-gas flow applications. *J. Eng. Gas Turbine Power* **137** (3).
- [299] PLANK, R. & KUPRIANOFF, J. 1929 Die thermischen Eigenschaften der Kohlensäure im gasförmigen, flüssigen und festen Zustand. *z. Ges. Kaiteind.* **1** (1).
- [300] POISSON, S.D. 1808 Mémoire sur la théorie du son. *J. École Polytech.* **VII**, 319–92.
- [301] POPE, A. 1961 Wind Tunnel Calibration Techniques. *Tech. Rep.* AG-54. NATO.
- [302] POPE, A. & GOIN, K. L. 1965 *High Speed Wnd Tunnel Testing*. John Wiley and Sons, new Jersey.
- [303] POPOVIĆ, IVAN, HODSON, HOWARD P., JANKE, ERIK & WOLF, TORSTEN 2013 The effects of unsteadiness and compressibility on the interaction between hub leakage and mainstream flows in high-pressure turbines. *J. Turbomach* **135** (6).
- [304] PRANDTL, L. 1933 Attaining a steady stream in wind tunnels. *Technical Memorandum* 726. NACA.
- [305] PREISSINGER, M. & BRUGGEMANN, D. 2016 Thermal stability of hexamethyldisiloxane (MM) for high-temperature organic Rankine cycle (ORC). *Energies* **9** (3), 183.
- [306] PRIGMORE, DARYL & BARBER, ROBERT 1975 Cooling with the sun's heat design considerations and test data for a Rankine cycle prototype. *Solar Energy* **17** (3), 185–192.
- [307] QUOILIN, SYLVAIN, BROEK, MARTIJN VAN DEN, DECLAYE, SÉBASTIEN, DEWALLEE, PIERRE & LEMORT, VINCENT 2013 Techno-economic survey of Organic Rankine Cycle (ORC) systems. *Renew. Sust. Energ. Rev.* **22** (0), 168 – 186.
- [308] RACHEDI, R. R., CROOK, L. & SOJKA, P. E. 2007 A study of supercritical jet fuel injection. In *Energy Systems: Analysis, Thermodynamics and Sustainability*, pp. 837–845.
- [309] RACHEDI, R. R., CROOK, L. C. & SOJKA, P. E. 2010 An experimental study of swirling supercritical hydrocarbon fuel jets. *J. Eng. Gas Turbine Power* **132** (8), 081502–081502–9.

- [310] RAGNI, D., SCHRIJER, F., VAN OUDHEUSDEN, B. W. & SCARANO, F. 2011 Particle tracer response across shocks measured by PIV. *Exp. Fluids* **50** (1), 53–64.
- [311] RANKINE, W. J. M. 1870 On the thermodynamic theory of waves of finite longitudinal disturbance. *Philos. Trans. R. Soc. Lond.* **18** (114–122).
- [312] RATHAKRISHNAN, E. 2019 *Applied gas dynamics*, 2nd edn. JohnWiley and Sons.
- [313] RAYLEIGH, J. W. S. LORD 1894 *Theory of sound*. Dover publications.
- [314] RAYLEIGH, J. W. S. L. 1910 Aerial plane waves of finite amplitude. *Proc. Roy. Soc.* **II**, 247–284.
- [315] RE, B. & GUARDONE, A. 2018 An adaptive ALE scheme for non-ideal compressible fluid dynamics over dynamic unstructured meshes. *Shock Waves* **29** (1), 73–99.
- [316] REINKER, F., HASSELMANN, K., AUS DER WIESCHE, S. & KENIG, E. Y. 2015 Thermodynamics and fluid mechanics of a closed blade cascade wind tunnel for organic vapors. *J. Eng. Gas Turbine Power* **138** (5), 052601.
- [317] REINKER, F., KENIG, E. Y., PASSMAN, M. & AUS DER WIESCHE, S. 2017 Closed loop organic wind tunnel (clowt): Design, components and control system. In *ASME ORC2017 - 4<sup>th</sup> International Seminar on ORC Power Systems - Milan 13 -15 september*, pp. 200–207.
- [318] REINKER, F., KENIG, E. Y. & AUS DER WIESCHE, S. 2018 CLOWT: A multifunctional test facility for the investigation of organic vapor flows. In *Proceedings of the ASME 2018 5th Joint US-European Fluids Engineering Summer Conference, Montreal 15 20 th June*.
- [319] REINKER, F., KENIG, E. Y. & AUS DER WIESCHE, S. 2019 Closed loop organic vapor wind tunnel (clowt): Commissioning and operational experience. In *ASME ORC2019 - 5<sup>th</sup> International Seminar on ORC Power Systems - Athens 09 -11 september*.
- [320] REINKER, F., WAGNER, R., HASSELMANN, K., AUS DER WIESCHE, S., FRITSCHKE, M., EPPLE, P. & RUSSWURM, H. J. 2019 Testing, modeling and simulation of fans working with organic vapors. In *Proceedings of 13th European Conference on Turbomachinery Fluid dynamics & Thermodynamics ETC13*.
- [321] REYNOLDS, W. C. & COLONNA, P. 2018 *Thermodynamics: Fundamentals and Engineering Applications*. Cambridge University Press.
- [322] RIEMANN, B. 1860 Über die Fortpflanzung ebener Luftwellen von endlicher Schwingungsweite. *Königl. Ges. Wiss.* **8**, 43–66.
- [323] RINALDI, E., PECNIK, R. & COLONNA, P. 2014 Exact Jacobians for implicit Navier-Stokes simulations of equilibrium real gas flows. *J. Comput. Phys.* **270**, 459–477.

- [324] RINALDI, E., PECNIK, R. & COLONNA, P. 2015 Computational fluid dynamic simulation of a supercritical CO<sub>2</sub> compressor performance map. *J. Eng. Gas Turb. Power* **137** (7), 072602.
- [325] RINALDI, ENRICO, PECNIK, RENE & COLONNA, PIERO 2016 Unsteady operation of a highly supersonic organic rankine cycle turbine. *J. Turbomach.* **138** (12).
- [326] RIX, JOACHIM, HAAS, STEFAN & TEIXEIRA, JOSÉ 1995 *Virtual Prototyping - Virtual environments and the product design process*. Springer US.
- [327] RIZZI, ARTHUR & VOS, JAN 1998 Toward establishing credibility in computational fluid dynamics simulations. *AIAA J* **36** (5), 668–675.
- [328] ROACHE, P. J. 1998 *Verification and Validation in Computational Science and Engineering*. Hermosa Publishers, Albuquerque.
- [329] ROACHE, P. J 2009 *Fundamentals of verification and validation*. Hermosa publ.
- [330] ROBERTSON, MILES, NEWTON, PETER, CHEN, TAO, COSTALL, AARON & MARTINEZ-BOTAS, RICARDO F. 2020 Experimental and numerical study of supersonic non-ideal flows for organic rankine cycle applications. *J. Eng. Gas Turbines Power* **142** (8), 081007.
- [331] ROBERTSON, MILES C., NEWTON, PETER J., CHEN, TAO & MARTINEZ-BOTAS, RICARDO F. 2019 Development and commissioning of a blowdown facility for dense gas vapours. In *ASME Turbo Expo 2019*, p. 14. ASME.
- [332] ROE, P. L. 1981 Approximate Riemann solvers, parameter vectors, and difference schemes. *J. Comput. Phys.* **43** (2), 357–372.
- [333] ROMBUSCH, U. K. 1962 Ein erweitertes korrespondenzprinzip zur Bestimmung von Zustandsgrößen. *Allg. Wärmetechnik Bd. 11* **43**, 175–184.
- [334] ROMEI, ALESSANDRO, VIMERCATI, DAVIDE, PERSICO, GIACOMO & GUARDONE, ALBERTO 2020 Non-ideal compressible flows in supersonic turbine cascades. *J. Fluid Mech.* **882**.
- [335] ROWLEY, R., WILDING, W., OSCARSON, J., YANG, Y., ZUNDEL, N., DAUBERT, T. & DANNER, R. 2004 *DIPPR Data compilation of pure chemical properties*. Design Institute for Physical Properties, AIChE, New York, NY.
- [336] ROY, C. & OBERKAMPE, W. 2010 A complete framework for verification, validation, and uncertainty quantification in scientific computing (invited). In *Aerospace Sciences Meetings*, p. 124. AIAA.
- [337] RUBINO, A., PINI, M., COLONNA, P., ALBRING, T., NIMMAGADDA, S., ECONOMON, T. & ALONSO, J. 2018 Adjoint-based fluid dynamic design optimization in quasi-periodic unsteady flow problems using a harmonic balance method. *J. Comput. Phys.* **372**, 220 – 235.

- [338] RUBINO, A., PINI, M., KOSEC, M., VITALE, S. & COLONNA, P. 2018 A look-up table method based on unstructured grids and its application to non-ideal compressible fluid dynamic simulations. *J. Comput. Sci.* **28**, 70 – 77.
- [339] RYZHENKOV, V. A., LEBEDEVA, A. I. & MEDNIKOV, A. F. 2011 Erosion wear of the blades of wet-steam turbine stages: Present state of the problem and methods for solving it. *Therm. Eng.* **58** (9), 713–718.
- [340] RYZHOV, Y. A., PIRUMOV, U. G. & GORBUNOV, V. N. 1989 *Nonequilibrium Condensation in High-Speed Gas Flows*. Gordon and Breach Science Publishers.
- [341] SATOSHI, U., WAKANA, T., YOICHI, K., NORIMASA, S. & TOSHIAKI, S. 2015 PIV measurement of carbon dioxide gas-liquid two-phase nozzle flow. In *ASME Proceedings: Symposium on Noninvasive Measurements in Single and Multiphase Flows*.
- [342] SAUER, R. O. 1946 Group and bond refractions in organosilicon liquids. *J. Am. Chem. Soc.* **68**, 954–62.
- [343] SCANIVALVE 2016 *Digital sensor array: DSA 3007, 3207, 3307 Series modules, Instruction and service manual*. Scanivalve Corp.
- [344] SCARANO, F. & RIETHMULLER, M. L. 1999 Iterative multigrid approach in PIV image processing with discrete window offset. *Exp. Fluids* **26** (6), 513–523.
- [345] SCARANO, F. & RIETHMULLER, M. L. 2000 Advances in iterative multigrid PIV image processing. *Exp. Fluids* **29** (1), S051–S060.
- [346] SCHNERR, G. & MOLOKOV, S. 1994 Exact solutions for transonic flows of dense gases in two-dimensional and axisymmetric nozzles. *Phys. Fluids* **6**, 3465.
- [347] SCHNERR, G. & MOLOKOV, S. 1995 Nonclassical effects in two-dimensional transonic flows. *Phys. Fluids* **7**, 2867.
- [348] SCHNERR, G. H. & LEIDNER, P. 1993a Two-dimensional nozzle flow of dense gases. In *ASME Symposium "Nonclassical Fluid Dynamics in Dense Gas and Two-Phase Flows"*, pp. 1–10.
- [349] SCHNERR, G. H. & LEIDNER, P. 1993b Numerical investigation of axial cascades for dense gases. In *PICAST'1–Pacific International Conference on Aerospace Science Technology*, pp. 818–825.
- [350] SCHNERR, G. H. & LEIDNER, P. 1994 Internal flows with multiple sonic points. In *Acta Mechanica, Supplement Issue No 4, edited by G. H. Schnerr, K. Bühler, R. Bohning, and W. Frank (Springer-Verlag, New York)*.
- [351] SCHUELER, C. J. 1960 An investigation of the model blockage for wind tunnels at Mach numbers 1.5 to 19.5. *Tech. Rep.* AEDC-TN-59-165. Arnold Air Force Station.

- [352] SERVI, C. DE, AZZINI, L., PINI, M., GANGOLI RAO, A. & COLONNA, P. 2017 Exploratory assessment of a combined-cycle engine concept for aircraft propulsion. In *Global Propulsion and Power Forum, Zurich, Switzerland*.
- [353] SETTLES, G. S. 2001 *Schlieren and Shadowgraph Techniques: Visualizing Phenomena in Transparent Media*. Springer-Verlag Berlin Heidelberg.
- [354] SIEVERS, U. & SCHULZ, S. 1982 Berechnung thermodynamischer Eigenschaften fluider gemische mit einer thermischen Zustandsgleichung unter Verwendung neuer Mischungs- und Kombinationsregeln (translation: Calculation of thermodynamic properties of fluid mixtures with a thermodynamic equation of state using new mixing and combination rules). *Forsch. Ing. - Wes* **48**, 143–153.
- [355] SOAVE, GIORGIO 1972 Equilibrium constants from a modified Redlich-Kwong equation of state. *Chemical Engineering Science* **27** (6), 1197 – 1203.
- [356] SONG, P., WEI, M., SHI, L., DANISH, S. N. & MA, C. 2015 A review of scroll expanders for organic Rankine cycle systems. *Appl. Therm. Eng.* **75**, 54 – 64.
- [357] SONODA, TOYOTAKA, ARIMA, TOSHIYUKI, OLHOFFER, MARKUS, SENDHOFF, BERNHARD, KOST, FRIEDRICH & GIESS, P.-A. 2006 A study of advanced high-loaded transonic turbine airfoils. *J. Turbomach* **128** (4), 650–657.
- [358] SOONG, C.Y., TZENG, P.Y. & HSIEH, C.D. 2001 Numerical study of bottom-wall temperature modulation effects on thermal instability and oscillatory cellular convection in a rectangular enclosure. *International Journal of Heat and Mass Transfer* **44** (20), 3855 – 3868.
- [359] SPINELLI, A., A., GUARDONE, COZZI, F., CARMINE, M., CHELI, R., ZOCCA, M., GAETANI, P. & DOSSENA, V. 2015 Experimental Observation of Non-ideal Nozzle Flow of Siloxane Vapor MDM. In *3rd International Seminar on ORC Power Systems*.
- [360] SPINELLI, A., CAMMI, G., CONTI, C. C., GALLARINI, S., ZOCCA, M., COZZI, F., GAETANI, P., DOSSENA, V. & GUARDONE, A. 2019 Experimental observation and thermodynamic modeling of non-ideal expanding flows of siloxane MDM vapor for ORC applications. *Energy* **168**, 285 – 294.
- [361] SPINELLI, A., CAMMI, G., GALLARINI, S., ZOCCA, M., COZZI, F., GAETANI, P., DOSSENA, V. & GUARDONE, A. 2018 Experimental evidence of non-ideal compressible effects in expanding flow of a high molecular complexity vapor. *Exp. Fluids* **59** (8), 126.
- [362] SPINELLI, A., CAMMI, G., ZOCCA, M., GALLARINI, S., COZZI, F., GAETANI, P., DOSSENA, V. & GUARDONE, A. 2017 Experimental observation of non-ideal expanding flows of siloxane MDM vapor for ORC applications. *Energy Procedia* **129**, 1125 – 1132, 4th International Seminar on ORC Power Systems September 13-15th 2017.

- [363] SPINELLI, A., COZZI, F., CAMMI, G., ZOCCA, M., GAETANI, P., DOSSENA, V. & GUARDONE, A. 2017 Preliminary characterization of an expanding flow of siloxane vapor MDM. *Journal of Physics: Conference Series* **821** (1), 012022.
- [364] SPINELLI, A., COZZI, F., DOSSENA, V., GAETANI, P., ZOCCA, M. & GUARDONE, A. 2016 Experimental investigation of a non-ideal expansion flow of siloxane vapor MDM. In *ASME Turbo Expo 2016*, p. 9. ASME.
- [365] SPINELLI, A., DOSSENA, V., GAETANI, P., OSNAGHI, C. & COLOMBO, D. 2010 Design of a Test Rig for Organic Vapours. In *ASME Turbo Expo 2010*, pp. 109–120. ASME, Glasgow, UK.
- [366] SPINELLI, A., PINI, M., DOSSENA, V., GAETANI, P. & CASELLA, F. 2013 Design, Simulation, and Construction of a Test Rig for Organic Vapors. *J. Eng. Gas Turb. Power - T. ASME* **135** (4), 10.
- [367] STARZMANN, J., CASEY, M. M., MAYER, J. F. & SIEVERDING, F. 2013 Wetness loss prediction for a low pressure steam turbine using computational fluid dynamics. *Proceedings of the Institution of Mechanical Engineers, Part A: Journal of Power and Energy* **228** (2), 216–231.
- [368] VAN DER STELT, T.P, NANNAN, N. R & COLONNA, P 2012 The iPRSV equation of state. *Fluid Phase Equilib.* **330**, 24–35.
- [369] VAN DER STELT, T. P. & COLONNA, P. 2014 Experimental vapor pressures and thermodynamic models of perfluorocarbons PP80 and PP90. *Fluid Phase Equilib.* **370**, 50 – 57.
- [370] STOKES, G. 1848 On a difficulty in the theory of sound. *Philosophical Magazine* **33(III)**, 349–356.
- [371] STRYJEK, ROMAN & VERA, JUAN 1986 PRSV - An improved Peng-Robinson equation of state for pure compounds and mixtures. *Can J Chem Eng* **64**, 323 – 333.
- [372] TABOR, H. & BRONICKI, L. 1964 Establishing criteria for fluid for small vapor turbine. In *SAE National Transportation, Powerplant, Fuels, and Lubricants Meeting*. Baltimore - MD.
- [373] THOL, M., DUBBERKE, F. H., RUTKAI, G., WINDMANN, T., KÖSTER, A., SPAN, R. & VRABEC, J. 2016 Fundamental equation of state correlation for hexamethyldisiloxane based on experimental and molecular simulation data. *Fluid Phase Equilib.* **418**, 133–151.
- [374] THOMPSON, P. A. 1971 A fundamental derivative in gasdynamics. *Phys. Fluids* **14** (9), 1843–1849.
- [375] THOMPSON, P. A. 1988 *Compressible Fluid Dynamics*. McGraw-Hill.
- [376] THOMPSON, P. A. 1991 Liquid-vapor adiabatic phase changes and related phenomena. In *Nonlinear Waves in Real Fluids*, pp. 147–213. Vienna: Springer Vienna.

- [377] THOMPSON, P. A., CAROFANO, G. C. & KIM, YOON-GON 1986 Shock waves and phase changes in a large-heat-capacity fluid emerging from a tube. *J. Fluid Mech.* **166**, 57–92.
- [378] THOMPSON, PHILIP A. & KIM, YOON-GON 1983 Direct observation of shock splitting in a vapor–liquid system. *Phys. Fluids* **26** (11), 3211–3215.
- [379] THOMPSON, P. A. & LAMBRAKIS, K. C. 1973 Negative shock waves. *J. Fluid Mech.* **60** (1), 187–208.
- [380] THOMPSON, P. A. & SULLIVAN, D. A. 1975 On the possibility of complete condensation shock waves in retrograde fluids. *J. Fluid Mech.* **70** (4), 639–649.
- [381] THORLEY, A. R. D. & TILEY, C. H. 1987 Unsteady and transient flow of compressible fluids in pipelines—a review of theoretical and some experimental studies. *Int J Heat Fluid Flow* **8** (1), 3 – 15.
- [382] TORO, E. F. 2009 *Riemann Solvers and Numerical Methods for Fluid Dynamics A Practical Introduction*. Springer, Berlin, Heidelberg.
- [383] TROPEA, C., YARIN, A. L. & FOSS, J. F. 2007 *Springer Handbook of Experimental Fluid Mechanics*. Springer-Verlag Berlin Heidelberg.
- [384] UUSITALO, ANTTI, TURUNEN-SAARETI, TEEMU, HONKATUKIA, JUHA, COLONNA, PIERO & LARJOLA, JAAKKO 2013 Siloxanes as Working Fluids for Mini-ORC Systems Based on High-Speed Turbogenerator Technology. *J. Eng. Gas Turbine Power* **135** (4), 9.
- [385] VALORI, V. 2017 Rayleigh-Bénard convection of a supercritical fluid: (PIV) and heat transfer study. PhD thesis, Delft University of Technology.
- [386] VARIOUS AUTHORS 2019 MATLAB version 9.7.0.1261785 (R2019b) Update 3. *Software*. The MathWorks, Inc.
- [387] VENKATAKRISHNAN, V. 1995 Convergence to steady state solutions of the Euler equations on unstructured grids with limiters. *J. Comput. Phys.* **118** (1), 120–130.
- [388] VERNEAU, A. 1987 Supersonic turbines for organic Rankine cycles from 3 to 1300 kW. In *Lecture series 1987-07: Small high pressure ratio turbines*. Von Karman Institute for Fluid-Dynamics, Rhode-Saint-Genèse - Belgium.
- [389] VIMERCATI, DAVIDE, KLUWICK, ALFRED & GUARDONE, ALBERTO 2018 Oblique waves in steady supersonic flows of bethe-zel’dovich-thompson fluids. *J. Fluid Mech.* **855**, 445–468.
- [390] VITALE, S., ALBRING, T. A., PINI, M., GAUGER, N. R. & P., COLONNA 2017 Fully turbulent discrete adjoint solver for non-ideal compressible flow applications. *J. Glob. Power Propuls. Soc.* **1**, 252–270.



- [391] VITALE, S., GORI, G., PINI, M., GUARDONE, A., ECONOMON, T. D., PALACIOS, F., ALONSO, J. J. & COLONNA, P. 2015 Extension of the SU2 open source CFD code to the simulation of turbulent flows of fluids modelled with complex thermophysical laws. In *Proceedings of the 22<sup>nd</sup> AIAA computational fluid dynamics conference*, pp. 1–12. American Institute of Aeronautics and Astronautics.
- [392] VOS, J. B., RIZZI, A., DARRACQ, D. & HIRSCH, E. H. 2002 Navier-stokes solvers in european aircraft design. *Prog. Aerosp. Sci.* **38** (8), 601–697.
- [393] VAN DER WAALS, J. D. 1873 Over de continuïteit van den gas- en vloeistoestand. PhD thesis, Leiden.
- [394] WALKER, M. & OBERKAMPE, W. 1991 Joint computational experimental aerodynamics research on a hypersonic vehicle. II - computational results. In *29<sup>th</sup> Aerospace Sciences Meeting*. American Institute of Aeronautics and Astronautics.
- [395] WARRICK, E. L. 1946 The application of bond refractions to organo-silicon chemistry. *Journal of the American Chemical Society* **68** (12), 2455–2459.
- [396] WEITH, T., HEBERLE, F., PREISSINGER, M. & BRUGGEMANN, D. 2014 Performance of siloxane mixtures in a high-temperature organic Rankine cycle considering the heat transfer characteristics during evaporation. *Energies* **7**, 5548–5565.
- [397] WELLER, H., TABOR, G., JASAK, H. & FUREBY, C. 1998 A tensorial approach to computational continuum mechanics using object oriented techniques. *Computers in Physics* **12**, 620.
- [398] WESTERWEEL, J. & SCARANO, F. 2005 Universal outlier detection for PIV data. *Exp. Fluids* **39** (6), 1096–1100.
- [399] WEYL, F. 1945 Analytical methods in optical examination of supersonic flow. *Tech. Rep.* Navord Report 211-45. US Navy Bureau of Ordnance.
- [400] WEYL, HERMANN 1949 Shock waves in arbitrary fluids. *Commun. Pure Appl. Math* **2** (2-3), 103–122.
- [401] WHEELER, ANDREW P. S. & ONG, JONATHAN 2013 The role of dense gas dynamics on ORC turbine performance. In *ASME Turbo Expo 2013*, p. 10. ASME.
- [402] WHITE, M. T. & SAYMA, A. I. 2018 Design of a closed-loop optical access supersonic test facility for organic vapors. In *Proceedings of ASME Turbo Expo 2016*, p. 13. ASME.
- [403] WIENEKE, B. 2015 PIV uncertainty quantification from correlation statistics. *Meas Sci Technol* **26** (7).
- [404] WILLERT, C. E. & GHARIB, M. 1991 Digital particle image velocimetry. *Exp. Fluids* **10** (4), 181–193.

- [405] WINTER, M. 2013 Benchmark and validation of open source CFD codes, with focus on compressible and rotating capabilities, for integration on the SimScale platform. Master's thesis, Chalmers University of Technology / Department of Applied Mechanics.
- [406] WOISETSCHLÄGER, J. & GÖTTLICH, E. 2008 Recent applications of particle image velocimetry to flow research in thermal turbomachinery. In *Particle Image Velocimetry* (ed. Andreas Schroder & Christian E. Willert). Springer-Verlag Berlin Heidelberg New York.
- [407] WOISETSCHLAGER, J., PECNIK, R., GÖTTLICH, E., SCHENNACH, O., MARN, A., SANZ, W. & HEITMEIR, F. 2008 Experimental and numerical flow visualization in a transonic turbine. *J. Vis.* **11**, 95–102.
- [408] WOLF, T., KOST, F., JANKE, E., HASELBACH, F. & WILLER, L. 2010 Experimental and numerical studies on highly loaded supersonic axial turbine cascades. In *Proceedings of ASME Turbo Expo 2010*, pp. 1669–1676. ASME.
- [409] WOODLAND, B. J., BRAUN, J. E., GROLL, E. A. & HORTON, W. T. 2012 Experimental testing of an organic Rankine cycle with scroll-type expander. *Publications of the Ray W. Herrick Laboratories*. Paper 52.
- [410] YAMADA, TOMOYOSHI 1973 An improved generalized equation of state. *AIChE J.* **19** (2), 286–291.
- [411] YANG, D. 2014 Experimental assessment of the internal flow behavior of supercritical carbon dioxide. Master's thesis, Massachusetts Institute of Technology.
- [412] ZAMFIRESCU, C., GUARDONE, A. & COLONNA, P. 2006 Preliminary design of the FAST dense gas Ludwig tube. In *9th AIAA/ASME Joint Thermophysics and Heat Transfer Conference*.
- [413] ZAMFIRESCU, C., GUARDONE, A. & COLONNA, P. 2008 Admissibility region for rarefaction shock waves in dense gases. *J. Fluid Mech.* **599**, 363–381.
- [414] ZEL'DOVICH, Y.B. 1946 On the possibility of rarefaction shock waves. *Zh. Eksp. Teor. Fiz.* **10** (4), 363–364.
- [415] ZÉMPLEN, G. 1905 Sur l'impossibilité des ondes de choc négatives dans les gaz. *C. R. Acad. Sci. Paris* **141**, Paris.
- [416] ZÉMPLEN, G. 1906 Sur l'impossibilité des ondes de choc négatives dans les gaz. *C. R. Acad. Sci. Paris* **142**, 142–143, Paris.
- [417] ZIEGLER, J. G. & NICHOLS, N. B. 1993 Optimum settings for automatic controllers. *J. Dyn. Sys., Meas., Control* **115** (2B), 220–222.
- [418] ZIPKIN, M. A. 1967 Alkali-metal, Rankine-cycle power systems for electric propulsion. *Journal of Spacecraft and Rockets* **4** (7), 852–858.

- [419] ZOCCA, M., GUARDONE, A., CAMMI, G., COZZI, F. & SPINELLI, A. 2019 Experimental observation of oblique shock waves in steady non-ideal flows. *Exp. Fluids* **60** (6), 101.
- [420] ZYHOWSKI, G. J. 2019 Honeywell refrigerants improving the uptake of heat recovery technologies. Available online: <http://www.honeywell-orc.com/wp-content/uploads/2011/09/Honeywell-Refrigerants-Improve-Uptake-Heat-Recovery-Technologies.pdf> [Accessed May 2015].

# ACKNOWLEDGEMENTS

There are many people who have accompanied me throughout this journey and without them this work could not have been achieved. What is work without family? First of all, to the love of my life Max Lammers. Thank you for your support, listening to the countless hours of complaints and participating in our work social environment. I could never have accomplished this without your encouragement. Secondly, I am thankful to my family: my parents, Benjamin Joseph Head and Kathryn Fay Head, because without them I would not be here, to say the least. Notably, our frequent video calls made the distance from home feel much closer. To my brother Luke and his wife Rachael and my little brother Joshua. It is a blessing to share your experiences and I hope to share more in the future. To my parents-in-law, Rita and Arno, thank you for the emotional support during our family gatherings.

To my friends, of course a bear-hug goes to Salvatore Vitale; a person who not only provided numerical expertise but also the psychological comforts during the hard times. **Thank you** Sebastian Bahamonde for the countless drinking sessions, dinners, movies and parties at Wolbodo. You are the analogous to a safety item on a process plant, e.g., a safety relief valve, for without them the process would not be safely regulated and suddenly explode. Similar can be said for our many conversations during our employment together.

The friends i made at *Menschenvereniging Wolbodo* kept me alive inside. The unfathomable amount of happiness and chaos generated at that place was priceless. Every person meant something to me, and I am honoured to have met you all. To Arend, Benjamin, Barry, Dexter, Gwen, Jelmer, Leslie, Lian, Lotte, Marinus, Max, Mike (the cook), Moniek, Naud, Niels S., Rienk, Roos, Ruben, Tim, and the countless newcomers. We spent many nice and often threw crazy parties together. A very special thanks goes to Remy. We often shared many interesting talks together and I enjoyed them considerably. Niels (Pluto) I really enjoyed your company when we were housemates, and loved keeping in contact long after we moved on. Marta, Marta, Marta, you never ceased to amaze me. Ever since we first met and even now your persistence and energy never reaches 0. Cheers to you Emiel, if patience and humbleness could be born into a beautiful shell you would take the cake. Thank you for the opportunity to be your friend and i hope to share many more memorable times in the future.

André I agree with your insights and solution to the many problems of this world. Who knows, perhaps we can enact them together. You have a good sense of humor. To Lucia and Nitish, it was really a pleasure to have known and worked with you and I sincerely hope that we share some more experiences together. Lastly, a special thanks to all the friends who encouraged and helped me achieve my goals: Tiemo, Maurice, Tomas, Tom, Francesco, Karthik, Marco, Matteo, Nando, Reno, Sonia, Sumit, Reynard, Imco, Antonio, Josh, and Roberto.

I want to thank Dr. Carlo de Servi for his patience, guidance, and help throughout the years. He has influenced my career by teaching me the work ethics and responsibilities, along with research skills, which are required of a good researcher. A special thanks goes to Wilfried Visser for he is the one who inspired me to pursue a Ph.D. degree and will always remain a long-term friend. I am grateful for the conversations and meetings I was able to secure with Fulvio Scarano, including the non-scientific ones. I appreciated our discussions since they were valuable to my research path; I wish I exploited your advice more frequently. Thank you Mauro Gallo for your help in the initial years of my Ph.D. and to Ferdinand Schrijer and Matteo Pini for their invaluable scientific input regarding the gas dynamic studies, arguably the most important scientific contributions I was able to communicate. To Richard Dwight for the few discussions on verification and validation of CFD codes.

The **countless** technical difficulties would not have been overcome without the support of four very important people; namely, Paul Straatman, Steve van Herk, Jos Meurs, Henk-Jan Siemer. Paul's efforts exceeded that of anyone, which is most definitely against the mentality one has in industry — your persistence was duly appreciated. Steve contributed to many intricate design aspects of the ORCHID and often went that extra step to complete the work given the time constraints. Jos executed the construction of many technical systems and aspects key to enabling the possibility to conduct scientific research. Thank you Jos, I am eternally indebted to your competence. There are no words to express the amount of invaluable expertise Henk-Jan parted to me and thus to the construction of the ORCHID. Thank you Nando Timmer for the support and references concerning the design of the Nozzle TS. Furthermore, Maximilian Hombsch also provided useful tips regarding the design of the Nozzle TS. Out of the many contributors to the realisation of the ORCHID Gert-Jan was the life-saver. We worked countless hours to "mop up" the numerous blunders made by personnel of the main contractor and subcontractors. A warm and hearty thanks to you, Peter Batenburg, for your creativity and assistance designing the ORCHID's control system. Your attention to detail and willingness to understand the problem at hand is something in rare supply today. I also appreciate the meticulous reviews you made of my thesis. Thank you Stefan aus der Wiesche for our motivational talks.

I would like to respectfully express my distaste towards CRE (formerly FMVG), the facility management and services of our faculty. You provided countless hurdles throughout my time here and working with you was simply an endless nightmare.

Last but not least, Prof. Piero Colonna. The unfathomable amount of enthusiasm for your work and dedication to your students is simply not measurable. I have learnt many valuable skills from you, which I am certain will allow me to advance my career. On a personal level, we have both been riding a roller coaster with a complex track. There have been many difficult and exciting moments. Upward and downward motions, side-way movements, which have left feelings of suspension, but always eventual relief. Thank you for the journey we travelled together.

The research work was conducted in the framework of two research programs on mini-ORC systems funded by the Dutch Technology Foundation STW and the partners Dana-Spicer Corp. and Robert Bosch GmbH (grant numbers 12811 and 13385). The financial support is gratefully acknowledged.



# CURRICULUM VITÆ

Name: Adam J. Head  
Born: 13/02/1988 in Laura, Australia.  
Voice: +31 (0)636184838  
E-mail: adam.head@uqconnect.edu.au  
WWW: [www.tudelft.nl/staff/a.j.head/](http://www.tudelft.nl/staff/a.j.head/)

Adam obtained his undergraduate education from the University of Queensland (UQ Australia) in 2012. A dual major in (Mechanical and Aerospace) engineering and a single major in (Applied mathematics) science was obtained with 1st class honours. He participated in a two year exchange program with the Delft University of Technology. Master coursework was undertaken from various faculties to accommodate the degree titles with an industrial based thesis undertaken at Micro Turbine Technology (MTT b.v. Eindhoven). The thesis involved a close collaboration with the automotive department of Netherlands Organisation for Applied Scientific Research (TNO). Shortly after graduation Adam relocated to the Netherlands in search for work in the Aerospace sector and proceeded to publish several European sanctioned reports dealing with Gas Turbine Performance. At the end of 2013 Adam was successfully appointed as a PhD candidate under the doctoral adviser Piero Colonna.



## RESEARCH INTERESTS

Gas dynamic experiments, laser diagnostics, gas turbine performance, trending analysis, waste heat recover and renewable energy power systems.

## WORKING EXPERIENCE

- |                 |  |
|-----------------|--|
| 01/2009–12/2009 | UQ, Brisbane, Australia<br>Teaching Assistant  |
| 08/2011–03/2012 | Micro Turbine Technology b.v., Eindhoven, The Netherlands<br>Heat transfer calculations between the system components of a mini gas turbine. |



## EDUCATION

2009–2012	Bachelor degree in Mechanical and Aerospace Engineering The University of Queensland (UQ), Australia GPA: 6.4/7 (1st Class Honors)
2010–2012	Bachelor degree in Applied Mathematics The University of Queensland (UQ), Australia GPA: 6/7
2014–2021	Ph.D. in Renewable Energy Systems Technische Universiteit Delft, Aerospace Engineering The Netherlands  <i>Thesis:</i> Novel Experiments for the Investigation of Non-Ideal Compressible Fluid Dynamics: The ORCHID and First Results of Optical Measurements.  <i>Promotor:</i> Prof. dr. P. Colonna

## AWARDS

2012	Deans accreditation for high achievement
------	--

## PUBLICATIONS

### CONFERENCE

1. **Head, A.J.**, De Servi C, Casati E, Pini M, Colonna P (2016) Preliminary design of the ORCHID: A facility for studying non-ideal compressible fluid dynamics and testing ORC expanders. In: ASME Turbo Expo, GT2016-56103, p 14
2. **Head, A.J.**, Visser, W. 2012. Scaling 3 - 36 kW Microturbines. In: ASME Turbo Expo, GT2012-68685, p 10
3. **Head, A. J.**, Iyer, S., de Servi, C., Pini, M. (2017) Towards the validation of a CFD solver for Non-Ideal compressible flows. IV International Seminar on ORC Power Systems.
4. Gori, G., Guardone, A., Vitale, S., **Head, A.J.**, Pini, M., Colonna, P. 2015. Non-Ideal compressible fluid dynamics simulation with SU2: Numerical assessment of nozzle and blade flows for organic Rankine cycle applications. In: 2015 International Seminar on ORC Power Systems
5. Keep, J. A., **Head, A.J.**, and Jahn, I. H., Design of an efficient space constrained diffuser for supercritical CO2 turbines. In: Journal of Physics: Conference Series, 2017

### JOURNALS

1. **Head, A. J.**, Novara, M., Gallo, M., Schrijer, E, Colonna, P. (2019) Feasibility of Particle Image Velocimetry for Low-Speed Unconventional Vapor Flows. Experimental Thermal and Fluid Science 102:589-594

2. Beltrame, F., **Head, A. J.**, de Servi, C., Pini, M., Schrijer, E., Colonna, P. (2021) First Experiments and Commissioning of the ORCHID Nozzle Test Section. In: Pini M., De Servi C., Spinelli A., di Mare F., Guardone A. (eds) Proceedings of the 3rd International Seminar on Non-Ideal Compressible Fluid Dynamics for Propulsion and Power. NICFD 2020. ERCOF-TAC Series, vol 28. Springer, Cham.
3. **Head, A. J.**, Beltrame, F., de Servi, C., Schrijer, E., Colonna, P. (2021) An expanding flow of MM. Experiments in Fluids (In submission)
4. **Head, A. J.**, Bills, L., Casati, E., Pini, M., Colonna, P. (2021) Validation of SU2. Physica (In submission)
5. **Head, A. J.**, de Servi, C., Casati, E., Colonna, P. (2021) Commissioning of the ORCHID. Experimental Thermal and Fluid Science (In submission)

## TECHNICAL REPORTS

1. Visser, W., **Head, A.J.**, Engine simulation models for the cycles of BE1 and report on obtained performance data. Technical Report
2. Visser, W., **Head, A.J.**, Engine Health Monitoring Demonstrator based on GPA. Technical Report
3. **Head, A.J.**, De Servi, C., Casati, E., Colonna, P., Design specifications and requirements of the ORCHID set-up: version 1.1. Technical Report
4. Ascione, E., Giuffrè, A., **Head, A.J.**, Abouelfotoh, De Servi, M. C., Colonna, P., Design specifications and requirements of the IRIS Facility: version 1.0. Technical Report

## INTERNSHIP ASSIGNMENTS

This section includes all the students for which I had the supervisory role.

*Sven Hockers*

**January, 2021**

Title: Environmental Control Systems for Aircraft: Instrumentation, Data Acquisition and Operational Fluid Handling Procedures.

*Michiel van der Groen*

**January, 2021**

Title: The Design of a Cascade Vapor Tunnel Test Section.

*Arnold Sukiato*

**January, 2021**

Title: General Arrangement of an Environmental Control System for Aircraft Applications.

*Emil Haur*

**January, 2021**

Title: Detailed Design of Rotating Cascade Test Section and Measurement Systems.

*Hendrik Aartse Tuijn-Barnwell*

**July, 2021**

Title: Detailed Design and General Arrangement of a Lab-Scale Vapor Compression Cy-

cle Facility.

*Masud Bin Mamun*

**July, 2021**

Title: Refractive Index and Point-wise Derived Density Measurements in Solid Materials and Organic Fluids.

*Zoltan Boros*

**July, 2021**

Title: Point-wise Density Measurements in a Low-speed Organic Vapor Flow.

*Noel Oosterling*

**July, 2021**

Title: Definition of control and operational procedures of a vapour compression cycle facility and development of a LabView Human Machine Interface.

*Leo Dragan*

**July, 2021**

Title: Detailed Design and General Arrangement of a Heat Exchanger Test Bed for Vapor Compression Systems with Application to Helicopters: Instrumentation, Data Acquisition and Design.

*Dardi Zuna*

**July, 2021**

Title: Mechanical Design of a Linear Blade Cascade.

## BACHELOR STUDENT THESES

This section includes all the students for which I had the supervisory role.

*Gabriel De Souza*

**January, 2021**

Thesis Title: Detailed Design of a Heat Exchanger Test Bed for Studying Performances of Environmental Control Systems on-board of Aircraft.

Graduated Bachelor of Science: Aeronautical Engineering.

## MASTER STUDENT THESES

This section includes all the students for which I had a primary supervisory role.

*Tony Chew*

**January, 2015**

Thesis Title: Design of Small Scale Shockwave Generators for the ORCHID.

Graduated Master of Science: Mechanical Engineering, University of Queensland.

*Siddharth Iyer*

**February, 2016**

Thesis Title: Influence of Thermodynamic Property Perturbations on Nozzle Design and Non-Ideal Compressible Flow Phenomena.

Graduated Master of Science: Mechanical Engineering, TU Delft.

*Harshil Lakkad*

**October, 2017**

Thesis Title: NICFD and the PIV technique: Feasibility in low speed and high speed flows.  
Graduated Master of Science: Mechanical Engineering, TU Delft.

*Fabio Beltrame*

**April, 2020**

Thesis Title: Accuracy assessment of the SU2 flow solver for Non-Ideal Organic Vapor Supersonic Expansions using Experimental Data.  
Graduated Master of Science: Aerospace Engineering, University of Turin.

*Liam Bills*

**June, 2020**

Thesis Title: Validation of the SU2 flow solver for classical NICFD.  
Graduated Master of Science: Aerospace Engineering, TU Delft.

*Dominic Dijkshoorn*

**September, 2020**

Thesis Title: Simulation of Two-Dimensional Steady State Boundary Layers Applied to Non-ideal Gas Flows.  
Graduated Master of Science: Mechanical Engineering, TU Delft.

*Riccardo Vello*

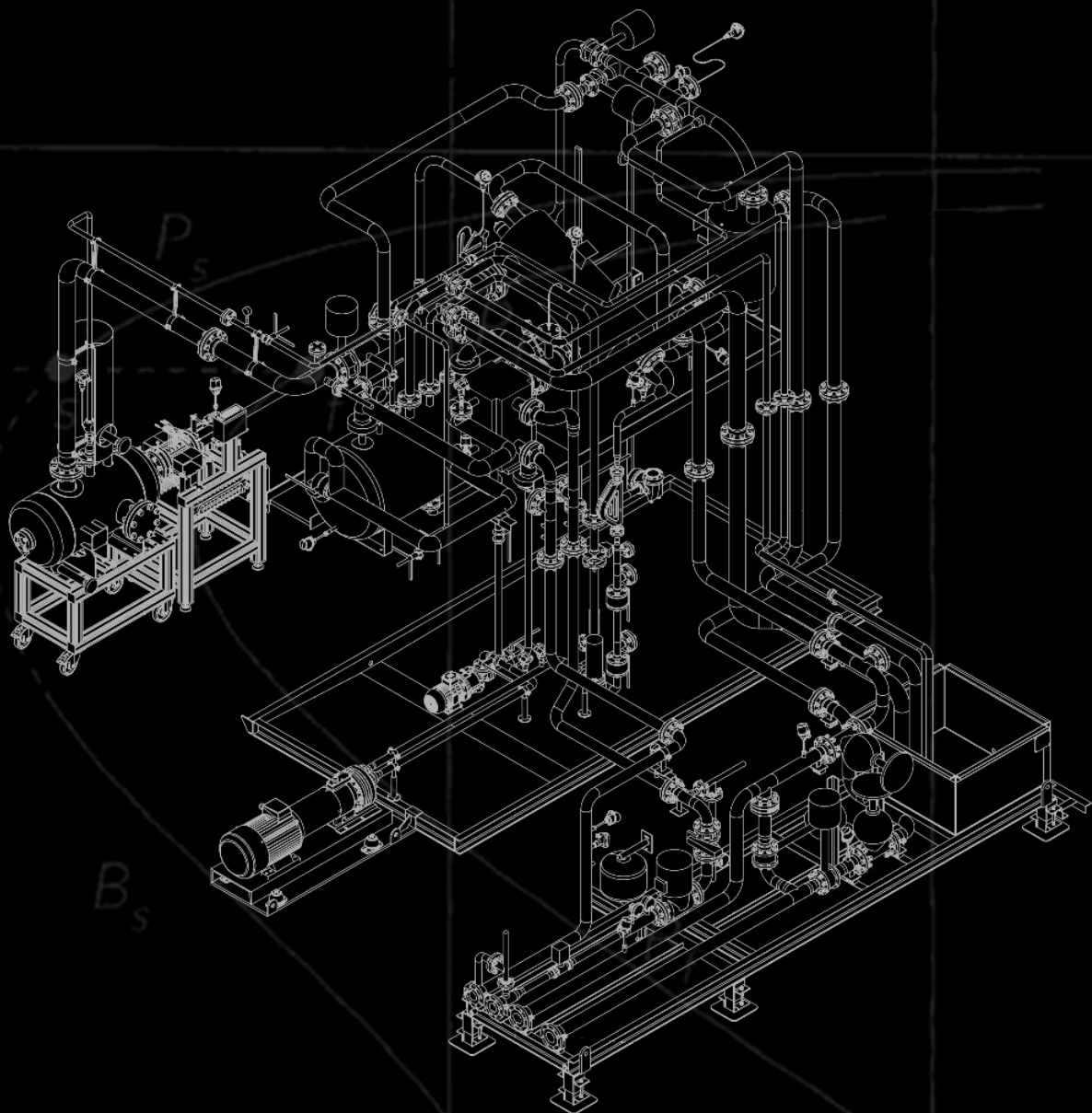
**July, 2021**

Thesis Title: A Validation Infrastructure for Non-Ideal Compressible Fluid Dynamics with applications to ORC Turbines.  
Master of Science: Aerospace Engineering, TU Delft.

*Gayathri Hariharan*

**December, 2021**

Thesis Title: Design of Experiments for an ORC Linear Turbine Cascade.  
Master of Science: Aerospace Engineering (In progress).



 **TU Delft**